Dynamics of glacier surges in High Mountain Asia from satellite remote sensing observations

Luc Beraud

THÈSE

Pour obtenir le grade de

DOCTEUR DE L'UNIVERSITÉ GRENOBLE ALPES

École doctorale : STEP - Sciences de la Terre de l'Environnement et des Planètes
Spécialité : Sciences de la Terre et de l'Environnement
Unité de recherche : Institut des Géosciences de l'Environnement (IGE)

Etude de la dynamique des "surges" glaciaires dans les hautes montagnes d'Asie à partir de données satellitaires

Dynamics of glacier surges in High Mountain Asia from satellite remote sensing observations

Présentée par :

Luc BERAUD

Direction de thèse :

Fanny BRUN CHARGEE DE RECHERCHE, IRD	Directrice de thèse
Amaury DEHECQ CHARGE DE RECHERCHE, IRD	Co-encadrant de thèse

Rapporteurs :

Duncan QUINCEY
FULL PROFESSOR, University of Leeds
Emmanuel TROUVE
PROFESSEUR DES UNIVERSITES, Université de Chambéry

Thèse soutenue publiquement le **17 décembre 2025**, devant le jury composé de :

Olivier GAGLIARDINI, PROFESSEUR DES UNIVERSITES, Université Grenoble Alpes	Président
Fanny BRUN BARRIERE, CHARGEE DE RECHERCHE, IRD délégation Sud-Est	Directrice de thèse
Duncan QUINCEY, FULL PROFESSOR, University of Leeds	Rapporteur
Emmanuel TROUVE, PROFESSEUR DES UNIVERSITES, Université de Chambéry	Rapporteur
Rachel CARR, FULL PROFESSOR, Newcastle University	Examinatrice

Invités :

Amaury Dehecq
CHARGE DE RECHERCHE, Université Grenoble Alpes

Abstract

Glacier surges are sudden and exceptional events that affect certain glaciers in glaciated regions such as the Pamir and Karakoram mountains in High Mountain Asia, the Alaskan ranges and the Svalbard archipelago. A surge event is a pseudo-periodic instability in a glacier during which the flow velocity increases sharply and temporarily over part of the glacier, associated with a significant displacement of ice mass. Previous research has made it possible to accurately map glaciers that have experienced surges in recent decades, but there is still a lack of precise understanding of the mechanisms that lead to surge events.
As part of this thesis project, we first develop a Digital Elevation Model (DEM) post-processing workflow that filters and interpolates the elevation of the glacier surface each month, while preserving the sudden variations corresponding to surges. This processing workflow is applied to a dataset of DEMs with a spatial resolution of 100 m, obtained from the ASTER optical satellite sensor and covering the period from 2000 to 2019 in the High Mountain Asia. At the heart of this processing method, we use a locally weighted scatterplot smoothing (LOWESS) method to filter out erroneous elevations. We then interpolate each month the elevation at each point on the glacier using the B-spline method named ALPS-REML. The performance of the workflow and of the dataset produced is evaluated in particular by comparing the volumes of ice displaced during surge events already assessed in the scientific literature.
This unique dataset allows for a detailed study of the dynamics of a large number of surge events. We then combine these time series of thickness changes with a dataset of glacier surface flow velocities (ITS_LIVE) interpolated temporally using the TICOI method. Using these two datasets, we calculate the propagation velocity of the instability and the evolution of the driving stress for a large number of surge events. This allows us to confirm the existence of a relationship between the glacier slip velocity during the surge and the propagation velocity of the instability, as predicted by certain theoretical models. Furthermore, for a number of glaciers, we can observe a continuous increase in driving stress until the surge is triggered, followed by a sudden decrease, which agrees with the existence of a maximum stress threshold beyond which the surge is triggered. This allows us to estimate the area where the surge is triggered. These two points provide keys to validating certain existing theories concerning the physics and conditions that allow these surges to occur.

Résumé

Les *surges* de glaciers sont des événements soudains et exceptionnels, qui affectent certains glaciers de régions englacées comme les montagnes du Pamir et du Karakoram dans les Hautes Montagnes d'Asie, les chaînes de l'Alaska ou encore l'archipel du Svalbard. Une *surge*, terme anglais, est une instabilité pseudo-périodique d'un glacier au cours de laquelle la vitesse d'écoulement augmente fortement et temporairement sur une partie du glacier, associée à un déplacement important de masse de glace. Des travaux de recherche antérieurs ont permis de cartographier précisément les glaciers qui ont connu des *surges* au cours des dernières décennies, mais il manque encore une compréhension précise des mécanismes qui conduisent à ces évènements.

Dans le cadre de ce projet de thèse, nous avons tout d'abord développé une chaîne de post-traitement de Modèles Numériques de Terrains (MNT) qui permette de filtrer et d'interpoler l'altitude de la surface des glaciers en chaque mois, tout en préservant les variations soudaines correspondants aux évènements de *surges*. Cette chaîne de traitement est appliquée à un jeu de données de MNTs d'une résolution spatiale de 100 m qui sont issus du capteur satellitaire optique ASTER, et couvrent la période de 2000 à 2019 dans les Hautes Montagnes d'Asie. Au cœur de cette méthode de traitement, nous utilisons une méthode de lissage de nuages de points pondérée localement (LOWESS) pour filtrer les altitudes erronées. Puis, nous interpolons chaque mois l'altitude en chaque point du glacier avec une méthode de B-spline nommée ALPS-REML. Les performances de la chaîne de traitement et du jeu de données produit sont notamment évaluées par la comparaison de volumes de glace déplacés pendant des évènements de *surge* déjà évalués dans la littérature scientifique.

Ce jeu de données unique permet une étude détaillée de la dynamique d'un grand nombre d'évènements de *surge*. Nous combinons ensuite ces séries temporelles de changement d'épaisseur avec un jeu de données de vitesses de surface de l'écoulement du glacier (ITS_LIVE) interpolé temporellement grâce à la méthode TICOI. Avec ces deux jeux de données, nous calculons la vitesse de propagation de l'instabilité ainsi que l'évolution de la contrainte de cisaillement locale pour un grand nombre d'évènements de *surge*. Grâce à cela, nous pouvons confirmer l'existence d'une relation entre la vitesse locale de glissement du glacier durant la *surge* avec la vitesse de propagation de l'instabilité, comme prédit par certains modèles théoriques. De plus, pour un certain nombre de glaciers, nous pouvons observer l'augmentation continue de la contrainte de cisaillement locale jusqu'au déclenchement de la *surge* puis sa diminution soudaine, ce qui est en accord avec l'existence d'un seuil maximal de contrainte, au-delà duquel se déclenche la *surge*. Cela permet d'estimer la zone où l'instabilité se déclenche. Ces deux points permettent de donner des clés de validation de certaines théories existantes concernant la physique et les conditions qui permettent ces *surges*.

Acknowledgements

Commençons mon ouvrage de thèse par mentionner celles et ceux qui lui ont permis d'avoir cette forme.

Merci tout d'abord aux membres de mon jury, Olivier Gagliardini, Duncan Quincey, Emmanuel Trouvé et Rachel Carr, pour avoir accepté de lire et d'évaluer mon travail.

Fanny et Amaury, vous qui avez dirigé ma thèse, je ne saurais estimer combien vous m'avez apporté, à moi ainsi qu'à mon travail à vos côtés. Depuis nos premiers échanges, vous m'avez accompagné et initié, tantôt inspiré, tantôt relancé et guidé, tout au long de ces dernières années. Que ce soit lors de nos réunions, moments de vie dans le labo, sur le terrain et même en dehors du travail, votre duo bienveillant et avisé a largement contribué à faire de ces 3 années un plaisir. Je n'ai nul doute que je garderai trace de votre vision des choses, de votre positivité et manière d'être, quelques saines manies aussi. À tous les deux, merci pour ce bout de chemin ensemble !

Je souhaite aussi remercier toutes les personnes avec qui j'ai richement collaboré. Merci Laurane Charrier, Romain Hugonnet et Adrien Gilbert pour toutes vos réponses, commentaires et avis éclairés, vous avez indéniablement grandement apporté à mon travail. D'autres ont aussi contribué à mon projet au détour de discussions informelles ou lors de réunions, tels que Christoph Mayer, Pascal Lacroix, Etienne Berthier ou encore Patrick Wagnon. Je souhaite aussi en profiter pour mentionner plus particulièrement mes ancien.ne.s encadrant.e.s, qui lors de mes précédentes expériences ont façonné ma manière de travailler et mon envie de poursuivre dans la recherche, à qui je dois aussi mon parcours. J'ai eu la chance de pouvoir travailler systématiquement avec des personnes exceptionnelles, au premier rang desquelles Sophie Fabre, Rūta Abaja et Agris Brauns, Antoine Rabatel et – tient – à nouveau Fanny. Enfin, merci aux membres de mes équipes CryoDyn et C2H, mon bâtiment et mon labo ainsi que de mon école doctorale, du personnel administratif et d'entretien jusqu'aux chefs, qui contribuent à garantir un cadre de vie exceptionnel que je quitte à regret et avec qui j'ai partagé moults repas, sorties terrain et autres activités – Bruno, Anne, Adina, Vincent, Manon... bref quasiment le trombinoscope, finalement.

Si ces quelques années m'ont été aussi chères, c'est beaucoup le fait de toute la vie des non-permanents qui ont gravité autour de moi, parfois trop vite hélas. Car vous le devinez au travers de ces lignes, mes années de thèse à l'IGE n'ont pas été que du travail mais aussi du bon temps passé avec désormais des amis. Avec mes co-bureaux successifs tout d'abord, Ari, Juliette et Hortense, avec qui j'ai partagé tant de banalités, de discussions tantôt sérieuses tantôt légères, d'entraide parfois, et que j'étais content de retrouver tous les matins dans le bureau. Merci à elleux et à la floppée d'autres non-permanent.e.s – Olivier, Pierre, Ian, Sara, Laurane, Audrey, Hippolyte, Xavier, Ailsa, Clémence, Lei ... – j'ai passé avec vous tant de repas dehors au soleil (ou non), de pauses et de soirées dans la bonne ambiance, de baignades dans les cuves, de périples à vélo ou au bout d'une corde d'escalade. Et je sais qu'on aura d'autres sorties ensemble.

Et puis, merci à mes colocs (qui désormais méritent plus que ce terme) Claire et Oscar à qui j'en ai fait voir pas mal, la soutenance maintenant passée ils se rendent compte que ce n'était peut-être pas à cause de la thèse ; ainsi qu'à mes amis qui ont partagé de plus ou moins loin cette aventure, Clémence, Yanis, Charlotte, et d'autres. Un grand merci à Marion, qui m'a supporté toute ma thèse et qui continuera à le faire. Enfin, il est des gens que je ne voyais pas tous les jours mais qui m'ont tout de même soutenu, et même bien avant ma thèse, à eux aussi je leur dois mon parcours : ma famille et mes proches – mes parents bien sûr, mon frère et mes sœurs, Philippe et Catherine.

À vous toutes et tous, merci !

Contents

Introduction

Glaciers are widely regarded as a symbol of climate change, which is one of the ongoing environmental crises. The proportion of climate change attributable to human activity exceeds that attributable to natural climate variability, with significant consequences for populations, and current commitments are not sufficient to address the challenges (Intergovernmental Panel On Climate Change (Ipcc), 2023). In recent decades, glacier mass loss worldwide has accelerated, with an increase of 36 ±10% from the first to the second decade of the 21st century (The GlaMBIE Team et al., 2025). Between 2000 and 2023, the average annual mass balance of glaciers globally (Greenland and Antarctic ice sheets excepted) is -0.41 ±0.02 m w.e. $year^{-1}$, which corresponds to the melting of a 0.41 m layer of water across their entire surface on average. They have thus lost an average of 5% of their mass over this period compared to 2000, with significant differences depending on the region of the world (from 2 to 39%; The GlaMBIE Team et al. (2025)). Current forecasts estimate that, by 2100 and compared to their 2015 state, they will lose between 26 ±6% (for a global warming of +1.5°C[1]) and 41 ±11% (+4°C) of their mass, depending on the warming scenarios that are still possible (Rounce et al., 2023). The impacts could be particularly significant (rising sea levels, water scarcity, etc.), especially in the High Mountain Asia (HMA), which is the largest glacial area outside the polar regions and whose populations' dependence the ecosystem services provided by its glaciers is among the most critical in the world (RGI Consortium, 2023; Wester et al., 2019; Immerzeel et al., 2020). In this region, glaciers are expected to retain between 14% and 51% of their 2015 mass, depending on the mountain range, for an average scenario of +2.5°C (Rounce et al., 2023).
Although our knowledge is already extensive and the consensus unequivocal, there are still mechanisms that are not yet fully understood. This is particularly true of the physical laws that govern the movement of glaciers on the ground on which they rest, which determine the movement of their mass and therefore their future and their contribution to the various changes currently underway (IPCC, 2022; Minchew and Joughin, 2020; Thøgersen et al., 2019).

Glaciers are moving masses, their flow rates varying with climate, seasons and even weather conditions. The mountain glaciers of the HMA flow at rates ranging from a few metres per year to tens or even hundreds of metres per year (Millan et al., 2022). However, although their speed remains of the same order of magnitude from year to year, their flow can sometimes be unstable. One of the main instabilities in glacier flow is the phenomenon of surge[2]. Glacier surges are quasi-periodic disturbances in the flow, characterised by abnormally high speeds over several months to several years. They transport large amounts of ice, which can change the glacier thickness by several tens of metres in some places. Glaciers that are prone to surges alternate between periods of quiescence and periods of surge, during which their velocity can increase by a factor of approximately 5 to 1000.

[1] compared to pre-industrial levels (1850–1900)

[2] En français, *surge* (terme anglais) n'a pas de traduction claire et l'anglicisme *une surge* est souvent retenu. Sont parfois utilisés *une crue glaciaire*, *un foirage glaciaire* ou *une avancée catastrophique*. Le mot anglais *surge* peut littéralement se traduire par *une poussée*, *un afflux*.

They are concentrated in certain parts of the globe, such as Alaska-Yukon, Svalbard or in the high mountains of Asia. Glacier surges, as fascinating and impressive as they are sometimes dangerous, remain relatively mysterious despite the efforts of the glaciological community. We therefore know little about the reasons for this instability and the common physical mechanisms that exist between all these events. However, understanding this instability would certainly help us to better quantify the friction of all glaciers.
However, we can observe surges in an increasingly comprehensive manner thanks to Earth observation satellites, which cover the vast majority of the world's glaciers (Guillet et al., 2025). After processing, the images acquired by the satellites can be used to measure 1) the elevation of the glacier surface at a precise date, which permits estimating by difference the elevation change between two dates (i.e., the change in thickness), and 2) the flow velocity of the surface. This data allows for the observation of these variables in detail for a large number of glaciers (Hugonnet et al., 2021; Millan et al., 2022). However, satellite data on surges are difficult to process because the changes are significant and sudden, and the usual filtering methods are often imperfect.

While a number of individual cases of surges have been well studied, and we now have good knowledge of where they occur, we still lack a comprehensive understanding of their dynamics and the changes they undergo during a surge and between events. This could be particularly useful for validating or at least testing various theories that have recently been proposed in the scientific literature. These are the main objectives I have attempted to address in my thesis.
The aim of my work is to observe the dynamics of glacier surges in the high mountains of Asia using satellite remote sensing observations. I have formulated this in two scientific questions, which constitute the two main areas of my work:

- What glacier surge dynamics can we observe from temporally dense elevation time series?
- To what extent can we test existing models of surge onset and propagation using remote sensing data?

I carried out this work by observing 44 surge-type glaciers in the high mountains of Asia. This region is one of the largest cluster of surge-type glaciers and exhibits a wide variety of glacier and surge characteristics.

This thesis manuscript begins (Chapter 1) with an in-depth presentation of the scientific literature on surges, explaining in detail what is known about surges, particularly in HMA. Then, I present the development of a workflow for the processing of elevation time series, which allows us to estimate monthly changes in glacier thickness even during surges (Chapter 2). Finally, by combining these new elevation data with surface velocity data, I show what can be learned from comparing remote sensing data with one of the theories of surge mechanics (Chapter 3). I conclude this manuscript by addressing the scientific questions raised and proposing further research perspectives on the subject.

Chapter 1

Glacier surges in High Mountain Asia

This chapter is a literature overview of what we know about glacier surge events, especially in High Mountain Asia. We introduce this instability, how we observe it, the forms it takes in this region, and finally summarise what we know about the mechanisms that govern glacier surges.

1.1 Glacier dynamics

1.1.1 Glacier flow

Glaciers are formed by the accumulation of snow, which compresses and turns into ice. A glacier has an area of mass gain (accumulation zone) and an area of mass loss (ablation zone). Ice flows with a continuous redistribution of mass from the high-elevation accumulation zone to the low-elevation ablation zone (Fig. 1.1.a). This movement is mainly driven by gravity that exerts a force on the ice masses, in the direction of the glacier bed slope. Ice flow allows for a dynamical equilibrium of the glacier by transporting accumulated ice downstream, where melt is larger than accumulation.
As synthesised in Cuffey and Paterson (2010, p223-228), glaciers' ice velocity is the sum of the velocity originating from the ice deformation (*creep* due to ice viscosity), glacier sliding over the bed, and from the bed deformation in the case of a basal sediment till (Fig. 1.1.a). These three processes can co-exist, and we generally encompass sliding and bed deformation under the terms *basal motion* or *slip*. The slip ratio accounts for the share of the basal velocity in the surface velocity of a glacier, and ranges from 0% (pure deformation) to 100% (pure slip) (Cuffey and Paterson, 2010). However, the sliding laws are very different, depending on whether the subglacial bed is deformable till (*soft bed*) or bedrock (*hard bed*). A condition for rapid sliding over the bed is temperate basal ice (at the melting point). A deformable bed can also deform rapidly when saturated by water (Cuffey and Paterson, 2010). Ice deformation increases with thickness and is most important at the glacier bed, where the pressure of a high ice column is highest (Dehecq et al., 2022).
The surface velocity of mountain glaciers typically ranges between several metres and a few hundred metres per year (Millan et al., 2022). On marine-terminating glaciers or outlet glaciers of icecaps and large icefields, surface velocities are generally higher, commonly several kilometres per year. As the main driver of this flow is the mass of ice, at equilibrium, an increase of the ice thickness (increase of mass) will result in a faster flow velocity (e.g., Fig. 1.1.e, Cuffey and Paterson (2010, p288)). In contrast, mass loss such as that caused by global climate change typically leads to a slowdown of glaciers (Dehecq et al., 2019).

The forcing of the current climate change puts glaciers off balance by, overall, enhancing mass loss (through melting) and reducing mass gain (decrease in snowfall). Glaciers have inertia due to their mass and geometry, and the climate currently evolves faster than some glaciers can adapt, leading to global thinning and retreat of glaciers (The GlaMBIE Team et al., 2025; Hugonnet et al., 2021; Cuffey and Paterson, 2010, p113). As a consequence, there is a delay between mass loss and general slowdown of glaciers on a decadal scale (Dehecq et al., 2022).
The flow velocity of a glacier also evolves at much shorter time scales. Heavy rain and melt increase the basal water pressure, and then can increase glacier slip velocity at timescales of hours to months (Allstadt et al., 2015; Dehecq et al., 2022; Hart et al., 2019; Nanni et al., 2023; Togaibekov et al., 2024; Cuffey and Paterson, 2010, p490-491). In particular, glaciers with a basal interface at the melting point commonly have higher velocities in spring due to meltwater entering inefficient drainage systems and increasing the basal water pressure. The drainage system then becomes more efficient during the summer as water fluxes increase the size and connectivity of drainage conduits, initiating a decrease in velocity (Fig. 1.1.d; Abe and Furuya, 2015; Copland et al., 2003; Cuffey and Paterson, 2010, p183). Autumn accelerations have also been reported on several glaciers, likely due to the drainage of supraglacial ponds or the gradual closure of the hydrological system (e.g., Nanni et al., 2023). The two speedups propagate in an opposite way along the glacier, according to temperature decrease (autumn, propagating down-glacier) or increase (spring-summer, up-glacier) over the seasons (Nanni et al., 2023).

The propagation of speedups, related to changes in the state of the subglacial drainage system, illustrates that velocity vary spatially. Among other drivers, the topography of the bed, its type and its characteristics affect the flow velocity (Zoet and Iverson, 2020). For example, funnelling effects cause high velocity in narrow portions of the glaciers, and low velocities in large areas (typically the case in accumulation areas of valley glaciers). The slope of the bed is also an important driver of the flow velocity. Thus, areas of high slope are faster. Both funnelling and slope effects are illustrated in Fig. 1.1.b-c.
The flow varies particularly longitudinally, depending on glacier geometry (e.g., Fig. 1.1.b). The principles of mass conservation and the near-incompressibility of ice imply that the faster area of a glacier is around the transition between the accumulation and the ablation zones, called the equilibrium line. Thus, glacier margins (at the bergschrund and at the front, for land-terminating glaciers, i.e. without calving) are generally areas of very low velocity (e.g., Fig. 1.1.b). Ice also flows slower near the side edge of the glacier and close to the glacier bed, due to friction (Cuffey and Paterson, 2010, p344).

Despite spatial and temporal variability, the flow velocity of a glacier is generally similar from year to year. Over time, the ice flow mainly evolves with long-term forcing (e.g., change in climate) or with seasonal cyclic patterns. However, it appears that unstable behaviours may occur on rare events, from punctual speedups to glacier collapse that can have dramatic effects and remain quite unpredictable (Kääb et al., 2021).

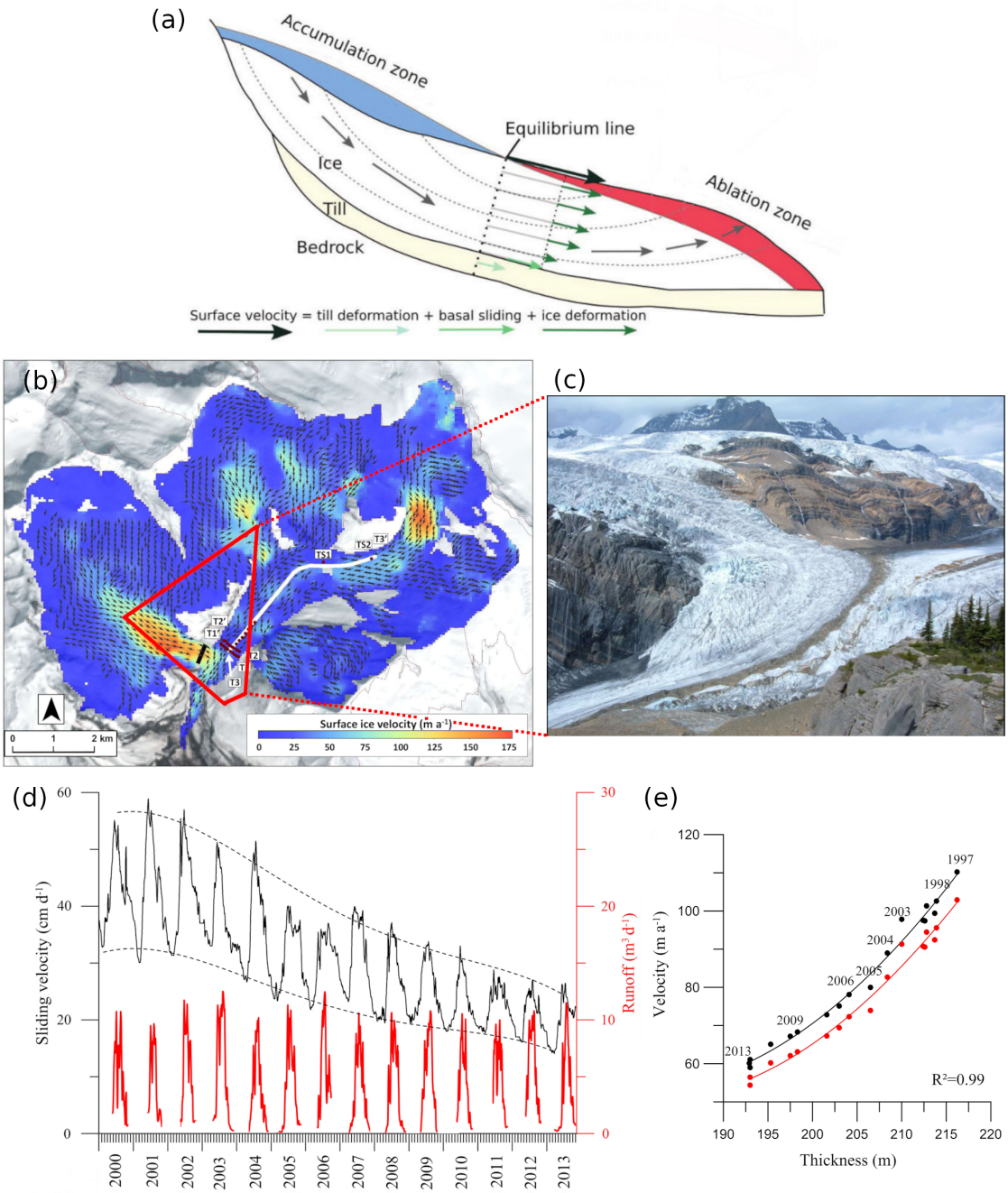

Figure 1.1: Illustrations of the flow of glaciers. (a) Longitudinal representation of ice velocity in a glacier, adapted from Dehecq et al. (2022). The size of the arrows shows the velocity amplitude, according to each displacement mode in color. (b) Surface flow velocity of Shackleton Glacier (British Columbia, Canada) derived from the satellite Radarsat 2. The flow direction is represented with arrows (only for speeds >15 m year^{-1}). The red area corresponds to the footprint of the photography (c). Panels (b) and (c) are adapted from Jiskoot et al. (2017). Panels (d) and (e) are velocity data from the bottom of Argentière glacier (Alps, Europe), adapted from Vincent and Moreau (2016). Panel (d) shows the measured basal sliding velocities and the subglacial runoff, panel (e) shows the measured annual surface velocity (black) and estimated sliding velocity (red), about 700 m upstream of the measurements of (d).

1.1.2 Glacier surges

One of the main glacier instabilities is the surge phenomenon. Surge events are quasi-periodic flow perturbations characterised by an abnormally fast flow over several months to years (e.g., Fig. 1.2). Large masses of ice are transported during surges, causing important thickness changes (e.g., Fig. 1.3; Bhambri et al., 2017, 2022). Surge cycles are divided into two main phases: quiescence and surge. The quiescent phase is long and characterised by low ice velocities. It includes a buildup period (or mass gain) in an elevated reservoir area. It is followed by a short surge phase with a local velocity increase of usually 1 to 3 orders of magnitude and a mass redistribution to lower reaches, from a reservoir area to a receiving area (Fig. 1.4 and Fig. 1.2).
The area between the reservoir and the receiving areas is called the dynamic balance line, which shows limited elevation change although the transported ice mass flows through it (e.g., Fig. 1.4; Kochtitzky et al., 2019). Its location sometimes moves downstream during the surge, due to changes in driving stress (Burgess et al., 2012). Surges often, but not always, result in spectacular and sudden front advances of the glaciers (e.g., Fig. 1.3; Hewitt, 2005). The glacier front advance is not related to the glacier length, with some large glaciers showing no front advance during their surge (e.g., Hispar glacier, around 50 km long), whereas small ones could have important front advances relative to their size (e.g., NN9 glacier advancing at least 1.8 km for a pre-surge length below 3.7 km, about +50%) (Paul et al., 2017; Goerlich et al., 2020; Paul, 2020). Small glaciers may even undergo the largest surface displacement (i.e., distance over which ice is transported during surge, not limited to glacier front advance in the study) in proportion to their total length than large glaciers (Herreid and Truffer, 2016).

There is no consensual and precise definition of surge events (Herreid and Truffer, 2016). The surge phenomenon is thought to affect around 1% of the glaciers worldwide (Guillet et al., 2025; Sevestre and Benn, 2015). However, first, there is possibly more given the more recent inventories and tributary distinction. Recent inventories are more systematic, relying on the large number of satellite images, and have detected more surge-type glaciers over recent decades (Guillet et al., 2025; Guo et al., 2023; Kääb et al., 2023). Second, recent studies show continuous spectra of instabilities and the simplistic binary surge/non-surge classification (Guo et al., 2023; Herreid and Truffer, 2016; Mattea et al., 2025b). On this note, Herreid and Truffer (2016) may be the first study to suggest a common metric (here, the relative displacement of surface features) to compare and assess speedups and other instability events such as surges. Finally, a glacier can lose its ability to surge over long timescales (discussed later, section 1.1.5).
One can distinguish the stagnation phase and the buildup phase that may partially or fully overlap, a pre-surge or transition phase with a gradual acceleration or post-surge gradual deceleration phase (e.g., Monacobreen and Negribreen in Fig. 1.2), and distinct surge peak activities (e.g., Kvalbreen or Recherchebreen in Fig. 1.2) (Benn et al., 2019b, 2023; Bhambri et al., 2017; Steiner et al., 2018; Sund et al., 2009).

1.1.3 Diversity of surge events

Increased scrutiny of surge events reveals a growing diversity of exotic types and cases. For example, a surge-type glacier can flow along a non-surge-type glacier, and two nearby surge-type glaciers can surge asynchronously and over different cycle lengths (Paul, 2020). Interestingly, the upper limit of surge reservoir areas does not extend beyond icefalls when there is one, as it has been observed for summer glacier speedups (Armstrong et al., 2017; Cuffey and Paterson, 2010; Echelmeyer et al., 1987; Nolan et al., 2021).
The quiescent phase of a surge-type glacier typically lasts one to several decades, and the

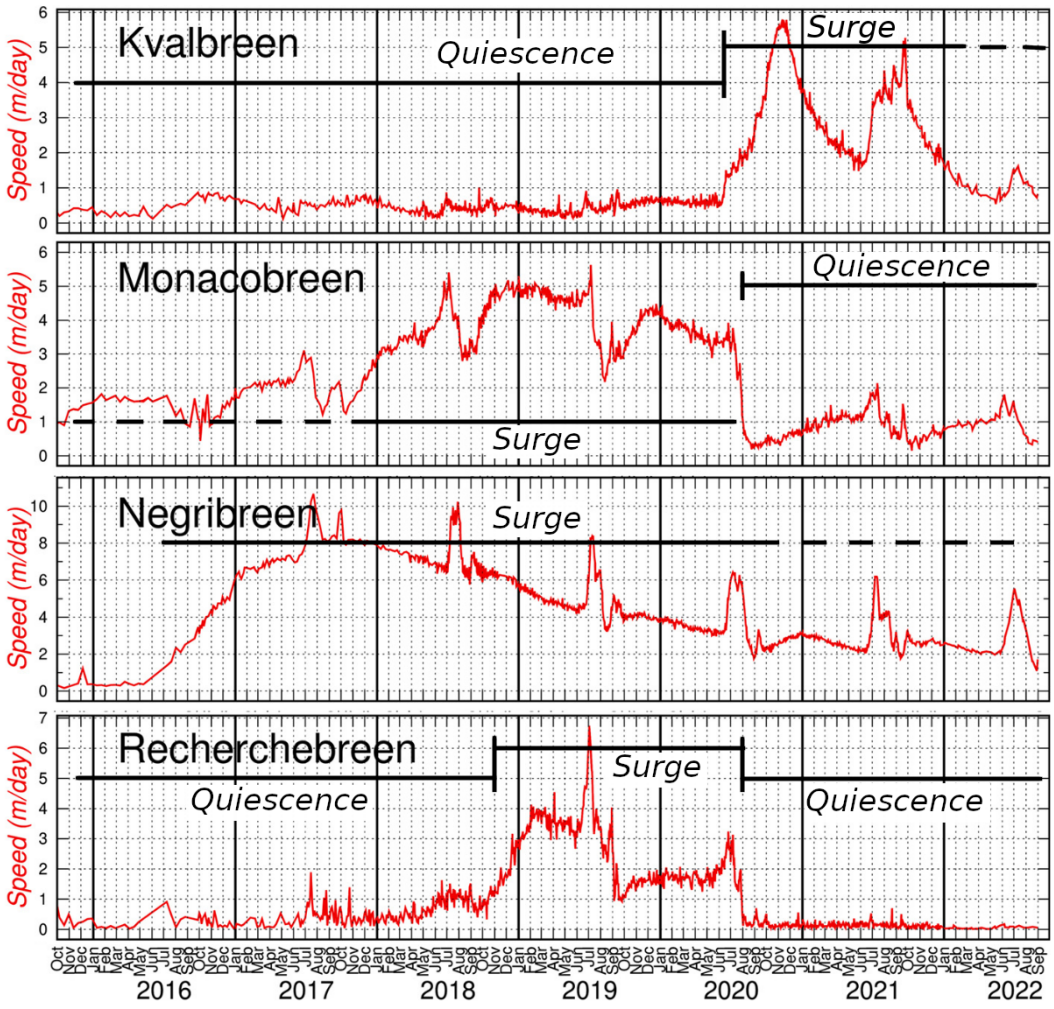

Figure 1.2: Velocity time series of four Svalbard glaciers. We label each phase of the cycle at the locations (dotted periods may be subjective). Figure adapted from Benn et al. (2023).

active phase lasts from a few months to a decade or more. The shortest duration known for a surge cycle may be 5 years for the Sít' Kusá Glacier, Alaska (Nolan et al., 2021). Surge velocities are generally lower and surge cycles are longer in cold regions (Cuffey and Paterson, 2010). Many surge events occur in regular periodicity, such as for Donjek glacier (Alaska) or Medvezhiy glacier (Western Pamir) (Kochtitzky et al., 2019; Kotlyakov et al., 2018), but not all do, such as Breiðamerkurjökull glacier (Iceland) or possibly Bualtar Glacier (Karakoram) (Björnsson et al., 2003; Hewitt, 2014). Estimating surge periodicity is challenging, as old events may have been unnoticed.

Dynamics of surge initiation may also change between events of the same glaciers, as observed for Donjek and Bering glaciers (Alaska), for which the velocities have likely initiated their acceleration at different locations and over different extents (Burgess et al., 2012; Fatland and Lingle, 2002; Kochtitzky et al., 2019; Roush et al., 2003).

The surge instability can propagate down-glacier, up-glacier or both (see section 1.4.2.3). However, propagation may not be continuous: for example, Fig. 1.5 shows the stagnating front of a Bivachny glacier surge (Western Pamir) ahead of a tributary confluence at 13 km, and then the propagation of the surge front to the end of the glacier. It seems that marine-terminating glaciers often initiate at the front and then propagate up-glacier

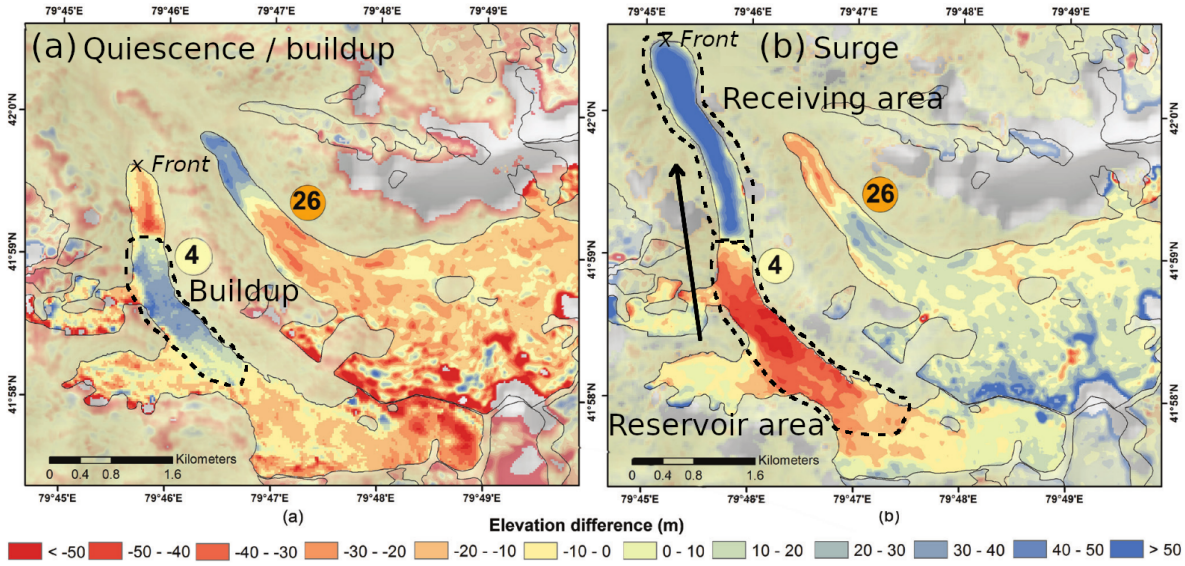

Figure 1.3: Thickness change of Samoilowich Glacier (Central Tien Shan), number 4, during the two phases of a surge cycle: (a) 1973–1999, and (b) 1999–2006. The end of the quiescent and buildup phase variation of glacier number 4 is visible on (a), and its surge phase is on (b). The pre-surge buildup is in blue (thickening) in (a). During the surge, ice mass moves from the reservoir area in red (thinning during the surge) to the thickening receiving area in blue (b), advancing the glacier front. Figure adapted from Mukherjee et al. (2017).

(Sevestre et al., 2018).

The surge characteristics described so far in this section may seem to depict a very discernible and defined event. However, there is a wide range of glacier instabilities: glaciers with steady flow and surge-type glaciers are endmembers of the whole flow behaviour spectra (Fig. 1.6; Herreid and Truffer, 2016; Mattea et al., 2025b). Hence, no universal indicator allows quantitatively classifying the glacier behaviour into two distinct classifications over the full instability spectrum, and previous studies have used different multi-criterion or threshold indicators (Bhambri et al., 2017; Guillet et al., 2022; Herreid and Truffer, 2016; Koch et al., 2023; Mattea et al., 2025b; Zhu et al., 2022). These indicators can include a minimal number of clues among supra-glacial surge evidence, elevation or velocity change pattern, and thresholds of velocity change magnitude index or in elevation change rate. In my PhD project, I focus on easily observable high-magnitude events, and each surge-type glacier appears in the two inventories from Guillet et al. (2022) and Guo et al. (2023).

Both land-terminating and tidewater glaciers can be prone to surge, as well as both polythermal glaciers (ice basal layer is locally at the melting point, and upper layers or other locations are below the melting point) and temperate glaciers (the main ice body, including the bed, is at the melting point). When known, the beds of surge-type glaciers are soft (deformable sediment till), although some of them may partially rest on hard beds (Cuffey and Paterson, 2010, p528). The lack of observations does not permit us to conclude, and a subglacier transition from hard to soft bed may promote a surge activity. The weakness and fractures of the bedrock and the nature of the lithology or its variations may favour the surge likeliness (Cuffey and Paterson, 2010; Crompton et al., 2018; Harrison and Post, 2003; Kochtitzky et al., 2019; Turrin et al., 2014).

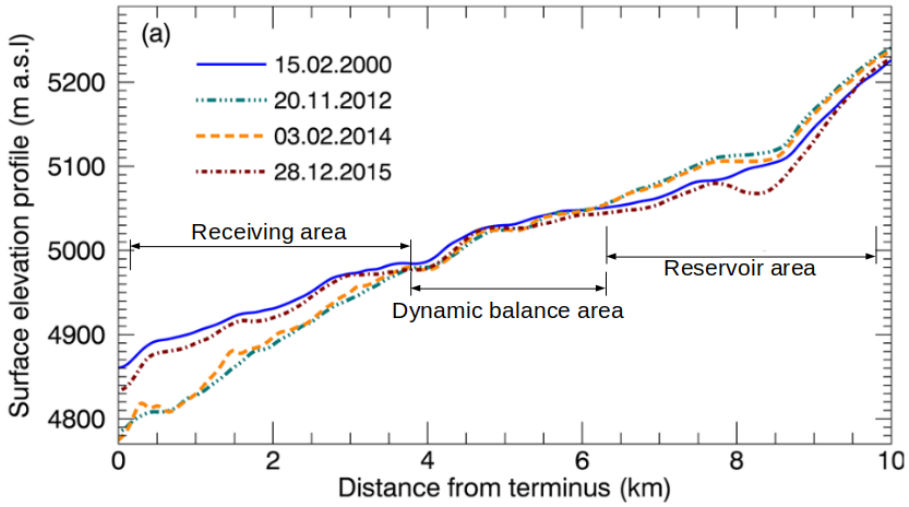

Figure 1.4: Longitudinal elevation profiles of the central flowline of the Kyagar Glacier (Karakoram). The profiles are at the beginning of the quiescent phase (2000), after the buildup (2012), at the beginning of the surge after a gradual velocity increase (2014), and at the end of the surge event (2015). The reservoir and receiving areas are visible with several tens of metres of elevation change in the 2 years that the surge lasted, from early 2014 to late 2015. There is a large dynamic balance area in between. While usually defined as a line (transversal, across glacier width), this figure highlights that the dynamic balance line can sometimes extend over a significant glacier length. From 2000 to 2014, the thickening pattern of the buildup stage is visible in the reservoir area. During this period, the lower part of the glacier suffers a strong thinning of what is probably the ice deposited by the previous surge, which occurred from 1995 to 1998 (Gao et al., 2024). Figure adapted from Round et al. (2017).

In summary, several factors have been observed or suggested to influence the probability of a glacier to surge: climate setting (Sevestre and Benn, 2015; Guillet et al., 2025), subglacier transition from hard to soft bed and bedrock fractures or nature of lithology (Crompton et al., 2018; Turrin et al., 2014), glacier geometry and especially subglacial topography linked to mass accumulation rate (Lovell et al., 2018; Kotlyakov et al., 2018), etc.

1.1.4 Pulses and seasonal variations on surge-type glaciers

Surge-type glaciers can show different varying velocity patterns, which interact with regular glacier variations. In particular, surges can be commonly modulated by seasonal flow modulations, with limited superimposed variations or dividing the surge into distinct yearly peaks (e.g., Kvalbreen or Recherchebreen, Svalbard, in Fig. 1.2). This is also observed in High Mountain Asia: for example, surges of Kyagar, Shisper glaciers, or glaciers in Qilian mountains have spring-summer speedups, while other surging glaciers have winter speedups (Beaud et al., 2022; Guo et al., 2025; Li et al., 2023; Round et al., 2017; Yasuda and Furuya, 2015). In addition, Abe and Furuya (2015) noticed different winter speedups on quiescent surge-type glaciers in Canada, and Beaud et al. (2022) shows both spring and fall speedups when air temperature increases and decreases for two surge-type glaciers in the Karakoram range.
The study Zhu et al. (2025) uses velocities from 12 and 24-days-appart SAR images over a Karakoram glacier: they link pre- and post-surge pulses with the main surge period, which itself is divided into four sub-surge events separated by quiescence-like velocities. It

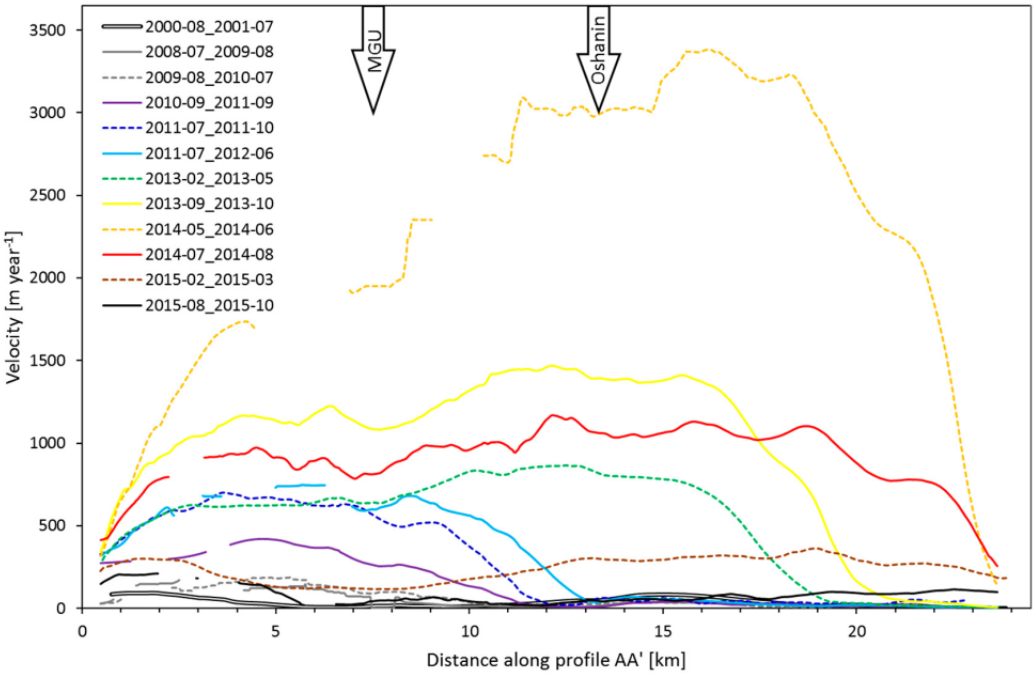

Figure 1.5: Surface velocity along the central flowline (starting at the confluence of four accumulation basins) of Bivachny glacier (Western Pamir) in its surge phase. Arrows show the confluence of tributaries. Figure from Wendt et al. (2017).

questions the search for similar pulses as a possible early-warning of incoming surge events.

Beaud et al. (2022) shows that a surge of the Shisper Glacier (Karakoram) initiates during a fall speedup, while its main phase starts the following spring. The surge events of other glaciers start in the fall or spring seasons, such as Hispar (Karakoram) or Karayaylak/Kelayayilake (Eastern Pamir) glaciers (Guo et al., 2020; Zhu et al., 2021). In general, in Karakoram, Quincey et al. (2015) found however no seasonal controls for surge onset.

1.1.5 Repartition, sensitivity to the climate and its change

Surge-type glaciers are found in a few distinct geographical clusters among glacier-covered areas: mostly in the Arctic Ring (including Alaska-Yukon, Greenland, Svalbard, etc.) and in High Mountain Asia (HMA) (Fig. 1.7; Guillet et al., 2025; Sevestre and Benn, 2015). There are only a few surge-type glaciers localised in other regions such as Andes, sub-Antactic and most latitudes in Greenland, and none in Scandinavia, New Zealand and probably central Europe. These clusters occur in specific climatic envelopes: overall, they concentrate in slightly colder areas than non-surge-type glaciers for a given precipitation, especially in summer, and are less present in areas at the higher end of total precipitation (Fig. 1.8; Guillet et al., 2025; Sevestre and Benn, 2015).

As surge-type glacier clusters occur in climatic envelopes defined by specific temperature and precipitation conditions, climate change can affect the distribution of surge-type glaciers and the surge-cycle period until it is ended (Hoinkes, 1969; Mann et al., 2024; Sevestre and Benn, 2015; Striberger et al., 2011). Accordingly, the peak velocity and lengths or front advances may have been reduced in recent cycles for some glaciers (Bhambri et al., 2017; Kochtitzky et al., 2019). One reason for this is straightforward: surge-type glaciers may require a sufficient amount of ice in the reservoir area (i.e., which results in a high shear stress) for a surge to be triggered. Then, lower accumulation due to climate

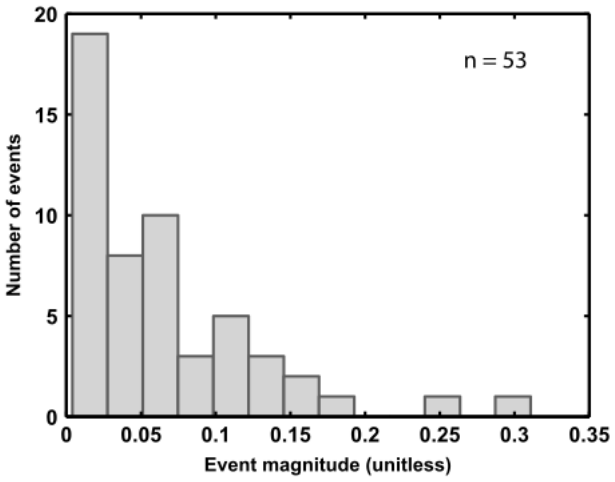

Figure 1.6: A continuous spectrum of speedup magnitudes from multiple glaciers in the Alaska Range. A non-surging glacier would have a magnitude of zero. A threshold at 0.05 differentiates between surge-type and pulse-type glaciers based on previous classifications, but this distinction is arbitrary based on the data shown here. Figure and caption from Herreid and Truffer (2016).

change directly extends the delay before replenishment (Eisen et al., 2001; Kotlyakov et al., 2018; Lovell et al., 2018).
Hence, surge-type glaciers of the European Alps may have recently lost or nearly lost their surge ability due to their mass loss (Hoinkes, 1969; Serrano and Martín-Moreno, 2018). One of the latest ones in this region may be the well-surveyed Vernagtferner that surged last around 1900 or possibly 1980 and is assumed to be no longer able to accumulate enough mass to surge again (Hoinkes, 1969; Reinwarth, 1993). Surges may have been more common in the past in different climates, for example, in the Pyrenees (Europe) for the small glaciers of Svalbard during the Little Ice Age (Serrano and Martín-Moreno, 2018; Sevestre et al., 2015). The Little Ice Age in Europe extended overall over 14^{th}-20^{th} centuries from a glaciological point of view, and 16^{th}-19^{th} from a climate point of view, although with large spatial and temporal variability (Matthews and Briffa, 2005). However, other surge-like events have occurred more recently, such as the 2001-2003 event on the Belvedere glacier (Alps, Europe) (Truffer et al., 2021), or a *mini-surge* event on the Bossons glacier (Alps, Europe) (Brun and Lacombe, personal communication).
A decrease in surging activity may also be ongoing in the Western cluster in Greenland, while the Eastern part remains similarly active since the 1980s (Lovell et al., 2023). In the Western cluster, a 1-degree warming occurred in the two periods of the study.

The sensitivity of surge-type glaciers to climate change, that is to say, the effect of surge events on the long-term mass balance of a glacier, is still debated. There is an important mass loss in the reservoir area after a surge event due to the deposition of dead ice at low elevations, and possibly due to the rougher surface caused by crevassing. Spatially averaged, during long-term periods or the full cycle duration, several studies in HMA found no significant differences in mass balance between glaciers of surge- and non-surge-type (Berthier and Brun, 2019; Gardelle et al., 2013; Glasser et al., 2022; Guillet et al., 2022; King et al., 2021). On a short timescale, mass balances of surge-type glaciers reflect not only a climate accumulation-ablation equilibrium, but also internal mechanisms and cycles not directly representative of the glacier state (Bhambri et al., 2022). The two models that investigated the long-term impact of surging activity on the glacier show

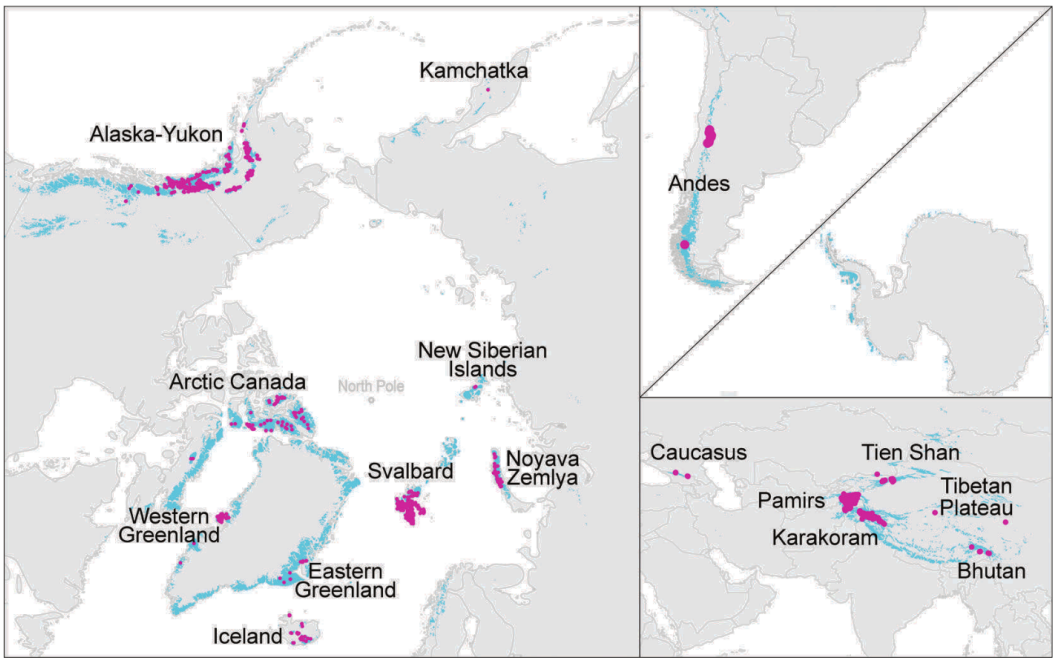

Figure 1.7: Global distribution of surge-type glaciers (pink dots) of the inventory from Sevestre and Benn (2015). Normal glaciers are represented in blue (Randolph Glacier Inventory (RGI) version 3.2). Figure from Sevestre and Benn (2015).

slightly more negative mass balances (Aðalgeirsdóttir et al., 2005; Oerlemans and van Pelt, 2015). For example, a study modelling a low-angled glacier in Svalbard shows that surge activity leads to faster glacier shrinking in a warming climate, along with greater sensitivity due to low surface slope (Oerlemans and van Pelt, 2015; Guillet et al., 2022).

1.1.6 What's at stake with the study of surges

The dynamics of glaciers and, more particularly, their basal friction remain not fully understood. They represent a major source of uncertainties in the prediction of future global mean sea level rise, especially since 2006 when land ice became the main contributor to sea level rise (IPCC, 2022; Thøgersen et al., 2019). Studying the dynamics of surges can help better understand the physics of basal friction and subglacial hydrology for glaciers in general, which remain one of the largest sources of uncertainties in these glacier evolution models.

Surge events are also part of mountain hazards, on a local scale. Surges are one of the sources of dramatic events such as Glacial Lake Outburst Floods (GLOFs), with a predicted increase in these events in some regions of HMA (Bazai et al., 2021; Chen et al., 2024; Compagno et al., 2022). For example, sudden glacier advance during a surge can block the flow of rivers across valleys and lead to sudden discharges up to several times per surge cycle that may threaten downstream population (Round et al., 2017; Truffer et al., 2021; Bazai et al., 2021). For example, the surge events of Kyagar glacier (Karakoram) regularly dam a river, creating a lake (Fig. 1.9). This well-known lake purged multiple times during and after the successive surge events (Round et al., 2017; Gao et al., 2024; Zhang et al., 2023b). The recent surge of Shisper glacier (Karakoram) is also a typical case (Fig. 1.10.c in 2020, drained lake outline in blue and exit channel near label B). There have been two lake outbursts in a one-year interval, with important socio-economic impacts (Muhammad et al., 2021).

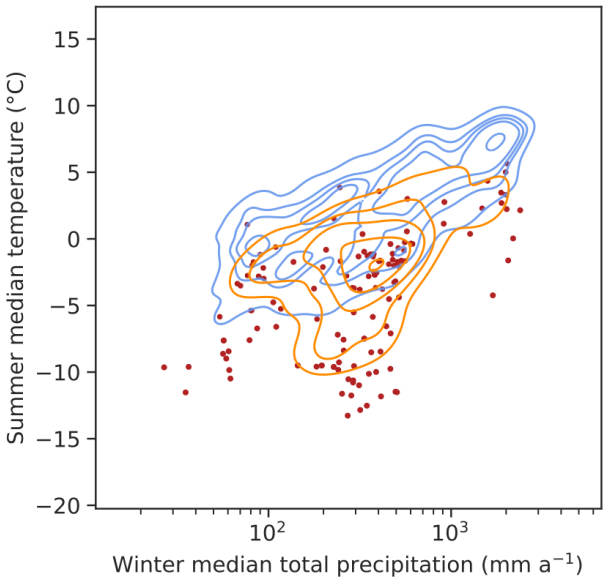

Figure 1.8: Distribution of surge-type glaciers into a climate envelope (in red and orange), versus non-surge-type glaciers (in blue). The red scatter plots are surge-type glaciers from the inventory Guillet et al. (2025), and the orange kernel density estimate combines several inventories (Sevestre and Benn, 2015; Falaschi et al., 2018; Guillet et al., 2022; Lovell et al., 2023; Kääb et al., 2023). Lines represent different density levels: 30%, 50%, 70%, 90% and 99%. Figure from Guillet et al. (2025).

Finally, some glacier detachment events that result in important casualties and damages have shown a number of similarities with surges (past surging activity or pre-failure dynamics and mechanisms) (Kääb et al., 2021).
There is certainly a combined knowledge to learn from these surge-like events, resulting in catastrophic failure and traditional surges.

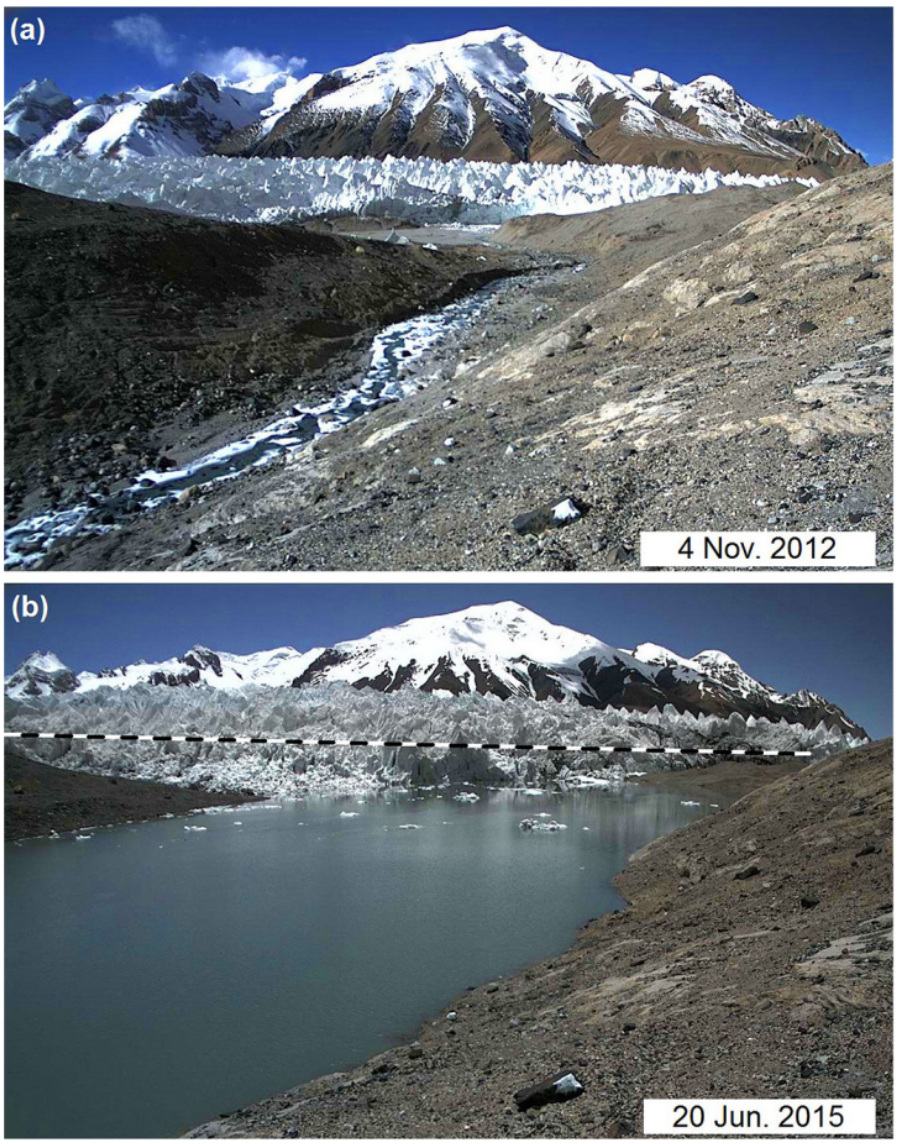

Figure 1.9: Terminus of the Kyagar glacier (Karakoram) from (a) before and (b) during the surge. The glacier, flowing from left to right, blocks the flow of the river and causes lake formation. The dashed line in (b) indicates the ice dam height from 2012 (a), highlighting the dramatic thickening at the terminus. The lake can reach a depth of about 100 m and a width of about 500 m at this location (Gao et al., 2024). Figure and caption from Round et al. (2017).

1.2 Observation of surge events

1.2.1 *In situ* observations

Direct observations of surge events are possible, but they often remain unnoticed because of their isolated location and their short duration. The surface of the surging area is often chaotic with the characteristic formation of crevasses and ice pinnacles (e.g., Fig. 1.10.a-b and Fig. 1.10.c; Cuffey and Paterson (2010); Kääb et al. (2023); Mannerfelt et al. (2025, p511)). In the case of an advancing glacier front, the glacier tongue thickens and is bulbous (e.g., Fig. 1.10.a and post-surge thinning; Bhambri et al. (2017)).
Several surge events have been intensively monitored and studied with field surveys, high-

lighting various mechanisms, such as Variegated glacier in Alaska, Trapridge glacier in Canada or Medvezhiy glacier in Western Pamir (HMA) (Eisen et al., 2005; Frappé and Clarke, 2007; Kotlyakov et al., 2018; Raymond and Malone, 1986). The fact that a surge event can hardly be anticipated complicates *in situ* measurements. *In situ* measurements can include bed temperature and structure in boreholes, the flow discharge rate and basal water pressure, surface velocity and elevation from theodolites or GNSS, seismic activity, etc. (Cuffey and Paterson, 2010; Charrier et al., 2025; Frappé and Clarke, 2007; Raymond and Malone, 1986).

Indirect observations are often based on glaciological and geomorphological evidences that persist after the event (Meier and Post, 1969; Sevestre and Benn, 2015). Folded moraines in bulb-like loops are often created at the interface between two glaciers, either by the regular flow of a tributary glacier in a quiescent surge-type one, or by the surge advance of the tributary glacier in the main one. The advance of the main glacier brings the loop up to several kilometres downward, often at regular spacing due to the periodicity of these events (Cuffey and Paterson, 2010). Fig. 1.10.d is representative of this phenomenon, with a long history of probably 6-7 surges of Khurdopin glacier that is still visible (Quincey and Luckman, 2014; Imran and Ahmad, 2021, inventoried surge events around 1979, 1999, 2017;). Another line of evidence also associated with a front advance is the deposit of specific moraine structures at the glacier front, which allows the occurrence and extent of surge events to be traced more than a century after the last surge of a glacier (e.g., Bradwell and Benn, 2025; Flink et al., 2015; Serrano and Martín-Moreno, 2018).

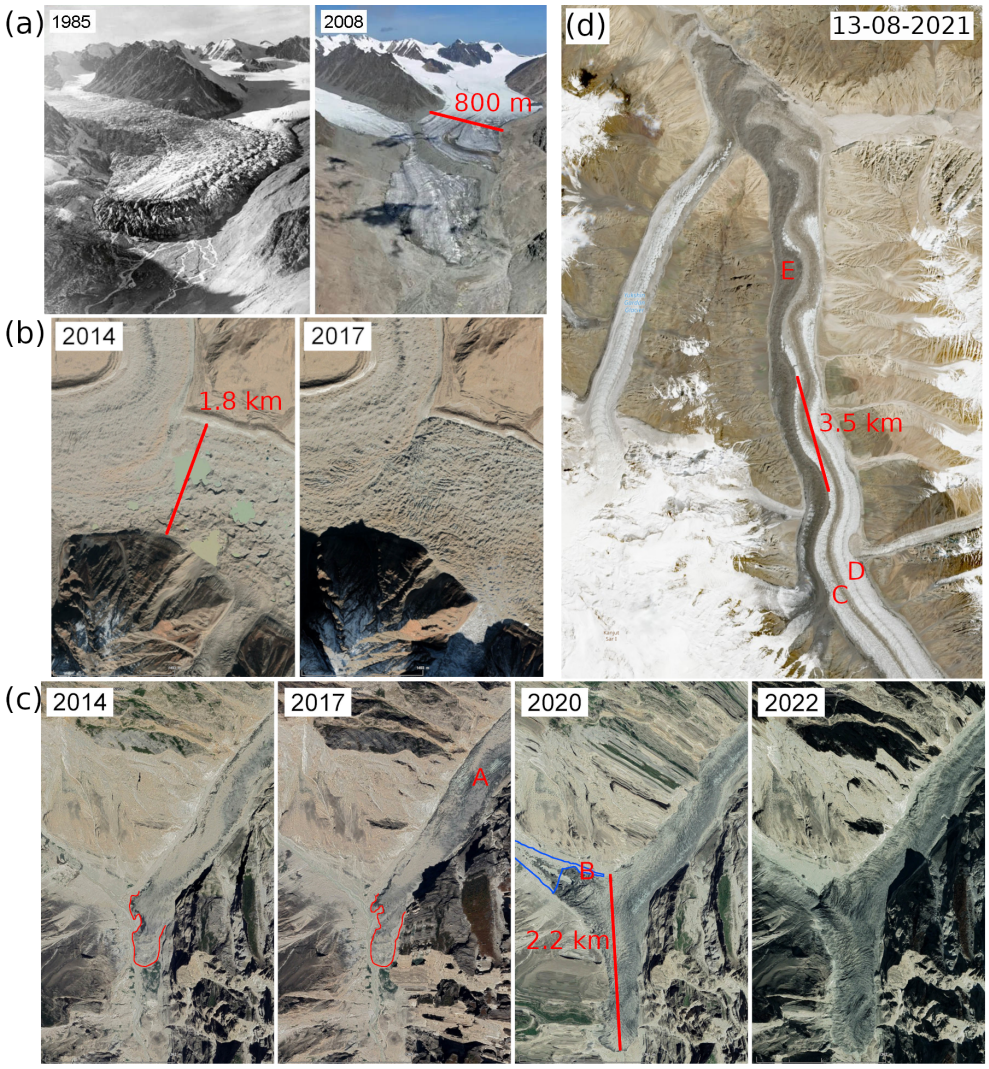

Figure 1.10: Surging activity and associated surface features. (a) Bogatyr Glacier (Northern Tien Shan) during its surge phase (left) and quiescent phase (right). Figure adapted from Mukherjee et al. (2017). (b) Crevassing surface of the area that surged with supra-glacial lakes drainage (diametres around 400-500 m) on the Hispar Glacier (flowing from the right) at the confluence with Kunyang Glacier (flowing from the top), in Karakoram. Before the Hispar Surge (left) and after (right). The Kunyang Glacier is in quiescent phase. Imagery: Google Earth - CNES / Airbus. (c) Surge development of Shisper Glacier (Karakoram): during late quiescence in 2014 - no crevasse, then thickening and crevassing at the surge front in A (2017, surge onset), and finally the surge end with full crevassing and then their disappearance during the new quiescent phase (2020, 2022). Red drawing: glacier tongue; blue drawing: ice-dammed lake extent, purged (Muhammad et al., 2021); A: possible surge front area; B: ice-tunnel entrance. Imagery: Google Earth - CNES / AirBus - Maxar. (d) Sentinel-2 (ESA, Copernicus Browser) imagery of Khurdopin glacier (Karakoram), showing looped moraines due to surging activity. Repeated loops on the left margin, such as E, originate from the junction C and are transported by the surges of the main glacier. The loop D originates from an ongoing surge of the tributary on the right pushing through the main glacier.

1.2.2 Remote sensing observations

Surge events are globally observed using remote sensing techniques, primarily with satellite images, which cover large areas and historical periods at high spatiotemporal resolution. Satellite images are mainly used in three ways: photo-interpretation, analysis of surface elevation changes and analysis of surface velocities.

First, photo-interpretation is the most basic usage, giving simple information. It can be used to retrieve the front advance of surges, determine the surge-cycle phase through front aspect (e.g., bulge) or crevasses and interpretation of their melt, distinguish surging glaciers and estimate their surging period with looped moraines, among other applications (e.g., Fig. 1.10). For example, Paul (2020) used satellite images dating back to 1961 to interpret visual evidences of surging activity on about thirty glaciers in Karakoram, completing the analysis with an historical map surveyed in 1937. Grant et al. (2009) also use complex visual evidences on satellite imagery to provide a surge-type glacier inventory among 692 glaciers in Novaya Zemlya archipelago (Russian Arctic).

Second, satellite imagery can monitor changes in surface elevation by producing multitemporal Digital Elevation Models (DEMs) (e.g., Fig. 1.3). Both optical stereoscopic imagery and interferometric synthetic aperture radar (InSAR) can be used for this purpose. The elevation maps produced at different dates allow for the retrieval of the elevation and volume changes of glaciers. Already widely used to calculate glacier mass balances, one can retrieve the ice volume displaced during a surge, delimit the reservoir and receiving areas, etc. (e.g., Bhambri et al., 2022; Frappé and Clarke, 2007; Gao et al., 2024; Glasser et al., 2022; Guo et al., 2020; Lovell et al., 2018; Lv et al., 2020; Round et al., 2017; Steiner et al., 2018). Both optical and radar have limitations, such as cloudiness/textureless snow, shadowing and layover or loss of coherence. These limitations often create data gaps in time series, not capturing the complete evolution of the surge event at short timescales (e.g., surge initiation and termination dates, full extent of the surge-affected area, etc.). Furthermore, the small number of accessible historical satellite acquisitions is a limit to the study of long surge events and surge cycles (Goerlich et al., 2017; Guillet et al., 2022; Round et al., 2017; Yao et al., 2023). The processing and analysis of DEMs can be automatised for wide-scale assessments (e.g., Brun et al., 2017).
Elevation data can also be acquired by satellite altimetry, in particular laser/lidar altimetry (ICESat and ICESat-2 satellites) and radar altimetry (Cryosat-2). Both altimetry products provide sparse elevation measurements along transects that follow the satellite orbit, either at nadir or off-nadir. Both sensors provide generally more accurate elevation measurements compared to other methods (e.g., elevation precision below 0.15 m for ICESat-2 on complex terrain, few tens of centimetres for CryoSat-2 with, however, possible metre-scale systematic bias; Gray et al. (2015); Shen et al. (2021)), but their sparse sampling generally restricts altimetry to large glacierized areas, such as Bering glacier (Paul et al., 2022; Trantow and Herzfeld, 2016, 2024). The recent SWOT radar altimeter could be promising for glacier altimetry and surge study, with a high revisit time, high accuracy, and large spatial coverage (e.g., Kacimi et al., 2025; Wu et al., 2025). However, to date, no published studies have yet used this sensor for mountain glacier elevation, and it may be ineffective in areas that are not flat, such as most of HMA glaciers.

The third major remote sensing product is the glacier surface velocity (e.g., Fig. 1.1). Surface displacement can be calculated between two images by feature-tracking on both optical and radar images (e.g., Dehecq et al., 2022; Gardner et al., 2025). Depending on image resolution and flow velocity, time series of velocities on a year, month scale or less can be analysed to determine surface flow velocities and accelerations (e.g., Charrier et al.,

2025; Millan et al., 2022; Nanni et al., 2023). They are often used to follow the development of surge events: date of onset and termination, peaks, surge front propagation, etc. (e.g., Abe and Furuya, 2015; Beaud et al., 2022; Guo et al., 2025; Quincey et al., 2015; Wendt et al., 2017). Velocity products can be used for automated processes, such as the detection of separated pulse and surge events by machine learning (Zhu et al., 2022).
For SAR, interferometry (InSAR) can also provide surface velocity in two or three dimensions – adding vertical velocity compared to other methods, but it has been used less frequently in glaciology due to more complex processing steps such as phase unwrapping and temporal decorrelation (e.g., Fatland and Lingle, 2002; Guo et al., 2020; Murray et al., 2003a). It has been used successfully in three dimensions by Guo et al. (2020) on Hispar glacier (Karakoram) to compute both horizontal and vertical velocities.

Other methods for observing surge events have been used to a lesser extent, especially SAR. For example, Leclercq et al. (2021) used radar images to detect glacier surges using the variation in backscatter, associated with the opening and closing of crevasses that occur during the surge. The radar backscatter sometimes increases distinctly even before velocity changes become noticeable in reference surface velocity data. This method has been extended to global coverage to retrieve surge events during 2017-2022 (Kääb et al., 2023). Mannerfelt et al. (2025) has a different approach with InSAR: the authors use the change of coherence between SAR images due to surging activity (e.g, crevasse, motion magnitude). They can in particular track the propagation of the surge front both up- and down-glacier. However, they report a high loss of coherence due to meteorological conditions. They also notice that with their method the onset is detected in advance compared to other methods. Finally, one study has observed by SAR interferometry the deformation of the earth's crust during a surge event with a front advance in Iceland, with a surface lowering up to 75 mm, and with a decreasing impact up to 10 km of the ice margin (Auriac et al., 2014).

These methods – photo-interpretation, elevation and surface velocities – are complementary and are regularly used conjointly (e.g., Round et al., 2017; Guillet et al., 2022). On one hand, velocity time series on surge events are regularly derived at short temporal intervals (weekly to monthly) (e.g., Bhambri et al., 2020; Beaud et al., 2022; Gao et al., 2024; Guo et al., 2020; Jiang et al., 2021; Singh et al., 2021; Van Wychen et al., 2025, etc.). On the other hand, the use of DEMs is often limited to a few dates or specific case studies. Examples using elevation data with similar temporal resolution (weekly to monthly) are much less frequent (e.g., Guillet et al., 2025; Li et al., 2023; Trantow and Herzfeld, 2024). However, there could be different applications for which dense temporal resolution of elevation would be necessary, such as build-up and driving stress monitoring, temporal variation of volume transferred, displacement of the dynamic balance line, analysis of kinematic waves, etc.
For such applications, temporally dense elevation time series from satellites covering a long period of time have recently become available to study glacier elevation change. These acquisitions started around the year 2000, with time series now spanning more than two decades, long enough to capture a number of surge events and a few complete surge cycles. In particular, the TERRA satellite with its ASTER sensor is the only optical stereo mission that provides systematic and global acquisitions (Berthier et al., 2023). We develop these new DEM applications using elevation from the ASTER sensor in Chapter 2.

Remote sensing surface velocity and elevation can be used to estimate several physical parameters of glaciers, owing to approximations such as steady state, models and mechanistic equations. For example, these two types of data have been used alone or in

combination to produce thickness estimates for each glacier, on a global scale (Farinotti et al., 2019; Millan et al., 2022). There is a good potential to improve these thickness estimates on surge-type glaciers (Morin et al., 2023). With a simple slope and thickness estimate, one can also retrieve the driving stress at the base of the glacier, and approach the basal shear stress under the equilibrium approximation (Cuffey and Paterson, 2010, p295). These methods have been applied, in particular, to surge-type glaciers (e.g., Beaud et al., 2022; Benn et al., 2023; Gao et al., 2024).

1.2.3 Inventories of surge events

Regional surge events and surge-type glacier inventories can be based on remote sensing techniques or reviews of the literature and archives. It is generally more correct to speak of inventories of *surge events* than of *surge-type glaciers*, due to the limited duration of their period of study, which often ignores glaciers that remain in quiescent phase for several decades, and because some glaciers lose their ability to surge due to climate changes in time. The first global inventory is compiled from direct and indirect observations in historical and scientific sources (Sevestre and Benn, 2015). The studies of Kääb et al. (2023) and Guillet et al. (2025) are the first worldwide consistent and data-driven inventories, and rely on remote sensing data covering 5 and 24 years, respectively.
Due to different criteria/observation time spans and the lack of a clear distinction between surge-type and non-surge-type glaciers, inventories classifying glacier instabilities can hardly be compared quantitatively (Herreid and Truffer, 2016). For example, global inventories based on remote sensing data find 261 surge events on 246 surge-type glaciers over 24 years (Guillet et al., 2025) and 115 surge events on likely 115 glaciers over 5 years (Kääb et al., 2023), while Sevestre and Benn (2015) inventories 2317 surge-type glaciers from reports and publications and without period constraint. In HMA, the inventories identify between 137 and at least 890 surge-type glaciers (Guillet et al., 2025; Guo et al., 2023; Sevestre and Benn, 2015; Yao et al., 2023).

Individualisation of tributaries or confluent glaciers of a glacier system is also an issue for the study of surges. This could be significant: for example, in HMA, Guo et al. (2023) found 175 surging tributaries in 86 distinct glacier systems.There are also surge events on the tributary glaciers of larger glacier systems in other regions, such as in Alaska (Altena et al., 2019). There are glacier systems that show many surge-type tributaries: for example, the Panmah glacier (Karakoram) may have at least 6 surge-type tributaries, with complex interactions and mechanisms (Fig. 1.11; Bhambri et al., 2017; Hewitt, 2007; Paul, 2020). In particular, some tributaries also reach the main glacier only during surge events and may be considered separately or not. Paul (2020) shows several interactions with tributaries such as for Drenmang with Nobande Sobonde glaciers (Panmah glacier system), including colliding masses during surges and mass redistribution, and even flow-blocking of the main trunk which is also observed between Hispar and Kunyang glaciers (Fig. 1.11). Hewitt (2007) analyses the surge of several distinct tributaries of the Panmah glacier system and interestingly concludes that their recent surge events (2001-2005) coincided unexpectedly, considering their past, long and different cycle durations. They propose several hypotheses for this, such as a change of thermal regime (warming) that affects particularly these high and small tributary glaciers, or a role of the Karakoram anomaly (see section 1.3.1).

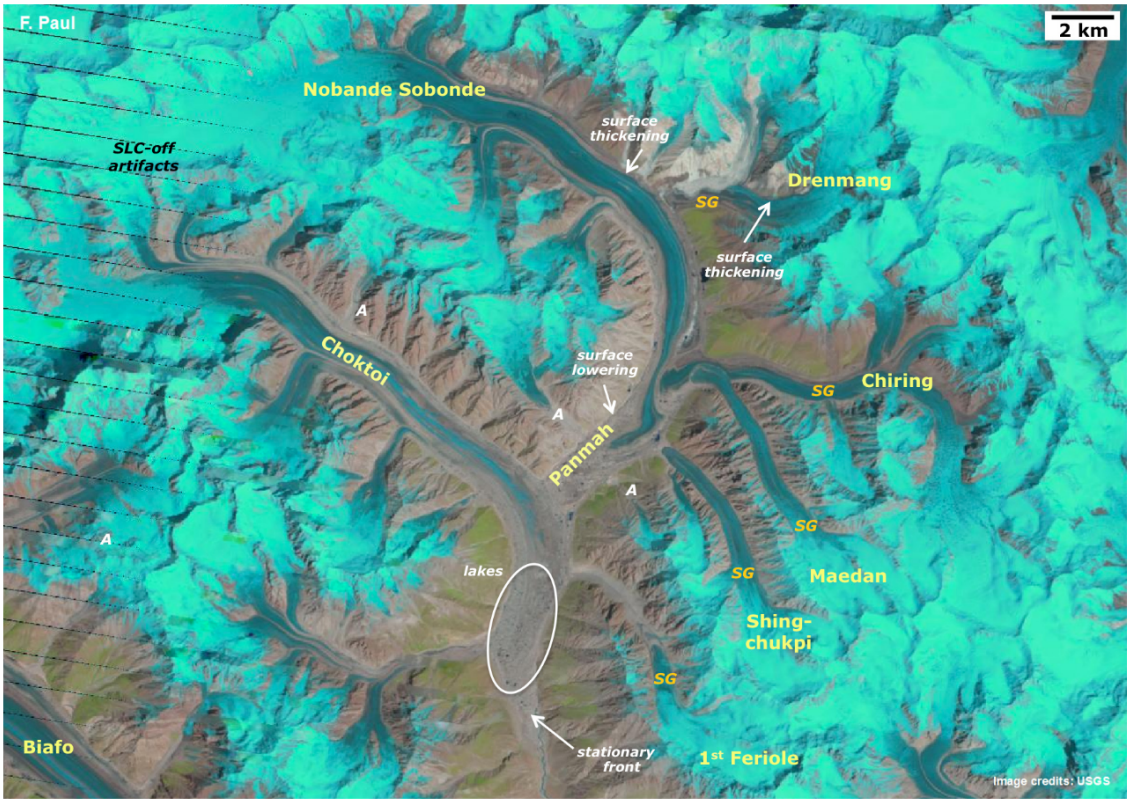

Figure 1.11: Satellite image of the Panmah system (Karakoram). The image in is false colour composites (i.e., snow and bare ice is in light blue to cyan, glacier debris cover in grey to brown and bare terrain in brown). SG (orange): surging glacier, A: advancing (non-surge) glacier. Figure from Paul (2015).

1.3 Surges in HMA

1.3.1 Glaciers in HMA: evolution and population

The region of High Mountain Asia represents a continuous mountain range that spreads over 11 countries in Asia (Fig. 1.12). HMA is the head of multiple major hydrological basins on the continent, which together are home to about 1.9 billion people. Major rivers originate in these mountains, such as the Ganges, Brahmaputra, Indus and Amu Darya. In particular, Immerzeel et al. (2020) established that some of the hydrological basins of HMA are among the most important and vulnerable water reservoirs in the world, particularly those of the Amu Darya, Indus and Tarim Interior. These regions and their downstream population concentrate the highest demands and dependencies on mountain water.

HMA, which hosts the highest peaks in the world, covers very diverse mountain ranges. For example, it includes very high and steep mountain ranges such as Karakoram, to large and relatively flat plateaus such as Tibetan Interior Mountains (Fig. 1.12). As a result, the climate in HMA is very variable, with variations depending on the regions (Maussion et al., 2014; Yao et al., 2022). Himalaya and the Eastern part of HMA are subject to high precipitation due to the seasonality of the monsoon, in contrast to the Tibetan Plateau, which is very dry. Karakoram and Pamir have moderate precipitation, predominantly influenced by westerly weather systems and the Tibetan anticyclone (Maussion et al., 2014). This leads to different regimes of accumulation on glaciers, with, for example, glaciers in Himalaya mostly accumulating in summer, in contrast to Karakoram glaciers, which accu-

mulate in winter/spring (Maussion et al., 2014).

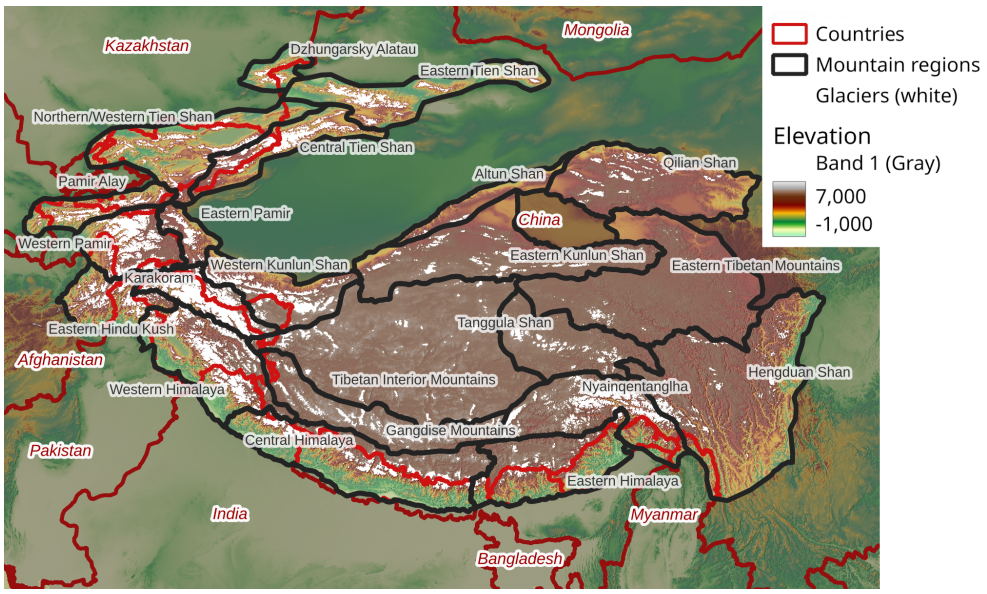

Figure 1.12: Map of HMA with countries. Data sources: countries are from ESRI, according to UN borders. The names of the disputed regions do not appear on the map. HMA delineation from (Bolch et al., 2019; Wester et al., 2019). The basemap is produced from GMTED2010 DEMs, USGS, EarthExplorer. Glaciers are from the RGI7.0 inventory (RGI Consortium, 2023).

HMA is the largest glaciarized area outside of the polar regions, with about 130 000 glaciers on the 275 000 that are inventoried globally (RGI Consortium, 2023; Wester et al., 2019). This represents about 100 000 km^2, the area of Iceland or a square of 315 km width and an ice thickness of 100 m (estimate for 2017-2018 Millan et al., 2022). This is equivalent to approximately a 2.4 cm sea-level rise. Note that glaciers in HMA are mostly land-terminating, compared to lake-terminating glaciers, which have different dynamics and more negative mass balances (Brun et al., 2019; King et al., 2019; Zhang et al., 2023a).

The state of glaciers in HMA is very variable between regions (Fig. 1.13). South and eastern regions, such as Eastern Himalaya or Nyainqentanglha, suffer strong mass loss, with regions that lost about a half-metre water equivalent per year or more on average over the two decades 2000-2020. Some other regions are in near equilibrium or on slight mass gain over this period, such as Kunlun, Pamir or Karakoram (Brun et al., 2017; Hugonnet et al., 2021; Shean et al., 2020). This particular behaviour is called the *Karakoram anomaly*, described below. However, since the 2010s, regions previously in equilibrium began in turn to lose mass (Bhattacharya et al., 2021; Hugonnet et al., 2021).

This mass loss is expected to continue throughout the 21st century. The current probable climate pathway (SSP2-4.5 scenario) implies a +2.5°C global mean temperature rise by 2100 relative to pre-industrial levels. In this scenario, estimates of their remaining mass in 2100 relative to 2015 in HMA vary from about 14% (South Asia East) to 51% (South Asia West) (Rounce et al., 2023). HMA will thus lose more mass in relative than other regions in the world, with about 72% mass remaining globally (Greenland and Antarctic ice sheets excepted). As a comparison of the different scenarios, Central Asia will conserve from 50% (SSP1-RCP2.6) to 38% (SSP2-RCP4.5) and 19% (SSP5-RCP8.5) of its mass in 2100 relative to 2015. The surge-type glaciers of HMA are mostly in the two regions that

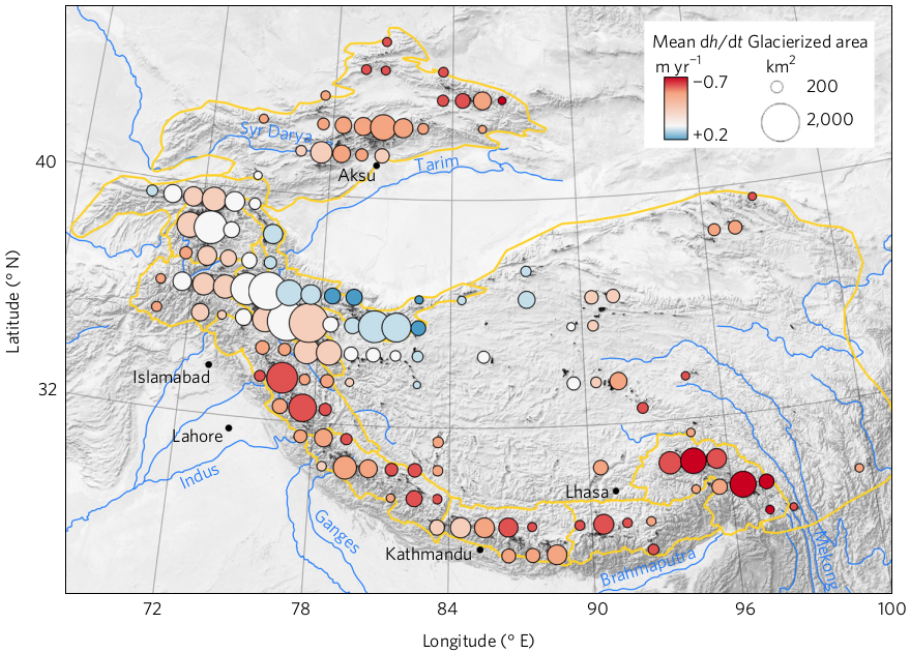

Figure 1.13: Mean glacier elevation change over HMA from 2000 to 2016, using satellite ASTER DEMs. Figure from (Brun et al., 2017).

will conserve the largest mass, South Asia West (including Karakoram) and Central Asia (Pamir, Tien Shan and Kunlun).

As highlighted above, *Karakoram anomaly* is characterised by a balanced or positive mass balance of glaciers in the past decades in Western Kunlun, Pamir and Karakoram, highly contrasting with other regions of HMA (e.g., Fig. 1.13). This behaviour is well assessed for the start of the twenty-first century, but may have started after the mid-twentieth century (Farinotti et al., 2020, and references therein). Glaciers in other regions of HMA have mainly experienced negative mass balance (Berthier and Brun, 2019; Hewitt, 2005). Recent studies claim that the anomaly ended in the 2010s, by observing glacier thickness changes or meteorological data in particular (Bhattacharya et al., 2021; Hugonnet et al., 2021; Jouberton et al., 2025; Xie et al., 2024; Xu et al., 2023). However, although the glaciers do not gain mass anymore, the mass loss remains much more limited compared to other regions.
Several explanations have been proposed for this anomaly, such as the topography of the glacier and overhanging headwalls with orographic concentration of snow causing mass input from avalanches (Hewitt, 2005). The most accepted hypothesis is the existence of a specific, favourable, climate setting: an increase in precipitation, a decrease in summer temperature, and an increase in air moisture and cloudiness, may have promoted snow accumulation and reduced melt. Possible external factors have been suggested to explain the occurrence of this anomaly: deforestation or the increase in irrigation to the north-west of China during the twentieth century (Farinotti et al., 2020).

1.3.2 Regional distribution of surge-type glaciers and surge characteristics

The most reliable and exhaustive inventories give from 666 to 890 surge-type glaciers in HMA, possibly up to 1226 (Guillet et al., 2022; Guo et al., 2023, which individualise tributaries). Several statistics can be retained from the inventory of Guillet et al. (2022) (Fig.

1.14). Note that this study considers glacier systems as a whole, hence biasing the results toward important and low-angled glaciers, as tributary surges often occur at higher elevation and on steeper glaciers (Bhambri et al., 2017). There is a strong clustering effect, with 223 surge-type glaciers in the Karakoram range (around 45% of glacier area), 222 in the Pamir regions (35%), 74 and 73 in Tien Shan and Kunlun Shan ($< 25\%$), respectively, and a remaining 74 surge-type glaciers in the 8 last HMA regions. Surge-type glaciers show, on average, greater areas/lengths and elevation ranges (parameters naturally linked together). However, some glaciers as small as 0.3 km^2 have been found to surge, so far (Goerlich et al., 2020). Compared to non-surge-type glaciers of similar area and at the tributary level, surge-type ones are slightly steeper (Guo et al., 2023).
Surges appear to have active phases of similar duration between regions: mostly below 3 years (median of 2.6 years) and up to 18 years or more, although long and very short surge cycles may be under-assessed (Guillet et al., 2022). However, Mukherjee et al. (2017) and Yao et al. (2023) find that the surge cycles in Tien Shan may be longer than in Karakoram. Finally, Karakoram surge-type glaciers may be steeper than in other regions (Paul, 2015; Guillet et al., 2022). Trends at the scale of HMA may be different from those of smaller regional scales. For example, there is no correlation between glacier length/slope and surge-type likeliness in Karakoram, and regional characteristics can be very different (topography and avalanche-fed mechanisms, debris coverage, climate, etc.) (Bhambri et al., 2017). However, studies regularly find different results: with the same previous example, Ke et al. (2022) found that Karakoram surge-type glaciers are longer and have smaller slopes than non-surge ones. They also reported 71 surge-type glaciers in Karakoram against 223 according to Guillet et al. (2022), with a very similar study area and temporal data coverage. These important disagreements may be explained by the different definitions used, the methodology, the data used (e.g., Ke et al. (2022) study includes MODIS data of coarse resolution for change detection), etc.
It is worth noting that a large number of surge events of low magnitude are certainly not inventoried by these studies. In a region of Pamir-Alay, Mattea et al. (2025b), detected a large number of surges or surge-like pulsations by photo-interpretation and using DEMs from a panel of satellite imagery. They detected 171 pulsating glaciers or low-intensity surge events in this area, where for exemple the studies of Guillet et al. (2022) and Guo et al. (2023) inventoried only five or fewer surge-type glaciers. This difference is probably due to better imagery resolution, a long study period, specific and manual processes focused on such low-intensity variations. They observe such pulsations on glaciers even smaller than 1 km^2, but there is a predominance on larger glaciers. The study of Mattea et al. (2025b) confirms the continuous spectrum of glacier pulse instabilities (Herreid and Truffer, 2016).

The recent global inventory from Guillet et al. (2025) allows quantitative comparison of surge events between HMA and the other clusters, noting however that a large number of surge events in Svalbard-Russian Arctic are not entirely captured in the study period due to their duration. Satellite observations show that surges in Alaska-Yukon have overall shorter durations (median of 2.3 years) than in Svalbard-Russian Arctic (median of 3.3 years during their study period), and HMA lies in between (median of 2.8 years). However, while there are no significant differences in the peak surface velocities during surges between the two other clusters (medians of 6.8 and 6.5 m day^{-1}), the peak velocities in HMA are approximately twice lower (median of 3.3 m day^{-1}). In all regions, the velocity surge events generally increase slowly several years before the peak velocity (up to about 10% of the maximum velocity) before an exponential increase from about 500 days before the peak velocity. Larger differences are found in the velocity change patterns, where surges in Alaska-Yukon end in a faster deceleration than in the Svalbard-Russian Arctic cluster. In

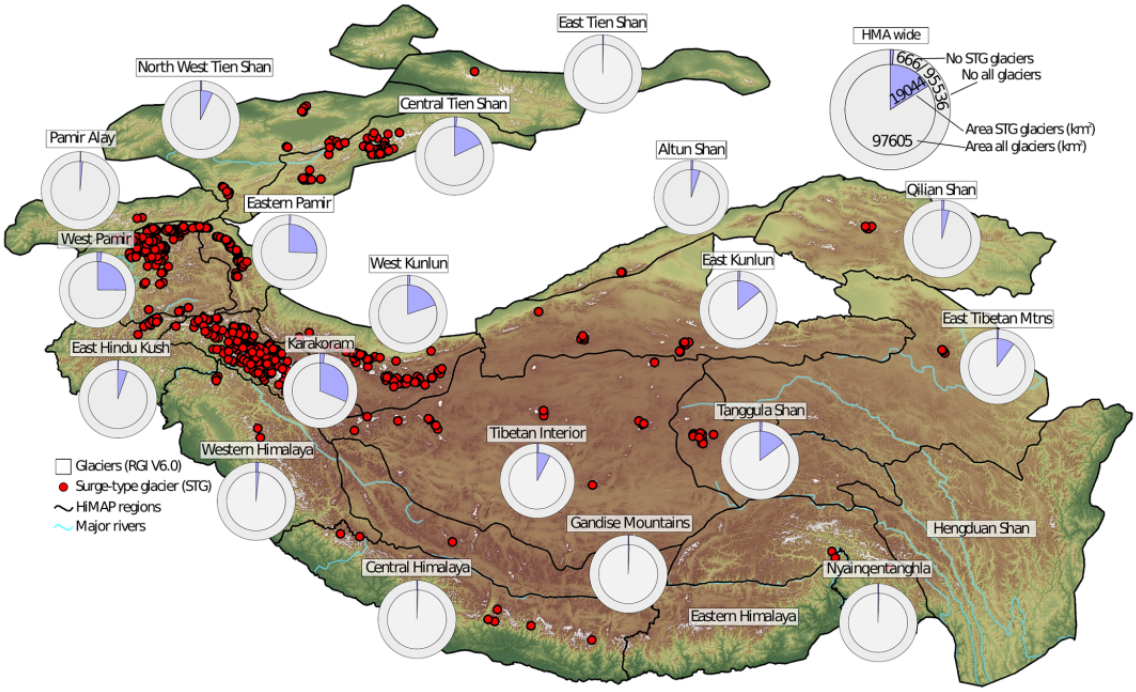

Figure 1.14: The distribution of surge-type glaciers (red dots) across HMA, with the number and area of surge-type glaciers within each HMA region compared to the total glacier population. Figure from Guillet et al. (2022).

HMA, the decrease profile is between those of the two other clusters, with around 30% of the maximum surface velocity at 180 days after peak, which is rather symmetrical to the velocity increase except for the rather heavy-tailed distribution of onset duration. Guillet et al. (2025) hypothesise that the longer surge terminations in Svalbard-Russian Arctic could be related to the fact that most glaciers in this region are marine-terminating, which implies different mechanisms at glacier fronts compared to those that are land-terminating. HMA region proves to host a particular diversity of events, which makes this region interesting for investigating new behaviours on a large number of surge events (Chapter 2) and for observing different mechanisms and settings (Chapter 3).

1.3.3 Surge dynamics in HMA

While numerous case studies have been conducted in this region, the following sections focus on a selection of significant examples, which are illustrative but not exhaustive. Different surge mechanisms have been highlighted in HMA and more particularly in Karakoram and Kunlun Shan, with both so-called Alaskan (hydraulical control) and Svalbard-types (thermal control) in the often-used binary classification (see box in section 1.4.2.2), or mixed types (Hewitt, 2014; Quincey et al., 2015; Bhambri et al., 2017; Chudley and Willis, 2019). Glaciers of all thermal regimes can be found in Karakoram: cold, polythermal and temperate, even though their thermal regimes remain largely uncertain (Hewitt, 2007; Cuffey and Paterson, 2010, p399-400).
Several studies find that surge-type glaciers in Pamir and Qilian Mountains are mainly obeying thermal mechanisms with long surge events and cycles, but also find, for example seasonal variations pointing towards hydrological controls (Gao et al., 2022; Wang et al., 2023). Regional-scale analysis considers that surge events in Western Pamir and Karakoram are probably also thermally triggered (Quincey et al., 2015; Wang et al., 2023). How-

ever, Yasuda and Furuya (2015) writes that surge events in Western Kunlun Shan would rather be hydraulically-triggered (e.g., related to velocity and speedups seasonality), despite the long duration and recurrence interval associated to the Svalbard type.
However, several glacier surges in Karakoram are considered as hydraulically-triggered , such as those of Shisper glacier (Beaud et al., 2022; Bhambri et al., 2020), Hispar (Paul et al., 2017) and Kyagar glaciers (Gao et al., 2024; Round et al., 2017). In contrast, close to these glaciers, the last three surges of Khurdopin glacier might have thermal control, but with possible hydrological influence (Steiner et al., 2018; Quincey and Luckman, 2014).

Other controls of surging cycles have been observed. Medvezhiy glacier, in Pamir, shows regular surge cycles of 10-16 years that may be caused by a topographic control of the flow and after an accumulation threshold is reached. An extreme surging velocity of 500 m day^{-1} was recorded in 1951 for this glacier (Kotlyakov et al., 2018). Lovell et al. (2018) shows that the recent surge of the Sabche glacier may also have been controlled, at least partially, by subglacial topography. This glacier, one of the very few surge-type ones inventoried so far in this Himalayan region, had maximum surge velocities of 1.6 m day^{-1}, with quiescent velocities that may be below 0.2 m day^{-1}.

Several studies report kinematic waves on surge-type glaciers of HMA. They are topographic waves of compression fronts traveling at a rate much higher than the ice flow velocity (Singh et al., 2011). The Hispar glacier surge had a kinematic wave, travelling down-glacier around 6 times faster than its maximum flow velocity (Paul et al., 2017). Quincey et al. (2015) found, in Karakoram, two surges with a down-propagating kinematic wave (e.g., Braldu surge), while three others show uniform velocity increase over the surface. A study indicates that Medvezhiy glacier had kinematic waves of about 25 m in height that propagate at one order of magnitude faster than the glacier flow velocity (Kotlyakov et al., 2018).

Spatially and temporally, velocity patterns can be complex. For example, the front of the 2015-16 Hispar surge remained very stable for 6 months, without any explanation proposed, until a second advance up to a tributary confluence (Fig. 1.10.b) (Paul et al., 2017). The 2011-15 surge of the Bivachny glacier shows a nearly stable front at the surge onset, at a tributary confluence, where the previous surge stopped (Wendt et al., 2017). It then surpassed this point after filling a quiescence-related depletion to propagate down-glacier up to the confluence with Fedchenko glacier. Although topographical junctions or bed features causing different surge dynamics remain, all surge events on the same glacier may not follow the same flow pattern (e.g., Kochtitzky et al., 2019).

1.3.4 Surge occurrence and glacier advance

Copland et al. (2011) noticed an increase in surge events in the Karakoram region since around 1990, combining literature review and satellite imagery over about fourty years. However, Paul (2020) and Rankl et al. (2014) find no increase in surge activity in this region. Guo et al. (2023) inventoried surge-type glaciers over two periods of 20 years or more: 1970s-2000 and 2000-2020. They find 30% fewer surge-type glaciers in the first period, but it may not be significant considering that i) the elevation data of the 1970s does not cover some parts of Tien Shan and Kunlun Shan, and ii) the nearly thirty-year time frame of 1970s-2000 can be enough to mask out the elevation pattern of some glacier surge, unlike the smaller temporal baseline over 2000-2020.
An increase in surge occurrence would be linked to climate evolution and, in particular, to the Karakoram Anomaly (see section 1.3.1), which would support the role of mass balance on the surge cycle.

As glacier surges need a certain mass buildup as a precondition to trigger, a shortening of surge-cycle periods of glaciers due to faster accumulation might have occurred (Copland et al., 2011; Cuffey and Paterson, 2010, p530). This has been observed for Medvezhiy glacier, in HMA, or Variegated glacier in Alaska (Eisen et al., 2001; Kotlyakov et al., 2018).
Also, the Karakoram anomaly causes the advance of all glaciers, complicating the surge-type distinction (Lv et al., 2020). It also complicates the determination of the surge phases and the dates of surge onset and termination, such as for North Chongtar glacier, which slowly advanced for 50 years before a clear surge signal.

1.4 The physics of glacier surges

1.4.1 Glacier mechanics: driving and resisting forces

Glaciers mainly flow because of the gravitational force that acts on their mass (Cuffey and Paterson, 2010, p295-297). The along-slope component of this gravitational force is called the driving stress τ_d (Fig. 1.15). It can be estimated with the expression:

$$\tau_d = \rho g H sin(\alpha) \tag{1.1}$$

with ρ the density of ice, g the gravitational acceleration, H the glacier thickness and α the surface slope (Cuffey and Paterson, 2010, p295). This expression assumes a parallel-sided slab of ice with limited surface slopes (i.e., a few tens of degrees) and ignores other forces that act on the ice column (e.g., lateral drag). The driving stress of a glacier typically ranges from 50 to 200 kPa (Cuffey and Paterson, 2010, p297-298, 232).

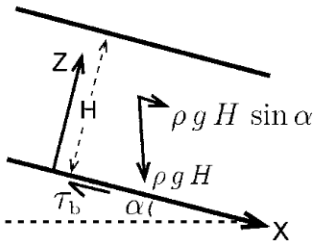

Figure 1.15: Gravitational force and driving stress on a simplified model for a parallel-sided slab of ice. Figure from Cuffey and Paterson (2010, Fig. 8.5.a)

For equilibrium, the most important resisting force to driving stress is the shear stress τ_b at the bed, opposed to the ice flow and relative to the friction as expressed by 1.2 (Cuffey and Paterson, 2010, p226),

$$\tau_b = \psi u_b \tag{1.2}$$

with ψ the apparent drag factor and u_b the sliding velocity.
In general, and especially for mountain glaciers, the shear stress can be approximated by the driving stress with a factor f':

$$\tau_b = f' \tau_d \tag{1.3}$$

In most situations, f' lies between 0.5 and 1.5, except in the case of floating ice shelves and some of their tributaries (Cuffey and Paterson, 2010, p301).

The water at the bed interface has a strong impact on glacier velocity. For hard-bedded glaciers, the presence of water at the bed lubricates the interface and reduces friction by increasing the water pressure P_w in cavities. The difference between the normal force P_i due to the weight of ice and the basal water pressure P_w is called the effective pressure N (Cuffey and Paterson, 2010, p238):

$$N = P_i - P_w = \rho g H - P_w \tag{1.4}$$

Thus, increasing the water pressure at the bed can increase the slip velocity of the glacier, varying approximately as N^{-1} (Bindschadler, 1983; Cuffey and Paterson, 2010, p240).

We can directly express the link between effective pressure and basal shear stress, for a steady state ($\tau_{b,ss}$) and at the pressure melting point, given by the parameterisation from Gagliardini et al. (2007):

$$\tau_{b,ss} = NCB \tag{1.5}$$

for which C (without unit) is the maximum friction threshold in steady state and B is a formula for which we redirect the reader to the cited studies, which depends mainly on C, N, the sliding velocity u_b, and a sliding parameter without cavitation.

1.4.2 Surge mechanisms

1.4.2.1 Overview of mechanisms

It has long been proposed that a surge is triggered when basal shear stress reaches a critical level (Meier and Post, 1969; Thøgersen et al., 2024; Cuffey and Paterson, 2010, p530). This stress mechanically increases at the glacier bed during buildup, generally in the lower part of the reservoir area due to thickening and the increase in surface slope (Meier and Post, 1969). The Variegated glacier is a good example of this: there is a strong correlation between the cumulative mass balance at a location in the reservoir area and the three previous surge events, with the average cumulative accumulation (ice equivalent) between events at this location being 43.5 m (Eisen et al., 2001).
But the consecutive trigger mechanisms can vary: several surge mechanisms have been observed or theorised, and can coexist (Terleth et al., 2021). The field is notably complex to synthesise due to the proliferation of both recent and long-standing theories, variations in terminology and mechanisms... This heterogeneity, combined with the absence of a systematic review, complicates the synthesis required in the following sections. In the following, we report the main mechanisms summarised by Benn et al. (2019a) and illustrated in Fig. 1.16.

Hydraulical switch Some surge theories are based on an effective pressure-dependent friction law: the relationship between the basal shear stress and the basal sliding velocity strongly depends on the water pressure at the ice-bed interface. Provided that the basal temperature is at the melting point, an increase in the basal water pressure decreases the basal shear stress and increases the glacier slip velocity, similar to what drives seasonal fluctuations of the velocity (Cuffey and Paterson, 2010, p490-492).
In case of important water input events (melt, rain), an inefficient drainage system leads to an increase of the basal water pressure (high glacier slip velocity), and an efficient channelised system permits fast drainage and preserves low water pressure (low glacier slip velocity) (right-hand table on Fig. 1.16).The state of the drainage system depends on the season: 1) at the beginning of the melt season, the drainage system is still inefficient, allowing a build-up of water pressure at the bed and increased flow velocity; 2) when the drainage system becomes efficient, the basal water pressure decreases, and can remain low even in case of large water input (strong melt, rain events) so the basal slip is low; 3) at the end of the melt season, the water input is not sufficient to keep the channels open and the drainage system returns to an inefficient one. In autumn, occasional water input can cause short speedup events, but basal slip remains low for most of the accumulation season.
This drainage-velocity relationship is the basis for the surge trigger often referred to as *hydraulical switch* or *trigger* (Fig. 1.16). Large water volumes entering an inefficient drainage system due to rain or significant melting (for example, through crevasses) will increase the basal water pressure and weaken the till (e.g., Sevestre et al., 2018; Turrin et al., 2014). Under a sufficiently thick ice column, the shear stress locally reaches a yield

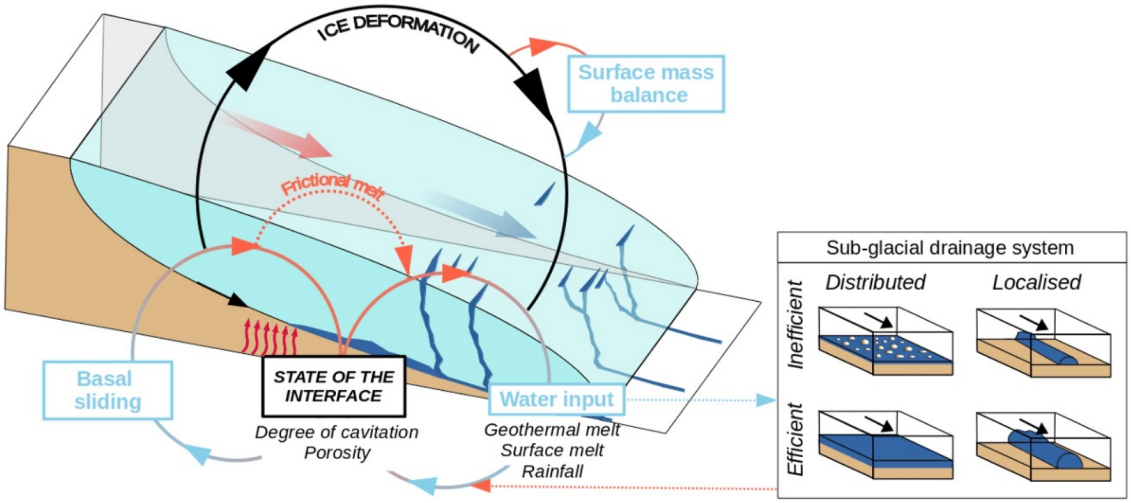

Figure 1.16: Sketch of the couplings between subglacial drainage and subglacial friction from Thøgersen et al. (2024). Hereafter, we provide a simplistic overview of the different mechanisms and theories we present in the text. For a hydraulical switch mechanism, the focus is on water input and the subglacial drainage system on the right-hand table, affecting friction. The thermal trigger, and in particular frictional heating, involves all the feedback loops. The theory derived from Thøgersen et al. (2019) puts the state of the interface and the corresponding feedback loops at the heart of its model. Minchew and Meyer (2020) isolate the left sliding-interface feedback loop from other surge mechanisms to study till behaviour (e.g., dilation, internal friction). The enthalpy theory estimates the quantities behind the arrows and variables rather than formulating mechanical relationships (Benn et al., 2019a, 2023).

stress of the basal sediment layer. Also, the drainage system may becomes progressively less efficient over the years with increasing glacier thickness, closing sooner and sooner at the end of the melt season (Thøgersen et al., 2024). Eventually, sediment starts to deform in a sufficiently large area, disrupting the drainage system. The sudden increase in water pressure that results from drainage failure further causes a rapid basal slip and the surge onset (Jay-Allemand et al., 2011). As till may fail under high shear stress, i.e. initiate a rupture in the material and lose its internal cohesion, rupture in a cascade effect due to stress redistribution could propagate the surge instability (Nolan, 2003; Truffer et al., 2000; Turrin et al., 2014). The surge front could also propagate as a destructive front of the drainage system, keeping high water pressure in the surging area until water can be drained out of the system (Fowler, 1987; Cuffey and Paterson, 2010, p533). A similar chain of consequences has been formulated for hard bed glacier. High shear stress increases the formation of cavities, also causing the collapse of the channelised system which triggers the surge (Cuffey and Paterson, 2010, p534).

Observations show that these surges stop rapidly after the opening of an efficient drainage system, such as the termination of the last surge of Recherchebreen glacier for which the drainage outburst created a sediment delta of several hundreds of metres, or the 1993-1995 Bering glacier surge that was divided in two seasonal peaks which both ended with an outburst flood at the summer ends (Fatland and Lingle, 1998; Kavan et al., 2024; Cuffey and Paterson, 2010, 529). The hydraulical trigger explains the seasonal pattern of several surge events that begin when drainage systems are inefficient: at the end of the melt season or during winter due to the water remaining, and during the beginning of the melt season (Eisen et al., 2005; Cuffey and Paterson, 2010, p535). Among minor findings, Terleth et al.

(2024b) shows that the drainage system can be intermittently efficient during a surge. A correlation has also been measured between basal water pressure and flow velocities during a surge of the Variegated glacier (Kamb et al., 1985). Finally, a recent study argues that till dilation, for glaciers with a soft bed of low permeability, has a fundamental control that further increases thinning and flow velocity at surge onset (Minchew and Meyer, 2020). In conclusion, subglacial till and hydrology often play a major role in surge events, independently of a possible hydraulical-switch trigger (Harrison and Post, 2003).

Thermal trigger The often-called thermal trigger relies on a thermodynamic feedback (Fig. 1.16). On cold-based glaciers, there is a cycle between a cold bed (quiescent phase) and a warm bed (pre-surge and surge phase). During the quiescent phase on a cold bed, the glacier thickens and insulates the bed, which reaches a pressure melting point over a portion of its bed due to warming from geothermal heat flux. Whatever the original thermal state, basal water is then produced, which modifies the bed interface, particularly for soft beds (Fowler et al., 2001; Murray et al., 2003b). The increase of basal water pressure, which reduces the effective pressure, weakens the till and causes its dilation. Then, there is a positive thermodynamic feedback: the accelerated deformation of the till, increasing the basal motion, causes frictional heating. Frictional heating adds more meltwater through thawing, which further affects the till and glacier velocity (Fowler et al., 2001). At this stage, the hydraulical trigger may intervene, as sudden water input can bypass the ongoing thermodynamic feedback. Dunse et al. (2015) name hydro-thermodynamic feedback the fact that repeated summer melt contributes to gradual surge/pre-surge onset by entering crevasses and warming the cold base (a frontal cold-ice plug here), retroactively extending the crevasse area. Surface velocity can also increase due to enhanced deformation, as a result of the decrease in ice viscosity with warming (Benn et al., 2019a; Cuffey and Paterson, 2010, p55,64,361-362). The termination may occur by refreezing of the bed due to the thinner ice (Cuffey and Paterson, 2010, p536). The thermal trigger can explain the slow onset or termination of several surge events. This is especially true in the case of a frozen bed and, even partially, for a polythermal glacier. Indeed, the propagation of the surge requires an area of basal cold ice ahead to also warm up progressively, leading to a slow propagation of the surge front.

1.4.2.2 A critical perspective on historical surge classification

Svalbard- vs Alaskan-type surges

Historically, the types of surges were often classified into two families considering their trigger mechanism and their specificity (Fowler et al., 2001; Murray et al., 2003b). These families were named after their predominance in some regions: Svalbard types and Alaskan types. In such a conception, Svalbard-type surges are thermally-triggered and show a gradual increase and decrease (several months or years) of their velocity at the bounds of the active phase. The surge typically lasts several years or more than a decade, with a trigger period independent of the season, and is more common for cold and polythermal glaciers, where the glacier base can switch from cold to temperate conditions. Alaskan-type surges occur on temperate glaciers and have a hydraulical-switch trigger. The surge has rapid velocity changes (e.g., termination in several days) and surge durations of a few years, with initiation and abrupt termination often occurring in winter and summer, respectively (Murray et al., 2003b; Quincey et al., 2015; Bhambri et al., 2017; Terleth et al., 2021).

The historical distinction of surge events into the Svalbard-type and Alaskan-type

classes (see box in section 1.4.2.2) is increasingly criticised. All surge events cannot be classified into one of these two families, and some of them show mixed mechanisms (Gao et al., 2025; Terleth et al., 2021). For example, the last surge of Morsnevbreen (Svalbard) started with a gradual acceleration over several years, probably with a thermodynamic feedback, until summer 2015, from which the velocity suddenly increased. The authors note that it coincides with a period of warm temperatures and frequent heavy rain events, and they also observe peaks during summer in the following years. This example shows well how different mechanisms can interfere, a short-term hydrological event bypassing long-term dynamics. Those are not isolated cases, and Sevestre et al. (2018) shows the same dynamics for two other surge events in Svalbard. The hydro-thermodynamic interactions can also occur on longer time scales, such as for the surge of Basin-3 glacier on the Austfonna ice cap, Svalbard. Dunse et al. (2015), who studied extensively this glacier, names hydro-thermodynamic feedback the fact that repeated summer melt contributes to gradual surge/pre-surge onset by entering crevasses and warming the cold base (a frontal cold-ice plug here), retroactively extending the crevasse area. Sevestre et al. (2015) also shows the great variability of the thermal regime of Svalbard glaciers, with large glaciers that seem generally polythermal with most of their basal interface being temperate, and small glaciers being cold.
The enthalpy theory (see section 1.4.3) and Benn et al. (2023) in particular show in which manner Svalbard and Alaskan types obey the same mechanisms (i.e., both with drainage ineffectiveness and then frictional feedbacks) and that this classification is misleading; they recommend abandoning it. The analysis and the statistics of surge event characteristics from the recent global inventory of Guillet et al. (2025) support these findings. They note a number of similarities between the different clusters that can contradict the historical classification, and argue that differences can be explained by different enthalpy budgets and propagation characteristics, aligned on a continuous spectra of the surging behaviour. The Svalbard-Alaskan classification originates from the detailed knowledge of a few specific cases (e.g., *Alaskan-type* with the Variegated Glacier or *Svalbard-type* with the Monacobreen), which may be end-members or the surge mechanism spectra (Murray et al., 2003b). Recent and systematic observations, in particular permitted by remote sensing, allow for the observation of a broader diversity of events.

1.4.2.3 Surge propagation

After initiation, the surge instability propagates over the glacier through a surge front, or, as observed with current data resolutions, an entire section can start moving simultaneously without discernible propagation (Quincey et al., 2015; Pritchard, 2005; Kochtitzky et al., 2019; Burgess et al., 2012). The surge front propagates down-glacier, up-glacier or both, at a velocity higher than the ice flow velocity. Downward propagation often takes the form of a compression/kinematic wave or a bulge.
Some propagation mechanisms have already been described in the hydraulical and thermal trigger paragraphs (see section 1.4.2.1), but other mechanisms have been proposed. For example, Thøgersen et al. (2019, 2024) also explore a rate-and-state friction theory. In this theory, which is more detailed in Chapter 3, the propagation of the surge front follows a principle of velocity-weakening friction which is governed by a characteristic length d_c. Once the surge is triggered, shear stress will accumulate at the surge front. When the basal friction can no longer balance the driving stress, the stress is reported to the next friction point by a characteristic length d_c, until the next failure, propagating the surge instability. d_c, typically in the range of 1-10 metres, can be related to the size of the cavity or the wavelength of the bed obstacles for hard beds, and would be linked to the properties of the sediment layer (e.g., thickness, till porosity, degree of localisation) for soft beds.

The surge front typically propagates at rates of hundreds or thousands of metres per year, but there is a high variability (e.g., Benn et al., 2019b). For example, the surge front of the Sít' Kusá glacier (Alaska) propagated at about 30 km year $^{-1}$, while the surge front of Morsnevbreen glacier (Svalbard) propagated at a rate varying over time from about 0.5 km year $^{-1}$ to 15 km year $^{-1}$ (Benn et al., 2019b; Liu et al., 2024). The slow surge of the polythermal Trapridge glacier is at the end of the spectrum, a warm-based bulge propagated at 30 m year $^{-1}$ over cold-based dead ice from the previous surge, a propagation rate that is somewhat equal to the ice flow velocity upstream. The propagation of the surge front may not be regular, with periods of slow or fast propagation, following the different phases of a surge (e.g., Benn et al., 2019b).
The propagation of the surge front can be associated with kinematic waves. Turrin et al. (2013) observed, using velocity data, the Bering glacier surge (Alaska). They report the propagation of a kinematic wave several years before the surge, triggered consecutively to the passage of the wave down through the reservoir area. Liu et al. (2024) observed a similar phenomenon: speedups propagated each year in the reservoir area before the surge, stopping before or at the dynamic balance line, while only the surge front propagated past it. Kamb et al. (1985) observed also the propagation of day-scale *mini-surges*, or speedups, in the few years before a surge of the Variegated glacier. They are caused by the propagation of a pressure wave in the basal water system.

1.4.3 From surge mechanisms to models

A number of surge mechanisms and triggers have been proposed since the first observations, and significant progress toward a model encompassing the broad surge mechanisms and various theories has been made recently (Benn et al., 2023; Thøgersen et al., 2024; Terleth et al., 2024a). In this section, I first present two mechanical approaches and then a thermodynamic one to provide an overview of some of the recent and advanced theories (Fig. 1.16).

Several studies investigate a *rate-and-state* friction approach, first introduced in a study of surge basal mechanisms by Thøgersen et al. (2019). This law, used for example more traditionally in earth mantle and rock geosciences, describes the friction evolution in function of the sliding velocity and the state of interface, and permits to model both stable and unstable behaviours (e.g., Dieterich, 1979; Handwerger et al., 2016; Helmstetter and Shaw, 2009). This is possible by incorporating both velocity-strengthening (friction increases with velocity) and velocity-weakening (friction decreases with velocity) mechanisms.
Thøgersen et al. (2024, 2019) and Gilbert et al. (2022) proposed a spatial model based on the basal friction and drainage interaction incorporated in a rate-and-state framework. The transition from a velocity-strengthening friction to a velocity-weakening friction when reaching a shear stress threshold can model surge onset and propagation, as well as other speedup events. The key point of this model is that friction and drainage - which are often modelled separately - not only interact through the resulting normal stress, but the basal interface also changes with the velocity evolution (Fig. 1.16).
The velocity-weakening frictional behaviour for glacier slip over a geometric bed has been tested experimentally by Zoet and Iverson (2016) and Zoet et al. (2022). Overall, for these models, the existence of a velocity-weakening behaviour is required, but this existence is still debated for both hard and soft beds (Thøgersen et al., 2024, and references therein). This mechanism in the domain of glaciology requires progress to be able to improve generalised slip law models, which are widely applicable to all glacier flows (e.g., Zoet and Iverson, 2020).

Minchew and Meyer (2020) emphasises the importance of till dilation and soft-bed mechanisms for surge modelling, which are often overlooked by other models (e.g., Thøgersen et al., 2024). They formulate the evolution of internal friction, porosity and pore water pressure within the deforming till layer as functions of the rate and history of shearing within the deforming till. For this, they develop a rate-and-state friction model. They isolate a single process from other surge-related mechanisms, such as the evolution of the hydrologic system or frictional heating (Fig. 1.16). Despite these limitations, the authors claim that the one-dimensional model of this study is very promising to be included in other models and it has good abilities to model surge onsets. This mechanism requires more work and attention, particularly in cold areas (Minchew and Meyer, 2020; Terleth et al., 2021). In particular, the mechanism they proposed does not depend on changes of the hydrological system, supporting the hypothesis that it is the surge motion that inhibits the efficiency of the drainage system, rather than the increase of the basal water pressure that triggers the surge.

Another way to approach surge modelling is through thermodynamic theory, with the formulation of an enthalpy theory (Benn et al., 2023). This enthalpy theory provides a single framework in which the different mechanisms or models could be described, integrated and linked altogether. Benn et al. (2019a), Sevestre et al. (2015) and other studies elaborated this non-spatial model or framework based on the energy balance of the enthalpy, through the sources and sinks of enthalpy (Fig. 1.17). Benn et al. (2019b) analyses a case study in light of this framework.
Basically, in this framework, a stable non-surge-type glacier is in balance between the inputs and losses of energy that form its enthalpy (such as ice temperature and stored water). This equilibrium operates on time scales of a year or more. The glacier mass and the glacier enthalpy are linked through basal dynamics: a high enthalpy promotes ice flow velocity through deformation or lubrication/high basal water pressure, and ice mass, in turn, is potential energy convertible into enthalpy through frictional heating (Benn et al., 2023). Small variations in some of these variables occur naturally. The instability arises when the system cannot dissipate energy efficiently, e.g. through water drainage, and maintain an oscillatory cycle. Benn et al. (2023) shows that hydraulical and thermal triggers obey the same mechanism: whatever the water originates from, seen from an enthalpy point of view (surface melt, geothermal heating, etc.), the surge initiates the same way with a thermal friction-velocity feedback. The frictional heating is an important dynamic in this framework, as this retroaction generates a non-negligible quantity of basal water. However, as observed for the case study surge they discuss in Benn et al. (2019b), hydrological events can outrun the thermal feedback onset. The case of cold-bedded glaciers is specific in the way the bed refreezes after the previous surge and has to warm up till the melting point before friction-velocity feedback initiates the surge. This framework includes and agrees, in a streamlined way, to the hydraulical and thermal mechanisms and their case-study variations that we developed in section 1.4.2.1. Terleth et al. (2024a) improved their framework to better retrieve velocity variability at different timescales through hydrological forcing. As this framework does not predict the spatial characteristics of surges nor precise mechanisms, it is difficult to compare it with observations and different specificities of surge events (Benn et al., 2023; Partington et al., 2025; Thøgersen et al., 2024). Progress must be made on the different theories to analyse them in this framework.

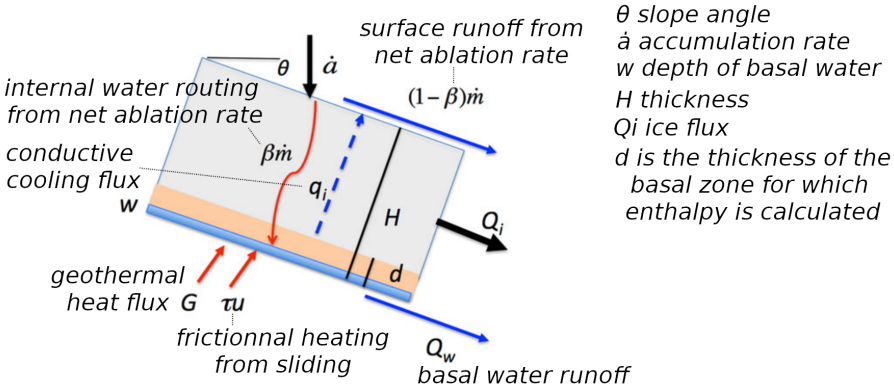

Figure 1.17: Sketch of the enthalpy model components, on an inclined parallel-sided slab. Enthalpy sources are in red and sinks in blue; the names of contextual variables of the system are on the right. Figure from Benn et al. (2019a).

1.5 Objectives of the PhD thesis

The goal of this work is to observe the dynamics of glacier surges in High Mountain Asia from satellite remote sensing observations. The philosophy is to contribute to the study of surge events with a large-scale and multi-event coverage. In this manuscript, I address two scientific questions.

1.5.0.1 What surge dynamics can we observe from temporally dense elevation time series?

Existing studies generally analyse surge events on the basis of a small number of elevation observations. Recent developments in the processing of ASTER stereo images (Brun et al., 2017; Hugonnet et al., 2021; Shean et al., 2020) provide, for the first time, dense elevation time series. But these noisy and irregular observations require specific filtering and post-processing to properly capture the elevation change signal associated with surges. Chapter 2 provides methodological developments for generating a filtered and regularly sampled elevation dataset and showcases the potential of this data for the study of surges.

1.5.0.2 To what extent can we test existing models of surge initiation and propagation with remote sensing data?

The models and theories developed are rarely based on observations or are generally compared against a limited number of case studies. In Chapter 3, we explore whether a newly generated dataset of elevation and velocity can contribute to our understanding of glacier surge mechanisms. In particular, we will compare our observations with constitutive laws derived from the model of Thogersen et al. (2019). Our focus is on the trigger area associated with driving stress evolution, and on the propagation of the surge front.

Chapter 2

Glacier surge monitoring from temporally dense elevation time series: application to an ASTER dataset over the Karakoram region

This chapter is the accepted version of Beraud et al. (2025), which is published in open access in the peer-reviewed journal *The Cryosphere*. A consequent part of the introduction of this chapter is thus redundant with Chapter 1.

As we introduced, glacier surges have been extensively observed in surface velocity time series. Much less work has used time series of glacier surface elevation at timescales of a year or less, and we believe there is still surge dynamics that we can highlight by observing this underrated side of surges. *What surge dynamics can we observe from temporally dense elevation time series?*
To answer this question, we need to find a suitable dataset and a way to extract information from it. We have chosen to rely on the existing dataset from Hugonnet et al. (2021). The data quality of the dataset and the characteristics of the surface attributes we want to obtain (e.g., interpolated so as to compute volume transfers and slope calculation) implied an important work of development. The purpose of this publication is thus to propose a processing workflow, developed on our source dataset but applicable to other datasets (e.g., TanDEM-X, WorldView or other time series of DEMs). Although the emphasis of the article is not on the analysis of the dataset produced, we showcase a number of observations and estimates that are possible with the developed workflow.

We want the code and dataset generated to be reused or improved as much as possible. The code of the workflow is made available on a public repository, along with regional elevation change maps we generated (Beraud et al., 2024). The complete interpolated elevation dataset we produced should be made publicly available in the same repository shortly after completion of the work of this PhD.
This work benefited from the contributions of Romain Hugonnet, who generated the input dataset and assisted with the data handling and algorithms. Together with Prashant Shekhar, the main contributor to the interpolation algorithm, they particularly contributed to the writing and reviewing of the article.

2.1 Abstract

Glacier surges are spectacular events that lead to surface elevation changes of tens of metres in a period of a few months to a few years, with different patterns of mass transport. Existing methods to derive elevation change associated with surges, and subsequent quantification of the transported mass, rely on differencing pairs of digital elevation models (DEMs) that may not be acquired regularly in time. In this study, we propose a workflow to filter and interpolate a dense time series of DEMs specifically for the study of surge events. We test this workflow on a global 20-year dataset of DEMs from the optical satellite sensor Advanced Spaceborne Thermal Emission and Reflection Radiometer (ASTER). The multistep procedure includes linear non-parametric Locally Weighted Regression and Smoothing Scatterplots (LOWESS) filtering and Approximation by Localized Penalized Splines (ALPS) interpolation. We run the workflow over the Karakoram mountain range (High Mountain Asia). We compare the produced dataset to previous studies for four selected surge events, on Hispar, Khurdopin, Kyagar and Yazghil glaciers. We demonstrate that our workflow captures thickness changes on a monthly scale with detailed patterns of mass transportation. Such patterns include surge front propagation and changes in dynamic balance line, among others. Our results allow a remarkably detailed description of glacier surges at the scale of a large region. The workflow preserves most of the elevation change signal, with underestimation or smoothing in a limited number of surge cases.

2.2 Introduction

Surge events are extreme cases of the continuous spectrum of glacier flow instabilities (Herreid and Truffer, 2016). Surges are quasi-periodic events characterized by abnormally rapid glacier flow, lasting from several months to years (Bhambri et al., 2017; Cuffey and Paterson, 2010). Large masses of ice are transported during surge events, causing thickness changes (Bhambri et al., 2017, 2022). They occur on a limited number of glaciers known as "surge-type" glaciers, which are clustered in a few regions of the globe, among which the Karakoram in High Mountain Asia (Guillet et al., 2022; Sevestre and Benn, 2015). Surges can occur on both land-terminating and tidewater glaciers, and on either polythermal or temperate glaciers (Cuffey and Paterson, 2010). The mechanisms behind the surge phenomenon (origin, surge trigger, etc.) are not yet fully understood and are an ongoing focus of theoretical investigations (e.g., Benn et al., 2023; Crompton et al., 2018; Terleth et al., 2021; Thøgersen et al., 2024).

Observations of glacier surface elevation change over time are extremely useful to document glacier surges, and can give insight into the current state of a glacier in its surge cycle. The surge period, active phase of the surge-type glacier, is characterised by thinning (i.e. decrease of surface elevation) in a reservoir area and thickening in a receiving area, representative of the ongoing mass transfer. The quiescent period consists in strong thinning in the receiving area of the previous surge, and a thickness increase (mass build-up) before the next surge and mostly in the future reservoir area. The differencing of elevation maps permits one to compute the volume of ice transferred during a surge event and determine the spatial extent affected (e.g., Bhambri et al., 2022; Gao et al., 2024; Steiner et al., 2018). A few surge-type glaciers may begin surging after a critical mass has built up in the reservoir; information that is accessible with elevation differencing (Kotlyakov et al., 2018; Lovell et al., 2018). Elevation data, and by extension surface slope, can be used to compute and analyse basal shear stress, which may play a critical role in the triggering of surges (Beaud et al., 2022; Thøgersen et al., 2024).

Remote sensing analysis from satellite imagery can produce a large amount of digital elevation models (DEMs), providing observations of the elevation of the glacier surface and its variation over time (e.g., Hugonnet et al., 2021). Such data have been used in numerous studies, ranging from the inventorying of surge-type glaciers to detailed case studies (e.g., Bhambri et al., 2022; Guillet et al., 2022; Guo et al., 2020; Round et al., 2017). However, the use of DEMs for the study of surges is often limited to a few dates or specific case studies, because the temporal availability of DEMs does not always match the surge phases. The retrieval of mass transfer variations happening during such surge events requires dense elevation time series with a resolution of one or a few months in principle. Meanwhile, temporally dense elevation time series from satellites covering a long period of time have recently become available for studying glacier elevation change. Such acquisitions started around the year 2000, with time series now spanning more than two decades, long enough to capture a number of surge events and a few complete surge cycles. In particular, the TERRA satellite with its ASTER sensor is the only optical stereo mission that provides systematic and global acquisitions (Berthier et al., 2023).

Dense elevation time series from this sensor have been successfully used to study long-term elevation trends and multi-year glacier mass balance (e.g., Brun et al., 2017; Hugonnet et al., 2021; Shean et al., 2020). It has also been used multiple times for surge observation with selected DEMs (e.g., King et al., 2021; Mattea et al., 2025a; Zhu et al., 2022), and with simple filtering (Lauzon et al., 2023; Li et al., 2023). The DEMs derived from ASTER have an elevation precision of about 5-20 metres and can have large artefacts caused by cloud sensitivity, satellite jitter, or lack of stereo correlation on saturated/textureless terrain (Berthier et al., 2023; Girod et al., 2017). Such noisy DEM time series require specific filtering techniques that preserve surge signals (i.e., preserve elevation observations before, during, and after the surge), as basic thresholds and linear methods used to assess long-term elevation changes might misinterpret surge signals as outliers. Furthermore, the estimate of volume transported and the surface slope are sensitive to data gaps and their interpolation. As a consequence, they need to be computed at similar dates across a whole glacier to ensure physical consistency. Thus, a temporal interpolation of the elevation time series is required.

Various approaches have been implemented in the context of glacier elevation time series analysis. Hugonnet et al. (2021) have implemented a complex workflow for ASTER elevation time series over glaciers at global scale. It captures a number of non-linear elevation changes, but fails to accurately reflect sudden changes associated with surge events. This is due to the filtering and interpolation methods which involve Gaussian Process Regressions, based on a multi-term kernel defined by the variance of elevation changes retrieved at global scale. This method is robust to assess global changes of glacier elevation, but fails to capture the relatively rare surge behaviour. Recent methodological improvements have allowed for sophisticated filtering that are able to preserve abrupt changes in noisy time series of elevation. For example, Wang and Kääb (2015) identified outliers in the absence of a reference elevation using the RANSAC algorithm and Derkacheva et al. (2020) applied a linear non-parametric local regressions (LOWESS) to filter and interpolate non-surge glacier surface velocities. At a higher level of complexity, Shekhar et al. (2021) developed a spline-based approximation framework to model elevation changes with heterogeneous data, which can also be used for filtering. These methodological developments paved the way for processing a large amount of DEMs in a systematic way to study glacier surges from the local to regional scale.

In this study, we develop a workflow to analyse outlier-prone, moderate-precision and

high-temporal-resolution elevation datasets adapted to the specificity of surge events. We use established algorithms to filter outliers and interpolate elevations at monthly scale while preserving surge elevation signals. We apply it to an ASTER DEM dataset from Hugonnet et al. (2021) to produce a regional dataset in the Karakoram region covering more than 100 surge-type glaciers. We evaluate the performance of the workflow compared to the results of Hugonnet et al. (2021) and other DEMs (SPOT and HMADEM). We also compare the surge characteristics such as timing and volumes transferred with other studies (e.g., Bhambri et al., 2022; Steiner et al., 2018; Gao et al., 2024).

2.3 Data

In this study, we focus on the Karakoram region (Fig. 2.1). We use two existing surge-type glacier inventories that cover at least the period 2000 to 2018 in this region (Guillet et al., 2022; Guo et al., 2023). According to Guo et al. (2023), which considers glaciers larger than 0.4 km^2, there are 354 surge-type glaciers (with individualized tributaries) in the Karakoram and 128 probable or possible ones, representing approximately 8.6% of the regional number of glaciers (39.5% in terms of area). Guillet et al. (2022) identified 223 surge-type glaciers larger than 5 km^2 not individualizing tributaries. These two studies indicate that surge-type glaciers represent 39% to 45% of the glacierized area in the Karakoram region. We use the DEMs produced in the global study of Hugonnet et al. (2021) (hereinafter referred to as H21), which ranged from 07/2000 to 09/2019 in the Karakoram and were generated from satellite images of the ASTER sensor. The DEMs have been processed at 30 m resolution with the MMASTER workflow, running under the open-source photogrammetric library MicMac (Girod et al., 2017; Rupnik et al., 2017). All DEMs have been reprojected to 100 m spatial resolution and co-registered to the TanDEM-X global DEM (Rizzoli et al., 2017). We use all ASTER elevations estimated by MicMac for any stereo-correlation score, with lower correlation associated with higher uncertainty (H21). Finally, we apply a preprocessing step specific to this dataset: 1) we filter pixels with a difference of more than 400 m between the ASTER DEM and the GLO-90 reference DEM (European Space Agency and Airbus, 2022), 2) we merge the same-date 180 km DEM strips generated by H21 by keeping, in each pixel, the elevation with the highest correlation score. We use the Copernicus DEM GLO-90 as a reference elevation for the coarse filtering of very large outliers. The Copernicus DEM GLO-90 is edited from data of the TanDEM-X mission acquired between 2011 and 2015. The impact of radar penetration in ice and snow (up to about 10 metres) creating a bias in TanDEM-X elevation estimate is negligible compared to the threshold we use (hundreds of metres) (Berthier et al., 2023; Rizzoli et al., 2017).

The sampling is not regular in time and space, and parts of the mountain range have about twice as many DEMs as others (Fig. 2.1). Overall, 30% (62%, respectively) of the dates in the time series periods are between observations that are less than six months apart (a year, respectively) (Fig. 2.2, solid orange line).

2.4 Methods

2.4.1 Workflow

We present a workflow to filter and interpolate stacks of ASTER DEMs, specifically designed to handle surge events. We use the ASTER DEMs of H21, but processed them with a different workflow, because the H21 workflow performs weakly on surge events (see for example figure S1). We use the H21 workflow as a baseline to compare our own workflow

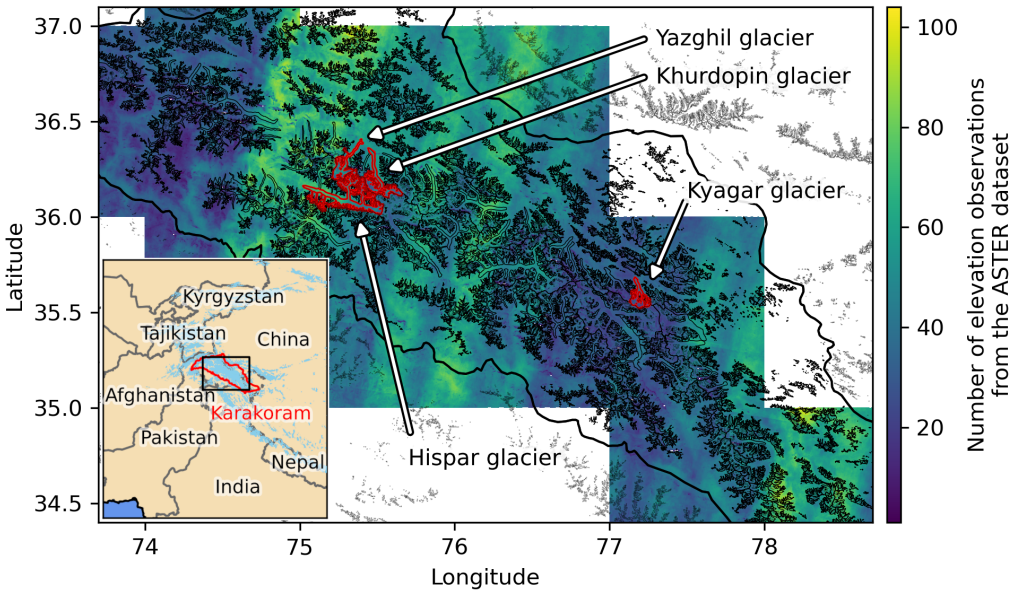

Figure 2.1: Map of the study area in the Karakoram, with regional location indicated in the inset map. The colour scale shows the number of pre-processed ASTER-derived elevation observations over the period 2000-2019 from H21. Glacier outlines from RGI7.0 are shown in black (RGI Consortium, 2023). The glaciers with the surge events analysed in section 2.5 and 2.6 are outlined in red.

to highlight improvements for surge cases. Our workflow is divided into two main steps (Fig. 2.3).
First, we filter the dataset to remove remaining outliers in three steps:

1. LOWESS workflow, core step of the filtering: we apply an iteration of the LOWESS algorithm (detailed in subsection 2.4.1.1).

2. Morphological 3x3 erosion: we implement a morphological erosion with a 3x3 kernel on the binary data mask. It removes pixels adjacent to outliers, as they also have reduced precision due to the photogrammetric processing.

3. Removal of time series with less than 10 points: we consider such time series not dense enough for our application.

Second, we interpolate the time series at regular time intervals using a B-spline method which includes an automatic hyperparameterisation algorithm (ALPS-REML), detailed in subsection 2.4.1.2. The interpolated elevations are provided as a monthly time series.

2.4.1.1 LOWESS filter

We filter the elevation time series by two iterations of the non-parametric LOWESS algorithm, which is a moving weighted regression (Cleveland and Devlin, 1988; Derkacheva et al., 2020). We use the Python *scikit-misc* implementation. For our dataset, the output of the regression is too sensitive to noise overall and too smooth over surges to be used directly as an interpolation of the elevation, so we use it for filtering only.
Here are the main parameters set for each LOWESS iteration. They have been manually tuned after visual evaluation on a number of time series samples, both with and without surge signal (Fig. 2.4). We caution that these parameters were chosen specifically for the ASTER DEM dataset and might not all be suitable for other datasets (as discussed in subsection 2.6.4).

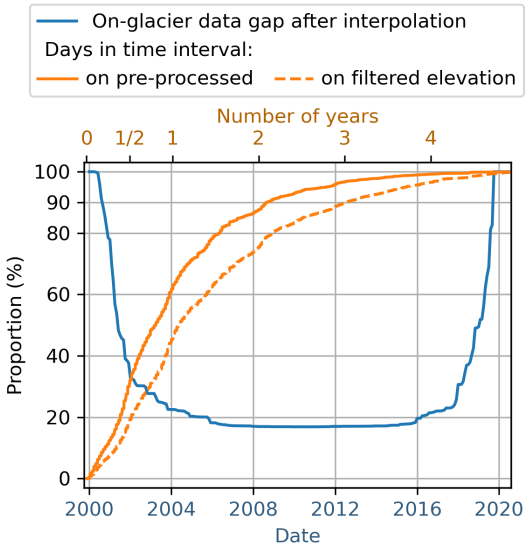

Figure 2.2: Data gap and temporal coverage of the time series at different processing level. In blue, the proportion of the interpolated on-glacier data gap over the time series period, after the processing workflow. In orange, the proportion of days that fall below the time interval range (e.g., 62% of any date in the time series periods are between pre-processed observations less than a year apart). The x-axis are independent, the y-axis is shared.

- Span: smoothing parameter, expressed as the fraction [0-1] of points of the time series used at each local regression. A larger value leads to more smoothing. We set it at 0.4 and 0.3 for the first and second iteration, respectively.
- Degree: degree of the local polynomial regression. We choose a degree 2.
- Family: assumed distribution of the errors, with a choice between "gaussian" (fit is performed with a least-squares) and "symmetric" (fit is performed robustly by redescending M-estimators). We use "symmetric".
- Weights: weights to be given to individual observations in the sum of squared residuals. We use the uncertainty provided for each elevation in H21, which models heteroscedasticity (variable error) as a function of slope and the quality of stereo-correlation based on elevation differences on stable terrain.

We use the LOWESS algorithm in the following sequence (Fig. 2.5): we run two iterations of the LOWESS regression with a decreasing smoothing factor. At each iteration, we compute a threshold envelope around the regression which is used to remove points falling outside of it. The envelopes are derivative-varying to prevent the filter from removing accurate observed signals close to surge events (see example in Fig. 2.5). We assume fast-varying elevation (high derivative) is a potential surge, and then use a larger threshold. For the first iteration, the threshold is 150 m for fast-varying elevation above 50 m yr^{-1} derivative, and then linearly down to 45 m at lower elevation change rate. The threshold is lower for the second iteration : 100 m above 50 m yr^{-1} elevation change rate, down to 30 m below. Time series with both large temporal data gaps and a noisy signal can create computational errors for small smoothing parameters. Therefore, at each regression, we implement a step-by-step increase in the smoothing parameter in case of such errors, depicted as the fraction value in Fig. 2.5. In case of computational error remaining after a +0.05 (resp. +0.10) increase of the fraction parameter, we filter out the full time series.

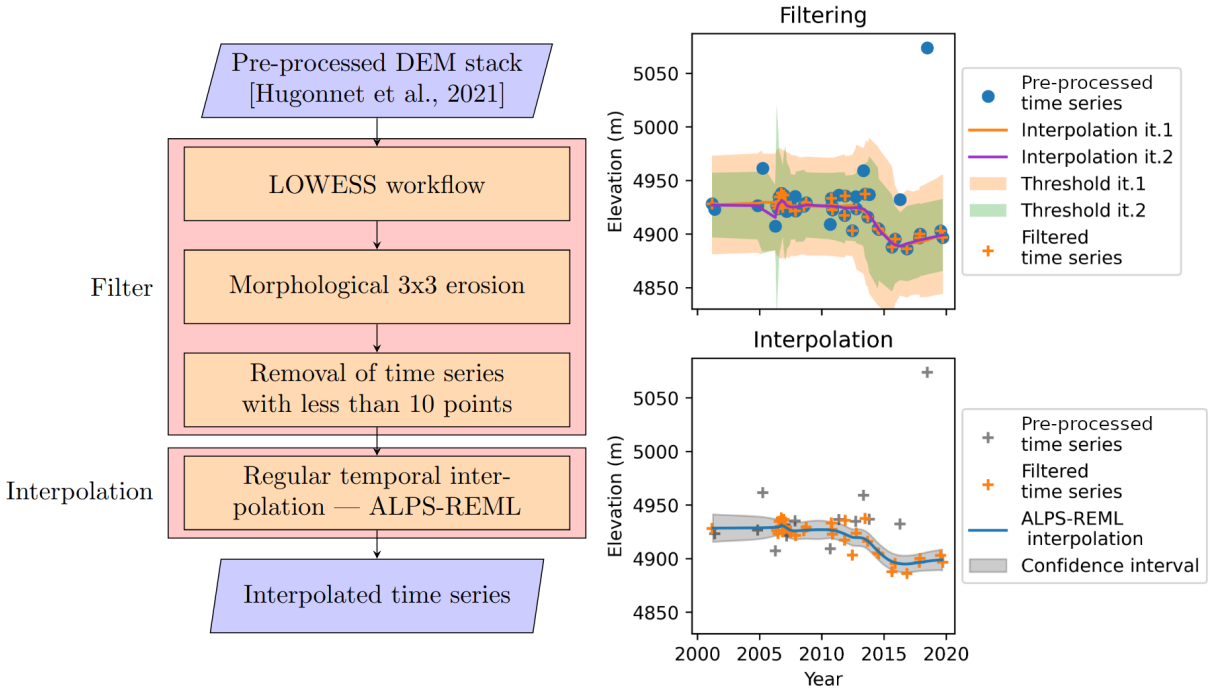

Figure 2.3: Workflow of the elevation time series processing, with an example of time series processed. "it." in the time series legend stands for iteration (of the LOWESS algorithm). The location of the time series exemplified is labelled "TSa" in the caption and map of Fig. 2.7.c. A version of the filtering of the time series, coloured by the elevation error estimate, is provided in Supplementary Fig. S8.

2.4.1.2 ALPS - REML interpolation

Approximation by Localized Penalized Splines (ALPS) is a unified time series modelling framework introduced in Shekhar et al. (2021). ALPS builds on the localized nature of B-spline basis functions to model time series with highly non-uniform sampling. In this research, we use a mixed modelling analogue of the statistical B-spline regression model introduced in Shekhar et al. (2021). This is motivated by the capability of the mixed models to segregate high-frequency and low-frequency components of the overall model, thus allowing us to narrow down the effect of the regularization/smoothing specifically on the high-frequency components. The latter are responsible for the over-fitting behaviour of the model, i.e., the fact that it fits too closely or exactly to the training data and becomes inaccurate for new data. This is particularly problematic for noisy time series like ASTER DEMs.

Another change inherent in our approach, as compared to the approach described in Shekhar et al. (2021), is the model fitting algorithm. The original ALPS model used the Generalized Cross Validation (GCV) metric for estimating the model parameters. However, here we take an alternative route and use the restricted maximum likelihood (REML) approach for fitting our model. The GCV metric quantifies the generalization error of the model by making prediction at data points that were not used to fit the regression model. Hence, the minimization of GCV metric forces the model to predict accurately at unseen locations as described in Wahba (1990). REML on the other hand formulates the problem from a statistical perspective and optimizes the regression parameters so that the probability of observing the data is maximized. A more detailed explanation of REML can be found in Ruppert et al. (2009). The reason for choosing REML over GCV in this work can be attributed to the fact that GCV is well known to underestimate model uncertainty, thereby providing over-confident predictions, which in some extreme cases

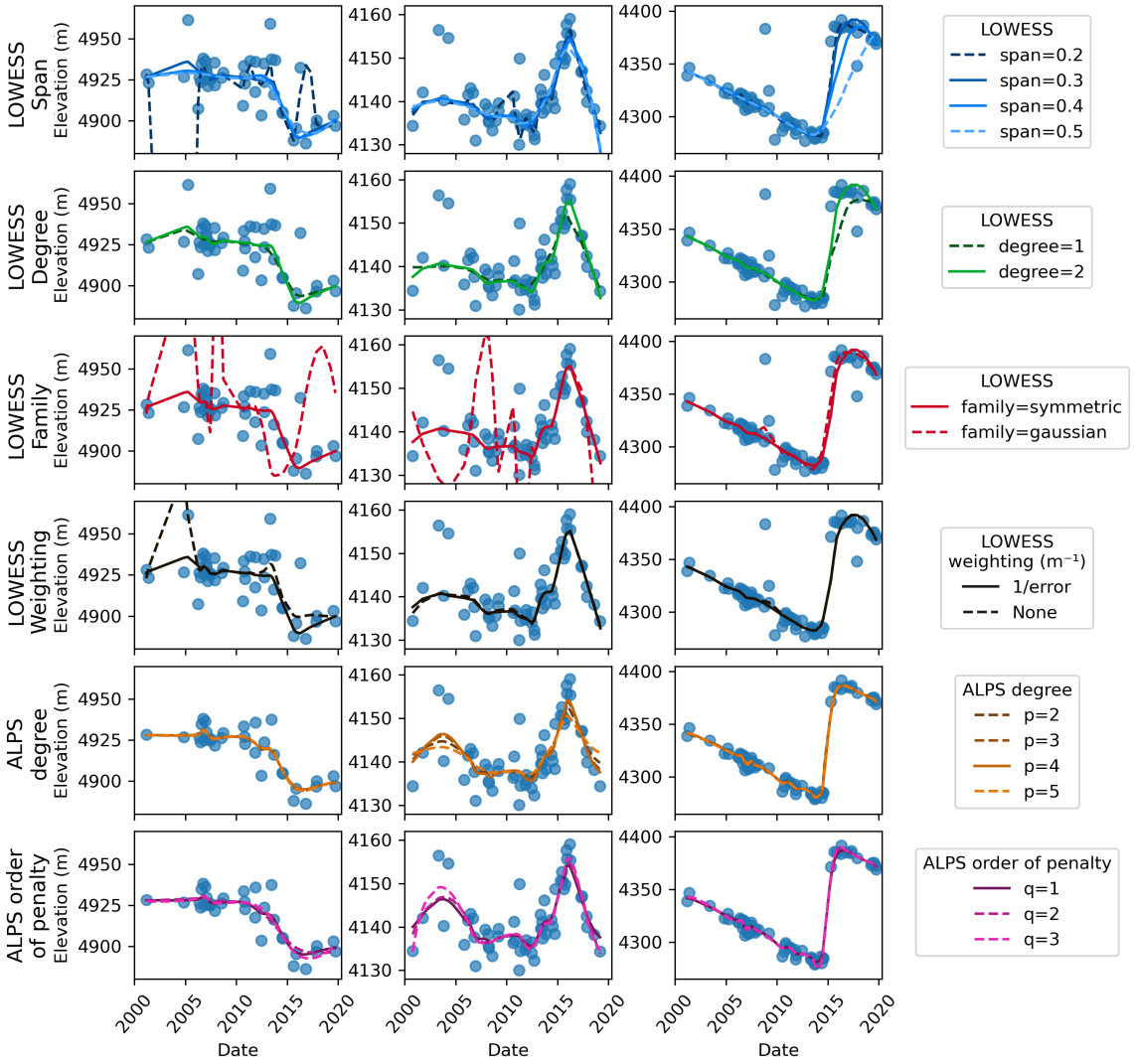

Figure 2.4: Impacts of the different LOWESS parameters (rows 1 to 4) and ALPS parameters (rows 5 and 6) on the regression/interpolation solutions. Plain lines are the final selected values. The columns correspond to three different data points (TSa-c, locations shown on Fig. 2.7.c).

can be misleading. Additionally, for the time series under consideration in this work, the ALPS model with the original GCV based model fitting was over-fitting to noise, making it unsuitable. In order to produce interpolated results in this paper, we use the ALPS-REML code provided. After visual tuning of the parameters on a sample set of time series, we set a degree of the basis functions p of 4, and an order of penalty q of 1 (Fig. 2.4). Note that the confidence interval estimated with the ALPS-REML algorithm and represented on the figures of this article is valid for the interpolation only and not for the whole workflow output.

2.4.1.3 Comparison with Gaussian Process regression

Gaussian Process (GP) regression is a non-parametric method that relies on estimating the data covariance to provide an optimized interpolator (Cressie, 1993; Rasmussen and Williams, 2005; Williams, 2007). Under certain assumptions, including notably second-order stationarity, GP regression has been shown to be the "best linear unbiased predictor". It is the method used by H21 on this same dataset, to compute long-term mass balance

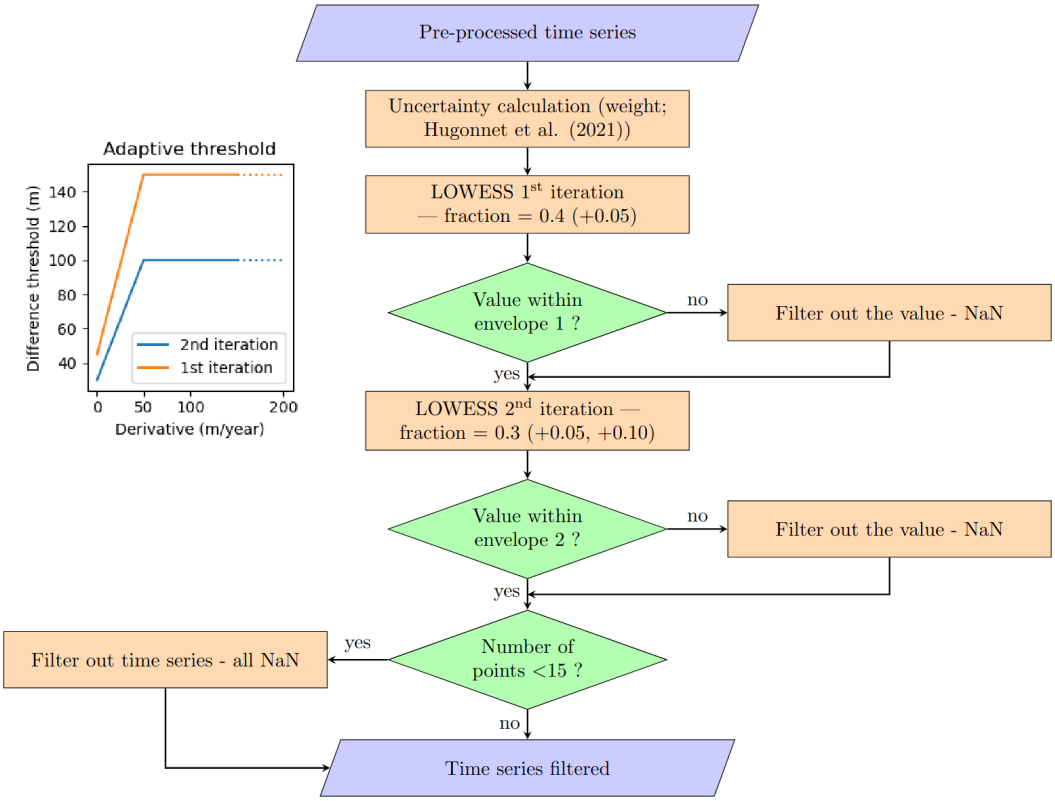

Figure 2.5: Complete workflow of the LOWESS filter step. The envelopes are the maximum distance threshold allowed between the LOWESS regression and the time series values, which vary with the LOWESS regression derivatives as shown in the inserted plot on the top-left.

estimations worldwide. We use a GP covariance with terms estimated in H21 through a global variogram analysis. This analysis identified several kernel components (periodic, local, linear, etc.), that are not specifically tuned for surges.

We note that, contrary to GP regression, ALPS approximates the data with polynomials under the assumption of a degree of smoothness of the data, with no need for us to inform the behaviour of the data. Although both GP regression and ALPS need domain knowledge to decide the covariance kernel and spline degree/penalty respectively, from a user's perspective using GPs can be more complex owing to the well studied difficulty of optimizing the kernel, mean function and dimensionality (Pu, 2024). For ALPS on the other hand, we simply manually select degrees and penalty orders from a small set of choices.

Reparametrization of the kernel used by H21 gave slightly worse results than those obtained with the ALPS-REML method. Our limitation with GP regression lies in the kernel definition which is done according to the variance of elevation changes. Each surge event is different in variances, which is also very different from the data variance in quiescent periods or on non-surge-type glaciers. We tried different settings of the kernels, that differ from the study of H21. We removed the seasonal term of the model. The length scale and the magnitude parameters of the remaining terms were manually tuned after testing. We added radial basis function terms of length scales of a few months and with a variance of a few tens/hundreds of square meters. The kernels that provided a suitable interpolation were slightly outperformed by the ALPS-REML algorithm. This could be reevaluated for other datasets (for e.g. less noisy), more complex steps or adapted GP regression processes and future advances (e.g., de-trending before GP regression or using other predictors).

2.4.2 Volume transfer estimate

We estimate the volume transferred during surge events by assessing both the positive and negative glacier net volume changes over specific areas. Unless specified, the extent is the surge-affected area manually drawn from the elevation change map calculated over the surge duration. We separate the reservoir and the receiving areas into two distinct polygons. It is difficult to constrain precisely the initiation and termination of surges. The surge dates (Table 2.1) are estimated visually from two sources: the pre-processed timeseries and the interpolated elevation changes. None of these sources permits us to be sure of the exact month of start or end of the surge. We estimate the dates from interpolated elevation change (e.g. Fig. 2.8) when computing volume transfers, such "apparent" dates are less exact but capture the overall mass transferred in our generated dataset. We may also estimate the dates from pre-processed time series (not affected by filtering and interpolation defects) for information or validation, which permits us to be more exact although we are still limited by the number of observations. For example, for the time series Fig. S2.a in the Supplement (from Khurdopin glacier), the surge period estimate at this location from the interpolated time series would be around 2016-06 to 2019-02, against 2016-12 to around late-2017 (there is no observation between 2017-06 and 2018-07, thus time series at other locations are required for a better estimate).
To compute the transferred volume, we subtract the interpolated elevation at two dates. We then mask the surrounding areas. We interpolate (small) data gaps in the elevation change maps with a bilinear interpolation. Finally, we retrieve the volume by multiplying the mean elevation change with the delineated area.
The sum of the volume changes in the two areas gives the volume imbalance in cubic metres. We divide the volume imbalance by the surge-affected area to provide the metric imbalance in metres (as if the imbalance was uniformly distributed on the surge-affected area).

2.4.3 Uncertainty of volume transfer estimates

We calculate indicative uncertainties of the volume transfer estimates. These uncertainties do not explicitly take into account possible errors introduced during the filtering and interpolation of each event.
Our uncertainty is estimated with the following formula.

$$\sigma_{\Delta V} = \sqrt{(\sigma h_{\Delta DEM}(p + 5(1-p))A_{area})^2 + (max(d\Delta V_{-100m}, d\Delta V_{+100m}))^2} \quad (2.1)$$

The first member of the formula account for the uncertainty in average elevation difference. $\sigma h_{\Delta DEM}$ is the uncertainty in the mean elevation difference obtained by propagating the pixel-wise measurement uncertainty. The pixel-wise uncertainty is estimated from elevation differences between the interpolated ASTER DEMs and reference DEMs (SPOT5 HRS, SPOT6 and HMA DEM; details in subsection 2.6.1), considered as the true elevation, over four surge events (Hispar, two dates on Braldu surge, and Kunyang glaciers; Fig. 2.10) within the surge-affected zone. It is therefore representative of the error on glaciers, during surge events. From each dataset, we reconstruct an empirical variogram using the *SciKit GStat* Python library and all variograms are normalized by their variance and aggregated by taking the mean. We then fit the experimental variogram with a double-range Gaussian model (estimated ranges of 1.4 and 19 km) and estimate the mean elevation difference uncertainty from the number of effective samples calculated from the model with the *xDEM* Python library (Supplementary Fig. S11). A_{area} is the area of the delineated zone and p the proportion of A_{area} with valid observations (ranging from 0.92 to 1, median of 0.99). This formulation assumes that the uncertainties of spatially interpolated observations is 5 times larger than the measurement uncertainties, as in Berthier et al. (2014).

The second member of the formula estimates the volume uncertainty due to the manual delineation of the area over which the volume change is computed. $d\Delta V_{-100m}$ and $d\Delta V_{+100m}$ are the differences between the volume change estimated over the delineated area and the volume change estimated over an area with a buffer of -100 or +100 m, respectively. This assumes an uncertainty in our manual delineation of 1 pixel, which is reasonable given the strong contrast in elevation on the edges of the surge reservoir and receiving areas.
We propagate the uncertainties to the volume imbalance, assuming independent errors, with the following equation:

$$\sigma_{V\_bal} = \sqrt{(\sigma_{\Delta V\_reservoir})^2 + (\sigma_{\Delta V\_receiving})^2} \tag{2.2}$$

The uncertainty in metric imbalance is then expressed as

$$\sigma_{V\_surface\_bal} = \frac{\sigma_{V\_bal}}{A\_total} \tag{2.3}$$

with A_total the total area considered.

2.5 Results

2.5.1 Performance of the outlier filtering

We compare the filter and the temporal interpolation developed in this study with those of H21 in locations that are affected by surges, but also for all glaciers in the region (Fig. 2.6, Fig. 2.7). In H21, the iterative GP regression filtering is responsible for removing some high-amplitude surge signals (Fig. 2.6.c1-2, or abnormal gap A1 circled in red in Fig. 2.7.a). In H21, the kernel of the GP regression filter does not model well the elevation change that is typically observed during some of the surge events (e.g., Fig. 2.6.c1). In our workflow, the LOWESS filter behaves with varying performance, depending on the time series quality (noise, temporal density, surge amplitude). It preserves well the surge signal of 3 of the 4 events we analyse in subsection 2.5.3, and this observation seems to extend to a number of surge events in the Karakoram. One exception is periods of low temporal density during surge events, especially when combined to strong melt before and after the surge. A typical example of such erroneous filtering is a part of the front of Khurdopin glacier (Supplementary Fig. S2.a). In this time series, two critical observations are filtered out around 2017 during the short surge. The ALPS-REML interpolation smooths the signal even further, as both LOWESS and ALPS fits are sensitive to the lack of elevation measurements at abrupt trend changes. Strong melt in the receiving area increases the elevation-change smoothing effect of the fits by reducing the average elevation change locally before and after the surge.

The LOWESS workflow is also sensitive to the weight estimate and noise in textureless and steep areas, for example, resulting in the filtering being oversensitive to noise compared to the original workflow (red circles B1-2 in Fig. 2.7.b). This filter oversensitivity occurs on time series with scattered elevations, and it is often due to the correlation score that is not very representative of the actual pixel quality: outliers may have lower uncertainties than more accurate observations (e.g., Supplementary Fig. S2.e or S7 at 15 km). These types of location are not predominant in surge-affected areas, and a number of them are completely filtered out during subsequent filtering steps. Thus, filtered areas (data gaps) and spurious elevations are more prevalent with our method than with the filter of H21 over textureless accumulation areas.

In summary, our filter better preserves the surge signals that were filtered out in the workflow of H21. However, the new filter is more noise-sensitive over textureless accumulation areas and rough terrain, leading to data gaps or artifacts with large elevation

changes. The preprocessing step removed 46% of the original regional dataset (number of on-glacier pixel), and the filtering step removed a further 42% of the preprocessed dataset (69% removed in total compared to the original dataset). After filtering, nearly 30% (62%, respectively) of any date in the time series periods are between observations less than 9 months apart (one and a half years, respectively). Before filtering, for the same percentage, it was a half-year (one year, respectively) (Fig. 2.2, solid orange line). The time series are about half as dense as before, temporally.

2.5.2 Performance of the temporal interpolation

The interpolation of H21 is a GP regression with the same kernel as for the filtering. Fig. 2.6.a-b1 shows edge effects at the temporal bound of the time series due to the linear term of the kernel. It is noteworthy to mention that by its design, the original kernel is optimized to preserve a linear trend to extrapolate out of the observation period of each pixel. The seasonal term of the kernel creates the one-year periodicity. In comparison, our workflow shows only limited border effects. The workflow presented in this study better fits changes in trends (ex. Fig 2.6.a1-2), and preserves most of the surge signal (Fig 2.6.c2). However, dense clusters of points are regularly over-fitted, creating spurious high frequency oscillations spanning typically about 6 to 12 months, as illustrated in Fig. 2.6.c2 around 2006 and 2011 or in Fig. 2.6.a2 around 2006. Comparing the final interpolated elevation changes over two years (Fig. 2.7.c-d), our workflow can capture the complete surge signal of Hispar and Braldu glaciers (red circles C1-3 in Fig. 2.7.c), which was not the case for the previous workflow. At these locations, the original method of H21 completely filters out the surge signal, filling the period with the global trend or a completely smoothed trend (e.g., Supplementary Fig. S1). Moreover, several reservoir or receiving areas of the surges show smaller elevation changes with the original method, which tend to smooth remaining surge signals, both in time and in elevation (e.g., Fig. 2.6.c1 and Supplementary Fig. S2.d). The maximum spatial coverage of on-glacier interpolated elevation over the Karakoram is around 80% from 2005 to 2015 (Fig. 2.2, solid blue line).

2.5.3 Analysis of selected surge events

To illustrate the outputs of our method, we analyse four surge events that have been studied in the literature. They occur on four glaciers: Hispar, Khurdopin, Kyagar and Yazghil glaciers. Fig. 2.8 shows the spatio-temporal evolution of the glaciers surface elevation along their centreline (green line on Fig. 2.7.d). Time series, extracted at regular intervals along the selected centrelines of each glacier are shown in Supplement (Fig. S3 to S7), and surge volume transfers are reported in Table 2.1 for each glacier.

2.5.3.1 Hispar glacier

We observe the influence of Kunyang tributary surge that reached Hispar main glacier tongue (around kilometre 40) in early 2008 (Fig. 2.8.a, area a1). The surge front propagates downstream for several years with a decreasing propagation rate (2009-2012; Fig. 2.8.a, area a1), while strong thinning starts at the junction and approximately 5 kilometres upstream of the surge front. Meanwhile, a slight and more regular build-up or thickening occurs above, upslope of 25 km (Fig. 2.8.a, area a6). The surge of Hispar main trunk seems to start in early to mid-2014 and end around June 2016 (area between the lines a2 and a3 on Fig. 2.7.d and Fig. 2.8), with small mass displacement until the end of 2017, downslope of the Kunyang junction. Sharp spurious high-frequency oscillations of positive and negative elevation changes from mid-2013 to mid-2014, which we attribute to artefacts

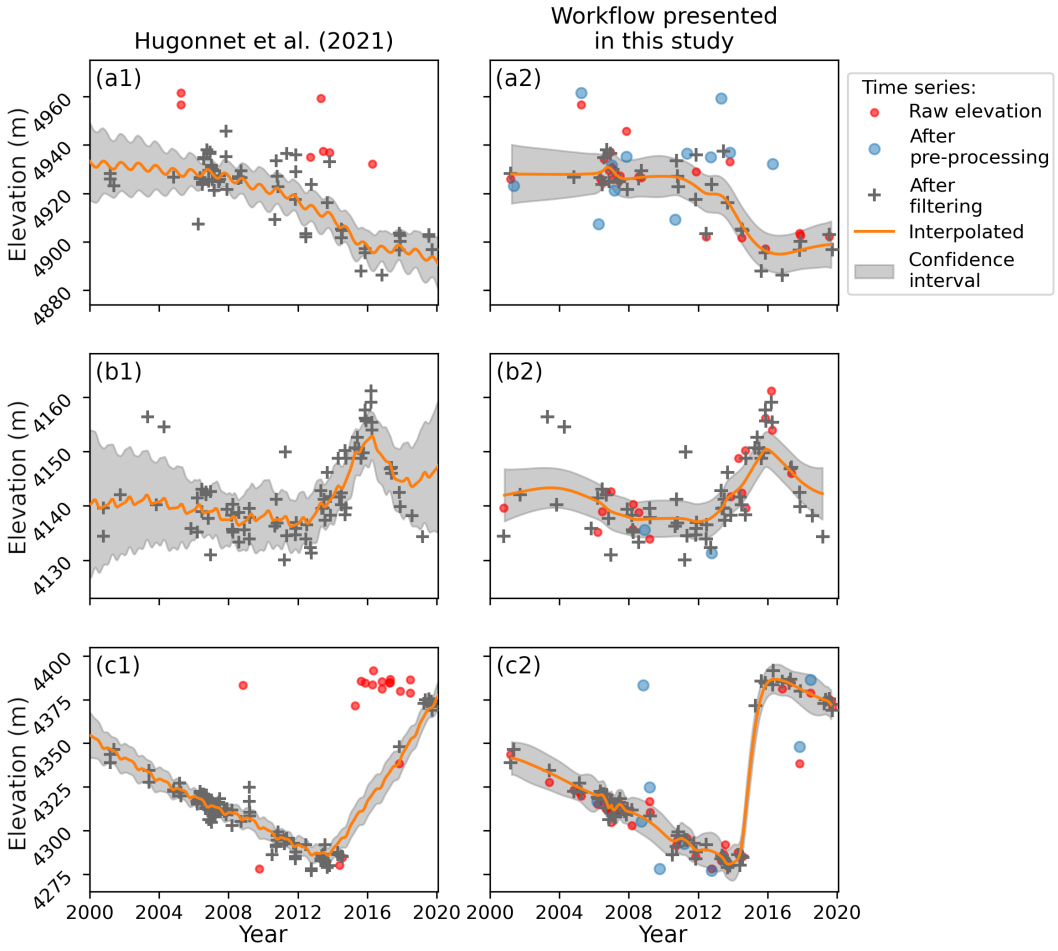

Figure 2.6: Comparison of the filter and interpolation methods: (a1-c1) from H21 against (a2-c2) the workflow presented in this study. The three time series all show a surge around 2015. Their location is represented on the map Fig. 2.7.c (points TSa-c). We avoid overlaying points for readability (i.e., points exist but are masked in lower-level time series, in legend order). The confidence interval is valid for the interpolation only and not the whole workflow output: it is the 1 σ standard deviation credible interval for GP regression (H21), and it is the 95% confidence interval for ALPS-REML (Shekhar et al., 2021)

of our method, are visible horizontally on Fig. 2.8.a. The time series shows dense and very scattered elevation observations at this period even on stable ground (Supplementary Fig. S2.c), causing these artefacts. This spread may be due to tilts or undulations remaining in the DEMs. The results indicate that the dynamic balance line location is not stable in time. On the branch of Hispar Pass (head of one of the main branches, location on Fig. 2.7.d), the reservoir area extends from 5 km from the pass, at an icefall (line a2 on Fig. 2.7.d and Fig. 2.8), down to 20 km from the pass at the junction with the Yutmaru tributary in the first part of the surge. From the end of 2015 to the termination of the surge, the reservoir area limit propagates down by 5-10 kilometres (below the junction) (line a5 on Fig. 2.7.d and Fig. 2.8). We plot an elevation time series at this location (Fig. 2.6.b2, location TSb on Fig. 2.7.c). The receiving area extends from the end of the reservoir area at 20-25 km from the pass along the centreline, down to nearly 40 km from the pass at the junction with the Kunyang tributary (line a3 on Fig. 2.7.d and Fig. 2.8.a).

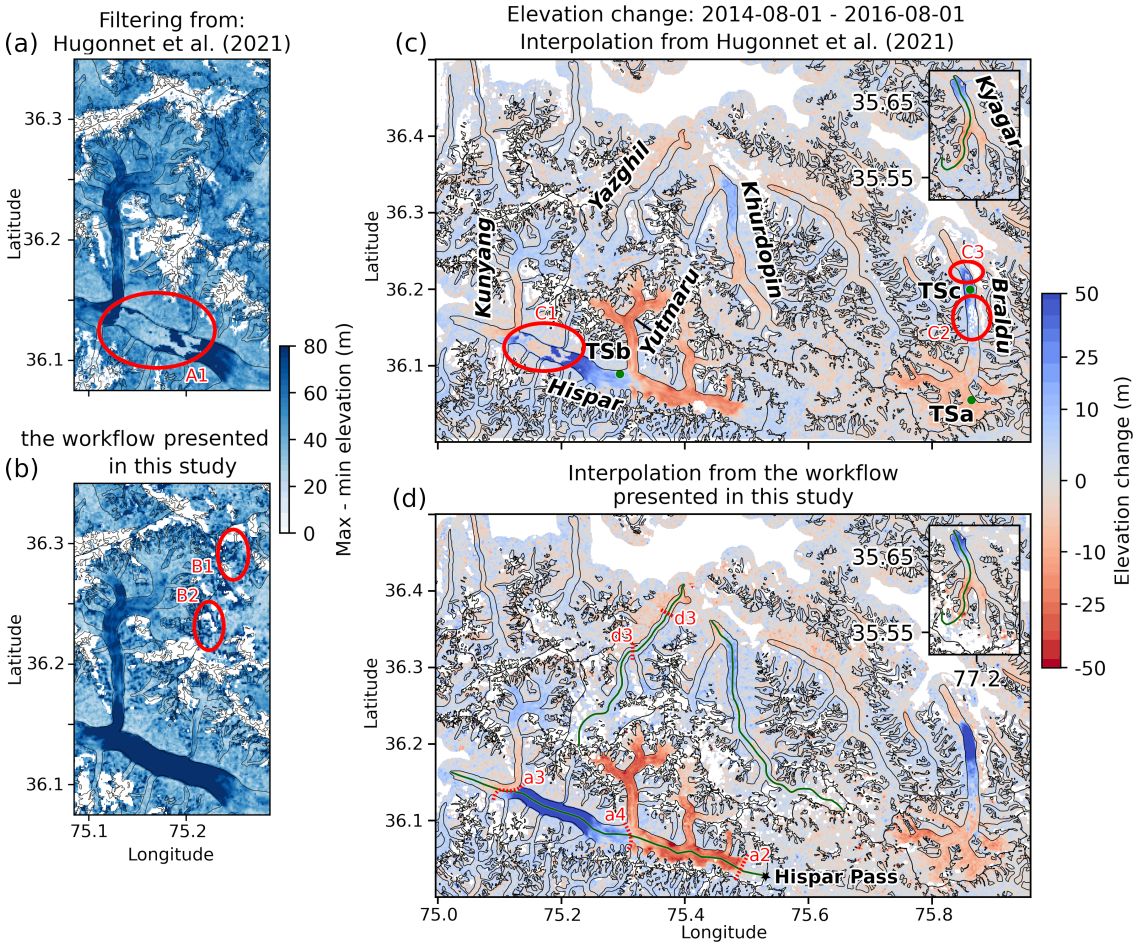

Figure 2.7: a-b: Maps of maximum elevation change after filtering. c-d: Elevation change maps over two years (Hispar glacier surge period). The green points and their labels (TSa-c) in c) correspond to the localisation of the time series in Fig. 2.6 (a-c). Their coordinates are (EPSG:4326): TSa (75.863, 36.055), TSb (75.295,36.089) and TSc (75.861,36.200). The green lines on d are the centrelines of the studied glaciers. The red circles (A1-C3) and the dotted lines (a2-4 and d3) show or delimitate areas discussed in the text. The insets for Kyagar glacier have the same scale as the main frames.

2.5.3.2 Khurdopin glacier

Khurdopin glacier has a strong mid-glacier thickening signal until the surge onset. The distinct area of positive elevation-change trend extends down-glacier during at least 15 years (Fig. 2.8.b, area b1). This mass build-up may be the geometry readjustment of the glacier in its quiescent phase, after the previous surge in 1998 (Quincey et al., 2011). The lower limit of this build-up area propagates downward from about 25.5 km of the glacier head in 2001 to about 33.5 km in 2015. The limit advances approximately 600 m per year during this period, which is about 7 times faster than the surface velocity (measured 2 km upstream of the front), according to velocities (temporal baseline from 300 to 430 days) from the NASA MEaSUREs ITS_LIVE project repository (Gardner et al., 2025). During this period, we do not observe a clear mass transfer from an upper reservoir area, which thus seems different from a slow surge onset. The upper limit of the build-up area (which will mostly become the reservoir area) is stable in time, at the bottom of two icefalls for the two main branches just above their junction.
The surge starts in 2016, with the build-up front becoming a surge front with a higher

propagation rate. Both our filter and interpolation methods here fail to fully capture the surge signal of the receiving area (see discussion section 2.6.3). This failure leads to an apparent surge end in early-2019 on interpolated data, which is overestimated by about a year and a half according to non-interpolated time series (Supplementary Fig. S2.a). A distinct and local positive elevation change pattern is visible after the surge around kilometre 23 (Fig. 2.8.b, area b2).

2.5.3.3 Kyagar glacier

Kyagar glacier is located about 110 km east of the other glaciers (Fig. 2.1). A slight mass build-up is visible since the beginning of the time series in the first 10 kilometres of the glacier, and extends down to about 14 km a few years before the surge (Fig. 2.8.c, area c1). The surge as visible on interpolated data starts in 2013 or the beginning of 2014, and ends around 2016 (Fig. 2.8.c, area c2). However, the actual surge is certainly shorter. The beginning of the surge appears sooner in the interpolated time series, and the end is also represented nearly a year later from what is visible on the non-interpolated time series of most of the receiving area. During the surge period, there are about 1-2 observations per year. An area or poor quality in the ASTER time series results in artefacts after processing, at 5 km from the glacier head, which is located around the equilibrium line of the glacier (Fig. 2.8.c, area c3). This area seems to be in the reservoir area, therefore causing a bias in the volume transfer calculation. We manually draw a mask to remove artefacts for a better estimate (Table 2.1).

2.5.3.4 Yazghil glacier

Our dataset captures a full surge cycle of Yazghil glacier. On this glacier, the surge signal has a low amplitude (approximately ten metres) compared to the time series, and thus noise is often overfitted resulting in frequent interpolation artefacts. Some seasonal signal seems also to be fitted, for example during the period 2013-2016 thanks to denser and consistent time series (horizontal lines on Fig. 2.8.d). A surge starts around August to November 2003 and ends around October 2006 to February 2007 (Fig. 2.8.d, area d1), and a new surge starts in 2016 or 2017 (the end is not captured; 2.8.d area d2). The build-up phase of the second surge is visible, representing about half of the quiescent phase (Fig. 2.8.d area d3, delimited by dotted lines d3 on Fig. 2.7.d). One of the tributaries of Yazghil glacier (junction at km 18) is also surge-type, and seems to have surged during our study period in about 2008-2013.

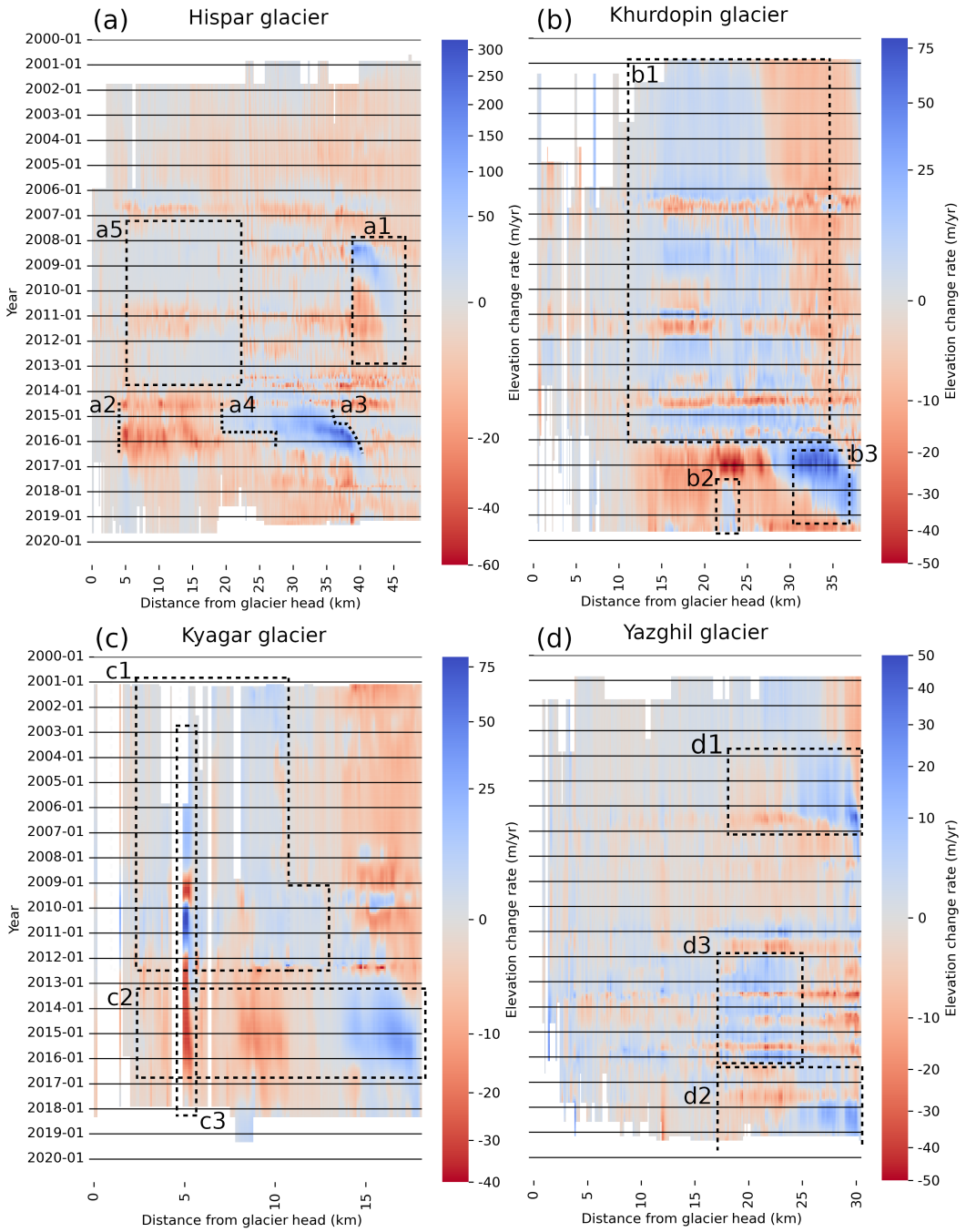

Figure 2.8: a-d: Interpolated surface elevation time series along the centreline of four glaciers (in green in Fig. 2.7.d). Glaciers flow from left to right on the different panels. Note that the colorscales represent different elevation change rate amplitude and that they are non linear.

Glacier RGI 7.0	Date start [time series]	Date end [time series]	Reservoir vol. change [Surface area]	Receiving vol. change [Surface area]	Imbalance
Hispar 21670	2014-01 [2014-05]	2016-09 [2016-06]	-2421 ± 374 x10^6 m^3 [106 km^2]	3108 ± 177 x10^6 m^3 [48 km^2]	687 ± 414 x10^6 m^3 4.46 ± 2.69 m
Yazghil 21865	2003-07 [2004-01]	2007-01 [2006-08]	-32 ± 30 x10^6 m^3 [8 km^2]	63 ± 26 x10^6 m^3 [6 km^2]	32 ± 40 x10^6 m^3 2.20 ± 2.77 m
Khurdopin 14958	2016-03 [2016-04]	2019-03 [2017-07]	-813 ± 136 x10^6 m^3 [33 km^2]	713 ± 64 x10^6 m^3 [15 km^2]	-100 ± 150 x10^6 m^3 -1.9 ± 1.64 m
Kyagar 14958	2012-11 [2013-10]	2017-01 [2015-12]	-271 ± 92 x10^6 m^3 [21 km^2]	269 ± 55 x10^6 m^3 [8 km^2]	-2 ± 107 x10^6 m^3 -0.07 ± 3.64 m
Kyagar ∅ artefact	—	—	-217 ± 116 x10^6 m^3 [20 km^2]	269 ± 55 x10^6 m^3 [8 km^2]	52 ± 128 x10^6 m^3 1.33 ± 3.54 m

Table 2.1: Timing and transferred volume of the surges of four glaciers in the study area. The main dates are given according to the interpolated elevation time series on the centrelines (Figure 2.8). We compute the transferred volume ("vol. change") from interpolated DEMs at these dates to estimate the corresponding volume change from both reservoir and receiving areas. The dates between brackets are those estimated visually on non-interpolated time series, thus less smoothed, given for indication. They are not accurate to the month due to ASTER acquisition dates. The volume change and the imbalance computation method is detailed in subsection 2.4.2. For these glaciers, the percentage of data gap after the workflow presented in this study is ranging from 0 to 5.6% (median 1.4%), and after bilinear interpolation it is 0 to 0.8% (median 0.2%). The prefix of RGI codes is "RGI2000-v7.0-G-14-" (RGI Consortium, 2023). The line *Kyagar ∅ artefact* corresponds to the version of the delineation without the area with the large artefacts, discussed in text.

2.6 Discussion

2.6.1 Processing quality

To assess the quality of our results, we 1) compare our interpolated elevations with external DEMs produced from high resolution satellite imagery, and 2) test the sensitivity of the interpolation to data gaps.

We compare the interpolated elevation with external DEMs, produced from optical very-high resolution satellite imagery (Fig. 2.9). This comparison provides a validation of estimated elevation during a few surge events. We use SPOT5 HRS and SPOT6 DEMs generated by Berthier and Brun (2019), and along-track HMA DEMs (Shean, 2017) (list in Table S2 of the Supplement). We co-register each external DEM on the ASTER interpolation on stable terrain. The Normalized Median Absolute Deviation (NMAD) after co-registration ranges from 6.8 to 15.6 m (median 7.4 m), which shows good agreement with discrepancies of a few meters. Extreme cases occur locally, with differences reaching tens of meters, but it is generally unclear which dataset is flawed. The case study of Khurdopin glacier surge shows that a wrong estimate of a hundred meters of our workflow can occur on exceptional events and at precise dates during the surge (Supplementary Fig. S2.a). The map of elevation differences on the glaciers shows differences of a few meters overall, which is moderate compared to the amplitude of the surge elevation change (Fig. 2.10). The difference may be important, such as several tens of metres locally at the surge front (e.g., Fig. 2.10.a-b at the Kunyang-Hispar junction). Across the entire glacier areas,

consistent discrepancies are observed. For instance, on 2015-10-13, Hispar glacier exhibited a median difference of -4.3 m with a standard deviation of 9.7 m. Similarly, on 2015-11-28, Braldu glacier exhibited a median difference of -5.2 m with a standard deviation of 8.7 m. Larger local differences are located around the surge front: e.g., up to 24 m at Hispar surge front on 2015-10-13. The elevation difference values during a surge event and during quiescence do not show important differences at the scale of the surge-affected area (Fig. 2.11). The discrepancy associated with a surge period is overall of the same magnitude as other noise, considering the large dispersions.

One of the main limitations of our results comes from the relative temporal sparsity of the input observations. Here, we investigate the impact of data gaps on our interpolated time series. Some parts of our study area are characterised by a low temporal density of observations during surge events (e.g., less than three observations per year) (Fig. 2.1). In such situations, our method of filtering and interpolation usually leads to an underestimate of the transferred volume and an overestimate of the surge duration (e.g., twice its duration for Kyagar glacier). Onset and end dates cannot be determined precisely between two observations separated by more than 6 months or a year, even on filtered series, as it occurs for Kyagar glacier.

To test the sensitivity of the ALPS-REML method to data gaps, we interpolate an elevation time series after removing all points in a 450-day moving window (Fig. 2.12). Each iteration results in a period of at least 450 days without observation, which is common in the filtered series. For instance, on the surge-affected area of Kyagar glacier, which is subject to a lack of observation for our processing, there are on average three time intervals of 400-to-500 days without observations per time series (one time interval for Hispar glacier, in comparison). For the selected time series Fig. 2.12.a and Fig. 2.12.c, the test shows strong smoothing, although the surge signal is still visible over large time frames. The interpolated dates of the surge onset (respectively ending) are advanced (respectively delayed) by up to two years compared to the original interpolation. The surge elevation change can be underestimated by up to 20 meters. This can be larger for longer time gaps or surges with stronger elevation changes before or after the surge. The case shown on Fig. 2.12.b is specific, as it lies close to the dynamic balance line (in the receiving area at an early stage of the surge, and then in the reservoir area). The surge signal is completely smoothed out when data gaps occur in the middle of the surge. Other specific surge cases, with limited elevation changes but with strong melt or strong build-ups before or after the surge, could be prone to the same problem.

2.6.2 Comparison with elevation change from H21

We assess pixel level differences in elevation change estimate between the processing workflow of H21 and this workflow. Previous figures showed local differences; here we compare the elevation changes of pixels belonging to eight surge events (Fig. 2.13, individual graphs on Supplementary Fig. S9). There is a strong smoothing of the original dataset which tends to filter the positive elevation changes occurring in surge receiving areas. They are better interpolated by our workflow (Fig. 2.13 zone A). No symmetric pattern is visible for negative changes in reservoir areas, probably due to the smaller rates of elevation changes. This erroneous filtering occurs mainly for surges with important and rapid elevation changes: surges of Hispar, Braldu, and Kunyang glaciers (Supplementary Fig. S9), and to a lesser extent of Khurdopin glacier surge. For such glaciers, major differences in total volume change are expected. This is clear in the transferred volume estimates from the original dataset of H21 on Hispar and Khurdopin glacier surges (Supplementary Table S1). Other glaciers also have smaller estimated volumes than with our method, but with smaller discrepancies. Compared with H21, our method finds larger absolute rates

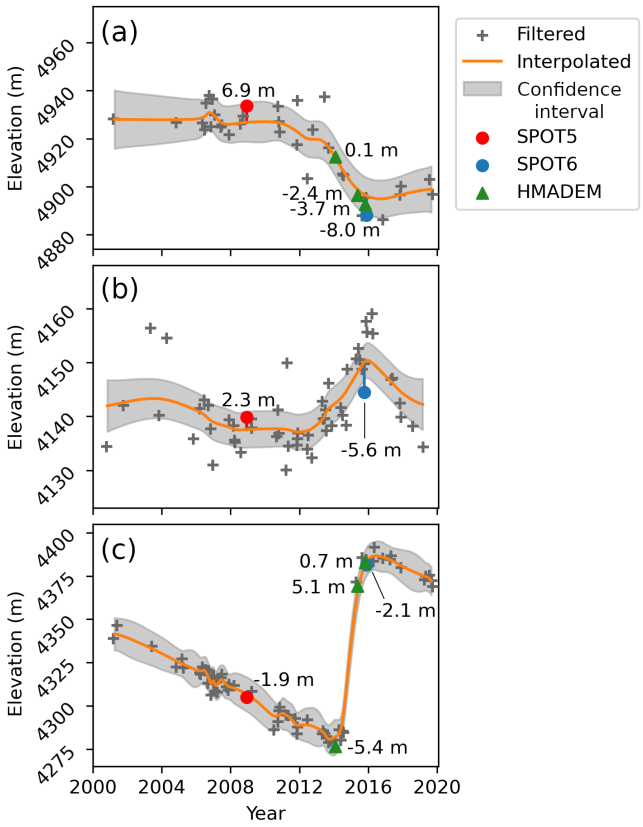

Figure 2.9: a-c: Comparison between elevations from SPOT DEMs (SPOT5 HRS and SPOT6) and HMA DEMs and ASTER elevations interpolated at the same dates. The time series are identical to previous ones (TSa-c in the panel order, Fig. 2.7.c). The confidence interval is valid for the interpolation only and not the whole workflow output.

of elevation changes (pattern B on Figure 2.13), probably due to the stronger smoothing of H21 (e.g., Fig. 2.6.a1 or Supplementary Fig. S2.d). On the other hand, our method creates some artefacts, especially in the accumulation areas where elevation changes are close to zero (zone C on figure 2.13). This is the case for Kyagar and Braldu glacier surges (Supplementary Fig. S9).
This figure also illustrates the unequal distribution of elevation changes between the reservoir and receiving areas, which is observed for all analysed surges (Fig. 2.13). Elevation changes are consistently much larger in the receiving areas, whether the glacier front is advancing or not. This is balanced by the extent of the reservoir areas which are larger than those of the receiving areas.

On a larger scale, we compare the individual glacier average elevation change between H21 and this workflow for the period 2005-2015 (Supplementary Figure S10). The mean elevation changes are more negative with our workflow (by about 0.44 m for the median value). The discrepancy is larger for surge-type compared to non surge-type glaciers (0.57 and 0.31 m with standard deviations of 1.1 and 1.02 m, respectively). Considering the better retrieval of positive elevation changes of our workflow for surges, we would expect a positive discrepancy for surge-type glaciers. A number of glaciers have artefacts in our dataset, especially negative elevation changes in accumulation areas. At regional scale and possibly glacier scale, the impact of noise may exceed the impact of the improved estimate in areas of positive changes, due to the small number of surge events happening during

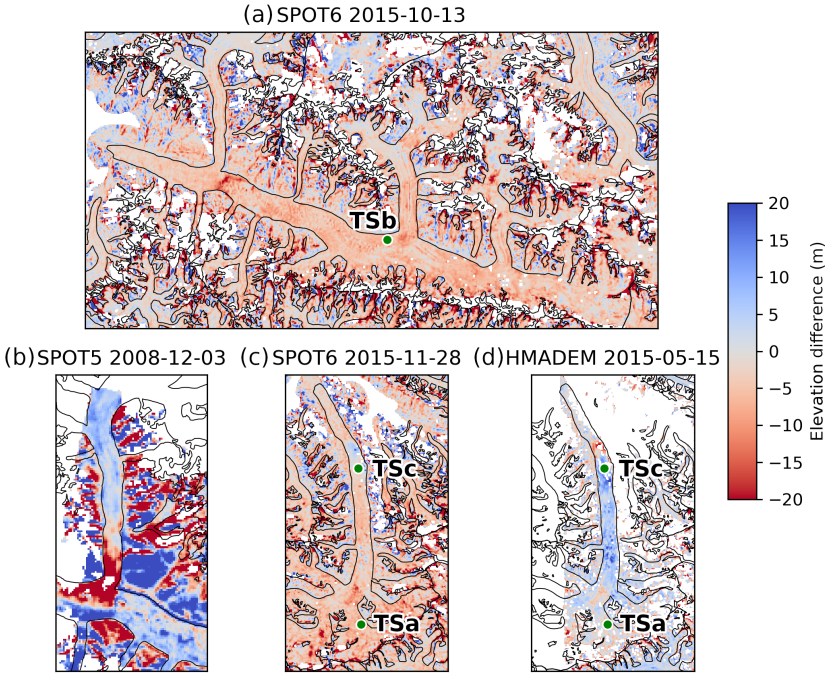

Figure 2.10: a-d: Elevation difference between SPOT DEMs (SPOT5 HRS and SPOT6) and HMA DEMs against ASTER DEMs interpolated at the same dates. The areas selected are Hispar glacier (a, surge in 2014-2016), its Kunyang tributary (b, surge in 2007-2008), and two over Braldu glacier (c-d, surge in 2013-2016). The panels have the same colour range. The green dots show sampled time series (Fig. 2.6, 2.7.c and 2.9).

this period. For calculating geodetic glacier mass balance, the H21 dataset is therefore the preferred choice for non-surge-type glaciers or quiescent periods, and a validation of the elevation interpolated by our method is recommended.

2.6.3 Comparison of surge characteristics with the literature

2.6.3.1 Hispar glacier

Regarding the surge of the main trunk of Hispar described in section 2.5.3, our date estimates from both interpolated and pre-processed time series (early-2014 to mid-2016) are close to the date estimated in previous studies (autumn 2014 to mid-2016), which were based on remotely sensed velocities (Guo et al., 2020; Paul et al., 2017). Paul et al. (2017) notice a 6-month stop of the surge front around 35 km, up to mid-2015 which is slightly visible here at a similar time (Fig. 2.8.a, line a3). The fact that the reservoir area does not extend above the icefall has already been observed on other glaciers, including Khurdopin in our study (Nolan et al., 2021; Echelmeyer et al., 1987). The displacement of the dynamic balance line during this surge has not been mentioned in other studies for Hispar, as the data they use (velocities and a limited number of DEMs spaced in time) may not allow this phenomena to be observed (Guo et al., 2020; Paul et al., 2017; Rashid et al., 2018). However, the phenomenon has already been reported and attributed to variations in driving stress (Burgess et al., 2012). Bhambri et al. (2022) estimate volume changes over the period 2014-2020 from ASTER DEMs of -2785 x10^6 m^3 in the reservoir area, and 2581.6 ± 465 x10^6 m^3 in the receiving area. Our estimate for the reservoir area differ by 13%, and 20% in the receiving area (Table 2.1). The smaller volume estimated by Bhambri et al. (2022) may be explained by the melting of the deposited ice volume during the three or

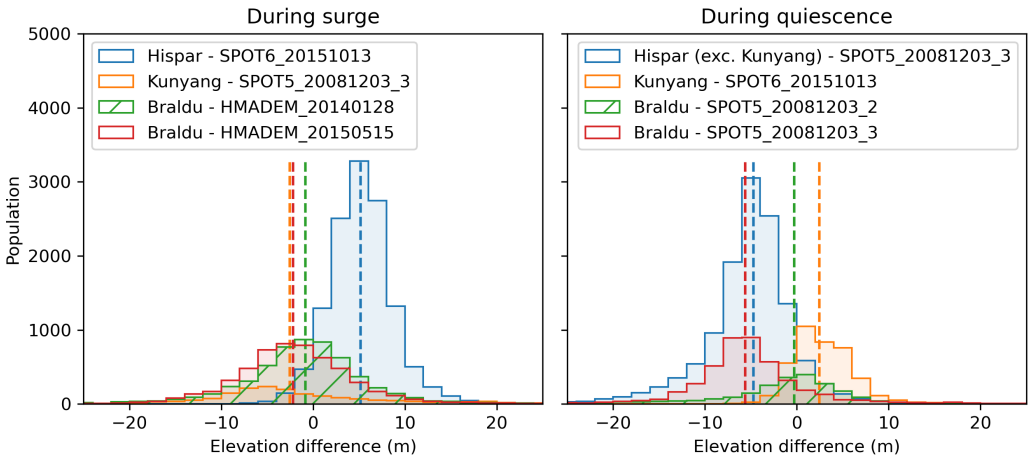

Figure 2.11: Histograms of the elevation difference between the reference DEMs and the DEMs of our workflow interpolated at the same dates. We consider only surge-affected areas. Vertical dotted lines are the median of each histogram. The largest median is 5.18 m (resp. -5.63 m) during surge (resp. during quiescence).

four years that separate the surge termination and elevation observations. If we extend the period of volume change calculation from 2014-10 to 2018-08 (the latest date before large data gaps in our time series) to better match that of Bhambri et al. (2022), we estimate a volume change of -2255 ± 181 / 2634 ± 410 x10^6 m^3 (19% and 2% difference, respectively) which is closer to their estimate. The differences are within uncertainties, although there is a two years difference between the two estimates periods.
The difference between our estimated volume gain and loss is equivalent to a layer of 4.46 ± 2.69 m thickness over the surge area. This imbalance is unexpected as the surge occurs over a short time period and mass should be roughly conserved. The imbalance is quite similar when using two filtered ASTER DEMs over a similar period, instead of the interpolated series, or when calculated over the full glacier system instead of over the delineated reservoir/receiving areas. Another possible source of imbalance is the impact of crevasse opening during the surge, which can represent a non-negligible volume change. As an example, the opening of crevasses can be equivalent to up to 0.2 m thickness at regional scale of the Greenland Ice Sheet (Chudley et al., 2025). As inland parts of these regions are largely crevasse-free, we can expect such impact on the volume to be significantly larger over the highly crevassed post-surge surface of Hispar glacier. By mid-2018 our imbalance is close to zero, as well as is the imbalance of Bhambri et al. (2022) with an end term in 2020, when a number of crevasses have already closed. Khurdopin and Kyagar glaciers were already highly crevassed before the surge, and such crevasse opening effect may be less important.

2.6.3.2 Khurdopin glacier

We now discuss the recent surge of Khurdopin glacier (March 2016 to March 2019; Table 2.1). The geometry readjustment and the propagation of a build-up front during quiescence have not been described on this glacier, to our knowledge. The existence of kinematic waves or surge fronts that propagate the surge instability have regularly been observed on other surges (e.g., Cuffey and Paterson, 2010; Kotlyakov et al., 2018; Turrin et al., 2013), with unclear definition of the phenomena. For Khurdopin glacier, the mechanism seems different from both a kinematic wave or a slow surge onset. As opposed to these processes,

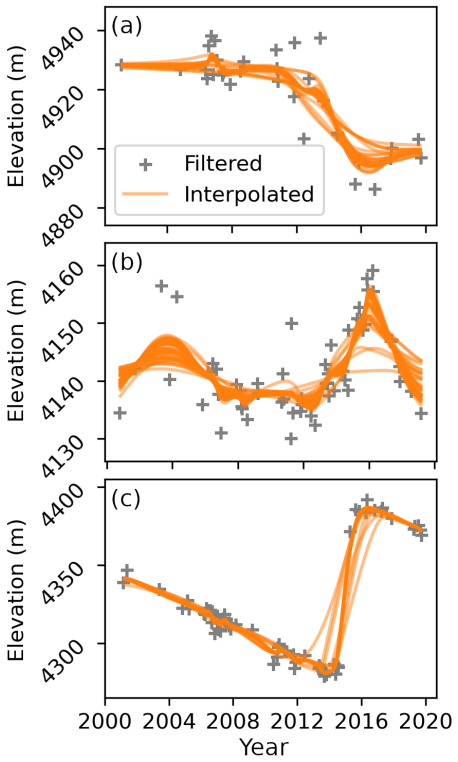

Figure 2.12: Sensitivity of our interpolation method to large data gaps. For the three selected time series (TSa-c of Fig. 2.6 and location visible on Fig. 2.7.c), we remove points during 450 continuous days over a moving window and run the interpolation, displayed with orange lines.

here we observe a constant thickening after the downward extension of the build-up area with no upper reservoir area drained. Turrin et al. (2013) observed, with velocity data, the propagation of a surge front (moving as a kinematic wave) several years before the surge of Bering glacier, triggered by the passing of the front through the reservoir area. The build-up lower limit for Khurdopin also propagated faster than the surface velocity. The surge started in October 2016 according to Imran and Ahmad (2021), about 7 months later than our estimate (Table 2.1), and late August 2015 according to Steiner et al. (2018). The volume received in the receiving area is estimated at 1182 x10^6 m^3 during late August 2015 (elevation extrapolated linearly from TanDEM-X in 2011) to May 2017 (ASTER) data (Jakob Steiner, personal communication). Our estimate over a similar period (2015-09-01 to 2017-06-01) is 426 $\pm$ 34 x10^6 m^3. Both estimates do not agree, although we do not have an uncertainty estimate for one volume. Our filter and interpolation methods fail to fully capture the surge signal of the receiving area, in the lower part of the glacier (Fig. 2.8.b area b3). This failure is due to a low point density combined with a strong thinning signal after the surge (Supplementary Fig. S2.a, in 2017). The filtering workflow removes some of the 2-3 DEM acquisitions over 2017 and 2018, which have credible values. May 2017 is the month with the largest difference between the DEM observations and the interpolation, with an elevation change underestimation that reaches 100 m compared to the pre-processed time series. Over a portion of the receiving area, the apparent surge signal duration after interpolation is about 3 years instead of approximately 1 year on pre-processed time series, and may miss locally a maximum of 40 m (about 30%) of the surge elevation amplitude over these three years. Our estimate of the transferred volume in Table 2.1 is thus underestimated in the receiving area. Our uncertainty estimate is also largely underestimated, as it does not take into account the erroneous filtering. The difference

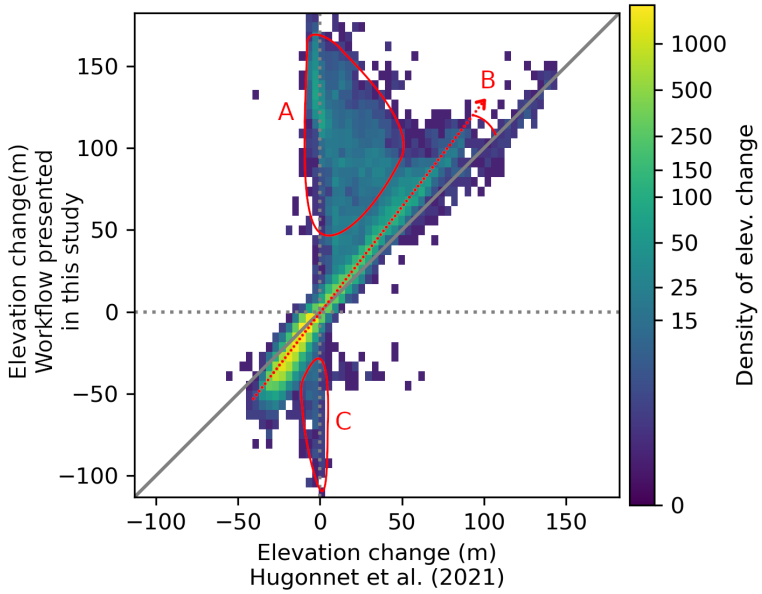

Figure 2.13: Histogram of interpolated elevation change comparison over 8 surges between the original processing from H21 and this workflow. The superimposed histograms of the 8 surge events are represented individually in Fig. S9 of the Supplement. The elevation changes are retrieved over the surge-affected areas and the surge period estimated from the interpolated elevation time series on the centre-lines. The areas and trends designated in red are discussed in subsection 2.6.2. They highlight areas of large surge smoothing or removal (zone A) or overall smoothing of elevation changes (trend B) by the original method (H21), and artefacts created by the presented workflow (zone C).

of the pre-processed DEMs from 2015-08-20 and 2017-05-21 shows a cumulative positive volume change of 650 x10^6 m^3. It is 153% more than with the interpolation, yet nearly half of the estimate of Steiner et al. (2018) which may be also partially overestimated due to their linear extrapolation, as the 2000-2011 trend does not accounts for the later build-up front propagation that we observe. The maximum thickness gain noted by Steiner et al. (2018) was 160 m over this period, against 122 m with our pre-processed DEMs (70 m on interpolated DEMs). The case of Khurdopin surge shows that our workflow may be inefficient to preserve a surge signal, in the case of a low number of observations, worsened by strong thinning outside the surge period.

2.6.3.3 Kyagar glacier

Kyagar glacier is located in an area of poor ASTER coverage, compared to other selected glaciers (Fig. 2.1). During the surge period, there are about 1-2 observations per year, which leads to a smoothing of the surge signal during interpolation. Thus, the onset and ending are visible around end-2012 and early-2017 on interpolated data, while pre-processed time series lead to a more restricted estimate of mid or end-2013 (sooner observation in October after a 14-month data gap) to December 2015. Round et al. (2017) uses satellite imagery to compute velocities and precisely describe the surge development. They find a surge onset in May 2014 after a pre-surge acceleration of 2.5 years, and a surge end between July and August 2015 with limited deceleration later. Li et al. (2023) find very similar timings, plus a continuing deceleration in 2016-2019. Gao et al. (2024) report similar timing, although considering a re-acceleration in 2016 as part of the surge. Gao

et al. (2024) estimated the volume transported from ASTER DEMs. During July 2012 to December 2017, they estimate the received volume to be 321 ± 12 x10^6 m^3, compared to 262 ± 46 x10^6 m^3 with our interpolated data. Their reservoir area volume change estimate is -383 ± 30 x10^6 m^3, against -326 ± 96 x10^6 m^3 for our dataset over the same dates and approximative area (-283 ± 104 x10^6 m^3 with bilinear interpolation of the area affected by artefacts). It represents differences in transferred volume estimate of 18% and 15%.

2.6.3.4 Yazghil glacier

Yazghil glacier has not been extensively studied. Bhambri et al. (2017) date the last surge in 2006, with a gradual increase in velocities before this year. The study estimates from 1972-2016 data that Yazghil glacier has a cycle length (surge repetition period, including quiescence and surge durations) of about 8 years, among the shortest surge cycles in HMA (Bhambri et al., 2017; Vale et al., 2021; Yao et al., 2023). The next surge, which was expected to occur around 2014 based on the cycle length, had not started by the end of 2016, according to the study. Our data suggest that it started 1-2 years later, implying a quiescent phase of 11-13 years for this cycle.

2.6.3.5 Conclusion of the case studies

Overall, the dataset produced by our workflow compares well with existing observations from the literature. The surge dates and the estimated transferred volume agree, except for the date of Kyagar surge and the transferred volume of Khurdopin surge (Table 2.1). The order of magnitude of the imbalances corresponds to the order of magnitude of the measurement uncertainty. For the two critical cases (Kyagar and Khurdopin surges), the workflow shows its limitations in the case of a low number of DEMs, worsened in the case of a strong thinning signal outside the surge period (Khurdopin surge). Our dataset offers new insights on some undescribed processes in these studies, such as the displacement of the dynamic balance line of Hispar surge or the propagation of a surge front during the build-up phase preceding Khurdopin surge.

2.6.4 Applicability to other datasets

Here we discuss the feasibility of applying the proposed workflow to different datasets, possibly including several data sources to increase temporal resolution (i.e., DEMs from different sensors). Even in the case of a similar ASTER DEM dataset processed differently, with lower noise/higher precision, several changes may be made to adapt the filtering. For denser series, a diminution of the span parameter along with a diminution of the filter threshold in the LOWESS workflow should be tested. Abandoning morphological erosion should also be considered. It addresses an issue specific to the photogrammetric processing which tend to affect pixels neighbouring outliers. Deleting this step would be beneficial given the large number of pixels it removes. The use of weighting could also be abandoned in the case of more precise DEMs, as the uncertainty values are not completely representative of the confidence in the measurement. The ALPS-REML prediction parameters could remain unchanged, although the hyperparameters degree of the basis functions p and the order of penalty q can be modified to adjust the smoothing and border effects. More complex considerations would be required in the case of several data sources. More particularly, the weighting may be defined differently to ensure consistency between the datasets.

2.7 Conclusions

We present a new workflow for processing DEM time series of high temporal resolution that is specifically designed to preserve the elevation signal of glacier surge events. We applied the workflow to a dataset from the ASTER sensor over 2000-2019. We filter the data with a LOWESS algorithm, which preserves the surge signal. Some filter issues can appear in difficult areas, which are often not located in surge-affected areas (e.g. textureless accumulation areas, steep slopes). The elevation interpolation (B-spline method ALPS-REML) allows for the observation of surge dynamics, and the estimate of mass transfers at a monthly interval. Surge events with too few DEM observations tend to be smoothed, resulting in an underestimation of the surface elevation change and surge duration. In our study area in the Karakoram range (HMA), our method provides interpolated time series for 80% of glacier pixels. Our workflow better preserves surge events compared to the original non surge-specific workflow. The data obtained are fairly comparable to those from independent studies on several events, except in a few cases. We find discrepancies in the estimated transferred volumes compared to previous studies ranging from 2% to 19% on two surge events and four volumes transferred, and 64% on Khurdopin surge. The workflow, applied to ASTER DEMs but which can be adapted to other datasets, can generate a unique elevation time series able to represent thickness changes of surge events on a monthly scale over a regional extent. It opens new possibilities for the combined analysis of elevation and velocity change during surge events, or more complex derivatives such as surface slope and driving stress.

Chapter 3

Observation of surge propagation and driving stress from remotely sensed data and contribution to theoretical advances

In the previous chapter, we developed a workflow that is used to generate a consistent monthly dataset in parts of High Mountain Asia (HMA) that have a large concentration of surge-type glaciers. We generate a similar surface velocity dataset using the workflow of Charrier et al. (2025) on the existing ITS_LIVE dataset (Gardner et al., 2025).
In this chapter, we attempt to bridge the gap between large-scale observation and modelling, often built and validated on a small number of detailed observations. We combine the surface velocity dataset and the surface elevation dataset to investigate more than fourty surge events and address the question: *To what extent can we test existing models of surge initiation and propagation with remote sensing data?*
In particular, we focus on investigating two particular key points or hypotheses of the model presented in Thøgersen et al. (2019, 2024). First, we estimate the propagation rates of the surge fronts and relate these values to the surface velocity in the surging area. Second, we compute the time series of driving stress as a proxy for shear stress to characterise the surge trigger area. Driving stress is calculated using surface slope and thickness estimates adjusted with relative elevation change, which are both calculated from our elevation dataset, except for the glacier thickness estimate originating from a global assessment.

This chapter is designed to be submitted for publication in a peer-reviewed journal, after being further improved compared to the text presented. The introduction may overlap with some of the content of Chapter 1.
The work on this chapter was challenging for me due to the acquisition of new knowledge through literature review and collaboration, to be able to build a multidisciplinary work. My two supervisors, Amaury Dehecq and Fanny Brun, and myself, have limited knowledge in the field of glacier physics and modelling, as our expertise is on the side of remote sensing and spatial analysis. Thus, this work benefited greatly from the contribution of Adrien Gilbert, an expert in this field. Laurane Charrier, the main contributor to the TICOI algorithm, contributed to the downloading and processing of the velocity data.

3.1 Introduction

Glacier surges have a very diverse range of behaviours and occur in broadly different contexts and glacier types, resulting in similarly diverse explanations and proposed mechanisms. Over time, progress has been made toward unified theories that can encompass several mechanisms (see sections 1.4.2 and 1.4.3). These progresses often rely on simplified case studies and generic equations, and they are generally compared to only a few real surge events. Several aspects of surge mechanisms can be studied, and in particular, the surge initiation and its propagation along the glacier.

It has long been proposed that a surge is triggered locally when shear stress reaches a critical level in a sufficiently large area of the glacier (Meier and Post, 1969; Thøgersen et al., 2024; Cuffey and Paterson, 2010, p530). As expressed by Thøgersen et al. (2024, 2019), the critical level that shear stress must reach to trigger the surge varies over time. It is a function of several parameters, including the effective normal stress which varies with the basal water pressure (eq. 1.5). Although Thøgersen et al. (2019) writes an expression of the minimum trigger area size (the critical nucleation length, in their model), showing that it depends on the rate of weakening that characterises the basal friction and that it should be inversely proportional to the sliding speed, little is known about the minimal area required. Thøgersen et al. (2024) shows that a surge can be triggered over a critical length of a few kilometres, and Altena et al. (2019) observes a similar proportion for the onset of a surge on Klutlan glacier (Alaska). One can expect the extent of some trigger areas to be smaller than these values because the spatial and temporal resolutions of satellite sensors do not, in principle, allow for the detection of propagations that occur below or close to these resolutions.
Satellite imagery can be used to estimate glaciological physical properties. Several studies have already analysed the evolution of shear or driving stress before and during case studies of single surge events, using remote sensing data (e.g., Banerjee et al., 2022; Beaud et al., 2022; Burgess et al., 2012; Gao et al., 2024). In general, they observe an increase in shear stress during quiescence and a decrease during or after the surge. They generally conclude on a trigger due to hydrological mechanisms without investigating in detail possible trigger areas and their extent. They also use a limited number of Digital Elevation Models (DEMs), which produces poor temporal monitoring of stress change.

Thøgersen et al. (2019) also developed a rate-and-state friction theory involving rate-weakening sliding to explain surge propagation. In this theory, a transition from a velocity-strengthening friction to a velocity-weakening friction when reaching a shear stress threshold can model surge onset and propagation. Once triggered over a critical length, the friction loss in the trigger region is transferred to the surrounding regions, locally increasing the basal shear stress and the sliding velocity at the upper and lower fronts of the surge. In response to this stress transfer, a maximum shear stress level can be reached that friction cannot accommodate, causing the surge front to enter a velocity-weakening regime. This reduces the local basal shear stress and triggers a new stress transfer further up and down the active surge area, thus propagating the surge instability. The time required for the frictional state to respond to a stress perturbation is characterised by the ratio of the sliding speed to the characteristic length d_c. d_c, typically in the range of 1-10 metres, can be related to the cavity size or the wavelength of bed obstacles for hard beds, or to the properties of the sediment layer (e.g., thickness, till porosity) for soft beds (Thøgersen et al., 2019, 2024). For this theory, the friction law should contain a transition from velocity-strengthening to velocity-weakening regime, as well as account for the non-instantaneous evolution of frictional strength. The existence and conditions of velocity weakening friction are still debated for both solid and soft beds, despite recent advances

(Thøgersen et al., 2024; Zoet et al., 2022).
To our knowledge, no other study has tried to observe the propagation-sliding relationship. A study of a surge event in Karakoram, by Beaud et al. (2022), compares driving stress with sliding velocities estimated from remote sensing. They conclude that high sliding velocities can increase independently of the driving stress, which would confirm the existence of rate-independent or rate-weakening regimes during the surge.
Alternatively, Minchew and Meyer (2020) also employed a rate-and-state friction model coupled with a pore water pressure model in subglacial till to demonstrate that surge propagation can still be sustained under rate-strengthening friction, as ice thinning results in a reduction in effective pressure during the surge event. However, this model has only been developed in one dimension and does not allow the characterisation of spatial characteristics of the surge propagation, which makes this theory difficult to evaluate with remote sensing data.
Satellite imagery allows the propagation of the surge front along the glacier length to be measured through surface velocity. For example, the surge front of the Sít' Kusá glacier (Alaska) propagated at about 30 km year $^{-1}$, while that of Morsnevbreen glacier (Svalbard) propagated at a rate varying over time from about 0.5 km year $^{-1}$ to 15 km year $^{-1}$ (Benn et al., 2019b; Liu et al., 2024).

Our goal is to exploit new datasets generated with recent advances in remote sensing to i) test the ability of these datasets to observe fine surge dynamics at the core of recent models, and ii) contribute to these theoretical advances by evaluating, against data, key features of the model proposed by Thøgersen et al. (2019, 2024). We focus on two key dynamics of surge events: their initiation and their propagation. Our first objective is to characterise different patterns of shear stress evolution and spatially constrain the location of the trigger areas. For this, we compute a dense time series of driving stress and analyse its evolution with regard to the surge onset and termination. Our second objective is to test the existence of the common state parameter d_c by observing the relation between the propagation rate of the surge front and the surface ice flow velocity after the loss of friction.
In this chapter, we address these two tracks by exploring the dynamics of more than fourty surge events.

3.2 Data and methods

3.2.1 Data

We use two remote sensing products generated at a monthly resolution: elevation and surface velocity. The elevation dataset, which covers 2000-2019, is from the ASTER sensor and DEMs have been generated by Hugonnet et al. (2021).
Surface velocities have been generated using auto-RIFT and provided by the NASA MEaSUREs ITS_LIVE project (Gardner et al., 2024, 2025). This ITS_LIVE product includes velocities computed from optical or radar imagery of the satellites LANDSAT-4 to 8, and Sentinel-1 and 2. We use image-pair product version 2 with temporal baselines from 0 day to the maximum available 546 days (to 100 days for five glaciers: Medvezhiy, RGI2000-v7.0-G-14-23475, 14-12226, 13-19276 and 13-14589).

3.2.2 Generation of elevation and velocity time series

The elevation time series are filtered and interpolated at monthly interval following Chapter 2 (Beraud et al., 2024, 2025).

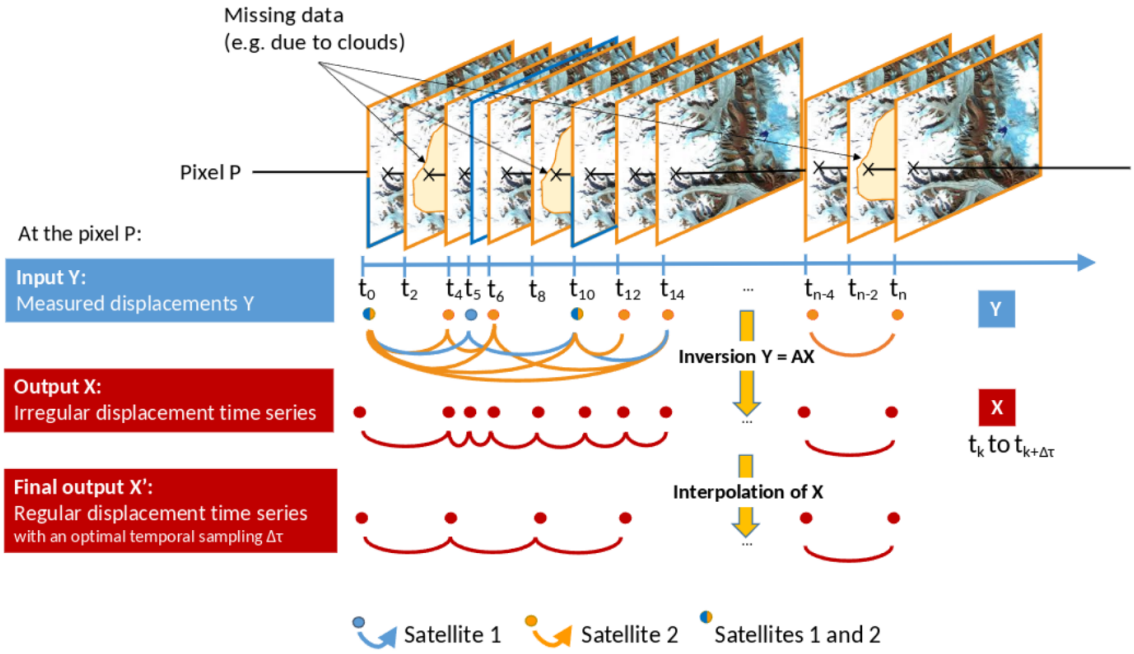

Figure 3.1: Principle of the TICOI workflow, which is applied pixelwise (pixel P here). First, the irregularly sampled and redundant observations are converted into an irregular unique time series using the temporal closure principle. Then, the time series is interpolated at a given regular temporal sampling. Figure from Charrier et al. (2025).

We interpolate velocities in monthly time steps using the TICOI package (Charrier et al., 2022, 2025). This algorithm takes as input velocity maps calculated over heterogeneous time intervals. It uses redundancy in the overlapping time periods and the temporal closure of the displacement (that is, the displacement between two dates equals the sum of displacements to and from an intermediate date) to build a linear system of equations (Fig. 3.1). These equations relate the velocities observed in irregular time intervals and the velocity at the smallest possible time steps. Because this system is ill-posed (it has more unknowns than equations), a regularisation term is needed. TICOI uses a regularisation that tries to minimise the difference between the estimated acceleration and the acceleration obtained using a rolling mean. This approach is more robust to strong changes, such as surges, compared to the traditionally used first-order Tikhonov regularisation. Validation of the TICOI results with GNSS data shows an improvement in RMSE of around 50% compared to traditional methods, and a very good match during a surge event in particular (Charrier et al., 2022, 2025).
These two methods, for DEM and velocity processing, have been successfully applied on several surge events by Guo et al. (2025).
For the exploitation of elevation and velocity data, we rely on time series extracted at regular intervals along the centrelines. The centrelines are manually corrected from the RGI 7.0 inventory (RGI Consortium, 2023), and sometimes drawn according to the major surging branch of the glacier. We extend the centrelines in case the surge creates an advance of the glacier terminus, according to a post-surge extent determined from the inventory of Guo et al. (2023) or satellite imagery.

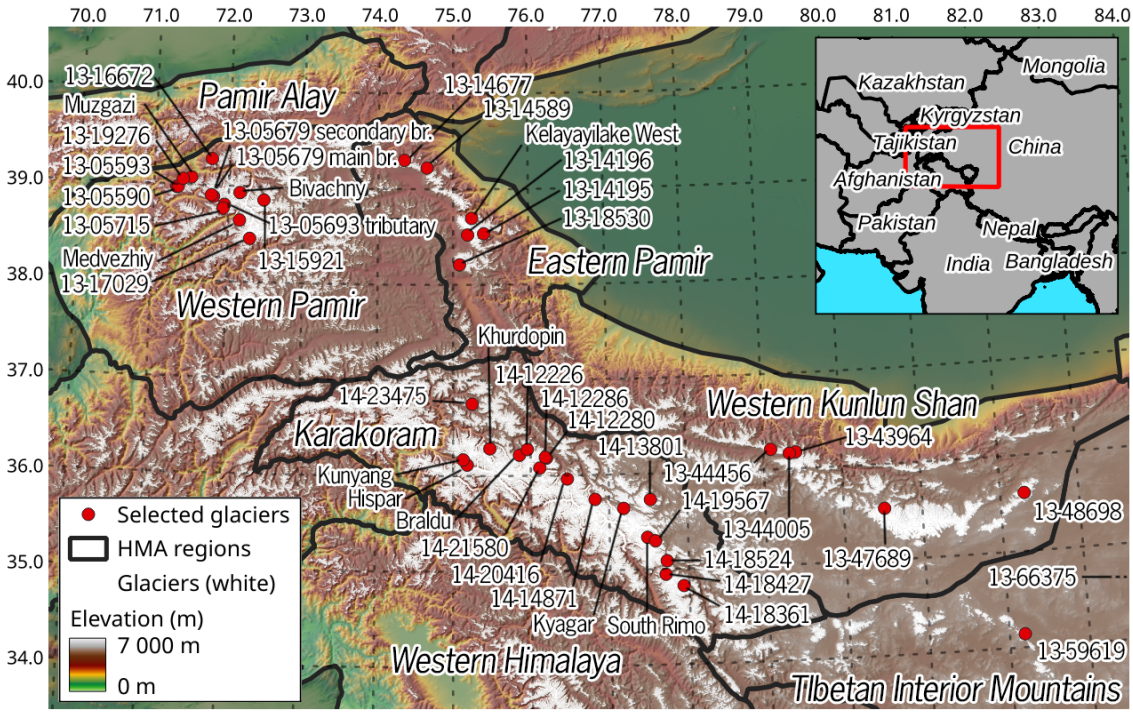

Figure 3.2: Map of studied glaciers. The delineation of HMA regions is from (Bolch et al., 2019; Wester et al., 2019). The basemap is produced from GMTED2010 DEMs, USGS, EarthExplorer. Glaciers, in white, are from the RGI7.0 inventory (RGI Consortium, 2023). The inset map shows the zoomed area (red rectangle). Geographic coordinates are in WGS84, the prefix of RGI 7.0 codes is "RGI2000-v7.0-G-"..

3.2.3 Studied glaciers

We select glaciers by manually investigating elevation change maps for several subperiods between 2000 and 2019 (see Chapter 2). For propagation analysis, we select glaciers for which a surge front propagation is visible in the velocity time series (e.g., Fig. 3.3.a). For the shear stress analysis, which we approximate by the driving stress (see section 3.2.5), we select glaciers with a surge event starting no less than about 5 years after the time series begins, and for which we can assess the surge onset period from the velocity time series. We also removed a few glaciers for which our elevation dataset was not good enough due to too large temporal data gaps in DEMs, or velocity estimates were too noisy to distinguish any surge event.

After selection, we perform our analysis in HMA on a subset of 27 glaciers for surge front propagation, and 35 glaciers for driving stress analysis, for a total of 46 different glaciers (complete list in Tables B.1 to B.3, in Appendix)They are chosen for their suitability for one of the two analysis, and they show at least one surge starting in the 2005-2020 period. There are 20 glaciers (43% of our selection) in Karakoram, 13 glaciers (28%) in Western Pamir, 6 (13%) in Eastern Pamir, 5 (11%) in Western Kunlun Shan, and 1 in each of Tibetan Interior Mountains and Tanggula Shan (Fig. 3.2). Note that no surge event matches our criteria in Central Tien Shan, as a number of surges start too soon for our analysis and have data of poor quality.

3.2.4 Determination of the surge front propagation

We investigate the surge front propagation by delineating the propagation of each surge. For this, we use surface velocity data, following different protocols listed below. For all protocols, we map the propagation of the surge front after surge initiation (e.g., Fig. 3.3.a), provided that there is a clear propagation pattern. For testing, we also map the surge front propagation from elevation change rate data on a limited number of events. All other protocols are used on velocity data only.
For all protocols, we virtually fit a constant propagation between two positions of the surge front. We do not follow detailed patterns, such as seasonal modulation of the surge signal, which are generally not sufficiently detailed despite being discernible, due to the temporal and spatial resolution of our dataset. However, for a few events, we delineate more than one trend along the surge period, which are clearly discernible with the temporal resolution of our velocity dataset (see for example #28 in Fig. 3.5).

Here are the different protocols we follow:

A. We map the surge front propagation by drawing on spatio-temporal representations of the time series (i.e., on Hovmoller diagrams; Fig. 3.3.a-b). We assist our delineation with a constant threshold that we manually change for each surge event, which is exemplified in purple on Fig. 3.3.a-b.

B. We map the surge front propagation by interpreting time series at defined distances along the centreline (e.g., Fig. 3.3.c). These distances are the same as those determined by protocol *A*. In principle, this method is more robust to changes in the amplitude of peak velocity along the centreline.

C. We test an algorithm based on cross-correlation, to compute automatically the time lag between the velocity time series at two locations along the centreline. This protocol has been abandoned due to poor results (see Appendix B.2).

We do not identify surge fronts propagating over periods shorter than three months due to limitations in dataset resolution and our ability to accurately determine onset timing. This in particular excludes the fronts that appear to propagate instantaneously given our temporal resolution – that is, when the front moves several hundreds of metres in roughly one to two months (e.g., for Bivachny glacier).
Although applicable to upward propagation of the surge, we focus on downward propagation (in the ice flow direction) as we observe up-glacier propagation less often and with lower data quality in our dataset. We do not map the surge front on glaciers' terminus advance (i.e., glacier advance on pro-glacial areas during surge) as the propagation is theoretically equal to the ice flow velocity.

Whatever the protocol, we interpolate for each month the location of the surge front between the two sampled points of the delineation. We then extract the median surface velocity (*aggregated* velocities) at the closest samples along the centreline with an upward offset of 500 m.The reason for the upward offset for velocity sampling is to sample locations that have already lost friction, for which the stresses have been reported downward to the next friction points.
Compared to the original study of Thøgersen et al. (2019), which uses basal sliding velocity, we use surface ice flow velocity under the assumption that the expected relationship remains unchanged. This is supported by the fact that surge events are dominated by slip rather than ice deformation (Morin et al., 2023; Cuffey and Paterson, 2010).
The original data from Thøgersen et al. (2019) are provided by the authors.

We estimate a first-order uncertainty of the rate of surge front propagation. We assume an uncertainty of 30 days when pointing at the surge onset at the start and end of our delineation (e.g., at 8.5 km and 11.4 km in the example Fig. 3.3). We also assume there is no error on the surge front position along the centreline: in the process, we rather define the date after choosing a distance at which we evaluate the passage of the front.
We compute the front propagation rate R_{FP} from Δm, the distance between the two positions of the surge front, and ΔT, the corresponding difference in time:

$$R_{FP} = \frac{\Delta m}{\Delta T} \tag{3.1}$$

Thus, as we consider that the error at both ends of the segment are independent, the uncertainty on the rate $\sigma_{R_{FP}}$ expresses as

$$\sigma_{R_{FP}} = R_{FP}\sqrt{\left(\frac{\sigma_{\Delta m}}{\Delta m}\right)^2 + \left(\frac{\sigma_{\Delta T}}{\Delta T}\right)^2} \tag{3.2}$$

with σ_Δ their respective uncertainty. As we assume $\sigma_{\Delta m} = 0$ m and $\sigma_{\Delta T} = \sqrt{30^2 + 30^2}$ days, we obtain

$$\sigma_{R_{FP}} = R_{FP}\frac{\sqrt{30^2 + 30^2}}{\Delta T} \tag{3.3}$$

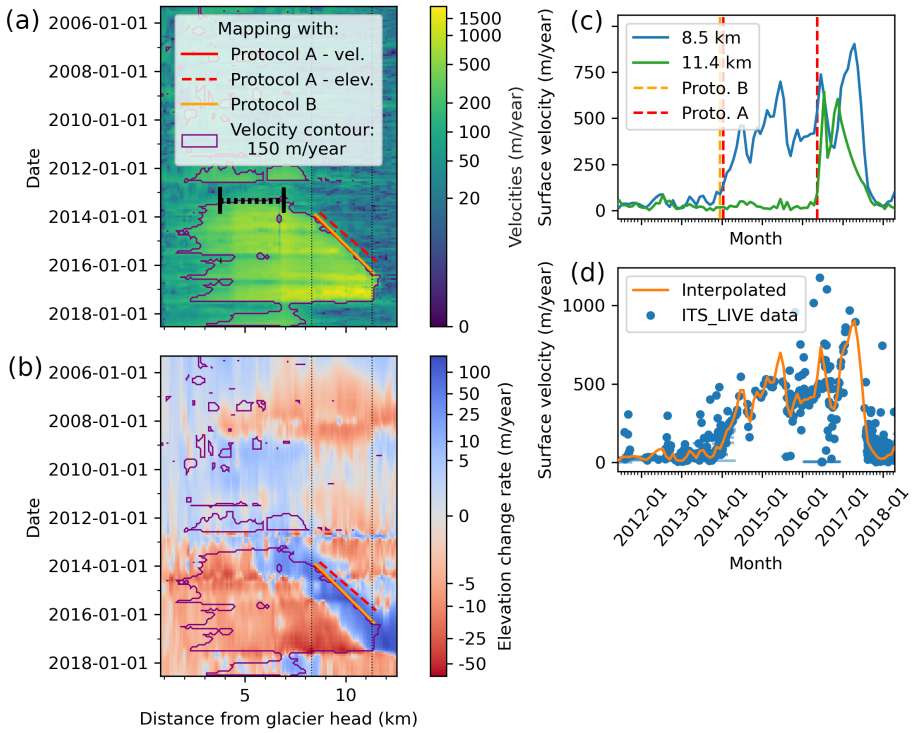

Figure 3.3: Determination of surge front propagation of the tributary glacier of RGI2000-v7.0-G-13-05693 (Western Pamir). Hovmöller visualisation of the surface velocity (a) and elevation change rate (b) time series along the centreline. The area delineated in purple corresponds to a velocity threshold of 150 m/year, assisting delineation for protocol *A* (in orange, drawn on Hovmöller diagram). (c) velocity time series sampled at two locations along the centreline (identical location as protocol *A* and *B*), and representation of the dates corresponding to the surge front passage that have been determined on these time series. Months marked at these locations: 2013-12 and 2016-05 with the protocol *B* (orange), 2014-01 and 2016-05 with the protocol *A* (red). Panel (d) shows the processing of ITS_LIVE velocities sampled at 8.5 km with TICOI. Each velocity observation shows the temporal baseline (horizontal segment; i.e., dates of the two acquisitions). The dotted line on panel (a) between 4 km and 7 km in August 2013 shows the onset period and the possible trigger area (i.e., area on which we focus the driving stress analysis and avoid propagation mapping). Note the seasonal pattern on the velocities. In the legend of panel (a), "vel." means the protocol is applied to the surface velocity dataset, "elev." to the elevation dataset.

3.2.5 Computation and analysis of the driving stress

We investigate the driving stress evolution and the area of the glacier where a critical shear stress threshold could have been reached, in order to identify trigger areas. We approximate shear stress with the driving stress, which can be directly estimated with the gravitational force and remote sensing data. In steady state, the value of shear stress is similar to that of driving stress, with a factor generally between 0.5 and 1 on mountain glaciers (eq. 1.3; Cuffey and Paterson, 2010, p295-298, p341). Thus, our approximation is only valid out of the surge phases, i.e., when the driving stress is fully accommodated by basal friction.
We compute driving stress using the formula 1.1 with ρ the ice density set to 900 kg.m^{-3}. Both the thickness and the surface slope are calculated from the interpolated ASTER elevation dataset. We compute driving stress in a relative way: we use the thickness estimates from Farinotti et al. (2019) as a baseline to which we add the monthly interpolated elevation anomaly. The elevation anomaly is the elevation minus the median elevation over 2000-2005. The 2000-2005 period is arbitrarily defined to be close to the DEM data (SRTM, february 2000) used for thickness estimate, and to ensure that a maximum number of pixels have at least one observation during this period. The thickness estimates of Millan et al. (2022) are not considered, as we think that this method, based on glacier dynamics and which relies in particular on ice flow velocities, could be more biased on surge-type glaciers than the consensus method from Farinotti et al. (2019) which uses several models. Furthermore, it uses surface velocities over 2017-2018, period over which more of our selected glaciers are surging compared to the year 2000 used for the elevation data by Farinotti et al. (2019). To compute the slope, we sample the elevation pixel-wise every 300 m along the glacier centreline. The slope is then computed along the centreline, at the centre location between two sample points, from the elevation gradient. We smooth the slope longitudinal profile with a rolling mean with a kernel size of 10 times the median thickness of the glacier to smooth out the effects of the local surface topography and account for longitudinal stress gradients (Benn et al., 2019b). The median thickness is extracted along the glacier centreline from the estimates of Farinotti et al. (2019).

We analyse the driving stress along the centrelines and inside the possible surge trigger areas. We delimit this area as the part with the earliest marked velocity increase, before any visible surge front propagation (e.g., Fig. 3.3.a, dashed extent in 2013). We define the surge onset by a sudden velocity increase, through visual interpretation of the surface velocity time series (e.g., Fig. 3.3.a).
We then assess whether a trigger area can be identified from the driving stress evolution along the glacier. This is possible by determining the area where the shear stress may have reached a critical threshold, resulting in the surge trigger. To do so, we analyse the temporal evolution of driving stress at several locations along the possible trigger area. We expect a gradual increase in driving stress with a peak at surge onset, and a low driving stress after the end of the surge, which implies a sharp drop in driving stress during the surge. We assume this pre-surge gradual increase permits us to distinguish the trigger area from the area where the driving stress drop is a consequence of the surge.
Based on visual examination, we classify each surge event (designated by the glacier name for clarity) into distinct categories:

- *Spatially constrained trigger surge*: we can generally determine a more restricted surge trigger area by driving stress analysis than by using surface velocity. This implies that the surge was very likely triggered after the stress accumulation exceeded a critical threshold.

- *Temporally ambiguous surge onset*: we do not have sufficient confidence in the di-

agnosis to evaluate the trigger dynamics and area. In particular, for all these surge events, we estimate that the dates of surge onset are not in agreement with the driving stress pattern.

- *Hydraulically-driven surge*: we cannot distinguish any shear stress increase before the surge and the trigger area, thus we postulate that the surge is largely driven by hydrological conditions only.

We also estimate the driving stress drop during the surge of glaciers that are classified as *spatially constrained*. To do so, we calculate the difference of the median driving stress along the length of the estimated trigger area, between the two estimated dates of the surge.

3.3 Results

Of the 46 studied glaciers, 6 of them have at least two surge events overlapping the study period (2000 - 2020). Their length varies from 5.3 km to 46.5 km (median of 14.5 km) (Tables B.1 to B.3 in Appendix) Their overall median velocity during surge ranges from about 130 m year^{-1} to 2900 m year^{-1}. It represents a speed-up factor of 2 to 88 times compared to their quiescence velocity (median 13.5). The surge-affected areas extend over distances of 3.4 km to 33.9 km (median of 9.45 km), which represents 38% to 100% of the glacier length (median of 73%). The amplitude of the surface elevation change during surge events ranges from -80 m to -10 m in the reservoir area (median of -40 m), and from 20 m to 260 m in the receiving area (median of 100 m).

3.3.1 Surge front propagation analysis

We analyse the surge front propagation of a diverse range of glaciers (Tables B.1 to B.3 in Appendix) The shortest glacier is RGI2000-v7.0-G-14-23475 (labelled #27 on figures) with a length of 7 km, a width of about 550 m, and a surge-affected area with a length of 4 km. The longest glacier covered is the #3 Hispar glacier, with a length of about 47 km along the Yutmaru branch and a width of about 2 km in the surge-affected areas – which covers several glacier branches over tens of kilometres.
We sample median surge velocities as low as 150 m year^{-1} over the surge period (e.g., #27 RGI2000-v7.0-G-14-23475 or #11 RGI2000-v7.0-G-13-14195) and as high as 1750 m year^{-1} (#3 Hispar glacier) (Fig. 3.4.b).
We confidently observe surge front propagations from 3 months to more than 5 years, with a median duration of 15 months. They extend over lengths of 400 m to 7.4 km (median 2.1 km). Note that these are only the portion of surge propagations that we are able to delineate according to our criteria, the actual numbers are larger for glaciers with velocity data of poor quality or with indistinct propagation (e.g., glaciers #20 and #22).

The delineation of surge front propagation with the protocols A and B on velocity data show very a similar rate of surge front propagation (Fig. 3.4.a, Fig. 3.5). The rates of front propagation have a median value of 1669 m year^{-1}, the median absolute difference between the protocols is 50 m year^{-1} (3% of the median value) and the RMSE is 257 m year^{-1} (15%).
The corresponding sampled velocity has more variability (Fig. 3.4.b), with a coefficient of variation (standard deviation divided by the mean) of the differences nearly three times higher than for the front propagation. For a median velocity value of 370 m year^{-1} (combining both protocols), the median absolute difference is 55 m year^{-1} (15% of the median value) and the RMSE is 138 m year^{-1} (37%). The delineation from the protocol B has generally lower velocities than A. This means that the front passage is generally anticipated

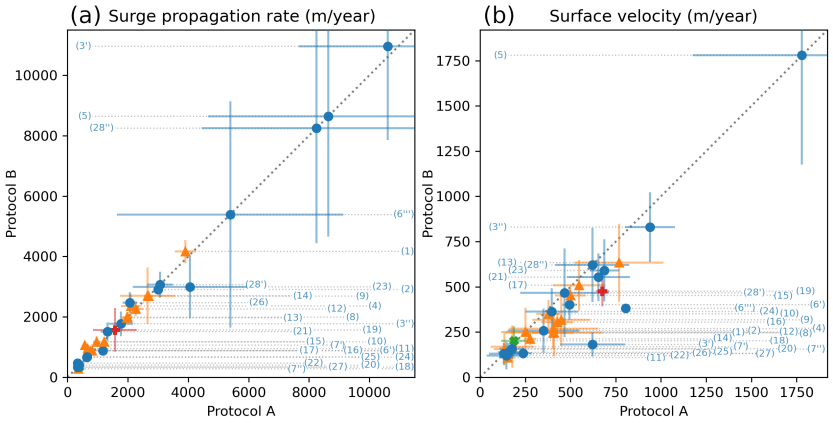

Figure 3.4: Comparison of the surfaces velocities and surge front propagation rate measured by the protocols *A* and *B*. The diagonal dashed line is the 1:1 line. The color and shape of points corresponds to each region, detailed in Fig. 3.6. The dispersion bars correspond to the propagation rate uncertainty (a) and to the standard deviation of sampled surface velocity along the delineation (b).

with *B* compared to *A*, for similar propagation rates.
Our delineation covers very distinct surge patterns (Fig. 3.5). On several surge events, significant seasonal modulation of the velocity is visible, which we ignore in most cases with our delineation (e.g., surges of the #7 Medvezhiy glacier on Fig. 3.5, #10 RGI2000-v7.0-G-13-05693 tributary). Sometimes, seasonal patterns mark a distinct change of propagation rate or surge dynamics. For example, we subdivided the surge propagation of #6 Kunyang and #28 South Rimo into different trends (Fig. 3.5 for #28 South Rimo).
The uncertainty in front propagation rate is very high for very high rates, which also occur to be short in time (e.g., second segment of #28 South Rimo, Fig. 3.5). For these, a small difference in timing has a large impact on the propagation rate. Overall, the propagation rates are in good agreement for both protocols. Values that do not agree within uncertainties are slow-propagating surge events (e.g., #7 Medvezhiy Fig. 3.5), for which a gradual velocity increase make the date choice more uncertain.
The important dispersion in sampled surface velocity (bars in Fig. 3.4.b) is generally more important for faster velocities, likely due to more important amplitude variations.

We plot front propagation rates against sampled surface ice flow velocities (Fig. 3.6). A first cluster (I) of surge events is characterised by propagation rates about twice as fast as the surface velocity (e.g., 22, 15), and a second cluster (II) by rates about seven times faster (e.g., 2, 23). The delimitation between the two clusters seems to occur at a rate of front propagation of about 2000 m year^{-1}. The two plots from the protocols *A* and *B* on velocity data show similar patterns, although results from *B* are more scattered (Fig. 3.6.a and b).
Glaciers with the highest variability of sampled velocities (largest error bars) match glaciers with strong seasonal modulation of the surge velocity (e.g., #7 Medvezhiy on Fig. 3.6.a and 3.5). Both protocols *A* and *B* on velocity data suggest a relation between the surge front propagation rate and the surface flow velocity. Both scatter plots (figures 3.6.a and b) show an alignment (on log scale) with non-aggregated observations of the Variegated glacier. The first cluster (I) aligns with the values of Variegated glacier and high values of Thøgersen et al. (2024) model prediction of the characteristic length d_c ($\geq$ 10 m for *A*). The second cluster (II) rather aligns with d_c between 2 and 6 m. The relationship and alignment with reference data seems to better fit with the protocol *A* than *B*.

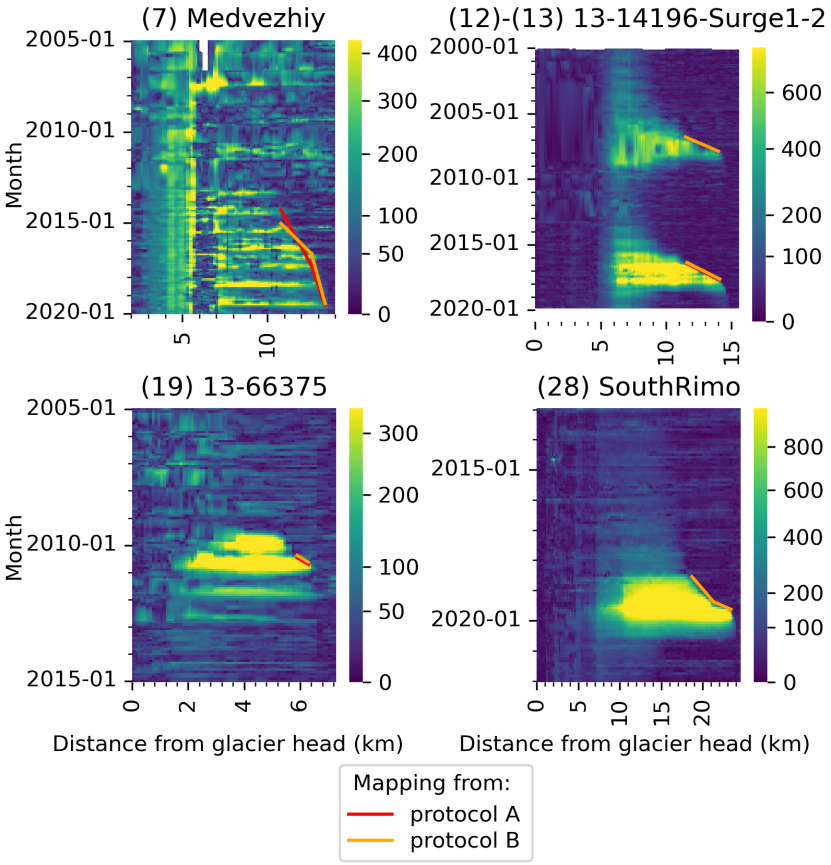

Figure 3.5: Delineation of surge front propagation on spatio-temporal representations of surface velocities for a selection of four glaciers. The representation of all the glaciers is in Appendix Fig. B.2. The prefix of RGI 7.0 codes is "RGI2000-v7.0-G-".

Two surge events have, each, two different trends in different clusters (#3 Hispar and #6 Kunyang glaciers), and the two surge events of RGI2000-v7.0-G-13-14196 (12-13) glacier are also split into the two clusters.
Surge events are uniformly distributed spatially (Fig. 3.7). The number of glaciers with surges in cluster I (resp. II) in the different mountain ranges is 5 (resp. 5) in Pamir, 4 (resp. 6) in Karakoram, 0 (resp. 1) in both Western Kunlun Shan and Tanggula Shan.

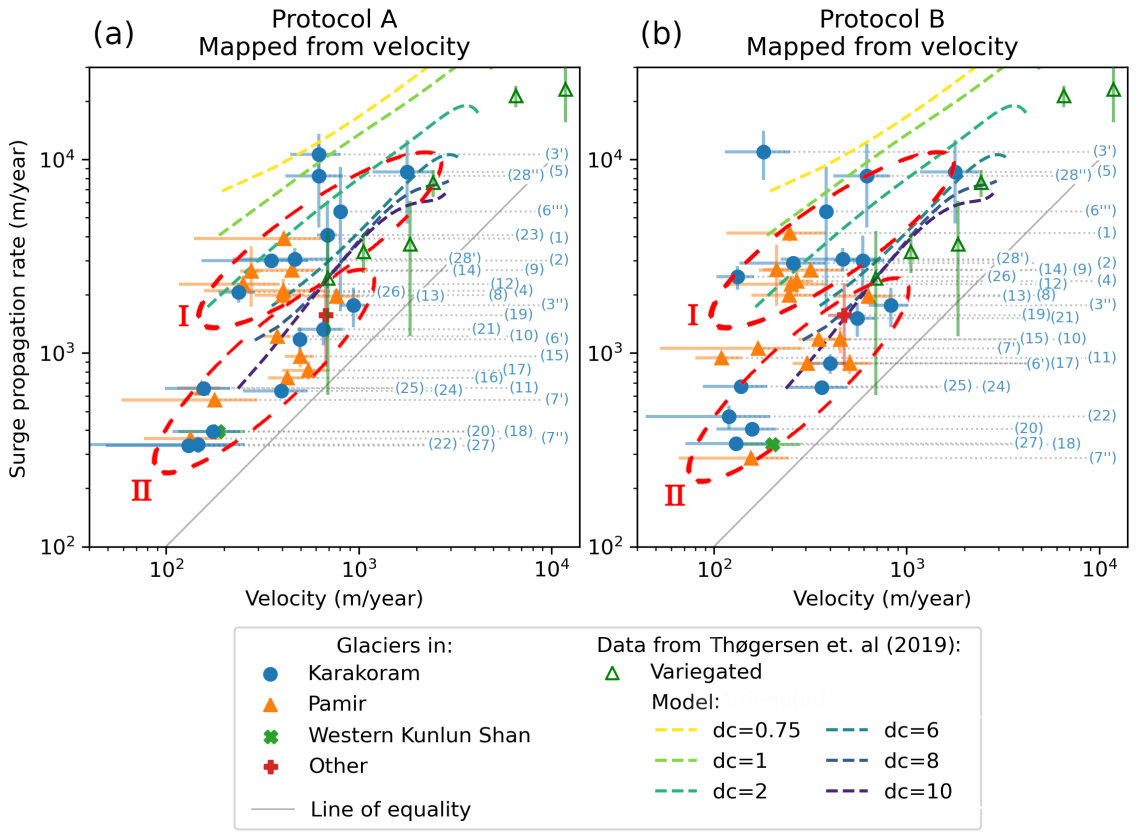

Figure 3.6: Relationship between surge front propagation rate and glacier surface velocity, aggregated per surge event (or trend). The surge front position is determined by the protocol A (a) and the protocol B (b). The correspondence of the surge number index is in Appendix, Fig. B.2 and Table B.3. Indices with n apostrophes correspond to the different trends of propagation rate n for the corresponding glacier. The error bars correspond to the propagation rate uncertainty (vertical, y axis) and to the standard deviation of sampled surface velocity along the delineation (horizontal, x axis). The data from Thøgersen et al. (2019) reported on the figure corresponds to: i) observations of the Variegated glacier surge of 1982 (not aggregated), and ii) model output simulated with different values of the parameter d_c on an idealized geometry of the Variegated glacier (fit of the original scatterplot with a polynomial, see Fig. B.5 in Appendix). The red dotted outlines highlight clusters I and II that are discussed in the text.

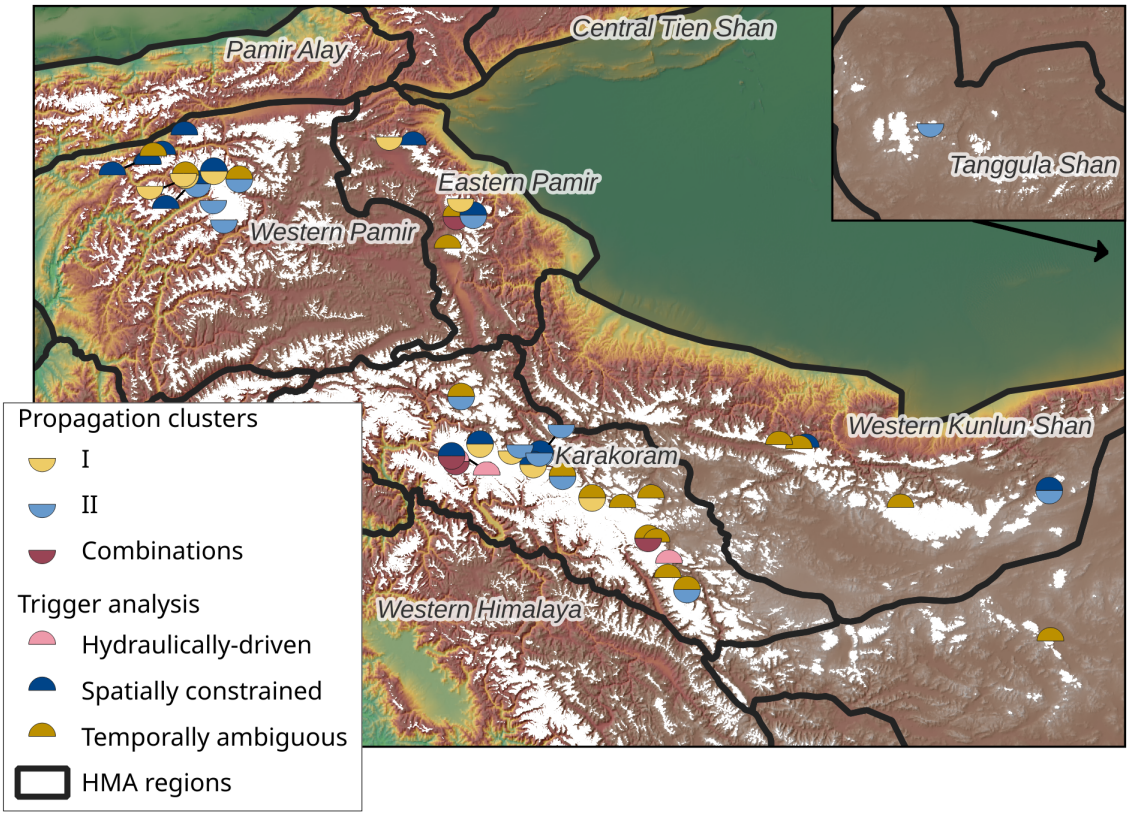

Figure 3.7: Repartition of the surge events. The lower half-circles represent the trigger analysis, and the upper ones represent the surge front propagation analysis. Contextual data source identical to Fig. 3.2.

3.3.2 Driving stress analysis

We analyse the time series of driving stress we computed along each glacier's centreline, and investigate indications of long-term accumulation of stress until the surge. For the data we use and the surge events we analyse, the slope has more impact on driving stress variability than the thickness, although it originates from the same elevation dataset (Fig. 3.8-3.10 panels d-e). Despite an important spatial smoothing of the slope, the driving stress shows abrupt short-term variability seemingly related to spurious effects of the interpolated elevation time series (e.g., Fig. 3.9.d in 2013, Fig. 3.8.d in 2006 and 2015).
Below, we present a selection of glaciers typical of the three surge cases we observe. Note that, in addition to surge events we did not select, we further removed four surge events/glaciers for which the quality of elevation or velocity data was not sufficient for the analysis (13-17029, 14-07912, Yazghil and Medvezhiy glaciers).

3.3.2.1 *Spatially constrained trigger surge* class – the Khurdopin glacier

Khurdopin glacier has a marked velocity peak limited to 2017, but we set a surge onset in spring 2016, during which the estimated velocity remains very high after the spring seasonal peak (about 250 m year^{-1}, against 50-80 m year^{-1} in the previous years). We analyse the driving stress between 25 km and 33 km from the glacier head, in between the up- and down-glacier surge front propagation. The driving stress time series shows the expected behaviour, with a long-term increase of stress until the onset of the surge, followed by a sharp decrease until the surge end (Fig. 3.8.d-e). The peak driving stress is about 180 kPa, followed by a decrease of about 80 kPa during the surge (note that the peak driving stress value is relative due to rather uncertain thickness). The peak is reached approximately between 26 km and 31 km from the glacier head, which we call the "trigger area" (Fig. 3.8.b, dotted area). Thus, we classify this glacier/surge event as *spatially constrained trigger surge*. Despite a few short-term artefacts, the interpolated elevation time series fits correctly with pre-processed elevations over this part of the glacier. According to the elevation change observations, the trigger area is centred on the dynamic balance line (i.e., transition from the reservoir to the receiving area; Fig. 3.8.b-c). The Khurdopin elevation change signal has a particularly marked pre-surge build-up signal compared to other glaciers, with a down-glacier expansion of the build-up area until the surge onset. The build-up area seems to range from 13 to 26 km from the glacier head in 2002, and 13 to 32 km in 2014. Note that at 31.05 km (the very edge of both the buildup area and the trigger area we defined), the driving stress increase is completely due to the slope increase as there is nearly no thickening (Fig. 3.8.e). This is probably due to the fact that the thickening, constrained to the area upstream of this point, increases the slope locally. This effect is certainly both amplified and extended in area by the slope smoothing along the centreline.

3.3.2.2 *Hydraulically-driven surge* – Hispar glacier

Hispar glacier is the largest in our glacier selection. The surge we analyse starts in 2014, seemingly simultaneously over a very large area (Fig. 3.9.a). The surge is divided into two peaks, with surface velocities reaching more than 3500 m year^{-1} according to velocity time series. The Yutmaru tributary joins the larger branch from the Hispar Pass at about 18 km (map and centreline on Fig. B.40 in Appendix). At least two studies claimed the Yutmaru started surging slightly before the other branch, which we also observe on our velocity data (Guo et al., 2020; Paul et al., 2017). From about 13 km to 27 km, where the surge may have been triggered, we notice no significant pattern of long-term increase in shear stress. The time series of driving stress shows variations throughout the pre-surge period without

a clear pattern, and a quite stable level of stress (e.g., Fig. 3.9.d-e). This is true both above and below the main junction. We estimate that due to the absence of a consistent driving stress pattern, the surge is likely purely driven by hydrological conditions, and we label it in the *hydraulically-driven surge* class.

3.3.2.3 *Temporally ambiguous surge onset* – glacier RGI2000-v7.0-G-14-13801

The velocity of glacier RGI2000-v7.0-G-14-13801 increases gradually, with a distinct acceleration in 2015 that may indicate the onset of the surge. However, although the velocity pre-2014 (seemingly of lower quality) does not indicate a significant speed-up, the elevation change rate shows a small surge-like mass transfer already years before, from about 2011 (Fig. 3.10.a and c). The driving stress analysis at 12.15 km shows a stable stress until 2011, followed by a sustained decrease. Close to the dynamic balance line in the receiving area, a *front* of sharp stress decrease slowly propagates down-glacier. We sample this dynamic at kilometre 13.65, where the stress evolution is close to what we would expect in the trigger area. However, the timing of the stress peak is very sensitive to the location at which we sample, to within a few hundred metres. We classify this surge as *temporally ambiguous surge onset*, due to 1) insufficient evidence that the stress accumulation triggered the surge and 2) uncertainty in the surge onset date.

3.3.2.4 Results of the analysis of all surge events

Over the 35 glaciers with sufficiently good data that we evaluated, we could define a trigger area for 15 of them (*spatially constrained trigger surge* category) for which we attest a distinct excess of shear stress, after stress accumulation (driving stress time series in Appendix, section B.4). They are in nearly all the regions investigated, but represent a higher fraction in Pamir (Fig. 3.7). Region by region, 9 out of 14 investigated glaciers in the Pamirs are classified as *spatially constrained*, 2 out of 5 in the Western Kunlun Shan, 4 out of 15 in the Karakoram, and the single surge event investigated in Tibetan Interior Mountains is *temporally ambiguous*. We do not explain the discrepancies between the mountain ranges.

We explore the different characteristics of the *spatially constrained trigger surge* events (Table 3.1). For these 15 glaciers, the lengths of the estimated trigger areas range from 0.6 km to 3.5 km (median 1.5 km). Note that the characteristics we present strongly depend on the centrelines that we have drawn, especially for tributaries and glaciers in glacier systems. The size of the trigger areas represents from 3% to 19% (median 11%) of the post-surge glacier length (or tributary length if the surge does not propagate significantly into the main branch). The centre of their trigger area is located at 33% to 83% (median 59%) of the glacier length (Fig. 3.11; i.e., trigger areas can be both closer to the glacier head or the glacier front). For example, the bottom of the trigger area is probably less than a kilometre away from the pre-surge terminus of the RGI2000-v7.0-G-13-43964 glacier.
The trigger area generally overlaps with the dynamic balance line at the onset of the surge (Fig. 3.11.b). It may be entirely in the receiving area (e.g., RGI2000-v7.0-G-14-21580) or nearly entirely in the overall reservoir area (e.g., Muzgazi). Note that the dynamic balance line may move down-glacier during the surge. We notice such displacement on nearly half of the surge events (Table B.2 in Appendix) The displacement ranges from 0.6 km to 9 km (median of 2.1 km), which represents from 5% to 40% of the glacier length (median of 17%). For example, the dynamic balance line of RGI2000-v7.0-G-13-05693 tributary shifts by about 5 km (glacier of 13 km); the early-surge dynamic balance line touches the lower estimated trigger area (Fig. B.10 in Appendix).
The driving stress change between the estimated surge dates ranges from -39 kPa to -

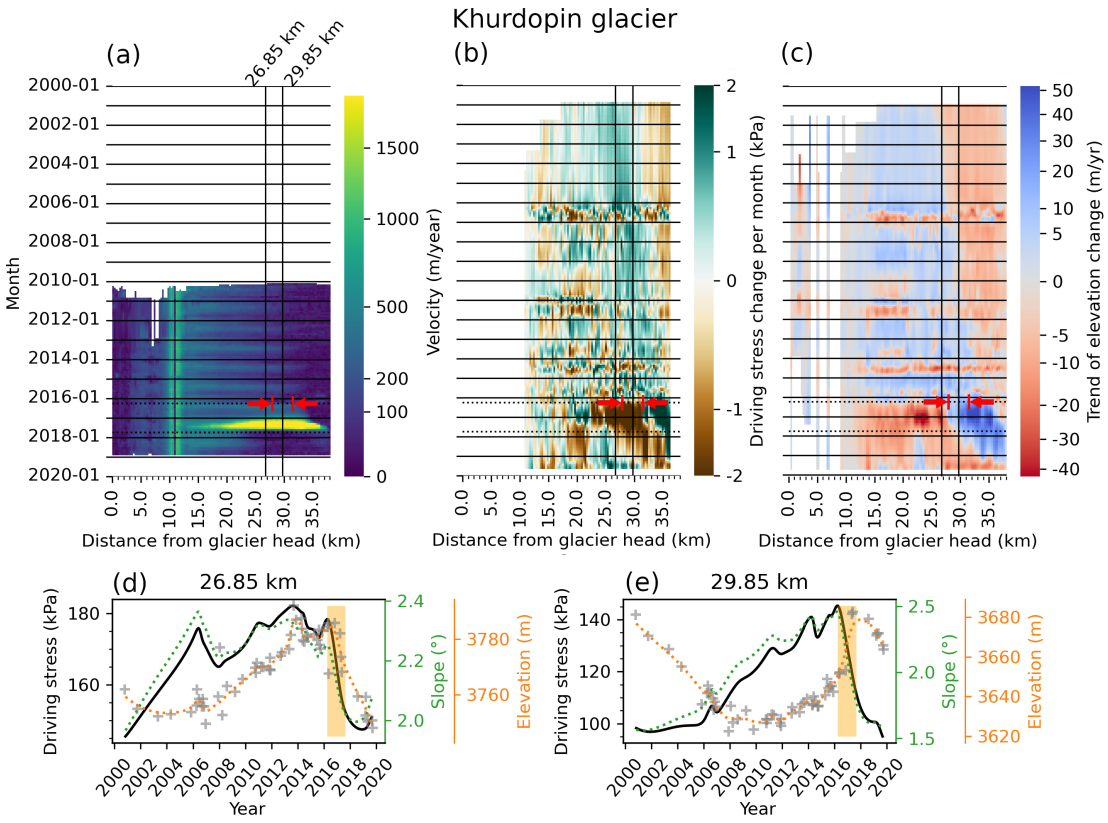

Figure 3.8: Longitudinal driving stress evolution over the centreline of the Khurdopion glacier (RGI2000-v7.0-G-14-21665). The panels show the time series of the surface velocity (a), the driving stress (b) and the trend of elevation change (b). The area in (a-c) between red arrows is the trigger area we estimate after the analysis of driving stress time series. Panels (a-c) show vertical bars on the locations where the time series of driving stress shown on (d-e) are extracted, and horizontal dotted lines at the estimated surge onset and end. On panels (d-e), which show time series of driving stress and its component slope and variation of thickness, grey crosses are pre-processed elevation time series, the dotted orange line is the interpolated elevation from which slope is computed, and the orange area is the surge period (same as horizontal dotted lines on panels a-c). These figures are available in appendix for all glaciers classified (Appendix section B.4).

81 kPa (median -43 kPa). However, large uncertainties in the thickness estimate do not permit a reliable absolute driving stress estimate.

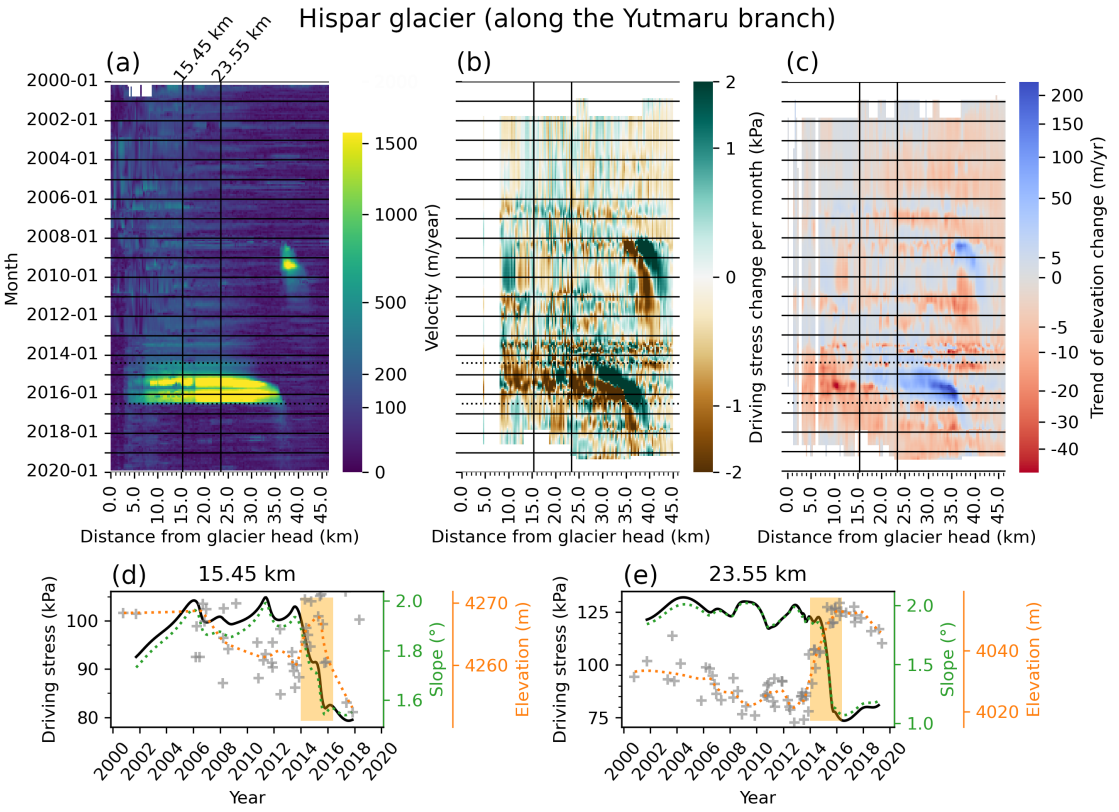

Figure 3.9: Same as Fig. 3.8 for the Hispar glacier along the Yutmaru branch (RGI2000-v7.0-G-14-21670).

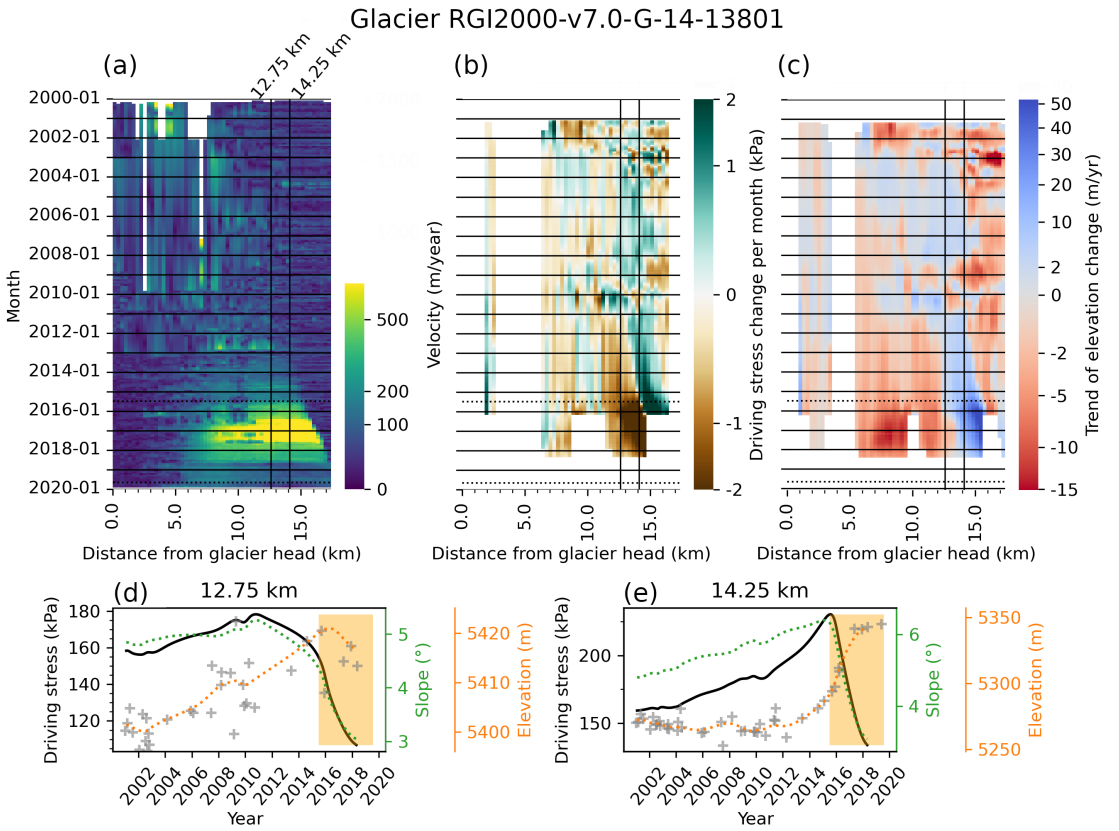

Figure 3.10: Same as Fig. 3.8 for the glacier RGI2000-v7.0-G-14-13801.

Glacier	Estimated Trigger area (km)			Driving stress variation (kPa)	Glacier length (km)	Figure (Appendix)
	Upper	Lower	Length			
14-21580	22.5	24.5	2	-41.7	41.9	B.17
Khurdopin	28	31.5	3.5	-43.4	38.3	B.7
Bivachny	14.0	16.0	2.0	-80.8	30.4	B.6
Kunyang	22.5	23.5	1	-38.8	29.9	B.18
13-14195	6	8	2		18.2	B.16
14-12280	11.7	12.5	0.8	-39.0	16.8	B.20
Muzgazi	4	7	3	-60.3	16.8	B.8
13-05693 Trib.	5	6.5	1.5	-42.6	13.2	B.10
13-43964	8.4	9.6	1.2	-38.9	10.9	B.14
13-05715	5.5	7.3	1.8	-47.3	10.8	B.11
13-48698	6	8	2		10.3	B.15
13-05593	6	6.6	0.6	-77.6	10.0	B.19
13-14589	3.7	4.5	0.8	-47.0	7.0	B.12
13-05590	3.7	4.3	0.6	-41.4	5.3	B.9
13-16672	1.5	2.1	0.6	-52.1	5.3	B.13

Table 3.1: Characteristics of the glaciers with a trigger area *spatially constrained*. The prefix of RGI 7.0 codes is "RGI2000-v7.0-G-". The location of the trigger area is given as distance along the centreline from the glacier head. We do not estimate the driving stress change for 13-14195, due to the end of the surge not being captured in our data, and for 13-48698, due to uncertainties in the surge date with poor elevation data.

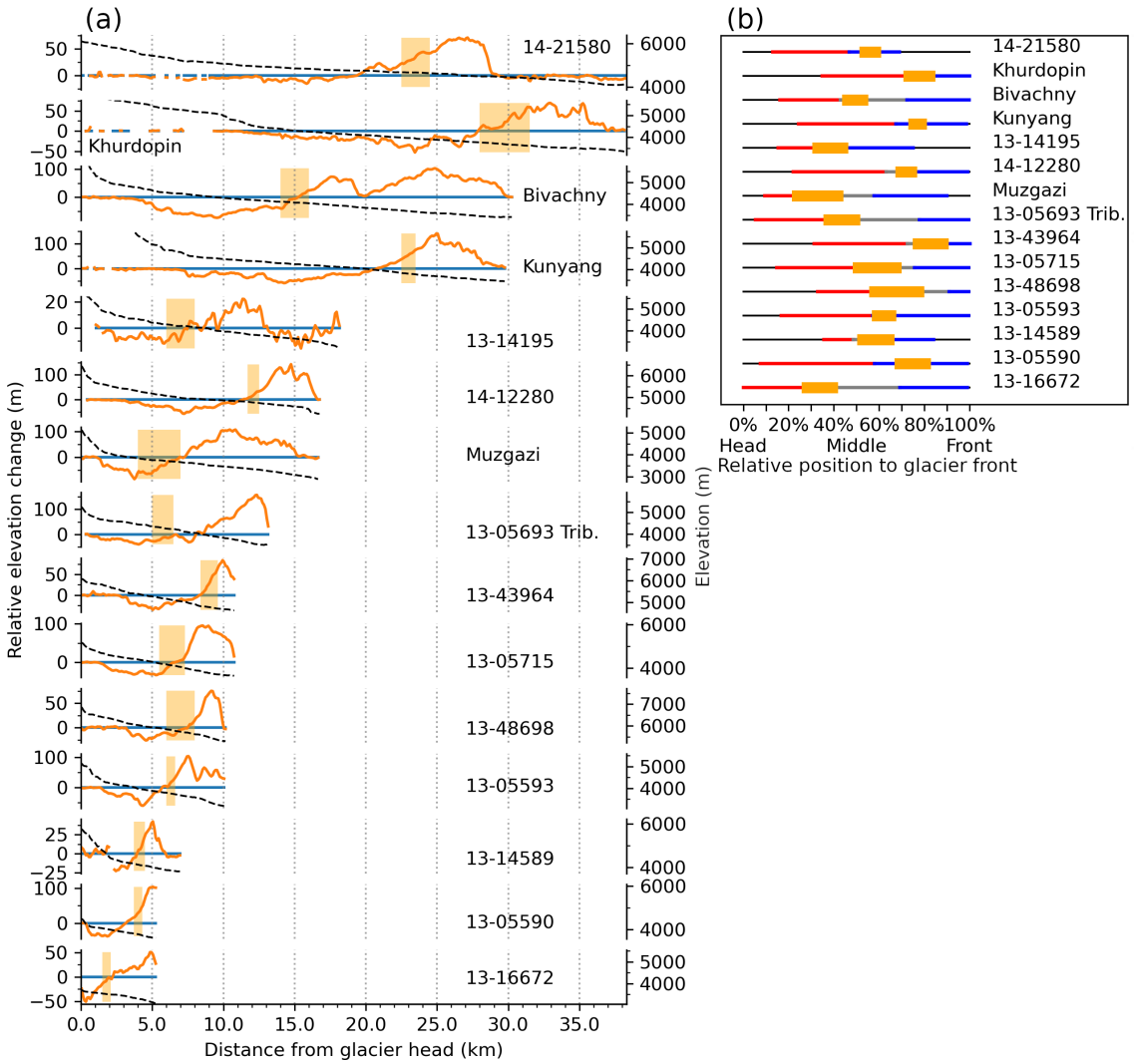

Figure 3.11: Location of the estimated trigger area (orange area) along the glacier's length, expressed in km (a) and % (b). (a): blue and orange lines are the longitudinal (centreline) elevation profile at surge onset and termination, respectively, expressed relatively to the onset elevation (left axis). The orange line thus represents the thinning during the surge with negative values and the thickening with positive values. The dashed line in black is the surface elevation (right axis), on a common scale. Note that the longest glacier (RGI2000-v7.0-G-14-21580) has a length of 41.9 km and does not appear entirely. For this glacier in particular, the elevation change in the reservoir area is not fully captured due to data processing reasons (smoothed by about half, see Fig. B.17 in Appendix). (b): size of the areas relative to the glacier length. The red line is the reservoir area, the blue line the receiving area. The dynamic balance line is between the two, represented as a grey area if the dynamic balance line shifts down-glacier during the surge.

3.4 Discussion

3.4.1 Front propagation

3.4.1.1 Suitability of elevation time series

We explored the suitability of elevation time series for investigating the propagation rate – surface velocity relationship. The results of the protocol A applied on elevation change rate instead of velocities is presented in Appendix (Fig. B.4). The low suitability of the elevation dataset to assess the flow velocity - surge propagation relationship can be mainly explained by two points. First, the method developed to process the elevation time series, applied to ASTER DEMs, tends to smooth the surge signal over a few months on a number of time series. Accurate interpolation requires dense observations in time, and data gaps of several months to years are common. While not predominant, this inconsistency in smoothing creates variability along the centreline and can represent a surge signal one or two years before what is contained in the raw time series. The sensitivity analysis discussed in section 3.4.1.2 show a strong sensitivity of the results to a temporal offset of 2 months backwards, whereas interpolated elevation time series often have more delays. This is what occurs for glaciers #2, #3 or #6 (Appendix Fig. B.2 and Fig. B.3), and it is especially true for regions with a low number of DEMs (see Chapter 2). Second, surface elevation does not respond directly and locally to velocity changes. Thus, it is probably not the most direct proxy for accessing the basal failure propagation.

3.4.1.2 Front propagation: sensitivity analysis

We estimate that the uncertainty in the propagation rate can be large for fast-moving fronts. The surge front propagation rates, which are manually delineated, are consistent between the two protocols, and there is a larger variability in the temporal shift (i.e., we pick dates generally sooner with B). In particular, protocol B, which uses one-dimensional time series, is more sensitive to the lack of contextual information (i.e., to the overall propagation front up and downstream). Hence, for surges with a strong seasonality pattern, we can pick a date one year apart (e.g., the first date of the surge front of the #7 Medvezhiy glacier, Figure 3.5). For a gradual velocity increase, we can also choose a propagation trend with a higher surface velocity, resulting in a faster propagation. For example, the end of the first segment of South Rimo's surge front is clearly distinguishable, but, at the beginning of the segment, one could delineate a faster front starting further up-glacier with faster surface velocity (#28 in Fig. 3.5).

We now discuss the sensitivity to the velocity. We carry out a sensitivity analysis with protocol A to assess the robustness in front delineation precision in time and space (Fig. 3.12). Shifting all delineations back in time (offset of -2 months in our test) and down-glacier (offset of 0 m, while the default is -500 m) have the strongest effect. While sampling velocities 2 months ahead (+2 months, i.e., closer to surge peak) slightly increases the median flow velocities, sampling 2 months before the mapped surge front location (- 2 months, i.e., closer to pre-surge) drastically reduces the estimated median flow velocities associated with fast propagation rates (Fig. 3.12, vertical axis). A shift along the centreline (-1000 m / 0 m) has a quite uniform effect: it increases or decreases the estimated mean flow velocities as a whole, with a major shift for an offset of 0 m. In conclusion, at each surge front position, our result is sensitive to the estimated date of the front's passage. This is increasingly critical for high surge front propagation rates (i.e., >2000 m year^{-1}). However, as long as the sampling is done on an actively surging location and period, the results show little change. Protocol B shows the same behaviour.

Qualitatively, pointing the surge front at a location along the centreline is also generally uncertain for surge with slow propagation and gradual velocity increase or with important seasonality of the velocity, due to noise or the gradual increase of peaks in velocity that tend to make the chosen date arbitrary. Due to such gradual onsets and noisy time series in particular, our delineation is hardly reproducible due to the personal interpretation of the surge onset date. Automatic break detection methods may be an alternative; they have been used in the literature for various applications. For example, Nanni et al. (2023) implemented an automatic detection of surface velocity change to map the propagation of seasonal accelerations. They partition the velocity by seasons and use a threshold of deviations. However, this method still requires the choice of thresholds, and surge events have much more variability than recurrent seasonal patterns in quiescent periods. In future attempts, new methods such as the BEAST algorithm (a Bayesian estimator) for the detection of changes in time series should be investigated. It has been applied by Li et al. (2023) on ASTER elevation time series on the Kyagar surge event, with promising results.

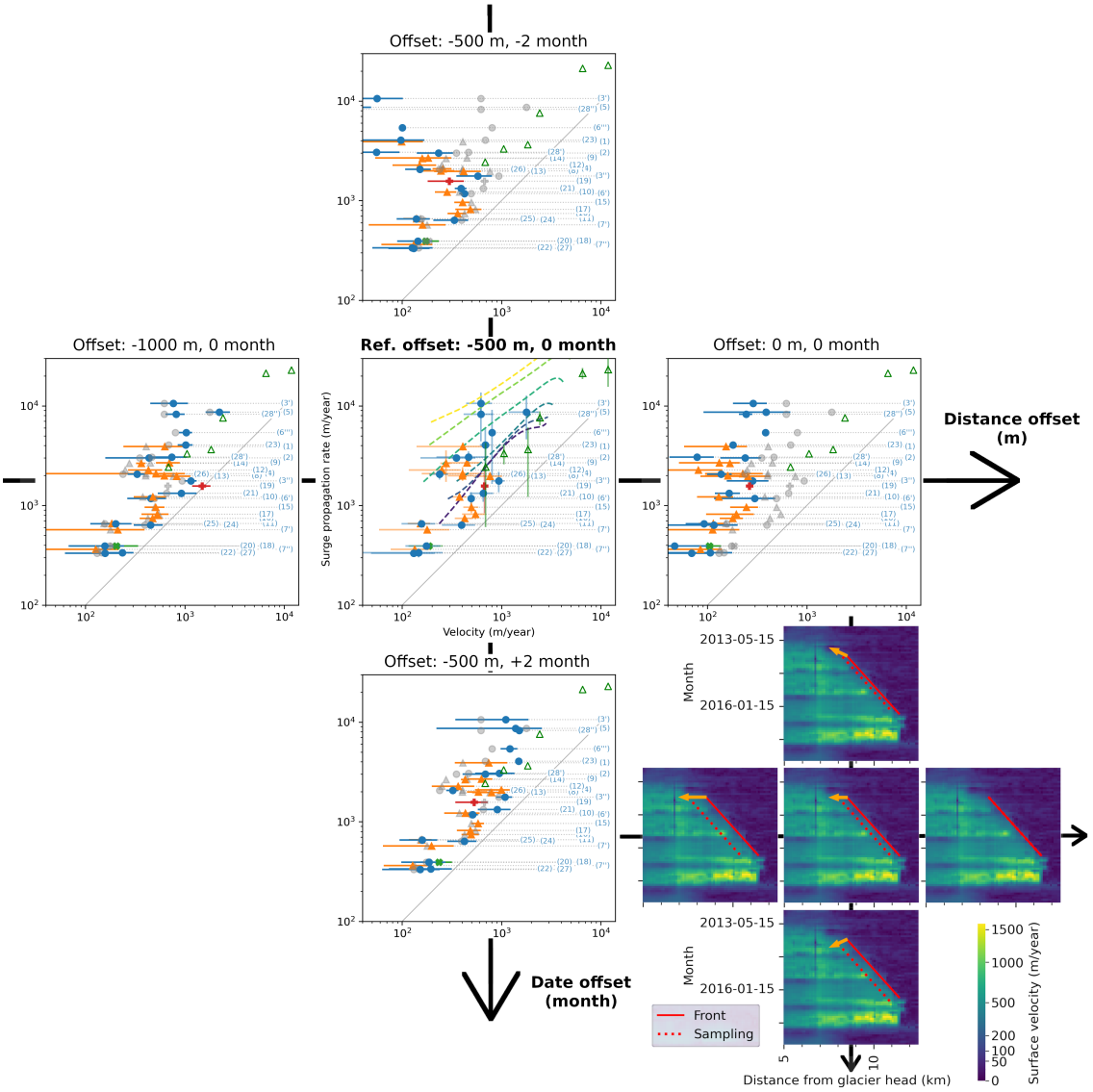

Figure 3.12: Sensitivity analysis of the relationship surge propagation vs flow velocity, for protocol *A*. We change the distance offset (default is -500 m, i.e., upward along the centreline) and the date offset (default is 0 months), for velocity sampling, compared to the original setting (central plot). On the bottom right, the front position and the sample pattern corresponding to each pattern are represented for an example (default setting on the central thumbnail).

3.4.1.3 Front propagation: interpretation

The data analysis shows that we can successfully estimate the average rate of surge front propagation with remote sensing data on a large panel of surge events. We provide a first assessment of the propagation dynamics proposed by Thøgersen et al. (2019, 2024). The overall relationship between the propagation rate of the surge front and the surface flow velocity seems to support the propagation model, although we use the surface velocity as a proxy of the basal slip velocity. However, using surface velocity is likely to be a good approximation, since most of the surface motion is due to basal sliding during surge events. Our analysis includes surges with velocities one order of magnitude lower than measured on Variegated Glacier. The relationship seems to align with the model predictions along two different values of high d_c ($\geq$ 10 m and 2 m$< d_c <$ 6 m). If confirmed, the seemingly clustering around these two d_c values could imply that there are two significantly different bed types and properties under these glaciers. The coefficient d_c can be related to the wavelength of the bed obstacles (i.e., distance between the cavities ridges) for hard beds. For purely soft beds, d_c would be related to the properties of the sediment layer (e.g., thickness, till porosity, degree of localisation) (Thøgersen et al., 2019). The wavelength of bed obstacles associated with cavitation is typically of a few metres (Helanow et al., 2021), whereas the thickness of soft till can also vary from a few metres to tens of metres (Engeln, 1938; Menzies and Shilts, 2002, p436-7,p187). Thus, concluding on the nature of the bed of these two clusters is quite speculative as they could be both associated with soft till but of different nature (grain size, porosity...). However, the second cluster with $d_c \geq 10$ m is unlikely to be associated with hard-bed as 10 m is likely above the length scale expected for the cavitation process. This cluster probably involves a more complex interaction with soft beds. Clusters I and II are both widely spread across the same regions, often appearing side by side. Although our preliminary conclusions seem to rule out geographical explanations, a more resolved analysis with, for example, geological data may be of interest to untangle more precisely the distribution.
The alignment we observe with the modelling of Thøgersen et al. (2019) may indirectly attest that a velocity-weakening friction occurs on these glaciers that likely rest on soft beds. The rate-weakening friction on a soft bed involves processes different from those on a hard bed, but is still realistic. The shear zone within a sediment layer is commonly modeled using the rate and state approach, including rate weakening (Minchew and Meyer, 2020). This analysis constitutes a second approach to validate a possible velocity-weakening friction mode from satellite imagery, following the study of Beaud et al. (2022). Note that the existence of this friction mode is still debated, for both hard and soft beds (Thøgersen et al., 2024).

Our propagation analysis remains indicative and semi-qualitative, and only permits us to give interpretations of these observations. First, the results of Thøgersen et al. (2019) have been produced on an idealized geometry (bed elevation and thickness) of Variegated glacier, and the applicability of the results of their model to other geometries has not been investigated. Although we expect little change with other geometries, there is a need for further investigations running the model on geometry-informed surge events.
In addition, the variable d_c is expected to vary spatially, with bed properties and geometric changes along the glacier length. Finally, the dataset we use strongly limits the spatial and temporal resolution of the surge front tracking. Higher temporal and spatial resolutions are required to resolve the surge front propagation rate variability at weekly to monthly scales, in particular the seasonal variability for which we can also expect a variation of the surge front propagation. It would also permits us to capture very high or slow propagation rates that we cannot observe, especially if they occur on rather short distances.

Several observations also mitigate our analysis. First, we can observe the propagation of surge front or an acceleration front at a similar rate along the surge, but with very different velocities. The example of RGI2000-v7.0-G-14-18361 is illustrative of this (#24 in Fig. B.2 in Appendix). Along our delineated surge front position, i.e., for the same rate of front propagation, the surface velocity is about 200 m year^{-1} during the first 10 months, and then about 400 m year^{-1} for the 13 consecutive months.
Finally, several features of our clustering raise some questions. In our cluster analysis (Fig. 3.6), the two distinct trends of #3 Hispar and #6 Kunyang surge events are distributed in different clusters. In addition, for the two surge events of RGI2000-v7.0-G-13-14196 (12-13), both are in different clusters, meanwhile those of RGI2000-v7.0-G-13-17029 (16-17) are very close to each other. These surge events are propagating at the same rate, with relative differences of 14% between #12 and #13, and 9% between #16 and #17, respectively. This different clustering is due to large differences in surface velocities, with relative differences of 102% and 25%, respectively.
These observations could be explained by the fact that basal properties can vary along the glacier, and pre-2013 velocities can be biased toward long-term velocities with a smoothing of short-term velocity peaks, which is due to fewer satellites. But it may also be that the reality is not as idealistic, with, for example, different hydrological conditions and unresolved state dependencies, till parameters different between the two surge onset.

3.4.2 Driving stress and trigger area

3.4.2.1 Is it possible to interpret the triggering mechanisms?

The unprecedented temporal resolution of the time series of surface velocity, elevation changes and driving stress we compute allow for a detailed investigation of surge events. The driving stress analysis shows that, for several surge events and possibly the vast majority of them, there are marked patterns supporting a long-term accumulation of shear stress until a surge trigger is possible. We show more evidence that the trigger of these surge events, whatever the mechanism, generally requires long-term accumulation of mass, and in turn an increase of driving stress.
This is in line with different theories and mechanisms of the surge trigger. A surge is triggered when the driving stress cannot be accommodated by basal friction over a sufficient area. The trigger condition can be expressed as $\tau_b > CN$, with τ_b the basal shear stress, C the maximum friction threshold and N the effective pressure (Thøgersen et al., 2024). This condition can be met by steepening and thickening that results in increased shear stress τ_b. The thickening also insulates and warms cold-based glaciers, favours frictional heating, and then contributes to the decrease in effective pressure N (Benn et al., 2023). Hence, the condition can be met under constant stress τ_b and with the effective pressure N decrease (increase in water pressure). This may be what we observe for two glaciers in our analysis that we classified as *hydraulically-driven surge*.

However, shear stress and effective pressure are related and can be co-factors: the increase in shear stress does not provide complete information about the trigger mechanism. The shear stress-drainage system efficiency dependence has been developed by several authors (Thøgersen et al., 2024; Eisen et al., 2005; Raymond, 1987; Cuffey and Paterson, 2010, p535). In these studies, it is theorized that the increase in shear stress on the long term opens cavities and causes the drainage system to collapse each year sooner and sooner. This drainage system collapse or frictional feedback is certainly what causes the gradual accelerations in our selected glaciers. Furthermore, for soft beds, shear stress combined with water pressure may cause the overshoot of the yield strength of the soft sediment

bed, which can significantly accelerate the glacier slip and thus favour frictional feedbacks (Benn et al., 2019a, 2023; Cuffey and Paterson, 2010, p530).

As an example, Gao et al. (2024) interpret that the trigger of Kyagar glacier (Karakoram) is hydraulically-driven, and that the shear stress, in addition to creating unstable conditions for the glacier such as lower drainage efficiency, opened crevasses and increased basal water input, thereby increasing basal water pressure. On this glacier which we also analyse, we distinguish a clear driving stress accumulation on a large area (Fig. B.23 in Appendix). We could not classify it in the *spatially constrained* class due to surge timing, but Round et al. (2017) report a gradual velocity increase a few years before, which may be the actual onset of the instability.

As shear stress and effective pressure are related in the trigger mechanism, we cannot untangle their respective contribution with our data. Thus, we could only classify surge events as *hydraulically-driven* those that showed no significant change in driving stress until the onset of the surge. However, we expect that hydrology is an important driver of the dynamics of a large number of these surges, as several dynamics highlight the sensitivity to drainage efficiency. We can notice that i) several surge events are divided in marked peaks modulated by seasonal variations, ii) a large number of them (e.g., Khurdopin or Bivachny; Fig. B.7 and B.6 in Appendix) show a uniform and very fast termination at the end, and finally iii) a few events show abrupt accelerations following a long gradual acceleration (e.g., RGI2000-v7.0-G-13-05679-secondaryBranch or Khurdopin; Fig. B.25, B.7 in Appendix). In addition, different mechanisms have been shown to coexist and interact, in a continuous range of combinations (Thøgersen et al., 2024; Benn et al., 2019a, 2023).
Several typical case studies illustrate such complex behaviours. For example, the last Morsnevbreen (Svalbard) surge started with gradual acceleration over several years, likely with a thermodynamical feedback, until summer 2015 when velocity suddenly increased (Benn et al., 2019b). The authors note that it coincides with a period of warm temperatures and frequent heavy rain events, and they also observe peaks during summer in the following years. The driving stress they compute shows a pre-surge stress increase at the top of the receiving area, although only the end of quiescence is captured, but does not show the pattern that we observe for the *spatially constrained* class except for the 20-30 kPa stress drop they estimate during the surge. Also, such a velocity increase pattern complexifies the dating of surge onset, and in such situation, we could likely have dated a surge onset after the thermal feedback initiation (e.g., possibly the Kyagar glacier discussed before; Fig. B.23 in Appendix). Other examples, particularly in Svalbard, show the gradual onset of surge events with a thermal feedback, until the hydraulic mechanism radically changes the surge dynamics due to the entry of water into crevasses (Sevestre et al., 2018). We can cite a last, broader example: the last surge events of Tunabreen glacier, Svalbard, shows well how hydrological events can *interfere* with the long-term dynamics and shorten the buildup period: Benn et al. (2023) note a surge of this glacier about 12 years after the previous one, out of the 40-year periods previously estimated. The recent surge may have been triggered by an extreme rain event, which likely drastically reduced the effective pressure.

Other studies estimate the evolution of shear stress during surge cycles, such as Beaud et al. (2022), Burgess et al. (2012) or Gao et al. (2024), but only at a few dates. In particular, the pattern of stress change in this study fits relatively well these of Gao et al. (2024) on Kyagar glacier, although there are differences in the position on the glacier and in the shear stress values. Burgess et al. (2012) and Beaud et al. (2022) conclude that hydrological events triggered the surges of the glaciers they study; the latter in particular

argue that the variation of effective pressure must be more significant than high values of driving stress to trigger a surge.
Interestingly, Burgess et al. (2012) observe that the driving stress on Bering glacier (Alaska) shows two high friction points that keep or accumulate high stress after a first surge step or peak, which may cause a shift in the dynamic balance line and trigger a second and final surge peak. A similar mechanism may occur for Bivachny glacier in our study, for which the front of the first surge peak stops at a valley junction at 21 km and accumulate driving stress right above (Fig. B.6 in Appendix). A second stage of the surge seems to initiate over a wider extent and travel down to Fedchenko glacier.

3.4.2.2 Estimation of the onset date

One of the major obstacles we face is the difficulty in estimating the precise date of the surge onset. We have chosen to rely on velocity patterns, but elevation change time series sometimes show mass transfers not or partially discernible on velocities for surge events possibly starting with a gradual velocity increase (e.g., glacier RGI2000-v7.0-G-13-15921, 14-18361 etc.; see Fig. B.26 and B.33 in Appendix). This is supported by the recent global inventory from Guillet et al. (2025): in all regions, the velocity generally increases slowly several years before the peak surge velocity (up to about 10% of the maximum velocity) before an exponential increase from about 500 days before the peak velocity.
Our difficulty is particularly critical before 2013 with ITS_LIVE dataset: the poor quality of this dataset before 2013 due to the limitation of available satellites strongly limits the dating of these surge onsets (Gardner et al., 2025). Thus, a number of surge events we analysed would benefit from a re-investigation with additional data or other indicators on surge onset. We emphasize that some investigated surge events could have shown convincing proofs of a trigger area and could have been classified in the *spatially constrained* class, due to an earlier date on surge onset. Sometimes, the elevation change analysis supports this, as it is the case for the surge of RGI2000-v7.0-G-14-13801 (Fig. 3.10.c, and in particular at 10.95 km on Fig. B.32 in Appendix). This issue may, for example, be solved by observing crevasse opening through radar coherence change due to surging activity with satellite SAR imagery. Several recent studies successfully demonstrated the ability of SAR remote sensing to detect the opening of crevasses or other surface changes related to surging activity. Both changes of radar coherence or backscatter have been shown to detect surge onset earlier than other methods, including surface velocities (Leclercq et al., 2021; Mannerfelt et al., 2025). Such an analysis, which is more detailed in the section Perspectives of this manuscript, may provide a better alternative than low-quality velocity time series.

Specifically for our study, the date of surge onset we consider may change the interpretation of a trigger area. For glacier RGI2000-v7.0-G-13-14196, the date of surge onset is hard to determine, although we consider the end-2015 (Fig. B.21 in Appendix). For this date, it is possible to define a trigger area from 7 to 8 km, or later and above 8 km. However, the surge instability may have initiated sooner and more gradually, between 6 to 7 km. This raises the broader question of what we want to observe. To illustrate this: consider the case of a surge that initiates with a gradual velocity increase over several years, for example with thermal feedback or year-to-year change of the hydraulic system, and then an abrupt velocity increase possibly due to large water input (e.g., as described previously for Morsnevbreen, Benn et al., 2019b). In this case, we can expect two trigger areas (with the definition we use in this analysis), overlapping or not; the first one may not be stable, or even defined precisely in time. This questioning is clear for RGI2000-v7.0-G-13-14196, which we thus define as *temporally ambiguous*, but we may have falsely analysed several other surge events, especially if the velocity time series are of bad quality. The

surge of glacier RGI2000-v7.0-G-13-05715 is a case where our onset interpretation can be debated, although we define a trigger area for its surge event. We can see both relatively high velocity and slight reservoir thinning (about -15 m change) during the few years before the date of onset we define (Fig. B.11 at 2.85 km in Appendix). Thus, our assumption or current understanding might often be simplistic; we may erroneously qualify as surge only the second phase for several events, or misplace the trigger area for which hydraulic forcing could occur at another place. The first trigger area (with a gradual onset) is the one that is the most interesting for this study, but however, which we are the most likely to miss.

3.4.2.3 Observations on the trigger areas

By analysing the different time series and in particular the driving stress, we could retrieve, or at least restrict, the area of initiation of 15 surge events. They occur at variable locations on the glacier, but are generally overlapping with the dynamic balance line. The surge often propagates in the flow direction from the bottom of the trigger area, but we see only occasionally up-glacier propagation from this point (e.g., for Khurdopin glacier Fig. 3.8.a). If trigger areas are correctly estimated, this would imply that some of the up-glacier propagation is much faster than what is visible on our velocity dataset and travels large distances (e.g., glacier RGI2000-v7.0-G-14-21580 on Fig. B.17 in Appendix). In Svalbard, Mannerfelt et al. (2025) observed, with SAR data, that, overall, up-glacier propagation rates are nearly twice faster than down-glacier ones. The propagation analysis we conducted for down-glacier propagation should be applied to up-glacier ones, provided that there is a sufficiently temporal resolution to capture this propagation, which is not possible with our dataset.
For these 15 glaciers, the lengths of the estimated trigger areas range from 0.6 km to 3.5 km (median 1.5 km), 3% to 19% (median 11%) of the post-surge glacier length. Note that the relative characteristics depend on the centrelines that we have drawn, especially for tributaries and glaciers in glacier systems. These lengths represent an improvement compared to the analysis of velocity alone. Indeed, the size of the trigger areas is smaller than what we can interpret as the maximal trigger area on the velocity time series of other publications from the literature. For example, in Altena et al. (2019), the area is limited to below 15 km or 23% of the length of Klutlan glacier (Alaska), before propagation in both flow directions. It is below 2 km / 33% and 3 km / 38% for two unnamed glaciers in Qilian mountains (Guo et al., 2025), and 6 km / 35% of the length for Shisper glacier (Beaud et al., 2022; Bhambri et al., 2020). For South Rimo, it is below 7 km / 28% (Jiang et al., 2021); unfortunately, we cannot estimate the trigger area size of this glacier in our dataset due to the coverage of the elevation time series (Fig B.24 in Appendix). Burgess et al. (2012) estimate the trigger area of Bering glacier surge with a different definition (strongest acceleration, fastest velocities and largest change in driving stress): 10 km length or 6% of the large glacier, which is comparable to our results.

With our method, we may not be able to fully distinguish the trigger area, which may be smaller than what we estimate, in particular for surges mainly triggered by hydrological settings. Similarly, we may not be able to narrow the trigger area sufficiently. On the surge of Kunyang glacier, we define a very narrow trigger area (Fig. B.18 in Appendix). Our interpretation is that driving stress matches our expected behaviour only on a very narrow band. At and before 22.35 km, driving stress is slightly decreasing before the surge, which we believe to be due to the thickening occurring mainly downstream than upstream, decreasing the slope. Thus, the peak stress may have passed at this location without triggering the surge. Downstream, at 23.85 km, the peak occurs slightly after surge onset, and it is in a part where the driving stress shift from a increase trend to

a decrease trend propagates downstream along the surge front propagation, rather highlighting a consequence of the surge than a cause. Thus, in our interpretation, the surge should have been triggered in-between, and the time series at 22.95 km fits our criteria. Note that the elevation interpolation fits particularly well with the elevation observations here. Thus, we can expect that driving stress timings are correctly estimated, unlike, for example, RGI2000-v7.0-G-14-14871 at 25.95 km which smooths the elevation signal by at least a year, possibly more (Fig. B.37 in Appendix).

3.5 Conclusion

In this chapter, we combined two temporally-dense remote sensing datasets over HMA: elevation and surface velocity. These observations were analysed over several tens of glaciers, to evaluate the model from Thøgersen et al. (2019, 2024).
First, we estimated the overall rate of surge front propagation for a large number of surge events. The analysis of joint propagation rates and monthly surface velocities shows a relationship between these two variables. The results support the existence of a velocity-weakening regime during surge propagation, as theorised by Thøgersen et al. (2019). In addition, it suggests the existence of two main bed types or properties in HMA, even though we could not unambiguously relate them to hard or soft bed types.
Second, we analysed the driving stress of a similar number of glaciers as a proxy for shear stress. The observation of monthly changes shows that almost all surge events are preceded by a long-term increase in shear stress. Two surge events are exceptions, and we interpret their trigger mechanism as hydraulically driven. We managed to identify, or at least restrict, a trigger area for 15 surge events. The interpretation of the data is sometimes subjective and challenged by large uncertainties, which highlight the complex dynamics and diversity of surge events. In particular, several surge events show a gradual velocity increase, which hinders our interpretation by complicating the estimation of the trigger date and location.
Further analysis on our data could be done, such as comparing the size of the trigger area with the velocity to evaluate the formulation in Thøgersen et al. (2019). Some challenges persist, such as the determination of precise surge onsets, especially for surge events with mixed mechanisms and dynamics, or the use of more realistic thickness estimates for absolute driving stress analysis.
This chapter is still a preliminary analysis and does not fully exploit the potential of this dataset. Further work and perspectives are detailed in the main conclusion of this thesis.

Conclusions and perspectives

Synthesis of the results

The goal of this work was to observe the dynamics of glacier surges in High Mountain Asia from satellite remote sensing observations. In this manuscript, I addressed two scientific questions.

What surge dynamics can we observe from temporally dense time series of elevation?

The answer to this question required significant methodological and computational development addressed in Chapter 2. The existing dataset suitable for achieving our objectives consists of digital elevation models (DEMs) from the ASTER satellite sensor, which have large noise and data gaps. Reaching a consistent dataset that can describe glacier changes on intervals of a few months required several steps of processing to filter and interpolate the elevation time series. The workflow we developed focuses on two key methods. First, most of the filtering is performed by the linear non-parametric algorithm *Locally Weighted Regression and Smoothing Scatterplots* (LOWESS). Second, the interpolation is performed with the *Approximation by Localized Penalized Splines* (ALPS) algorithm. The LOWESS algorithm and the threshold developed require tuning, which is relatively dependent on the data, and in particular, their quality. However, the overall workflow is adaptable to other datasets with mostly minor parameter changes, including for multi-sensor sources.
Despite being perfectible and sensitive to defects in input time series, the workflow marks an improvement over the existing methodologies. The dataset produced shows good agreement with reference data and studies in most cases.
This dataset is the first of its kind to cover such a large study area and allows systematic analysis of dynamic elevation-change patterns during surge cycles in High Mountain Asia. Before surge events, the build-up pattern is generally marked, and the time series represents varying patterns such as extension or propagation of the build-up area. During surge events, the downstream displacement of the dynamic balance line appears as a relatively common feature, which was previously largely unnoticed, and in particular not captured by velocity datasets. However, the propagation of the surge front remains more accurately captured in velocity datasets. Several surge propagation in the up-glacier direction are visible; they are less visible and propagate at higher rates than in the down-glacier direction. The variations of mass along the surge period in the reservoir and receiving areas of the surge can be computed over short time intervals.
This work focused on the development of the workflow, rather than on the interpretation and valorisation of this dataset. We plan to distribute the output dataset publicly, and we hope that the community will further explore the potential of such an elevation dataset. This dataset is unique due to its regional coverage of analysis-ready data, which is suitable for the study of surge events.

To what extent can we test existing models of surge initiation and propagation with remote sensing data?

Surface velocity and elevation measurements from satellite remote sensing data offer different perspectives to analyse single surge events (Chapter 3). For the first time, we provide observations, on a large sample of glaciers, of two important surge features.
First, we estimate the rate of surge front propagation from surface velocities at timescales of several months or years. We evaluated the relationship between this propagation rate and the surface flow velocity. Surge events cluster around roughly factors of 2 or 7 between surface flow velocity and propagation rate, which could be explained by differences in the type and geometries of the glacier bed, as proposed by recent studies (Thøgersen et al., 2019, 2024). In light of the recent theoretical formulation of surge propagation, our analysis supports the existence of a velocity-weakening friction law during surge events.
Second, we calculate driving stress time series on a monthly scale. The time series highlight the importance of shear stress increase in the trigger process for the vast majority of surge events. However, driving stress series are complicated to interpret because of the complex interplay of surge mechanisms. We successfully estimate the area of the surge trigger (i.e., the area where the surge has not propagated yet and where we could identify a shear stress rise across a threshold at surge onset, followed by a sharp drop by the termination) for 15 surge events. Our results highlight variable lengths of this trigger area, which are below one kilometre long on four surge events, and they generally overlap the dynamic balance line at initiation. A large number of surge events have data of insufficient quality, in particular to estimate the onset date, and two glaciers are more likely to be purely hydraulically driven. This analysis remains preliminary at this stage. These two analyses highlight the complex and multi-factor mechanisms of surge events, especially in HMA. However, it demonstrates that remote sensing offers promising perspectives for assessing, on a large number of glaciers, a possible surge propagation mechanism based on rate-weakening friction and other mechanisms.

Perspectives

The work presented in this thesis raises a number of perspectives, whether methodological improvements or research-related.

Methodological perspectives

A large part of my contribution is rather methodological, with newly developed processing and methods that could be improved. Although this process can never end, some short-term and possibly easy-to-achieve improvements are worth presenting. In the order the topics appear in the manuscript, here is a short list of these opportunities.

▷ More DEMs

One of the first improvements that can be implemented is to include other dataset into the processing of elevation change time series. In Chapter 2, we used data from other satellite missions or products (SPOT5 HRS: 2002-2015, SPOT6-7: 2012-present and HMA DEM: 2002-2016) to validate our interpolated time series. Along with previous altimetry missions such as Cryosat-2, data from these sparse datasets can be included in the processing. In particular, it may be interesting to explore the potential of the Spot World Heritage images (SPOT1-5), covering 1986-2015 (Nosavan et al., 2018). Except for SPOT-5, their suitability should be confirmed, especially as they require across-track DEM generation (Toutin and Cheng, 2002). Data from existing or future commercial satellites can also be integrated (e.g., Pleiades, WorldView, CO3D), but they are hardly generalisable due to

their cost and tasking mode. The Pléiades Glacier Observatory is a great initiative in this way, but the 5-year revisit and the limited coverage (e.g., in HMA, Yazghil glacier, possibly others we studied such as Khurdopin, Medvezhiy, etc., depending on polygon areas) make it poorly adapted to this use (Berthier et al., 2024b). This program provides systematic, very-high resolution imagery from sub-meter stereoscopic Pléiades satellites and associated DEMs on 140 glacierized areas around the globe.
One of the most important challenges to add other sources of data is probably assigning a representative and homogeneous uncertainty to each observation from different sources. DEMs from optical stereoscopic imagery might follow the same uncertainty assessment as the ASTER data of our work, as a function of slope and the quality of stereo-correlation based on elevation differences on stable terrain (Hugonnet et al., 2021). However, the filtering part of the workflow, which exploits these uncertainties, is not particularly sensitive to the uncertainty of each observation.
Including data from other satellite sensors will however not be enough to continue such dense time series after the end of the ASTER mission. This sensor, which has survived several problems over the past 25 years, will likely disappear in 2026 or 2027 without a successor or alternative (Berthier et al., 2024a).

▷ Improvement of the elevation workflow

Our filtering and interpolation can be improved, and other algorithms may outperform the workflow of elevation time series processing that we developed. In Chapter 2 we discussed a problem of spurious and short-timescale interpolation problem of ALPS-REML (e.g., Fig. 2.6, 2.8.a). Detecting the temporal clustering of elevation observations in time series causing this problem and aggregating them with a suitable uncertainty could, however, be relatively straightforward and would largely benefit the quality of the time series. Further development of the ALPS algorithm would be beneficial in greater respects but more complex to implement.
However, it is probable that no or few interpolation algorithms are able to fill temporal gaps of one or several years of elevation measurements during surge events. One method to attempt overcoming this problem would be to rely on velocity time series to ponder the interpolation and force breakpoints of elevation change trends in more restricted time frames. A few studies automatically detect changepoints in surge elevation time series, and use both elevation and velocity time series, although not in such a way (Guillet et al., 2025; Li et al., 2023). Nevertheless, such a velocity-informed method would certainly be rather complex to develop and require intense processing at large scale.

▷ Better thickness estimates

The lack of reliable glacier thickness estimates is an important limitation to our driving stress analysis. It prevents reliable estimates of basal shear stress and the analysis of trigger thresholds of some surge events.
The recent study of Morin et al. (2023) is, however, very promising for such an application. Their rationale is to benefit from the surging activity to better retrieve glacier thickness. This is made possible by the fact that the slip-dominated flow regime of surge events better reflects the bed topography than mixed or deformation-dominated regimes (Hilmar Gudmundsson et al., 2003; De Paoli and Flowers, 2009; Roush et al., 2003). One can take advantage of our unique monthly elevation and velocity dataset to estimate the thickness along glacier centrelines. Other models, such as Instructed Glacier Model (IGM) or pure full-Stokes simulations, could make possible the estimate of thickness with such data (Jouvet and Cordonnier, 2023; Jouvet, 2023). However, there is a lack of *in situ* thickness measurements to validate these thickness estimates, in particular for surging glaciers.

▷ Estimation of surge onset

One major challenge of our analysis of driving stress in Chapter 3 is the difficulty in accurately estimating the date of surge onset. Several recent studies successfully demonstrated the ability of SAR remote sensing to detect the opening of crevasses or other surface changes related to surging activity (Guillet et al., 2025; Kääb et al., 2023; Leclercq et al., 2021; Mannerfelt et al., 2025). Both changes of radar coherence or backscatter have been shown to detect surge onset earlier than other methods, including surface velocities (Leclercq et al., 2021; Mannerfelt et al., 2025).

Leclercq et al. (2021) demonstrated that the radar backscatter sometimes increases distinctly even before velocity changes become noticeable on some velocity data. This is especially relevant for long surges, as they rely on winter measurements and compare yearly backscatter. Additionally, Mannerfelt et al. (2025) proposed a different approach: the authors use the change of coherence between SAR images. They can track the propagation of the surge front, although they report coherence loss due to meteorological conditions. While the backscatter can increase directly due to the increase in surface roughness due to crevasse opening, the coherence loss from one image to another can represent phenomena as diverse as important surface displacement, including crevasse opening, or a change in reflective properties such as water content.

These methods offer promising complementary indications on surge onset. They both use Sentinel-1 satellite data, which does not cover the 2000-2013 period over which the onset dating is the most difficult for our study, hence the need to explore older sensors (i.e., Envisat or ERS-1/2 which, however, have a long revisit period). However, it may be important to consider whether crevasses can open under high basal stress before any surge trigger.

Finally, the possible inclusion of ASTER-based velocities into the ITS_LIVE product, which is currently undergoing a feasibility assessment, would improve the time series, especially before 2013 (Gardner et al., 2025).

Research perspectives

▷ Differences of volume transfer estimates in the reservoir and receiving areas: flaws in the methods or actual processes at play?

The Chapter 2 left unresolved the difference between volume transfer estimates from the reservoir and the receiving area. It is particularly high for Hispar glacier, while for other surge events we assessed, the difference is more within uncertainties and within the expected variability of the mass balance. It may be interesting to solidify this possible bias and further investigate the reasons, reasons which seem not related to the processing workflow in a first approximation.

The hypothesis of the impact of the opening of a crevasse field during surge events on the average surface elevation could be tested, as an order-of-magnitude reasoning indicates that the impact could be significant (section 2.6.3.1; Chudley et al. (2025)). Theoretical quantitative estimates are possible under a strong hypothesis on the crevasse depth. For a crevasse depth value, *in situ* drone measurements would be insightful although complex to obtain logistically. Instead, the analysis of data from lidar satellite altimetry has already proven to be able to retrieve crevasse density and depth. Although simple elevation profile analysis as implemented by Liu et al. (2014) is possible, a more complex photon point-cloud analysis as implemented by Herzfeld et al. (2021) on Negribreen glacier (Svalbard) during surge seems very promising for this analysis. For example, on a profile, Herzfeld et al. (2021) estimates against validation airborne altimetry crevasse spacings of about 50-60 m and depths of about 10 m. One could finally use high-resolution DEMs, such as those mesured on Muzgazi glacier close in time to a recent surge onset, to reduce the volume

transfer uncertainty (Jouberton et al., 2025).
An approach that spatialises the surface mass balance could also permit to differentiate the elevation surface change that is due to the glacier dynamics or due to the surface mass balance. This kind of analysis has been implemented using surface velocity and elevation change from remote sensing into a physical modelling (Kneib et al., 2024). *In situ* observations, in particular with accumulation measurements and meteorological records, can also be used to model the surface mass balance. Abramov glacier and Kyzylsu catchment (which includes Muzgazi glacier) are, or cover surge-type glaciers, with such measurements (Jouberton et al., 2025; Kronenberg et al., 2021).

▷ Estimation of accumulation and shear stress thresholds

Some surge events, such as those of Variegated glacier, have been shown to surge at a precise recurrent amount of accumulation in the reservoir, related to the increase in shear stress (Eisen et al., 2001). Such dynamic behaviour shows that a variable but certainly significant share of variability in surge interval time depends directly on the climate variations. In our study, several glaciers show at least two surge events, but only a couple of them permit us to confirm that the amount of driving stress at surge onset is similar, and no change in the cycle duration with cumulated accumulation and climate can be estimated. It would also be interesting to relate the volume transferred to the cumulative accumulation, especially for recent surges that appear limited in magnitude compared to older records. The data quality and the portion of the cycle captured do not permit such scientific investigation in more detail, with only one full quiescent phase captured by elevation data for each of these glaciers.
First, a first-order analysis should be possible with the processing of the last years of life of the ASTER sensor, in particular if a higher DEM quality is reached, and with the addition of other DEM sources to fill large data gaps. Second, recent ASTER imagery could be complemented and validated by very-high resolution DEMs. For example, Jouberton et al. (2025) acquired several DEMs seemingly very close in time to a recent surge onset of Muzgazi glacier. We estimated the trigger area of the large 2009-2011 surge of this glacier. Analysing the 2023 surge, which seems to be of a much smaller magnitude, may be interesting to assess the accumulation and trigger context. Finally, historical imagery from declassified reconnaissance satellite images would allow us to generate DEMs over the 1960s and 1970s (Bhattacharya et al., 2021; Dehecq et al., 2020; Goerlich et al., 2017). Depending on the potential of the Spot World Heritage images (SPOT1-5) presented previously, the temporal gap could then be partially filled from about 1986 (Nosavan et al., 2018; Toutin and Cheng, 2002). With such data, one could thus compare shear stress with the recent surge events captured in the current work. However, the low number of dates would hinder the analysis and make it difficult to estimate the surge onset and termination.

▷ Improvement of the propagation rate analysis of the surge front

Our study on surge front propagation can be extended and improved along three main axes. First, our analysis should be extended to up-glacier propagation of surge instabilities. On our data, up-glacier propagations are faster than down-glacier propagation and travel large distances. On mostly marine-terminating glaciers in Svalbard, Mannerfelt et al. (2025) observed, with SAR data, that, overall, up-glacier propagation rates are nearly twice as fast as down-glacier ones.
Second, this should be facilitated by the improvement of our velocity dataset: one of its limitations is the inability to resolve very fast or sub-seasonal surge front propagations. Very fast propagation requires improvements in temporal resolution. More testing should be done in this way with the current dataset after 2013 and TICOI processing. Furthermore, it may also permit better distinguishing fast-propagation phases from simultaneous

accelerations and narrow down possible trigger areas.
Third and finally, the low number of high-velocity surge events is a gap in our surge database (above 1000 m year^{-1} flow velocity behind the surge front), which can be filled by adding surges in other regions worldwide. The recent inventory from Guillet et al. (2025) shows that HMA surge events tend to have slower surge peak velocities than those of the other clusters (Svalbard-Russian Arctic and Alaska-Yukon).
Examples of algorithms for detecting the onset of surge or speedup events also open new possibilities to automate the process (Guillet et al., 2025; Li et al., 2023; Nanni et al., 2023)

▷ Investigation on properties of surge-type glacier beds
The possible existence of two different types of subglacial bed under the glacier we selected for the propagation analysis is one of the main results from Chapter 3. The characteristic length d_c for a soft bed may depend on several parameters of the till. All the more if confirmed by further investigation (in particular with better pre-2013 velocity data), this result shows the poor knowledge we have of surge-type glacier beds. Thus, the most informative research project may be to plan boreholes under estimated trigger areas of glaciers in each of the two clusters (Fig. 3.6). In addition to determining basal sediment thickness, different experimentation could be conducted to characterise parameters of d_c, such as pore-water pressure, till sampling and tests such as yield strength, porosity or permeability (e.g., Harrison et al., 2004). In addition, dye-tracing experiments could be conducted to assess the drainage efficiency (e.g., Kamb et al., 1985). Such important field work would be the opportunity for other measurements, such as ground-penetrating radar to estimate the glacier thickness.

▷ Detailed and glacier-scale modelling of the theory from Thøgersen et al. (2024)
More progress should be made to test the rate-and-state theory of Thøgersen et al. (2024) on the model side. One or two surge-type glaciers should focus attention in our selection, as a detailed analysis of a large number of glaciers is demanding. Simulations should use their geometry and conditions (e.g., surface mass balance). With such a setting, comparisons or forcings including the rate of surge propagation, ice flow velocity, cycle duration etc. may be considered. On this work, Muzgazi glacier, for example, could be a suitable case study, with *in situ* measurements and high-resolution remote sensing data (Jouberton et al., 2025).

▷ Valuation of the elevation and velocity dataset for modelling purposes.
Finally, there is interest in further glaciological modelling, further than thickness estimates mentioned above. For example, one could use remote sensing datasets and the flux divergence principle to estimate distributed surface mass balances of surging glaciers (e.g., Kneib et al., 2024). One contribution to such an estimate is to untangle post-surge relaxation from surface mass balance, or from build-up caused by a high-frictional basal feature. In addition, and especially by dynamics modelling such as with the Instructed Glacier Model (IGM), one may also be able to untangle gradual acceleration from the glacier thickening and the increase of surface slope and gradual acceleration from a possible change of basal state caused by frictional feedback or other trigger mechanisms (Jouvet and Cordonnier, 2023; Jouvet, 2023).

Appendix A

Appendix - Chapter 2

A.1 Additional time series

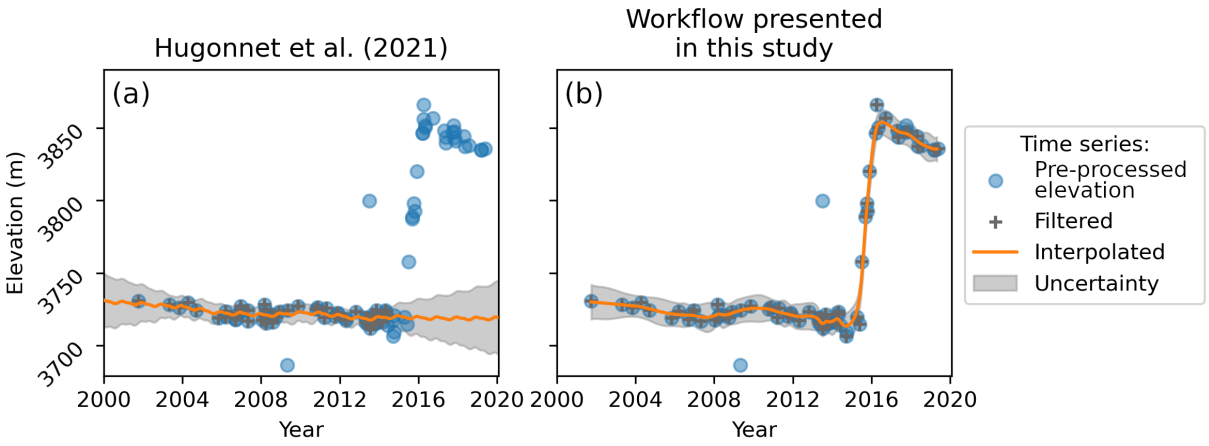

Figure A.1: a-b: additional time series complementing the figure Fig. 6, at coordinates (36.126, 75.158) over the Hispar glacier.

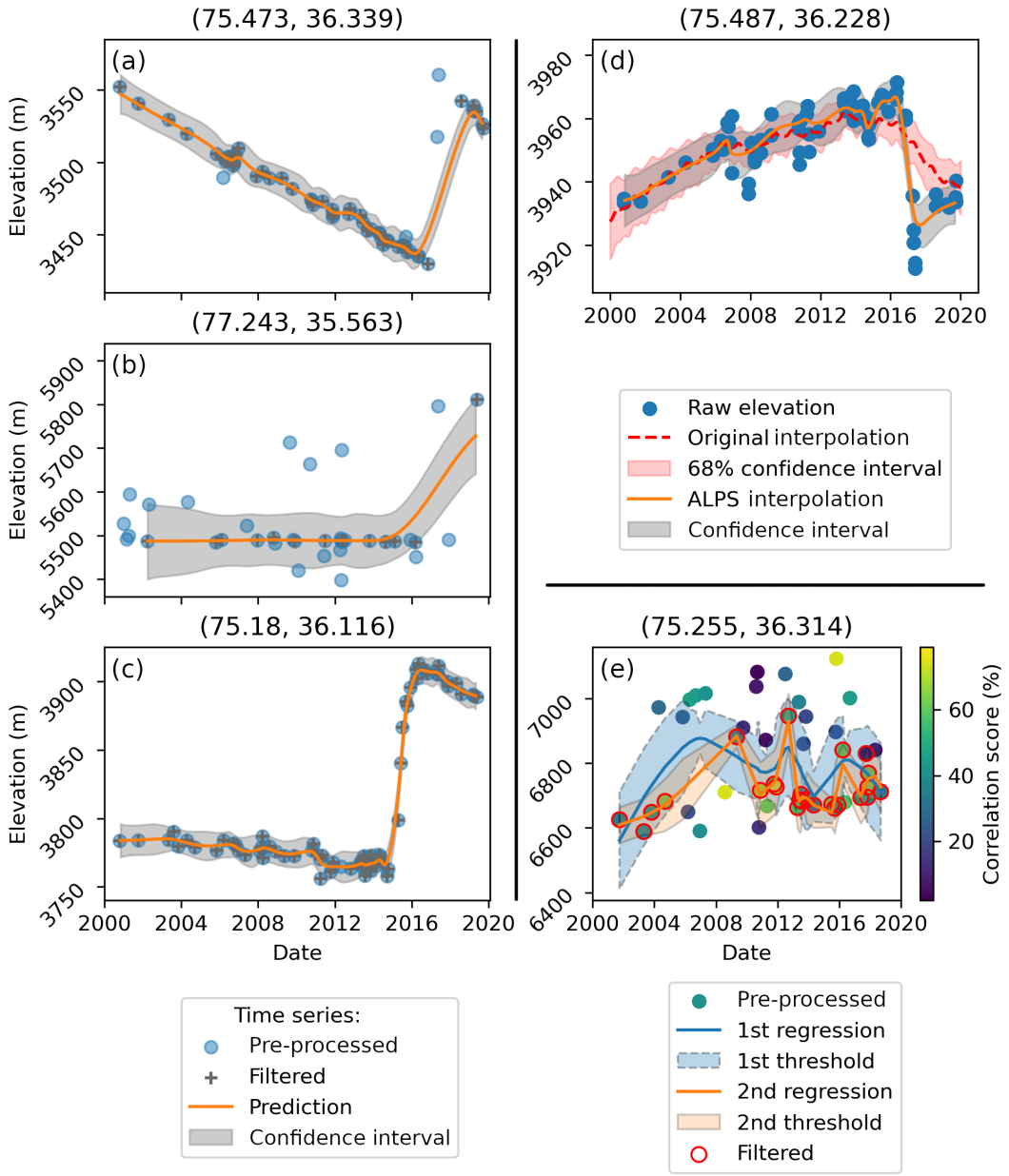

Figure A.2: Additional time series. Panels a-c show more examples of ALPS-REML interpolation with distinct flaws. The panel d compares the interpolation results of Hugonnet et al. (2021) ("Original interpolation" and its 60% confidence interval) and this study ("ALPS interpolation" and its confidence t-interval). The panel e show the successive iteration of the LOWESS regression, with points coloured by their correlation score. For this time series, the estimated elevation error (which is used to weight the LOWESS algorithm) is very close to the opposite of the correlation score, in relative.

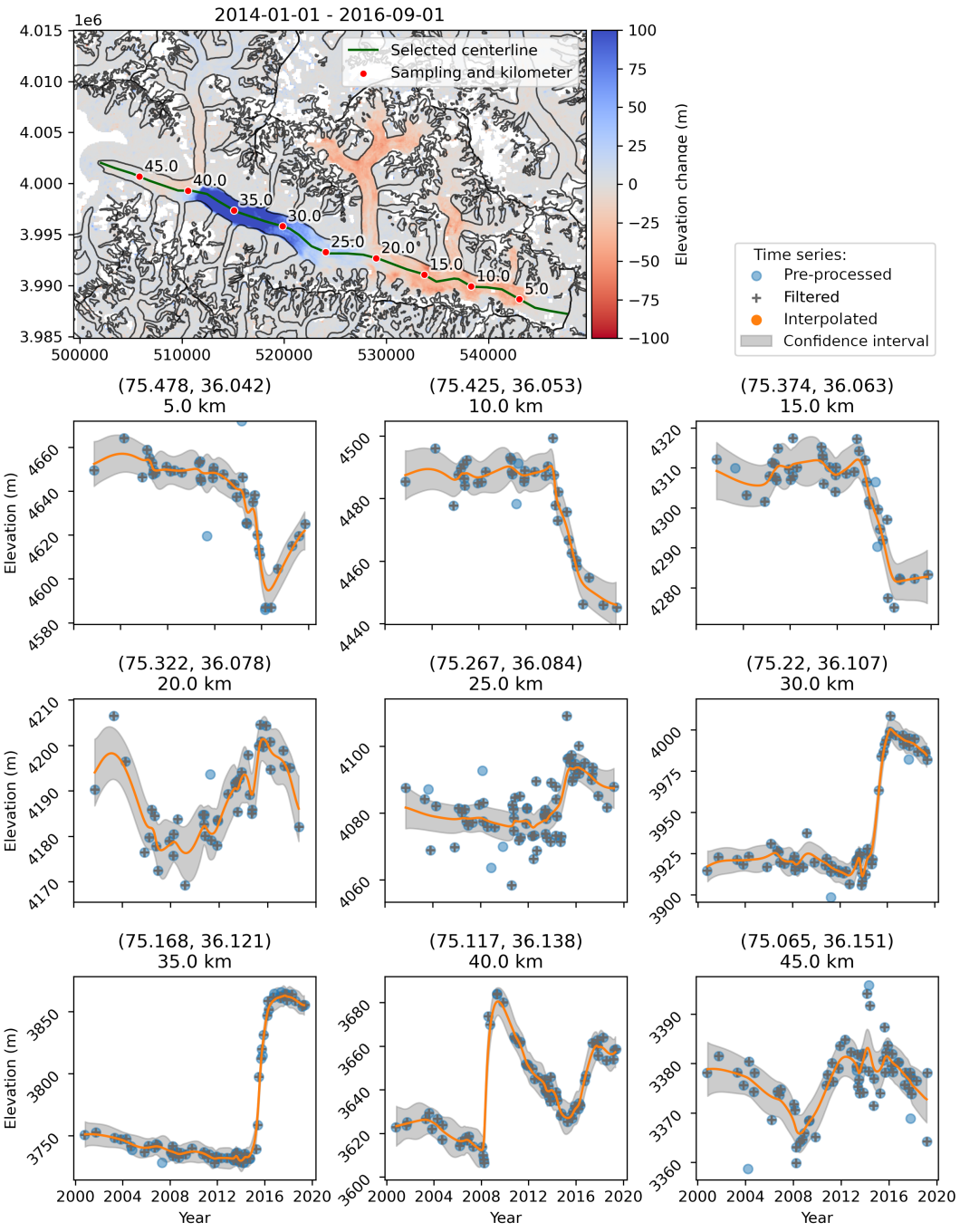

Figure A.3: Additional elevation time series for Hispar glacier sampled regularly along the selected centerline. The map shows the sampling and the elevation change over the estimated surge period. The coordinate reference system of the map ticks is UTM 43N (EPSG:32643), and points coordinates in the title of time series are in WGS84 (EPSG:4326).

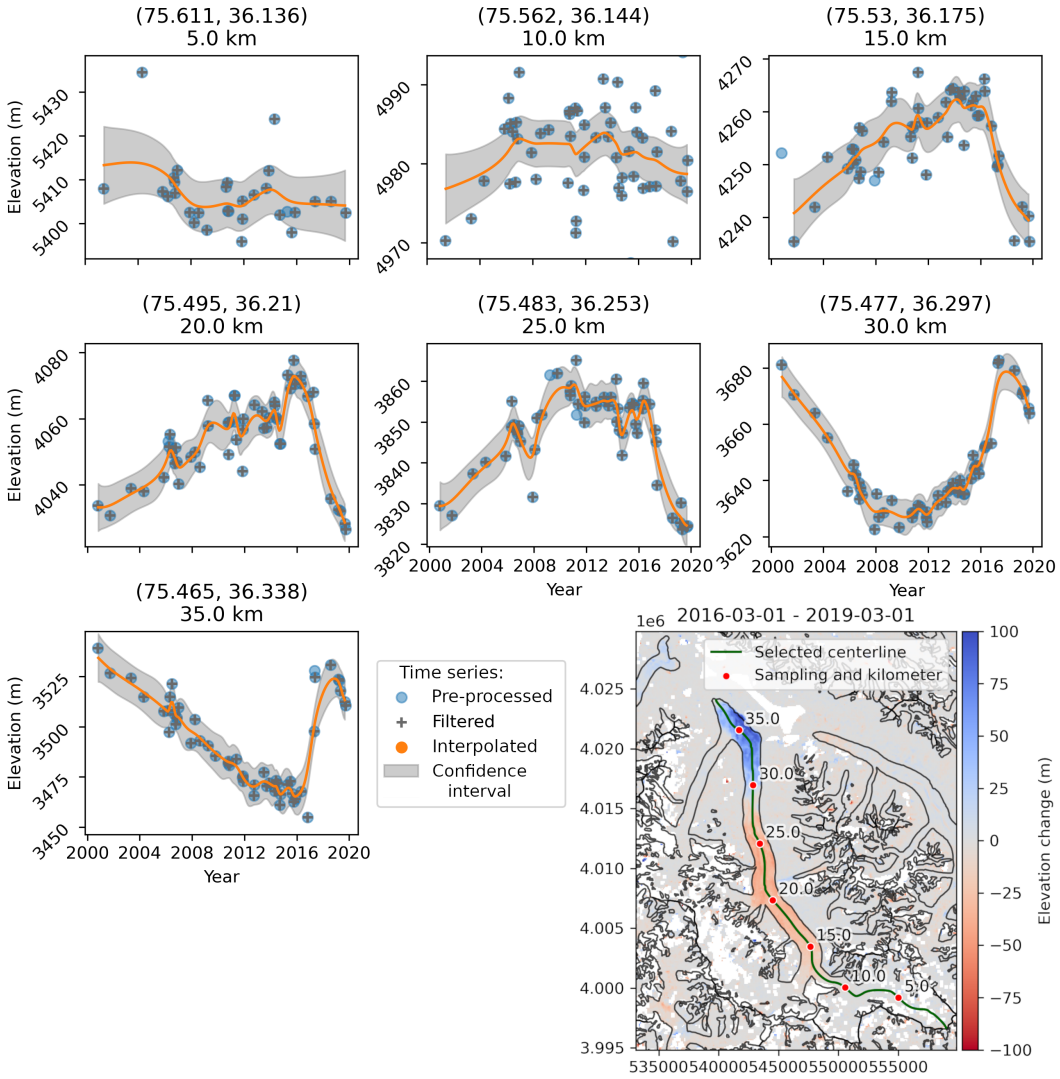

Figure A.4: Additional elevation time series for Khurdopin glacier sampled regularly along the selected centerline. The map shows the sampling and the elevation change over the estimated surge period. The coordinate reference system of the map ticks is UTM 43N (EPSG:32643), and points coordinates in the title of time series are in WGS84 (EPSG:4326).

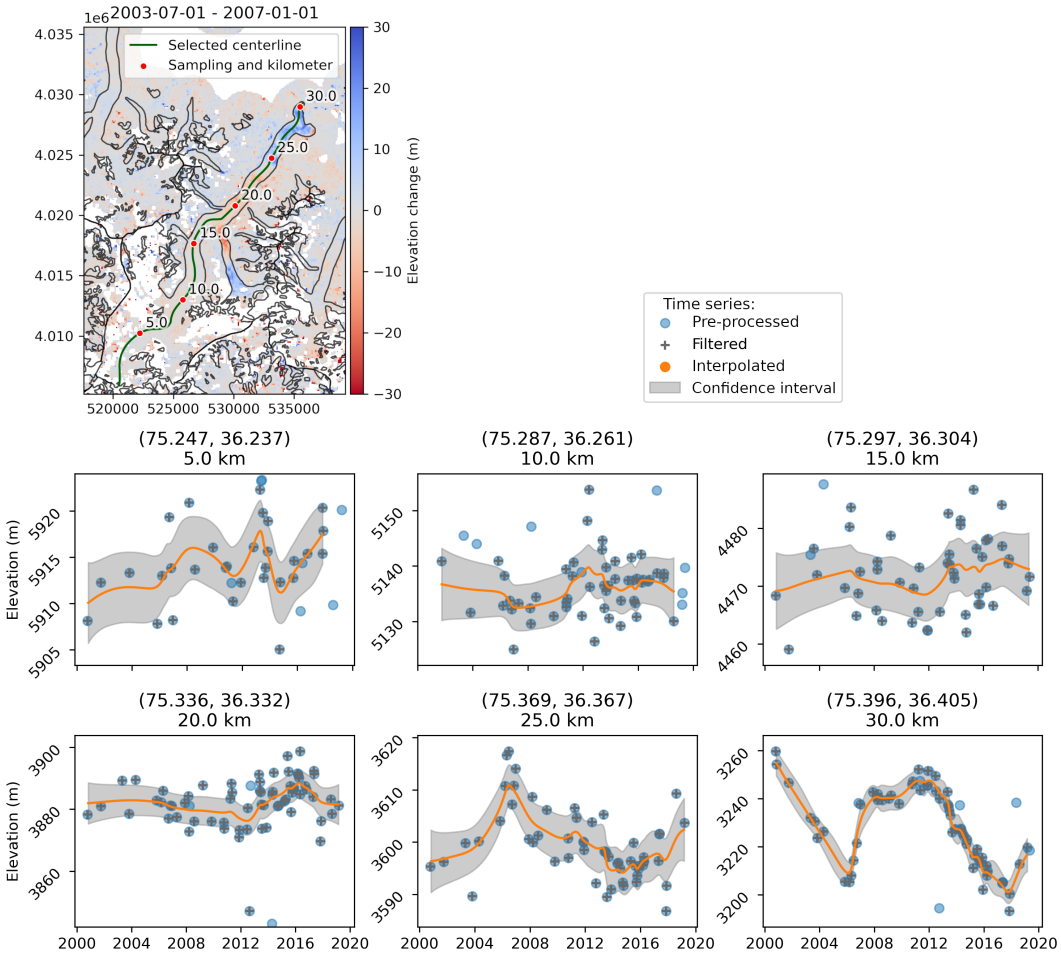

Figure A.5: Additional elevation time series for Yazghil glacier sampled regularly along the selected centerline. The map shows the sampling and the elevation change over the estimated surge period. The coordinate reference system of the map ticks is UTM 43N (EPSG:32643), and points coordinates in the title of time series are in WGS84 (EPSG:4326).

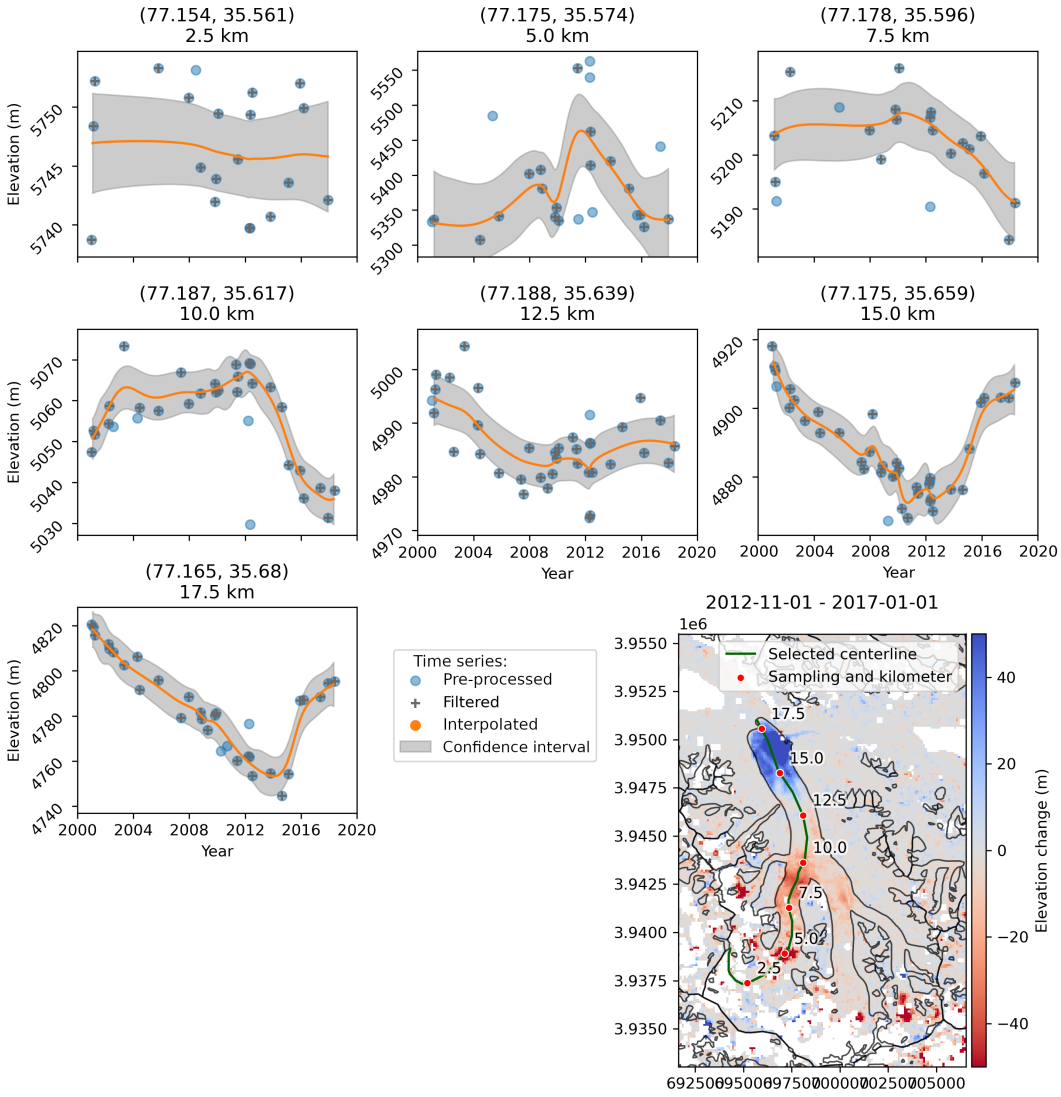

Figure A.6: Additional elevation time series for Kyagar glacier sampled regularly along the selected centerline. The map shows the sampling and the elevation change over the estimated surge period. The coordinate reference system of the map ticks is UTM 43N (EPSG:32643), and points coordinates in the title of time series are in WGS84 (EPSG:4326).

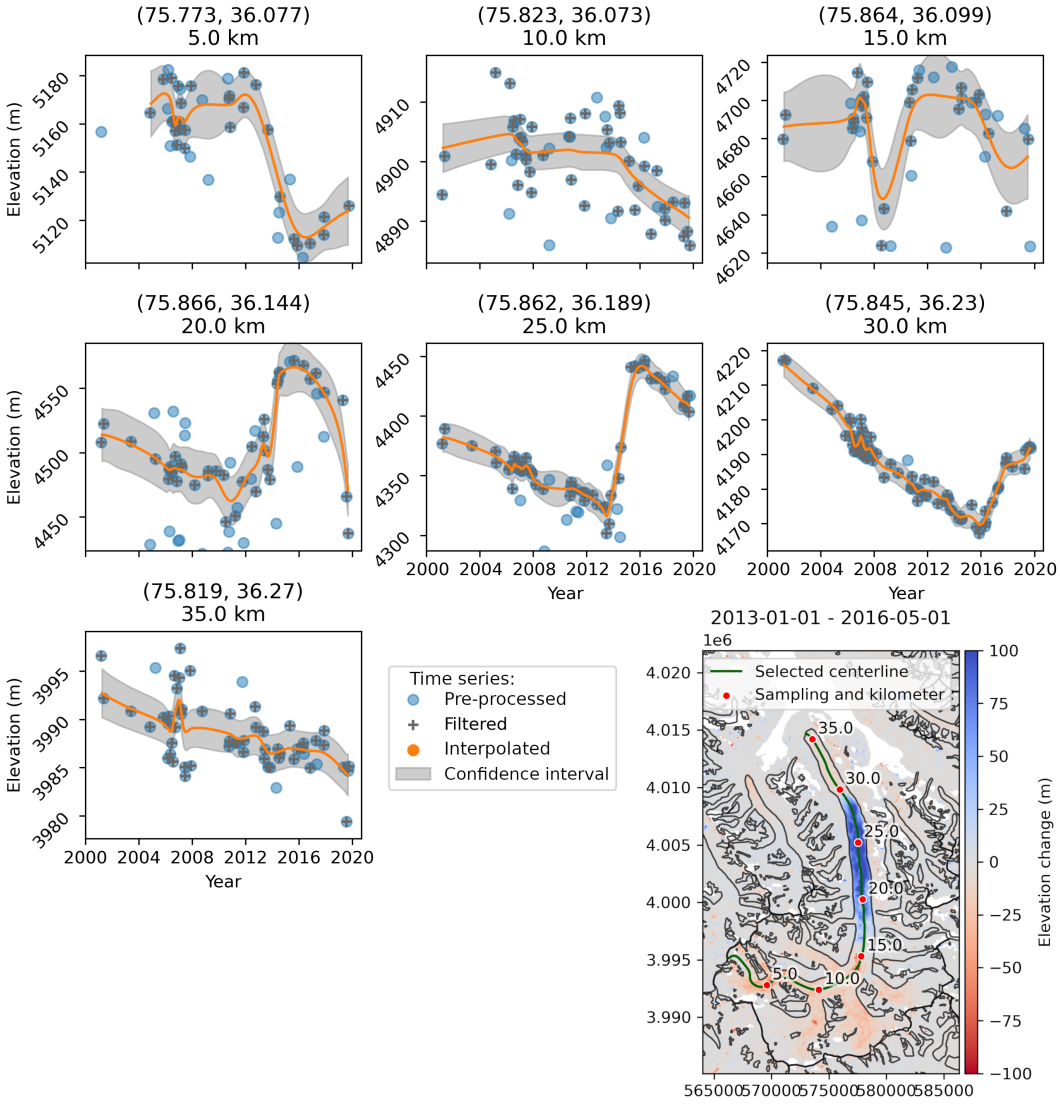

Figure A.7: Additional elevation time series for Braldu glacier sampled regularly along the selected centerline. The map shows the sampling and the elevation change over the estimated surge period. The coordinate reference system of the map ticks is UTM 43N (EPSG:32643), and points coordinates in the title of time series are in WGS84 (EPSG:4326).

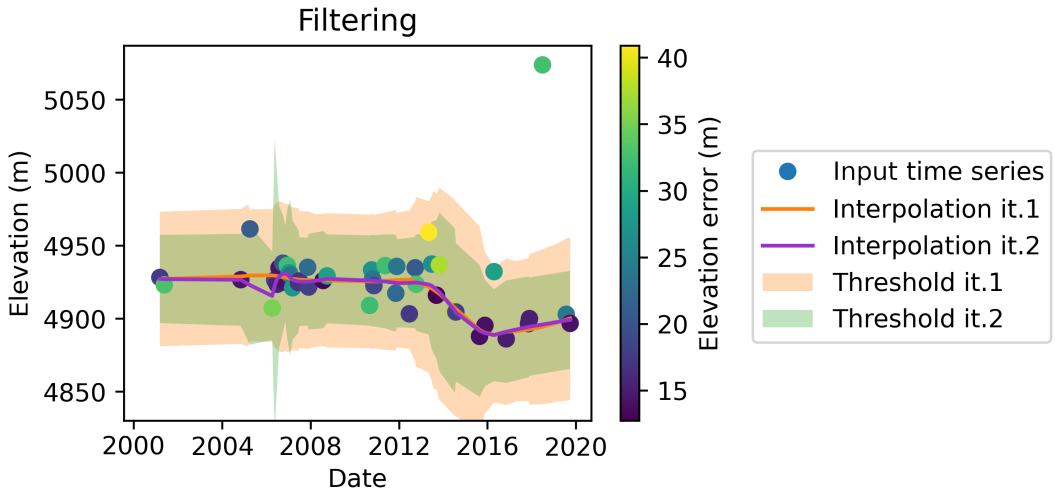

Figure A.8: Filtering of the time series from Fig. 3, coloured by the elevation error estimate. The weight of the LOWESS regression is *1/"elevation error"*.

A.2 Volume transferred on original ASTER data

Glacier RGI 7.0 code	Date start	Date end	Reservoir vol. change	Receiving vol. change	Imbalance
Hispar 21670	2014-01	2016-09	-1595 ± 376 x 10^6 m^3	1122 ± 169 x 10^6 m^3	-473 ± 412 x 10^6 m^3 -2.68 m
Yazghil 21865	2003-07	2007-01	-38 ± 30 x 10^6 m^3	34 ± 25 x 10^6 m^3	-4 ± 39 x 10^6 m^3 -0.29 ± 2.73 m
Khurdopin 14958	2016-03	2019-03	-585 ± 120 x 10^6 m^3	453 ± 60 x 10^6 m^3	-132 ± 134 x 10^6 m^3 -2.80 ± 2.82 m
Kyagar 14958	2012-11	2017-01	-191 ± 79 x 10^6 m^3	198 ± 45 x 10^6 m^3	8 ± 91 x 10^6 m^3 0.27 ± 3.09 m

Table A.1: Volume transferred of surges for the four selected glaciers this time according to the original interpolated ASTER dataset from Hugonnet et al. (2021), during the same period as in Table 1. For these glaciers, the percentage of data gap after the workflow presented in this study is ranging from 0 to 1.1% (median of 0.1%), and after bilinear interpolation it is of 0% for all of them. The prefix of RGI 7.0 codes is "RGI2000-v7.0-G-14-".

A.3 Elev. change and M.B. comparison

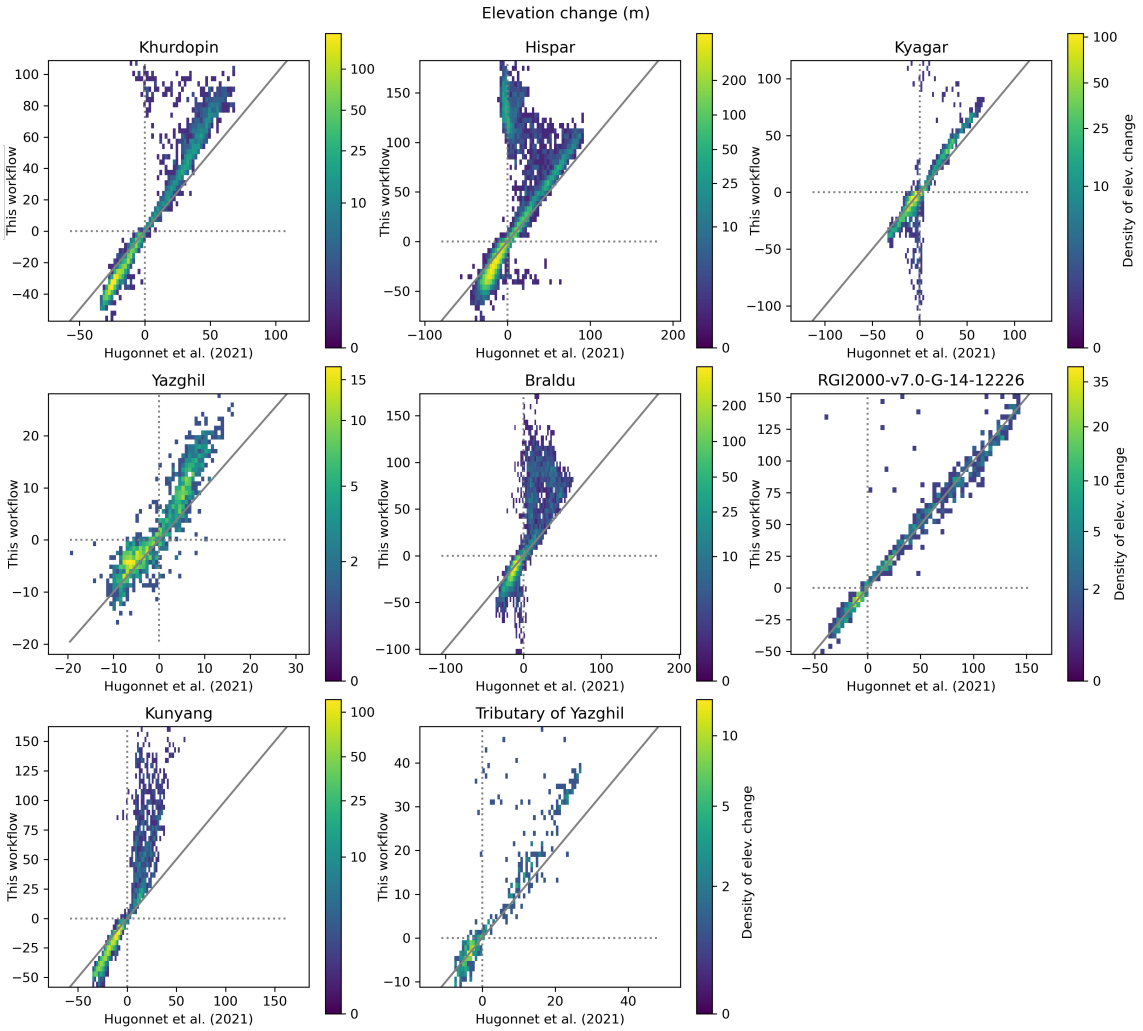

Figure A.9: Individual representation of Fig. 13, elevation change comparison histogram per surge. Each surge is the single one occurring during our study period on the glacier designated, except for Yazghil glacier for which the surge is the 2003-2007 one. Note that the reservoir area of the unnamed glacier (RGI code RGI2000-v7.0-G-14-12226) is captured over only a third of its extent here.

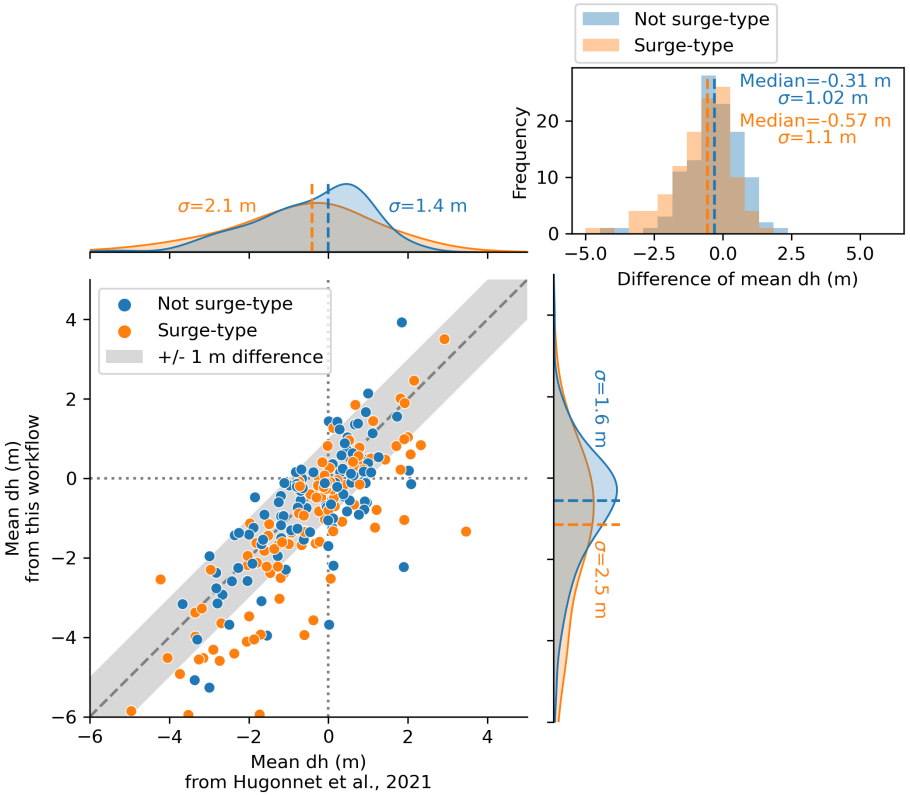

Figure A.10: Comparison of mean elevation change (dh in the figure) per glacier from 2005 to 2015, between the interpolated dataset of Hugonnet et al. (2021) and this workflow. It is calculated over the same valid pixels to avoid different data gaps. It represents 224 glaciers in the center of Karakoram, with 112 glaciers in each surge and non-surge type category. We extract surge-type glaciers from the inventories of Guillet et al. (2022) and Guo et al. (2022) (categories I and II during 2000-2020). The top right histogram represents the difference of mean dh between the two datasets. The dotted lines represent the median of the distributions. The sigma symbol represents the standard deviation.

A.4 Reference DEMs

Satellite	Acquisition date
SPOT5 HRS	2008-12-03
SPOT6	2015-11-28
	2015-10-13
HMADEM	2014-01-28
	2015-05-15
	2015-10-29

Table A.2: Dates of the reference DEMs used in the subsection 5.1 .

A.5 Spatial variogram

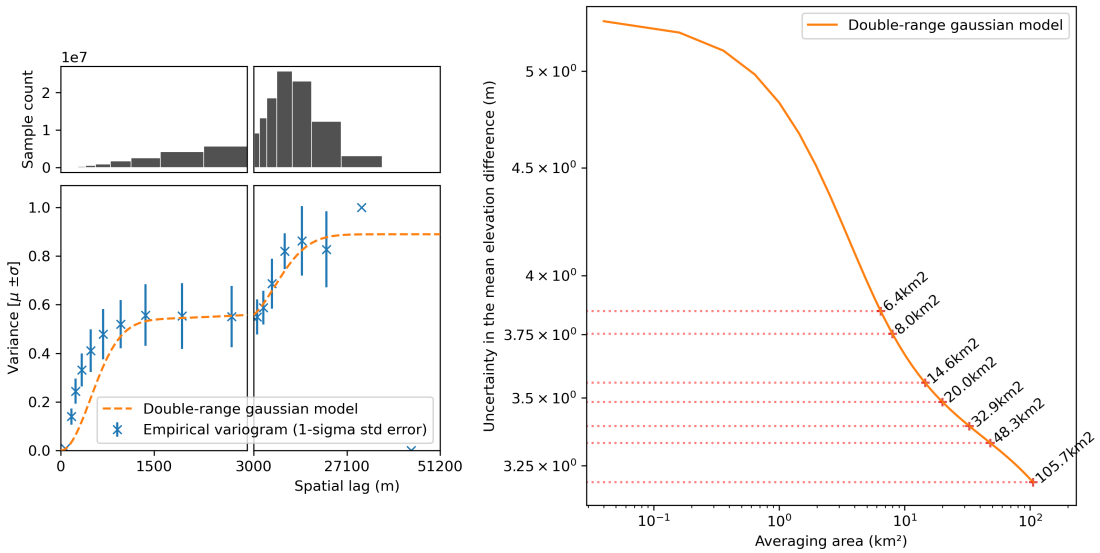

Figure A.11: Left: fit of the experimental variogram with a double-range Gaussian model (fitted ranges of 1.4 and 19 km). The variogram is computed as detailed in subsection 5.1. Right: mean elevation difference uncertainty estimated from the number of effective samples calculated from the model with the *xDEM* library. We indicate the area of each delineated zone used for the transferred volume estimated in Table 1

Appendix B

Appendix - Chapter 3

B.1 Inventory of glaciers and surge events

Lon	Lat	RGI7.0 code RGI2000-v7.0-G-	Glacier name	Region	Length (km)	Date of surge onset and termination	Type
72.14941	38.93291	13-16736	Bivachny	Western Pamir	30.3	2011-05 – 2014-08	Trib.
75.47533	36.28687	14-21665	Khurdopin	Karakoram	38.3	2016-04 – 2017-09	Main
71.49531	39.0785	13-19267	Muzgazi	Western Pamir	16.7	2009-11 – 2011-12	Main
71.30222	38.9737	13-05590	13-05590	Western Pamir	5.3	2013-09 – 2015-02	Main
71.9461	38.80286	13-05693	13-05693 tributary	Western Pamir	13.2	2013-08 – 2017-08	Trib.
71.92884	38.76501	13-05715	13-05715	Western Pamir	10.8	2015-06 – 2017-03	Main
75.19259	38.52247	13-14196	13-14196	Eastern Pamir	15.5	2005-09 – 2008-06, 2015-08 – 2018-04	Main
74.65116	39.22319	13-14589	13-14589	Eastern Pamir	7.7	2011-08 – 2015-09	Main
71.76386	39.2781	13-16672	13-16672	Western Pamir	5.3	2011-01 – 2012-10	Main
79.41637	36.17415	13-43964	13-43964	West. Kunlun Shan	10.9	2011-05 – 2013-10	Main
79.3338	36.16333	13-44005	13-44005	West. Kunlun Shan	5.8		Trib.
82.30647	35.60923	13-48698	13-48698	West. Kunlun Shan	10.3	2009-09 – 2015-05	Main
77.48292	35.33663	14-20250	South Rimo	Karakoram	24.5	2018-07 – 2020-04	Main
75.18215	36.11705	14-21670	Hispar - Yutmaru	Karakoram	46.5	2014-06 – 2016-07	Main
75.13022	36.17111	14-21670	Kunyang	Karakoram	29.9	2007-05 – 2009-09	Trib.
77.18473	35.64467	14-14958	Kyagar	Karakoram	18	2014-05 – 2016-09	Main
71.32121	38.97681	13-05593	13-05593	Western Pamir	10.1	2015-05 – 2016-12	Main
71.79601	38.88443	13-05679	13-05679 sec. br.	Western Pamir	20	2018-06 – 2021-09	Trib.
75.40629	38.53516	13-14195	13-14195	Eastern Pamir	18.2	<2000-01 – 2007-09, 2011-05 – >2020-01	Trib.
72.47116	38.86203	13-15921	13-15921	Western Pamir	10.9	2011-10 – 2014-08	Trib.
72.29478	38.45729	13-17029	13-17029	Western Pamir	11.5	2001-03 – 2005-08, 2011-08 – 2015-08	Trib.
75.08511	38.21091	13-18530	13-18530	Eastern Pamir	10.3	2012-03 – 2019-06	Main
71.38296	39.06048	13-19276	13-19276	Western Pamir	9.3	2011-10 – 2015-11	Trib.
79.0954	36.21248	13-44456	13-44456	West. Kunlun Shan	7.3	2012-02 – 2019-02	Main
80.51789	35.53881	13-47689	13-47689 branch1	West. Kunlun Shan	17.5	2010-07 – 2017-01	Main
82.19138	34.14248	13-59619	13-59619	Tibetan Interior M.	7.3	2011-08 – 2013-09	Main
74.04352	36.76846	14-07912	14-07912 / Chllinji	Karakoram	11.5	2006-01 - 2009-01, 2014-06 – 2016-08	Main
76.20462	36.18444	14-12280	14-12280	Karakoram	16.8	2009-08 – 2011-12	Main
77.52971	35.73105	14-13801	14-13801	Karakoram	17.7	2015-07 – 2019-08	Main
76.82175	35.74508	14-14871	14-14871	Karakoram	28.1	2009-10 – 2011-03	Main
77.92964	34.82314	14-18361	14-18361	Karakoram	27.5	2016-09 – 2018-09	Main
77.70482	34.94613	14-18427	14-18427	Karakoram	13.9	2010-04 – 2013-03	Main
77.72425	35.08699	14-18524	14-18524	Karakoram	14.3	2008-06 – 2010-04	Main
77.58267	35.29792	14-19567	14-19567	Karakoram	9.4	2010-09 – 2013-05	Main
76.46913	35.96343	14-20416	14-20416	Karakoram	21.2	2014-07 – 2019-08	Main
76.11696	36.08129	14-21580	14-21580	Karakoram	42	2011-07 – 2013-07	Main
75.24726	36.75436	14-23475	14-23475	Karakoram	7	2013-07 – 2018-02	Main
75.36736	36.36388	14-21865	Yazghil	Karakoram	30.5	2005-03 - 2011-09, 2018-03 – 2021-09	Main
75.855834	36.21771	14-21584	Braldu	Karakoram	35.8	2012-11 – 2015-08	Main
74.347481	38.64548	13-16779	Medvezhiy	Western Pamir	14.7	Approx. 2007 – 2012, 2013-03 – >2019-07	Main
71.768409	38.89989	13-05679	13-05679 main br.	Western Pamir	21	2009-09 – 2012-07	Trib.
91.525725	33.4425	13-66375	13-66375	Tanggula Shan	7.3	2009-07 – 2011-01	Main
75.958962	36.2765	14-12226	14-12226	Karakoram	18	2007-04 – 2013-07	Main
76.190104	36.19403	14-12286	14-12286	Karakoram	11.4	At least 2006 – 2013	Trib.
74.347481	39.30217	13-14677	13-14677	Eastern Pamir	9.6	2011-05 – 2012-12	Main
75.24499	38.69575	13-14183	Kelayayilake West	Eastern Pamir	22	2014-06 – 2015-08	Trib.

Table B.1: Inventory of glaciers and surge events studied in Chapter 3. Note that most of the values are indicative. In case of multiple surge events on one glacier during the study period, statistics are separated by a comma. The coordinate reference system of coordinates is WGS84 (EPSG:4326). "Trib." is tributary, "sec" is secondary. For tributary-type glacier, the length do not include the end of the main glacier, unless the surge event reaches it.

Glacier name	Length (km)	Upper reservoir (km)	Dynamic B.L. Position (km)	Lower receiving (km)	Amplitude of elev. change (m)	Med. surge vel. (m yr^{-1})	Med. quiesc. vel. (m yr^{-1})
Bivachny	30.3	4.9	13 to 22	30.3	-60 / 90	1780	40
Khurdopin	38.3	13.3	28	38.3	-35 / 100	2900	90
Muzgazi	16.7	1.6	5.8 to 9.7	15.1	-70 / 110	1410	20
13-05590	5.3	0.4	3.1	5.3	-60 / 130	460	30
13-05693 tributary	13.2	0.7	5.5 to 10.3	13.2	-30 / 100	510	60
13-05715	10.8	1.6	6.1 to 8.2	10.8	-50 / 120	630	50
13-14196	15.5	5.5	7.9 to 12.7	15.2	-30 / 50	560, 830	40
13-14589	7.7	2.5	3.4 to 4.6	5.9	/ 40		
13-16672	5.3	0	1.6 to 3.7	5.3	-40 / 50	140	20
13-43964	10.9	3.4	7.9 to 9.4	10.9	-40 / 140	310	40
13-44005	5.8	1.6	4.6 to 5.2	5.8	-30 / 70		
13-48698	10.3	3.4	7.6 to 9.4	10.3	-20 / 80	230	50
South Rimo	24.5			24		1200	50
Hispar - Yutmaru branch	46.5	3.7	14.8 to 19.3	37.6	-40 / 170	1750	80
Kunyang	29.9	7.3	20.2	29.5	-50 / 130	1200	30
Kyagar	18	2.8	13	18	-40 / 50	560	50
13-05593	10.1	1.7	5.8	10.1	-50 / 100	530	40
13-05679 sec. branch	20					740	50
13-14195	18.2	2.8, 2.8	10.6 to 13.6, 7.9	17.5, 13.7	/30 ,-10 / 25	210, 200	80
13-15921	10.9	1.6	6.5	10.3	-30 / 120	550	40
13-17029	11.5	4.3, 4.3	8.8	10.9, 10.9	-30 / 50, -30 / 50	550, 380	30
13-18530	10.3	5.8	8.2 to 9.7	10.3	-30 / 80	130	30
13-19276	9.3	0.4	2.8 to 3.4	5.6	-30 / 60		
13-44456	7.3	3.1	4.7 to 6.4	7.3	-50 / 100		
13-47689 branch1	17.5		11.5	17.5	/ 140	320	<70
13-59619	7.3	1.6	5.2	7.3	-40 / 160	390	20
14-07912 / Chllinji	11.5	4, 4	7.6, 8.5	, 11.5	-20 / 30, -25 / 40	, 240	, 30
14-12280	16.8	3.7	10.6 to 11.5	16.7	-80 / 170	880	10
14-13801	17.7		13.6		< -40 / >140	450	40
14-14871	28.1	16.6	21.4	28.1	-40 / 100	1260	20
14-18361	27.5	6.1	19.3	27.5	/ 110	450	<40
14-18427	13.9	1.6	7.9	13.9	-80 / 260	>750	30
14-18524	14.3		12.1	14.3	/80		
14-19567	9.4	2.5	7.3	9.4	-40 / 150	280	50
14-20416	21.2	3.6	10.0 to 13.0	19.7	<-30 / >70	270	<50
14-21580	42	5.5	19.6	28.9	-30 / 150	750	30
14-23475	7	3.1	4.6 to 5.8	7	< -30 / 90	150	50
Yazghil	30.5	19.0 / 18.0	24.1 / 23.2	30.5	-15 / 20, -15 / >20	220 / 200	100
Braldu	35.8	3.7	15	30.1	-70 / 120	1120	50
Medvezhiy	14.7	7.3 / 7.3	11.8 / 10 to 11.8	14.7 / >13.6	Approx -10 / 50	/ 160	
13-05679 main branch	21	3.4	9.4 to 13.0	16.6	-30 / 70	580	20
13-66375	7.3		4	6.5	/ 60	530	20
14-12226	18	0	10.6	17	-30 / 180	200	30
14-12286	11.4	3.1	7.6 to 10.6	11.4	-40 / 100		
13-14677	9.6	3.1	3.7 to >6.4	9.6	-60 / 40	360	30
Kelayayilake West	22	<8.2	13.3 to 18.1	21.1	-80 / 50	640	20 – 100

Table B.2: Continuation of the table B.1. "Dynamic B.L." is dynamic balance line, "elev." the elevation, "Med. [...] vel." the median velocity for the corresponding surge cycle step. The third and fith columns are the position of the upper limit of the reservoir area and the lower limit of the receiving area (i.e., which both delimitates the surge-affected area). Median velocities are computed by manually defining the area and period, which avoid propagation areas.

Glacier name	Region	Length (km)	Propagation rate (m yr^{-1})	Propagation cluster	Label for propagation	Driving stress pattern
Bivachny	Western Pamir	30.3	3903	I	#1	Spatially constrained
Khurdopin	Karakoram	38.3	8640	I	#5	Spatially constrained
Muzgazi	Western Pamir	16.7				Spatially constrained
13-05590	Western Pamir	5.3				Spatially constrained
13-05693 tributary	Western Pamir	13.2	1220	II	#10	Spatially constrained
13-05715	Western Pamir	10.8				Spatially constrained
13-14196	Eastern Pamir	15.5	2266, 1964	I & II	#12, #13	Temporally ambiguous
13-14589	Eastern Pamir	7.7				Spatially constrained
13-16672	Western Pamir	5.3				Spatially constrained
13-43964	West. Kunlun Shan	10.9				Spatially constrained
13-44005	West. Kunlun Shan	5.8				Temporally ambiguous
13-48698	West. Kunlun Shan	10.3	393	II	#18	Spatially constrained
South Rimo	Karakoram	24.5	3063 & 8248	I and other	#28	Temporally ambiguous
Hispar - Yutmaru branch	Karakoram	46.5	10604 & 1767	II and other	#3	Hydraulically-driven
Kunyang	Karakoram	29.9	1178 & 5390	I and II	#6	Spatially constrained
Kyagar	Karakoram	18				Temporally ambiguous
13-05593	Western Pamir	10.1				Spatially constrained
13-05679 sec. branch	Western Pamir	20	2686	I	#9	Temporally ambiguous
13-14195	Eastern Pamir	18.2	660	II	#11	Spatially constrained
13-15921	Western Pamir	10.9	964	II	#15	Temporally ambiguous
13-17029	Western Pamir	11.5	744, 816	II	#16, #17	
13-18530	Eastern Pamir	10.3				Temporally ambiguous
13-19276	Western Pamir	9.3				Temporally ambiguous
13-44456	West. Kunlun Shan	7.3				Temporally ambiguous
13-47689 branch1	West. Kunlun Shan	17.5				Temporally ambiguous
13-59619	Tibetan Interior M.	7.3				Temporally ambiguous
14-07912 / Chllinji	Karakoram	11.5				
14-12280	Karakoram	16.8	1326	II	#21	Spatially constrained
14-13801	Karakoram	17.7				Temporally ambiguous
14-14871	Karakoram	28.1	4058	I	#23	Temporally ambiguous
14-18361	Karakoram	27.5	4058	II	#24	Temporally ambiguous
14-18427	Karakoram	13.9				Temporally ambiguous
14-18524	Karakoram	14.3				Hydraulically-driven
14-19567	Karakoram	9.4				Temporally ambiguous
14-20416	Karakoram	21.2	655	II	#25	Temporally ambiguous
14-21580	Karakoram	42	2062	I	#26	Spatially constrained
14-23475	Karakoram	7	332	II	#27	Temporally ambiguous
Yazghil	Karakoram	30.5				
Braldu	Karakoram	35.8	3007	I	#2	
Medvezhiy	Western Pamir	14.7	573 & 363	II	#7	
13-05679 main branch	Western Pamir	21	1988	I	#8	
13-66375	Tanggula Shan	7.3	1571	II	#19	
14-12226	Karakoram	18	393	II	#20	
14-12286	Karakoram	11.4	337	II	#22	
13-14677	Eastern Pamir	9.6	2651	I	#14	
Kelayayilake West	Eastern Pamir	22	2095	I	#4	

Table B.3: Continuation of the table B.1 and B.2. The corresponding figures for the propagation analysis are Fig. B.2 (delineations) and Fig. 3.6 (results). The corresponding links to the figures of driving stress are in Table B.4

B.2 Cross correlation

We designed a third protocol (C) to delineate the surge front propagation. Our goal was to do this task automatically with signal processing methods, and in a more constant way that human interpretation. For this, our choice was to use a cross-correlation algorithm on the surge signal at two different distance along the surge centerline, and retrieve the time delay between the two surge peaks. The principle of such algorithm is to correlate the pair of signals by applying a variable time shift, ensuring to find the time delay that ensure a best match which is the time travel of the surge front. For this, we use the *correlate* function from Python library *SciPy*.

To prepare the time series, we isolate the surge's first peak, normalize the signal, and then we complete the peak with the signal from the other time series inverted in time (symmetry in time) to preserve the peak shift and not produce symmetric peaks. The surge's peak is determined by finding the largest increase of surface velocity on each time series. A Savitzky-Golay smoothing of variable width may be applied for the peak detection only in case of moderate noise, to remove minor negative velocity trends. This procedure permits to compare time series with different numbers of peaks (i.e., in case of surge affected by seasonal variations).
We obtain a temporal lag in days between the two peaks, separated by a distance, and we infer a propagation rate associate to a surge initiation date. This protocol has only been applied to a limited number of surge events.

The analysis of individual velocity time series cross-correlated show a major defect of the algorithm tested: it is very sensitive of the variability of surge onset along the centreline (Fig. B.1, right columns). The first surge detailed (Fig. B.1, surge on the glacier RGI2000-v7.0-G-14-20250) show a progressive step on the velocity increase, seemingly a seasonal pattern. This seasonal step is only visible close to the trigger area and not anymore visible further downward along the glacier. The second surge detailed (Fig. B.1, surge on the glacier RGI2000-v7.0-G-14-18361) show a progressive acceleration at the start of the surge front propagation, which is not visible at the end position of the front. Taking the first time series further down helps to reduce the gradual acceleration signal. Both these cases show that this algorithm is too much sensitive to the variations of the acceleration pattern along the centerline to be reliable and time-efficient on a number of surge events.

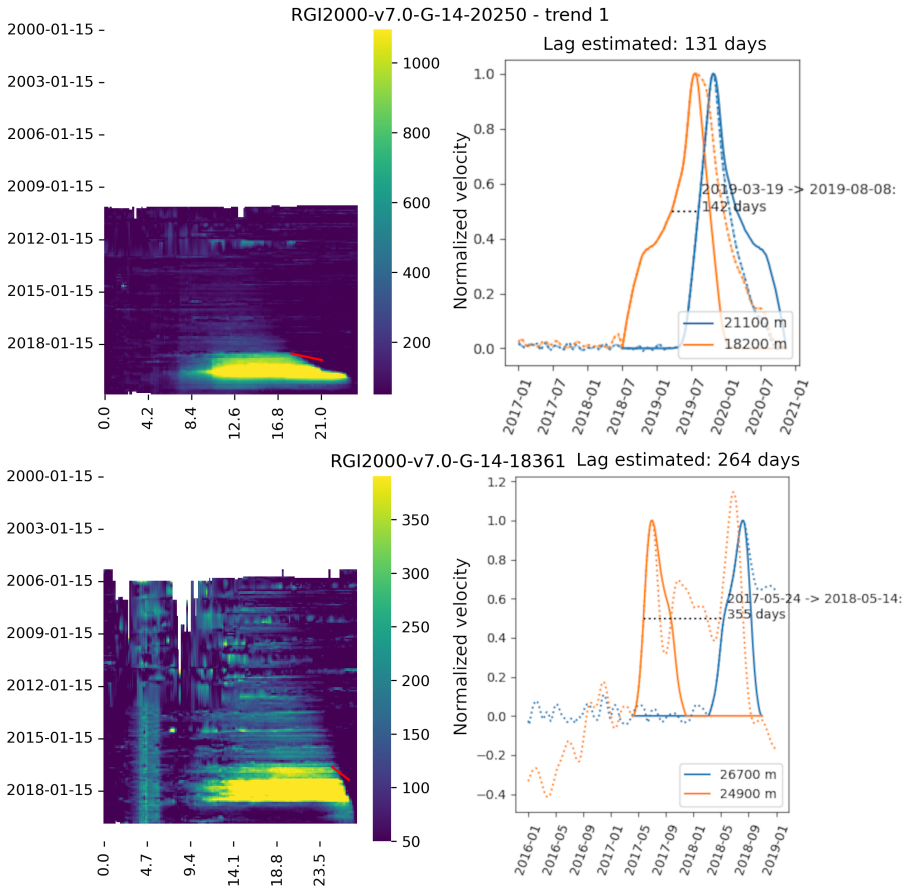

Figure B.1: Major defects of the cross-correlation algorithm: automatic delineation (left) and associated time series and peak compared (right).

B.3 Delineation of surge front propagation

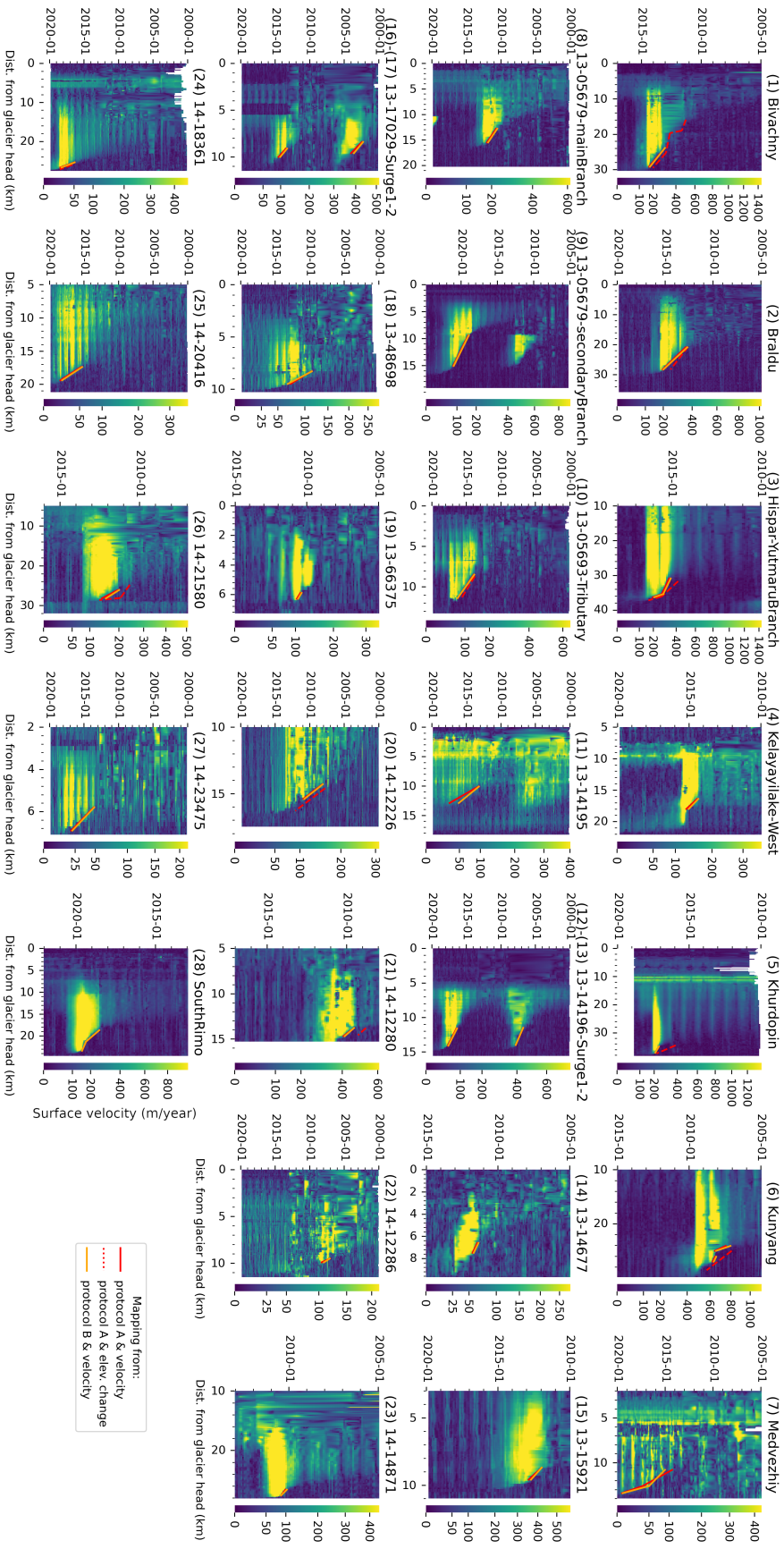

Figure B.2: Delineation of surge front propagation on spatio-temporal representations. Extended version of Fig. 3.5.

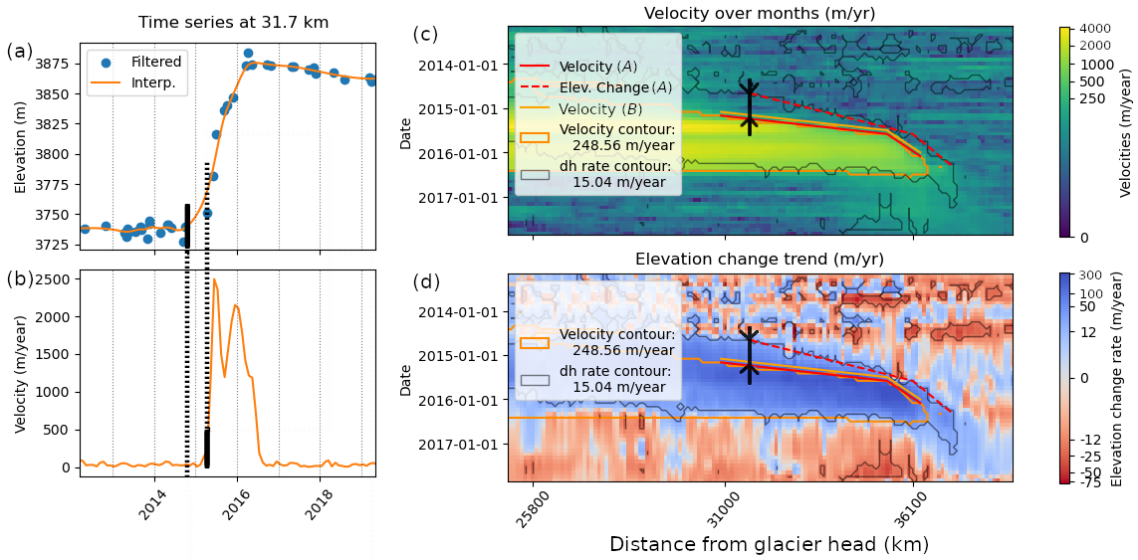

Figure B.3: Time series of elevation (a) and velocity (b) associated to the delineation of the surge front propagation on (3) Hispar glacier (c-d). The date and location we sample on each dataset is represented by black lines. There is a difference of several months between the markings (April 2015 from velocity with the protocol *A*, September 2014 from elevation change with *A*). On the elevation time series (a), there is only one observation in early 2015 to constrain the interpolation, and the surge signal seems to be smoothed with an onset date a few months earlier than what is visible on the velocity time series. In the legend (a), "interp." is the interpolated elevation time series.

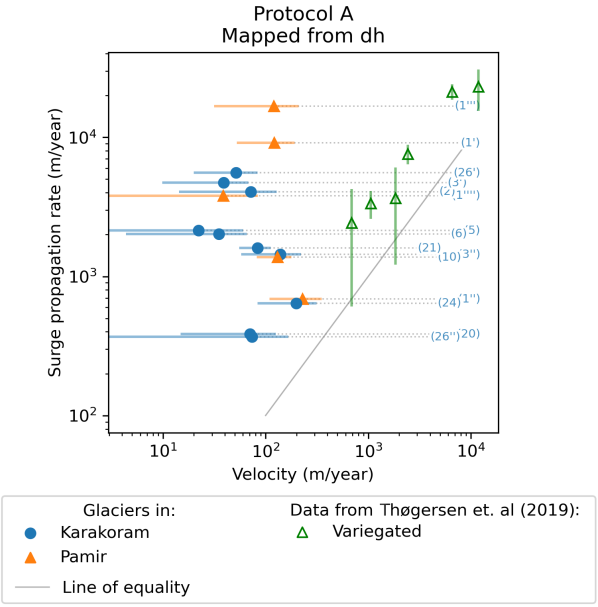

Figure B.4: Analysis similar as Fig. 3.6 applied, this time delineated on maps of elevation change trends, on a subset of glaciers: relation between propagation velocity and glacier surface velocity, aggregated per surge event (or trend). The protocol A tested on elevation change dataset show no visible relationship to velocity. At the time sampled by protocol A on elevation change rate, no velocity surge signal is visible yet on a number of events (e.g., Fig. 3.3, and more explicit for glaciers (3), (5) or (25) in Appendix Fig. B.2).

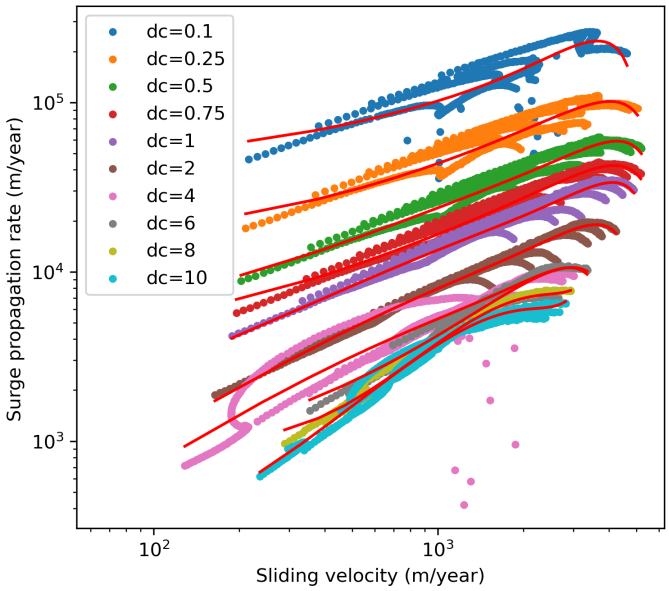

Figure B.5: Fit of the model simulations from Thøgersen et al. (2019), for each d_c parameter value (including all values of q). We fit a polynomial of degree 4. We do not include the fit with d_c= 4 m in Fig. 3.6 due to the diverging pattern of the simulation not represented by the fit. The data is provided by the authors, and it corresponds to the inset of Figure 6 in the original study.

B.4 Driving stress analysis

The following figures show longitudinal driving stress evolution of all the classified glacier, see Fig. 3.8-3.10 in Chapter 3, and Tables B.1-B.3 in Appendix. See the table of content B.4 for a reference for each figure. Time series are sampled the labeled positions along the centreline, and the surge period is highlighted in orange bar on the time series.

Glacier	Class of driving stress	Figure
Hispar - Yutmaru branch	Hydraulically-driven	B.40
Bivachny	Spatially constrained	B.6
14-18524	Hydraulically-driven	B.39
Khurdopin	Spatially constrained	B.7
Muzgazi	Spatially constrained	B.8
13-05590	Spatially constrained	B.9
13-05693 tributary	Spatially constrained	B.10
13-05715	Spatially constrained	B.11
14-21580	Spatially constrained	B.17
13-14589	Spatially constrained	B.12
13-16672	Spatially constrained	B.13
13-43964	Spatially constrained	B.14
13-48698	Spatially constrained	B.15
13-05593	Spatially constrained	B.19
13-14195	Spatially constrained	B.16
Kunyang	Spatially constrained	B.18
Kyagar	Temporally ambiguous	B.23
13-05679 sec. branch	Temporally ambiguous	B.25
South Rimo	Temporally ambiguous	B.24
13-44005	Temporally ambiguous	B.22
13-15921	Temporally ambiguous	B.26
13-18530	Temporally ambiguous	B.27
13-19276	Temporally ambiguous	B.28
13-44456	Temporally ambiguous	B.30
13-47689 branch1	Temporally ambiguous	B.29
13-14196	Temporally ambiguous	B.21
13-59619	Temporally ambiguous	B.31
14-12280	Spatially constrained	B.20
14-13801	Temporally ambiguous	B.32
14-14871	Temporally ambiguous	B.37
14-18361	Temporally ambiguous	B.33
14-18427	Temporally ambiguous	B.38
14-19567	Temporally ambiguous	B.34
14-20416	Temporally ambiguous	B.35
14-23475	Temporally ambiguous	B.36

Table B.4: Link between glaciers and the corresponding driving stress time series. The prefix of RGI 7.0 codes is "RGI2000-v7.0-G-".

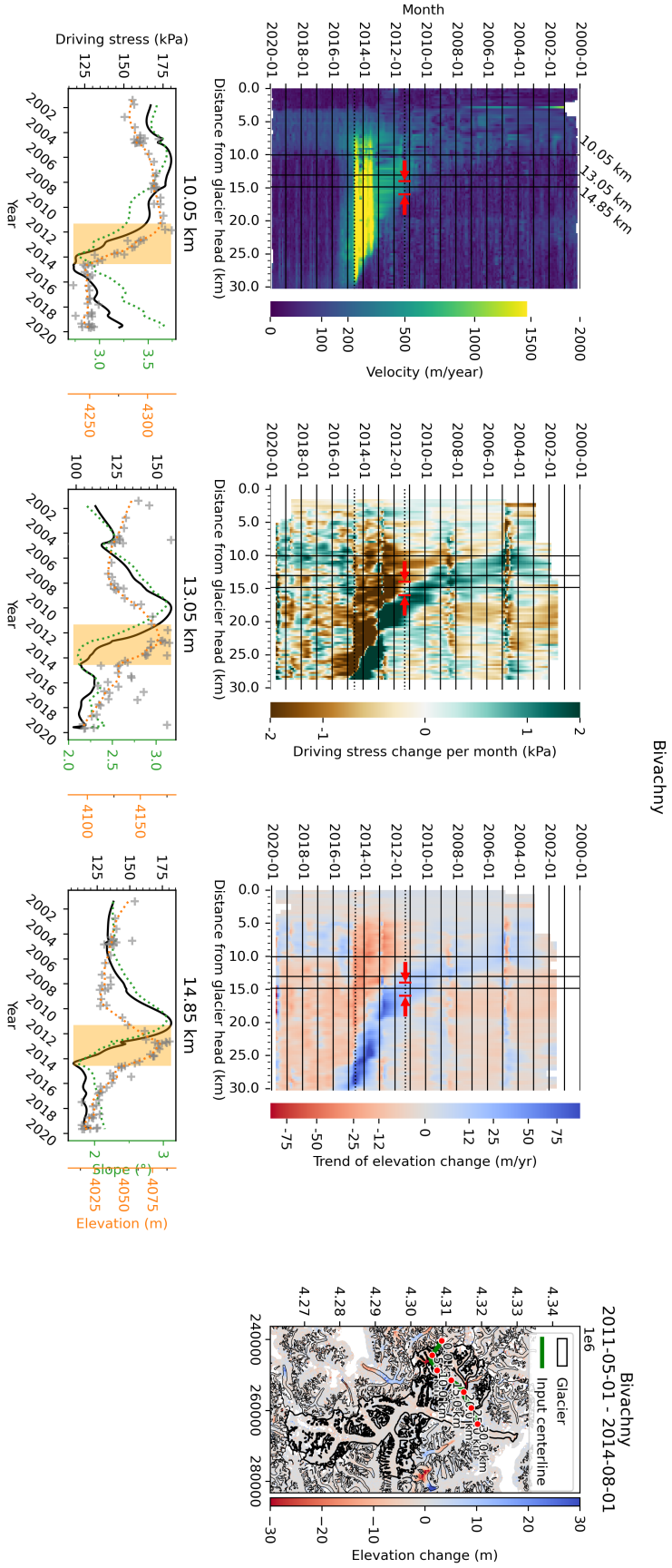

Figure B.6: Identical to Fig. 3.8, but for the Bivachny glacier, which is of type *Spatially constrained trigger surge*

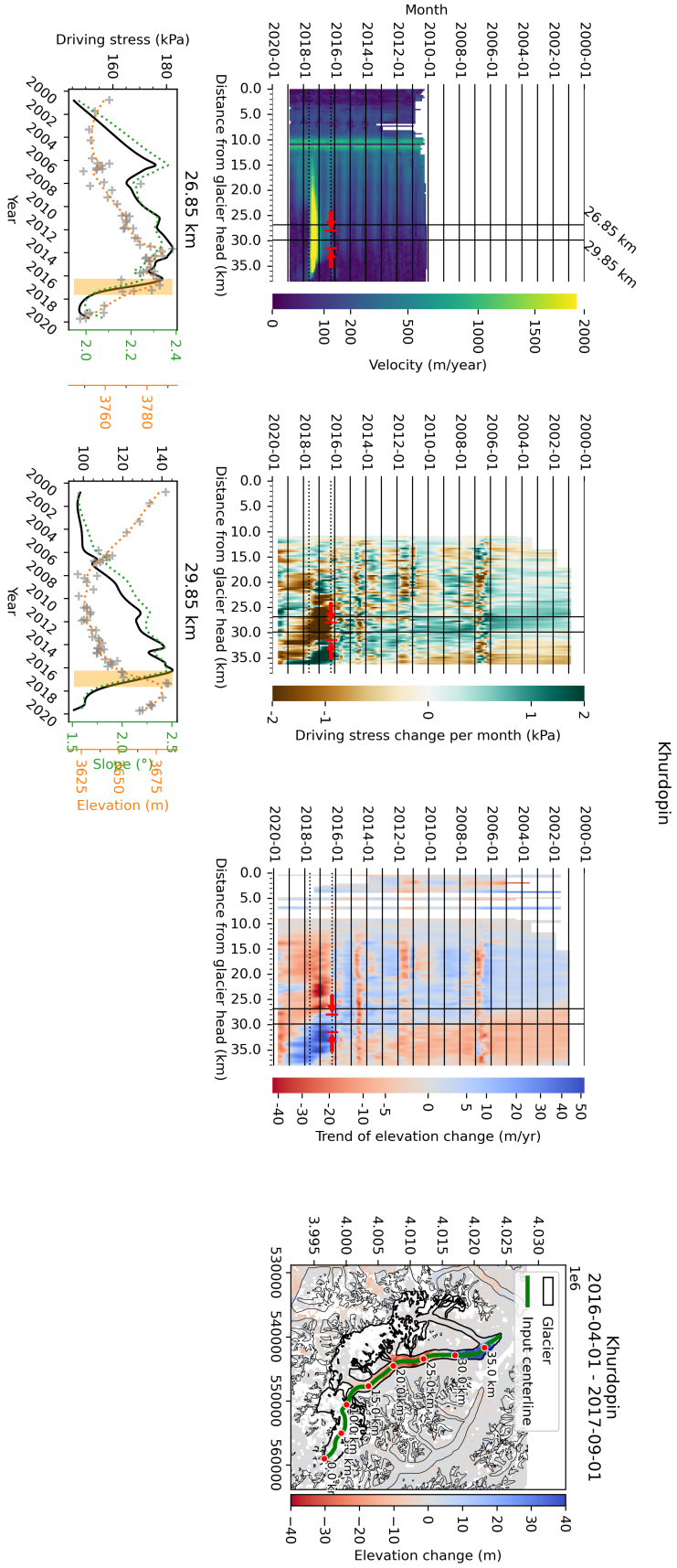

Figure B.7: Identical to Fig. 3.8, but for the Khurdopin glacier, which is of type *Spatially constrained trigger surge*

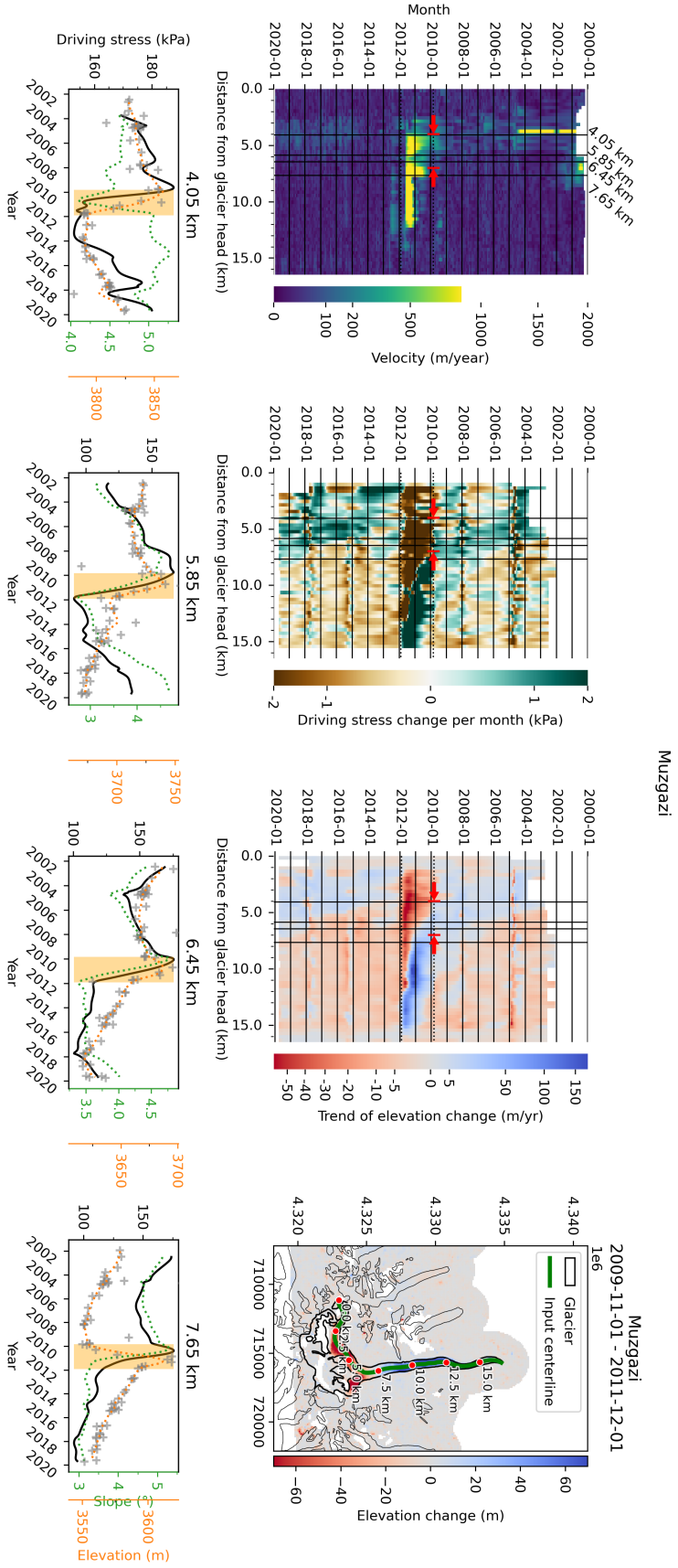

Figure B.8: Identical to Fig. 3.8, but for the Muzgazi glacier, which is of type *Spatially constrained trigger surge*

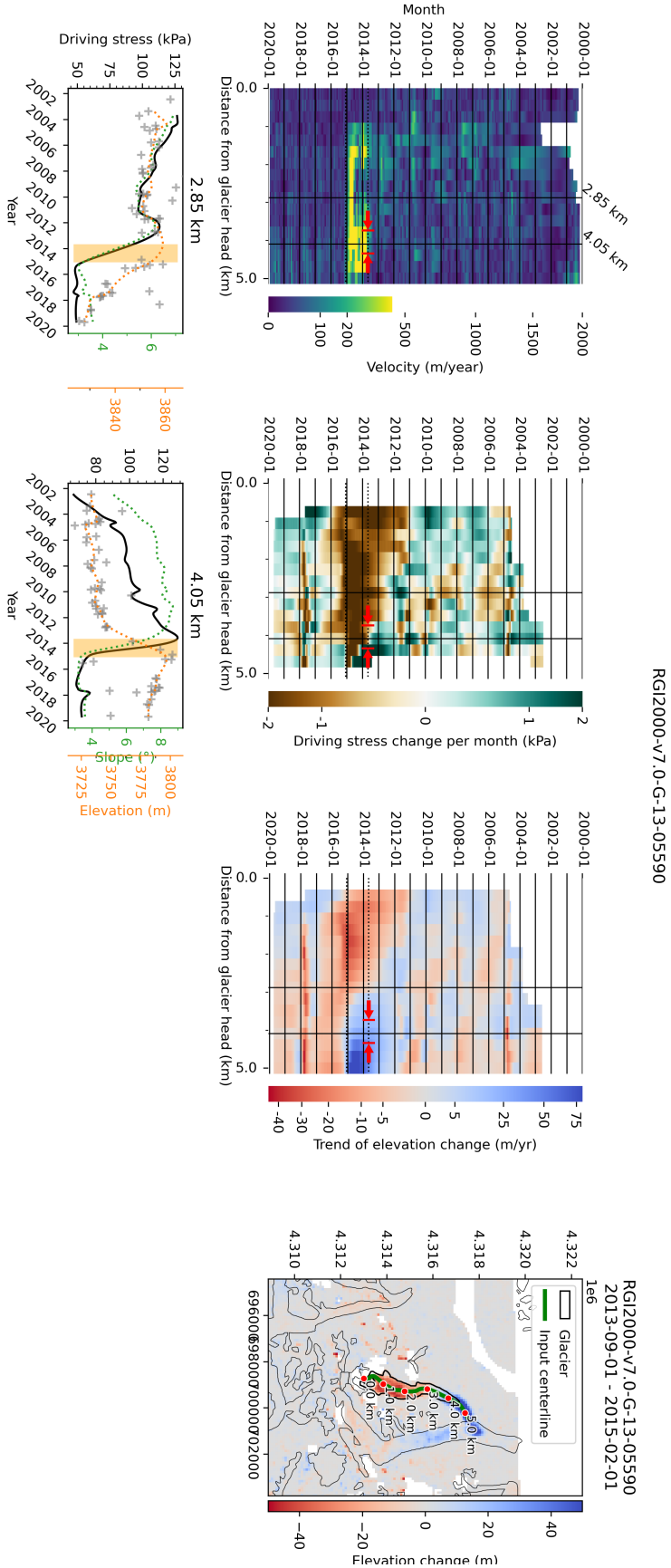

Figure B.9: Identical to Fig. 3.8, but for the glacier RGI2000-v7.0-G-13-05590, which is of type *Spatially constrained trigger surge*

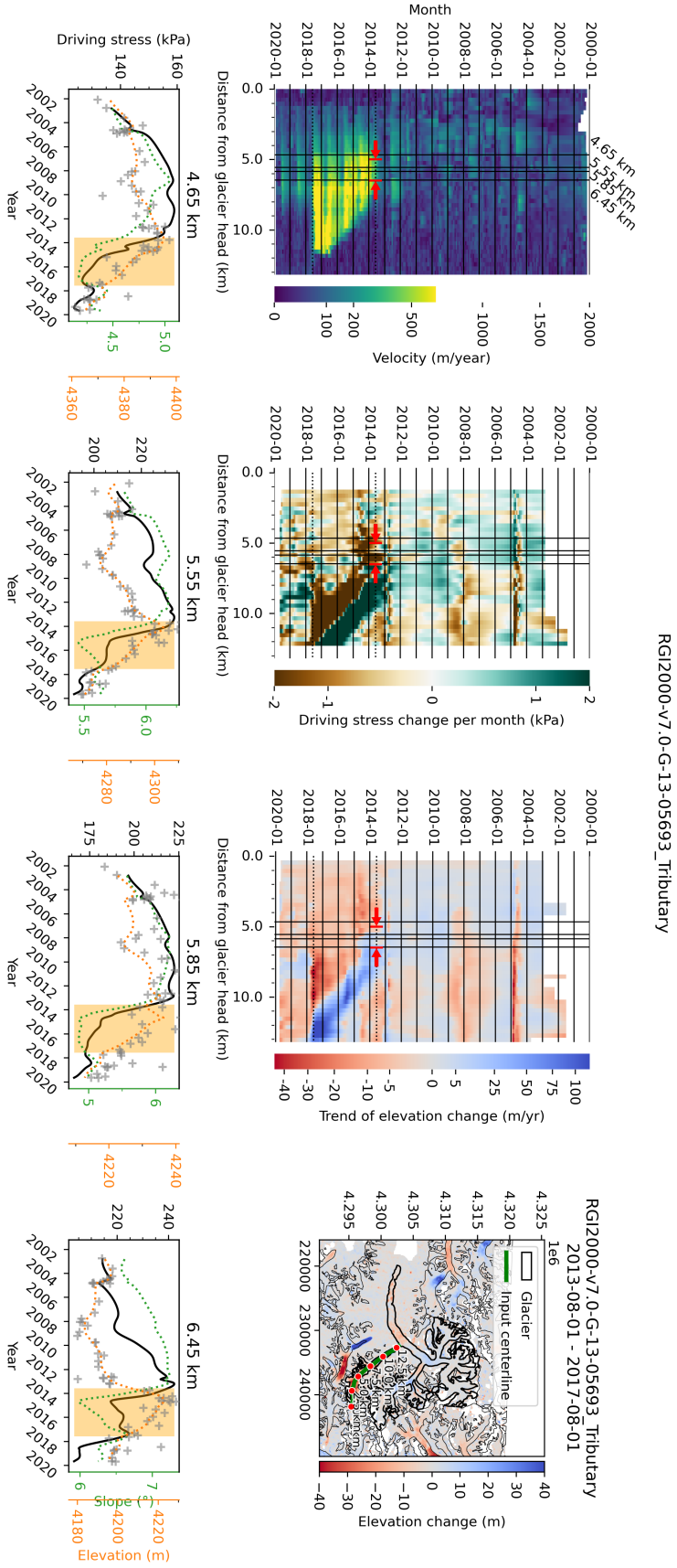

Figure B.10: Identical to Fig. 3.8, but for a tributary of glacier RGI2000-v7.0-G-13-05693, which is of type *Spatially constrained trigger surge*

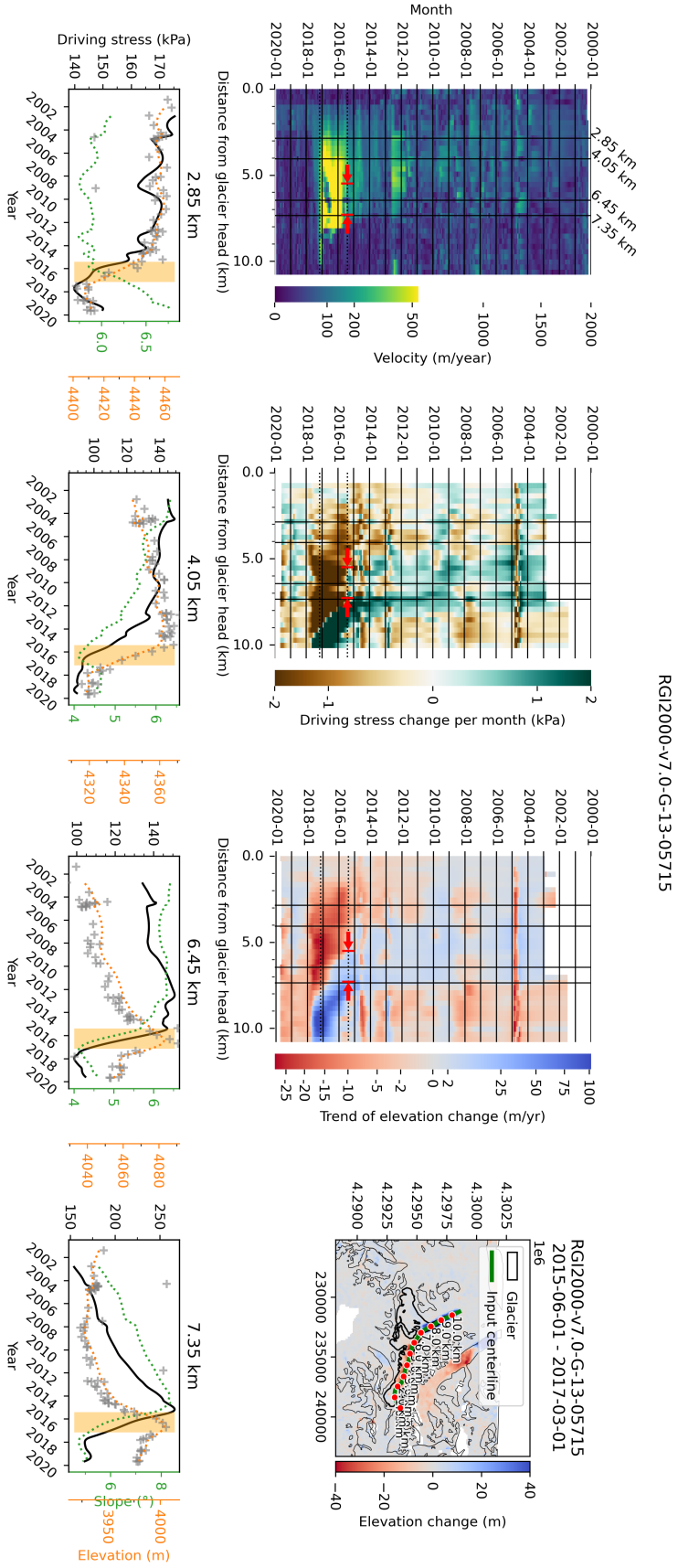

Figure B.11: Identical to Fig. 3.8, but for the glacier RGI2000-v7.0-G-13-05715, which is of type *Spatially constrained trigger surge*

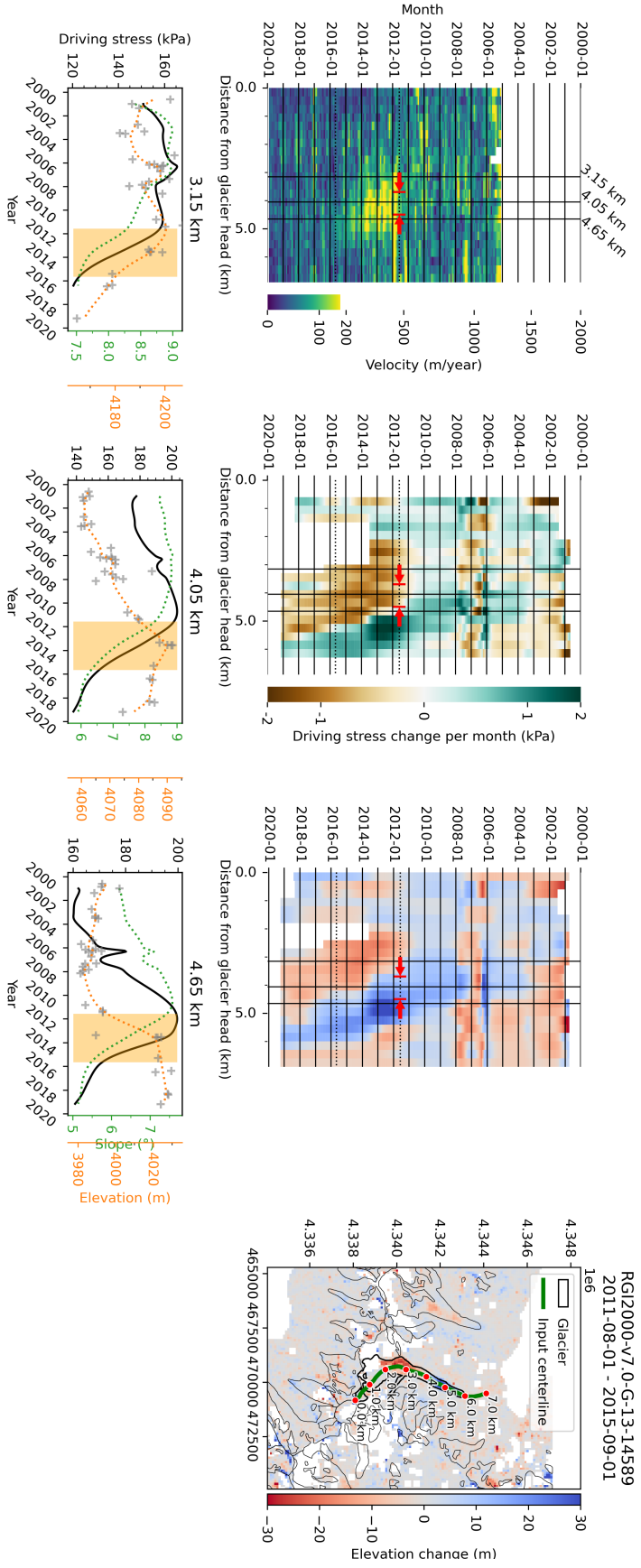

Figure B.12: Identical to Fig. 3.8, but for the glacier RGI2000-v7.0-G-13-14589, which is of type *Spatially constrained trigger surge*

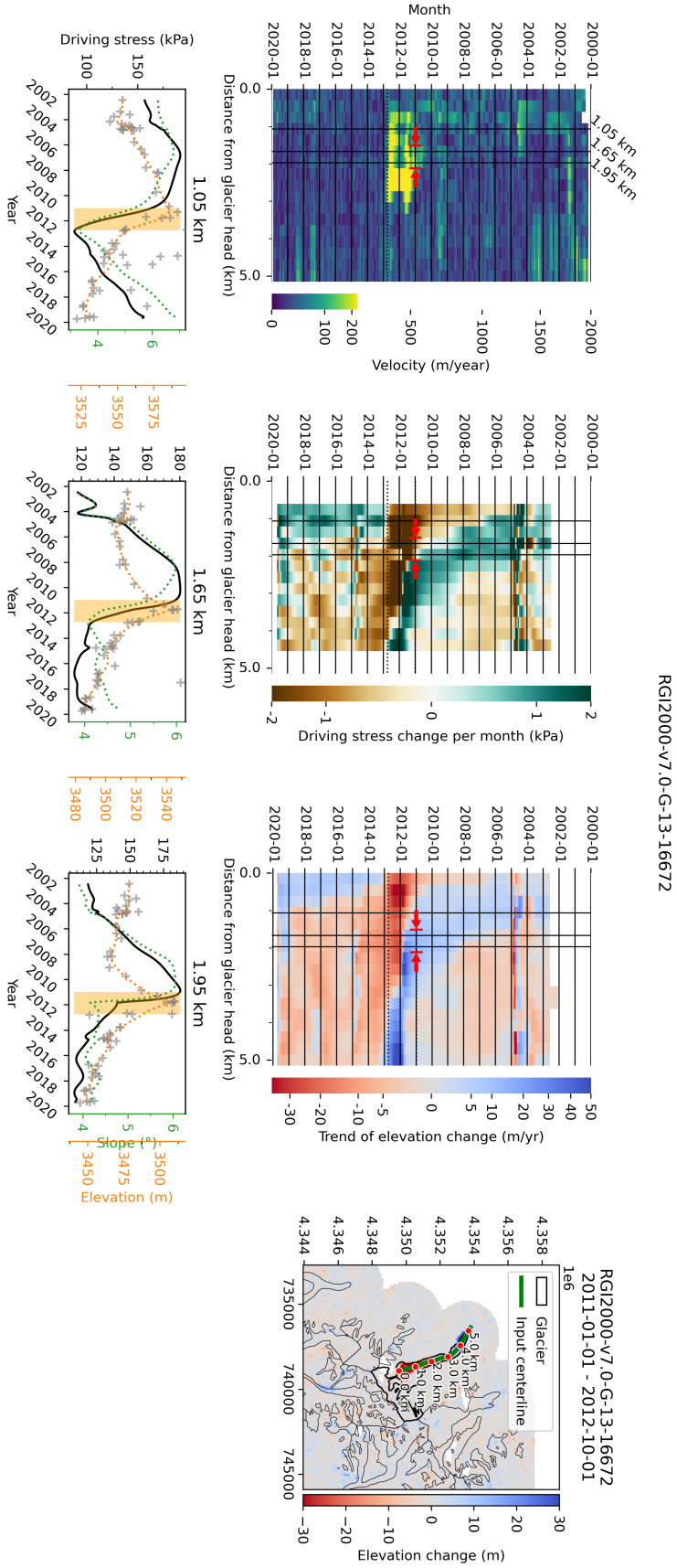

Figure B.13: Identical to Fig. 3.8, but for the glacier RGI2000-v7.0-G-13-16672, which is of type *Spatially constrained trigger surge*

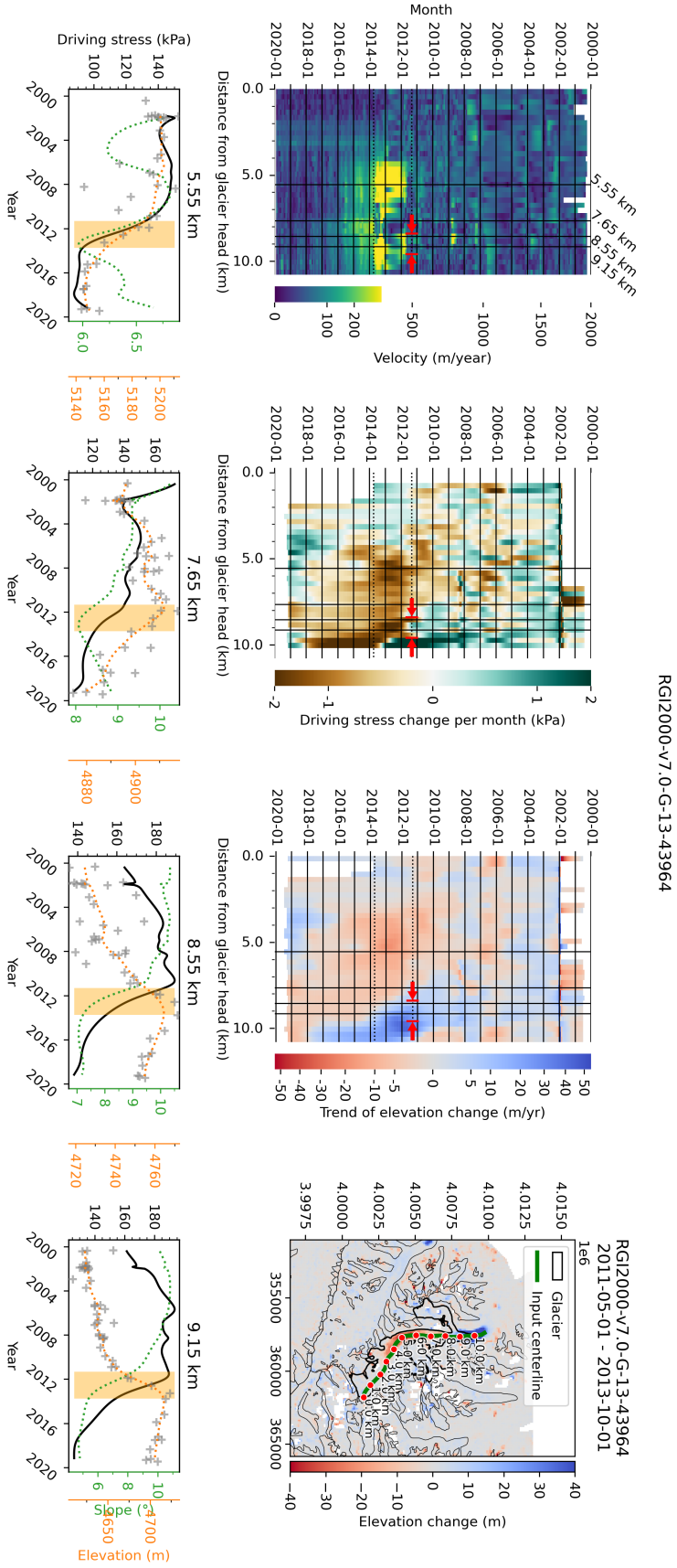

Figure B.14: Identical to Fig. 3.8, but for the glacier RGI2000-v7.0-G-13-43964, which is of type *Spatially constrained trigger surge*

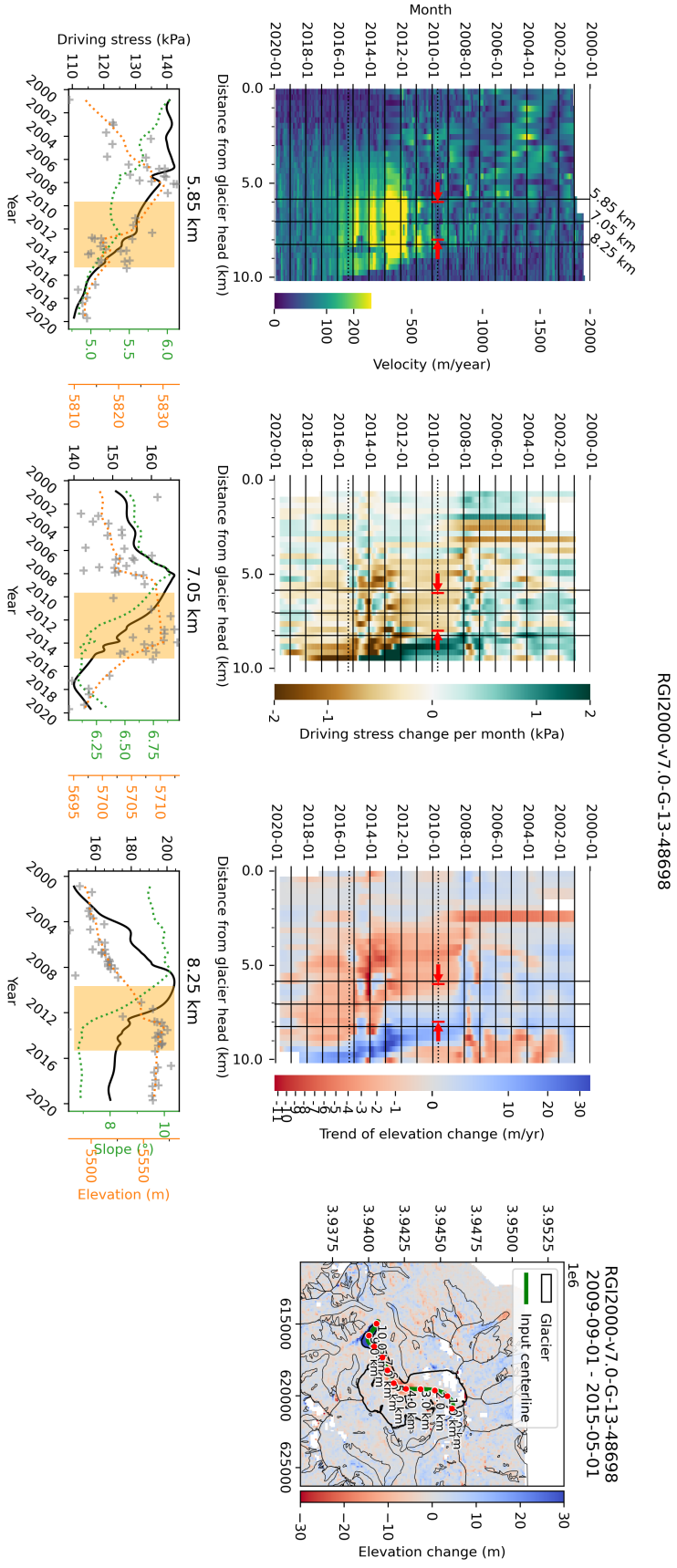

Figure B.15: Identical to Fig. 3.8, but for the glacier RGI2000-v7.0-G-13-48698, which is of type *Spatially constrained trigger surge*

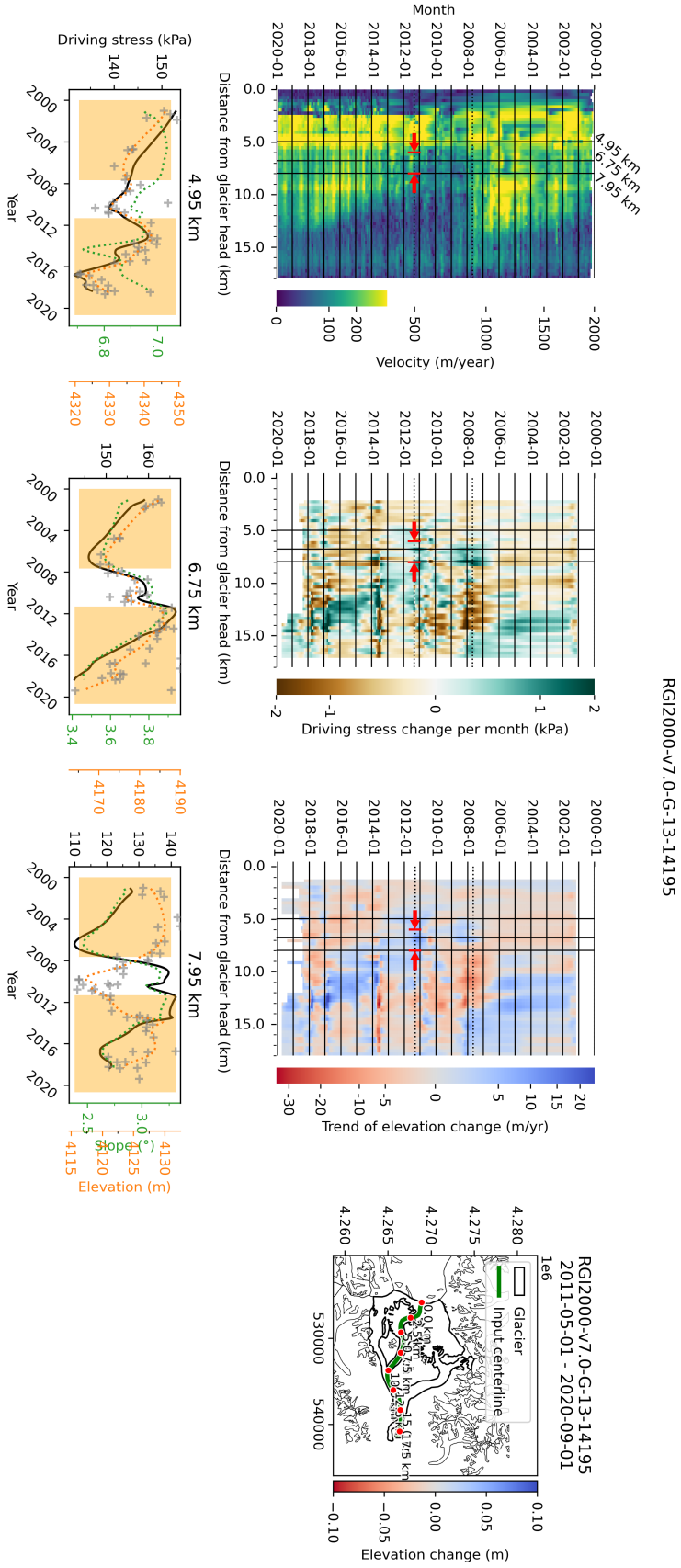

Figure B.16: Identical to Fig. 3.8, but for the glacier RGI2000-v7.0-G-13-14195, which is of type *Spatially constrained trigger surge*

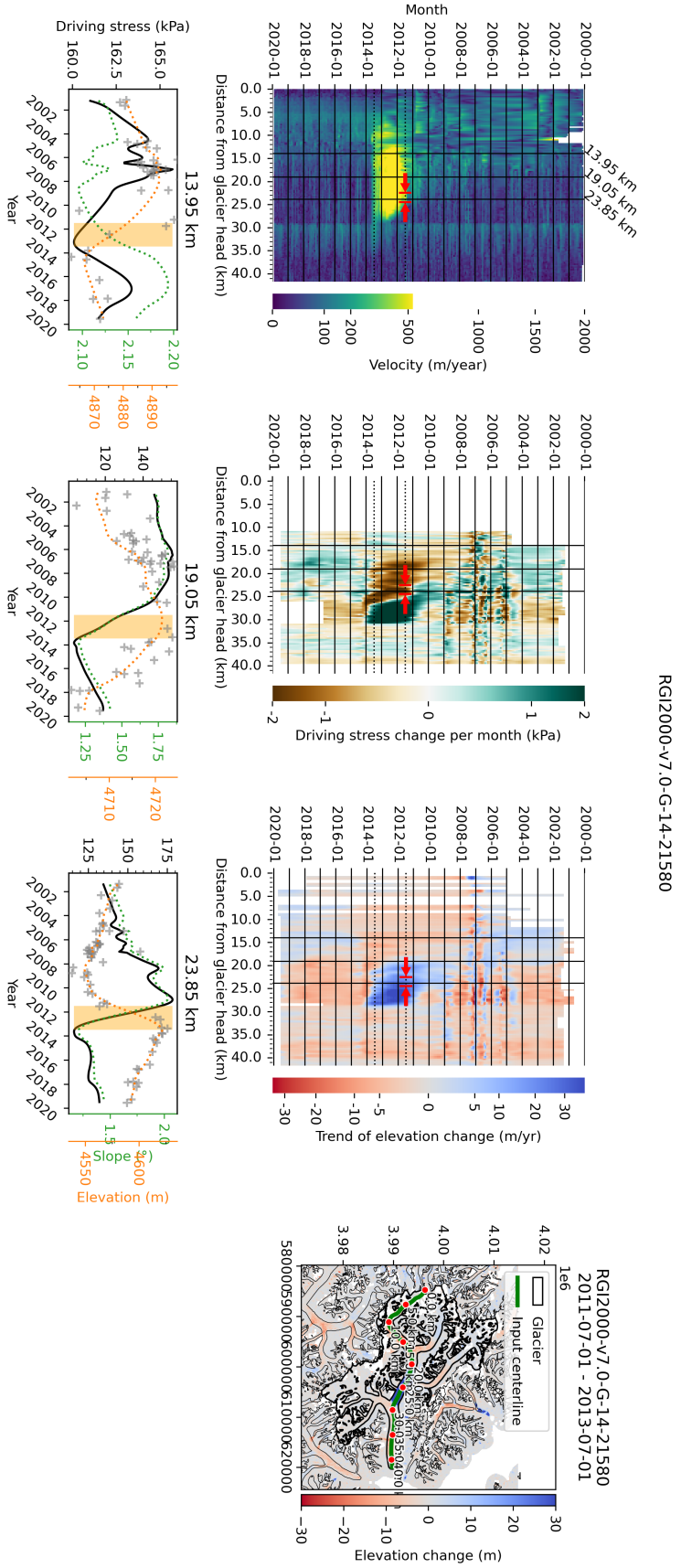

Figure B.17: Identical to Fig. 3.8, but for the glacier RGI2000-v7.0-G-14-21580, which is of type *Spatially constrained trigger surge*

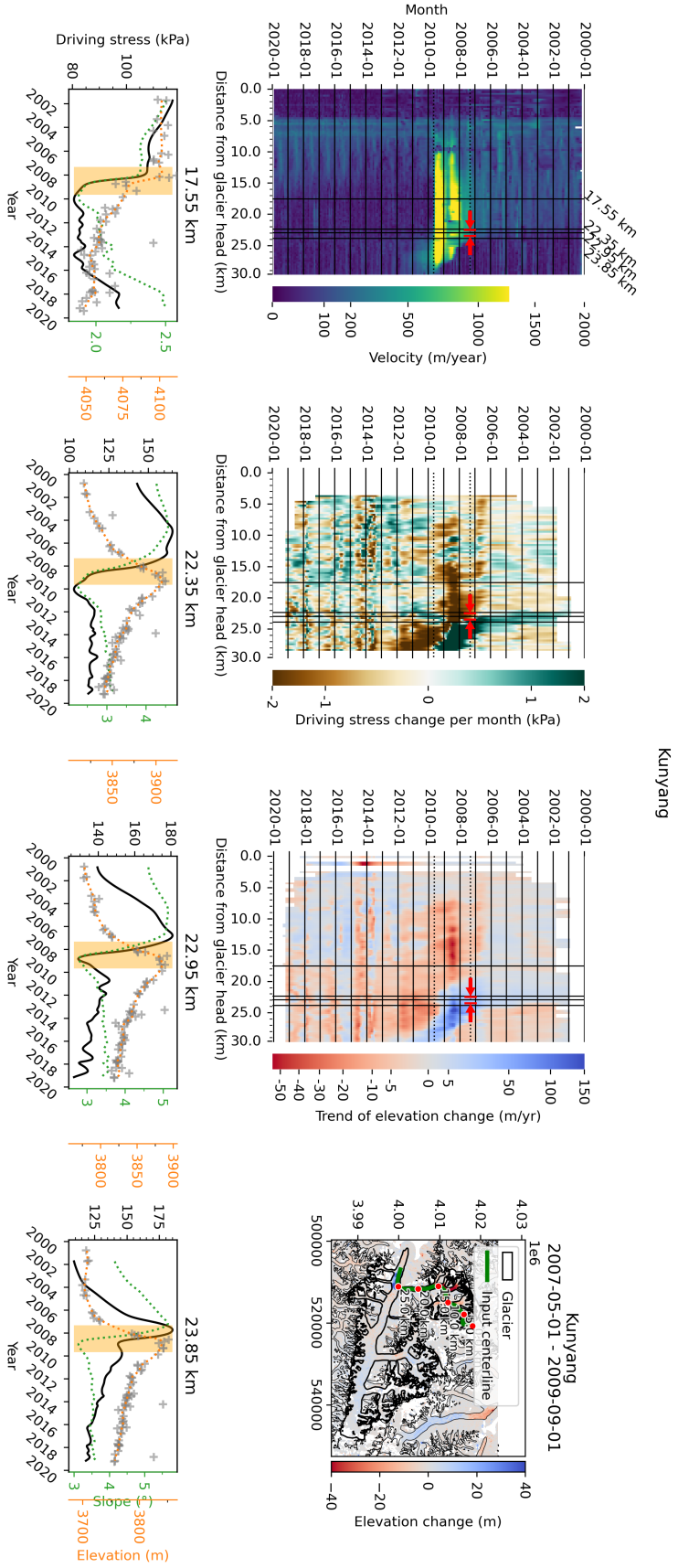

Figure B.18: Identical to Fig. 3.8, but for the Kunyang glacier, which is of type *Spatially constrained trigger surge*

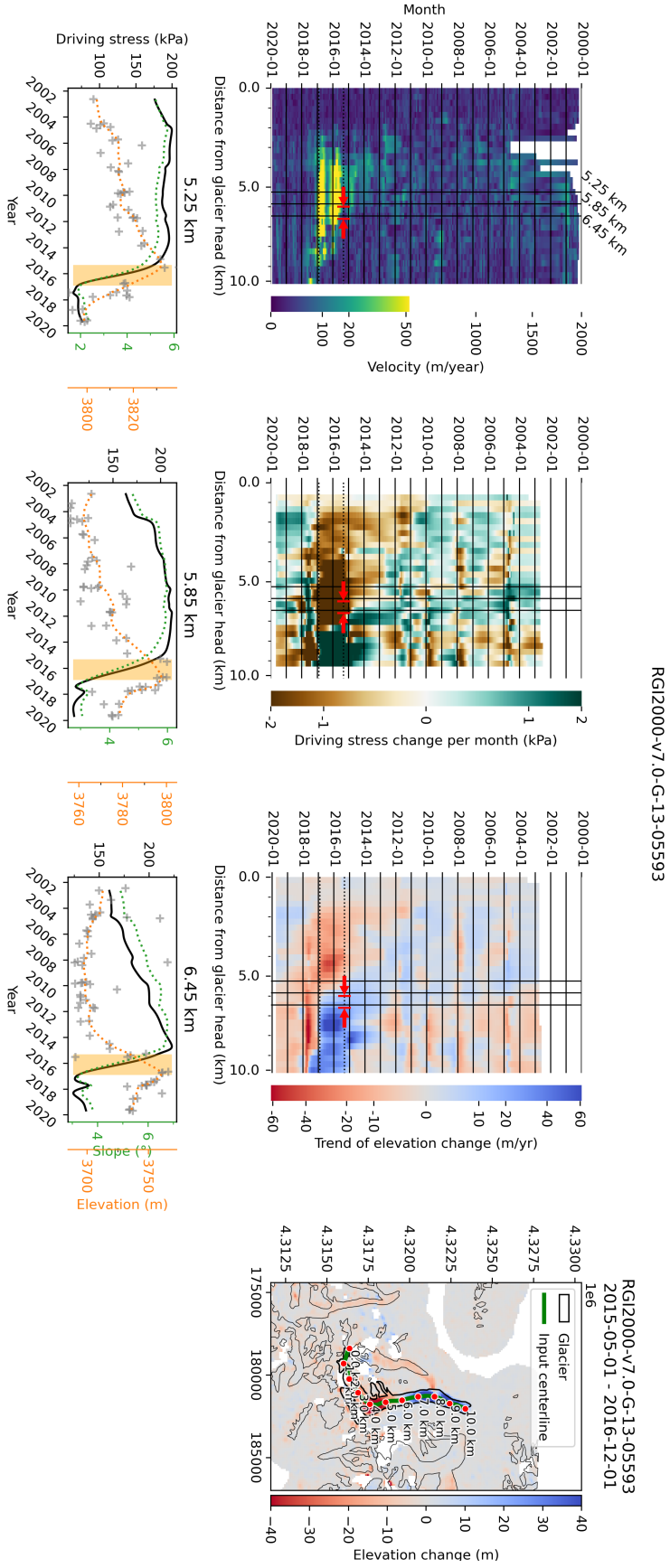

Figure B.19: Identical to Fig. 3.8, but for the RGI2000-v7.0-G-13-05593 glacier, which is of type *Spatially constrained trigger surge*

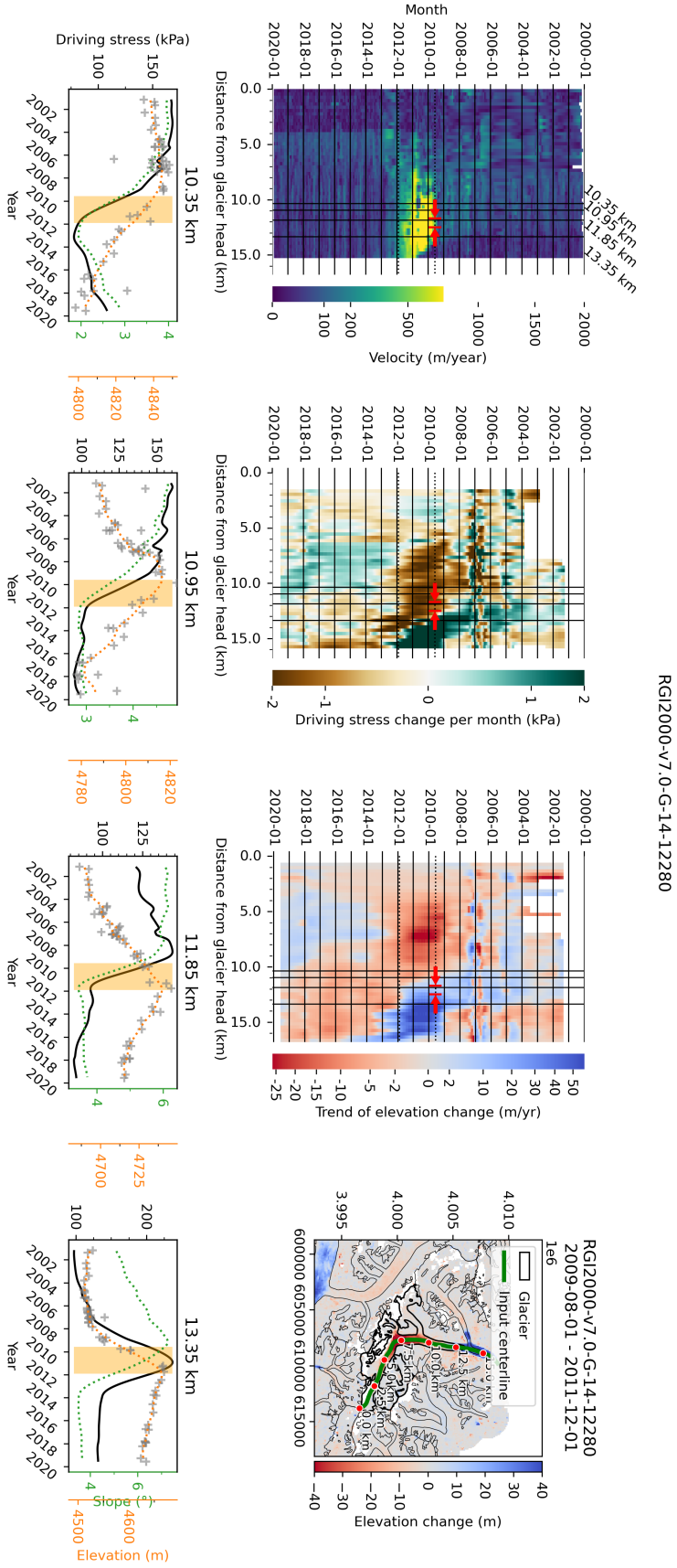

Figure B.20: Identical to Fig. 3.8, but for the glacier RGI2000-v7.0-G-14-12280, which is of type *Spatially constrained trigger surge*

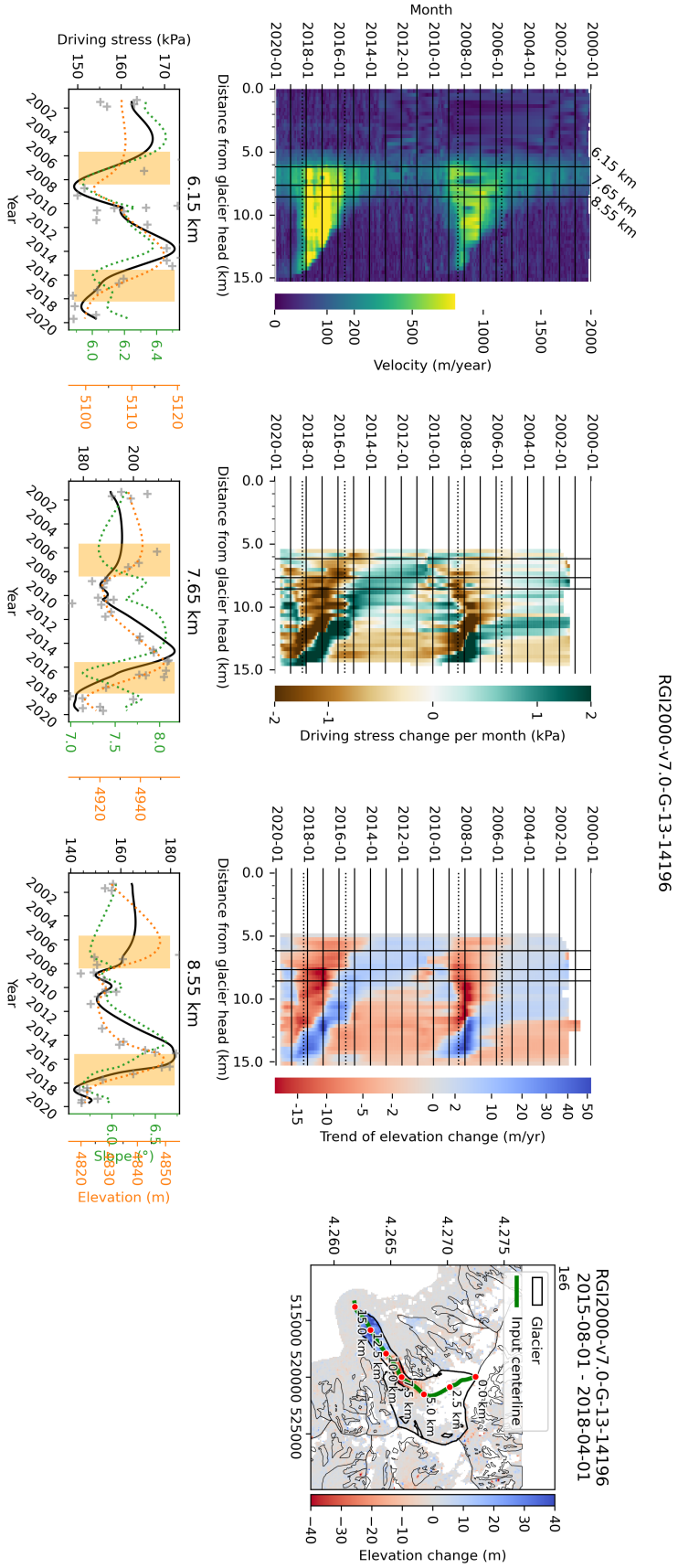

Figure B.21: Identical to Fig. 3.8, but for the glacier RGI2000-v7.0-G-13-14196, which is of type *Temporally ambiguous surge onset*

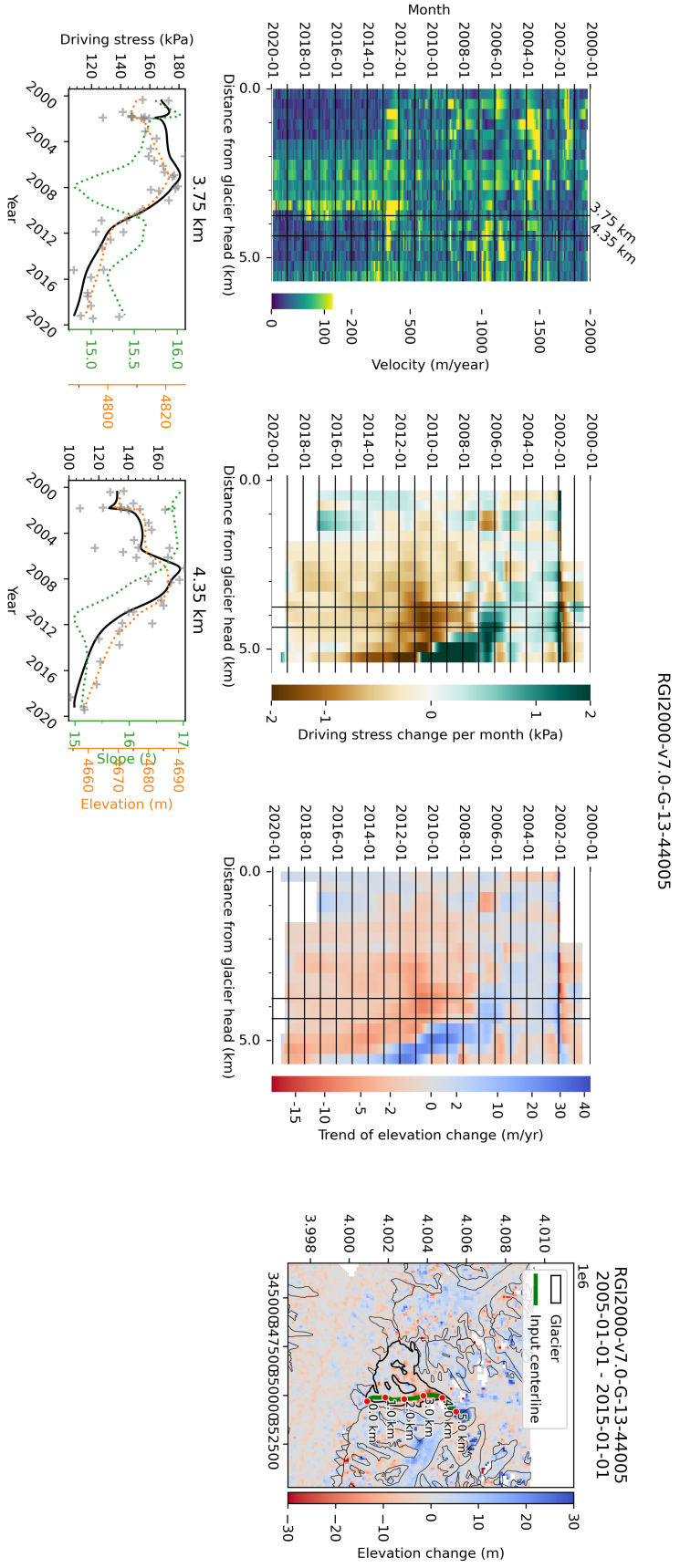

Figure B.22: Identical to Fig. 3.8, but for the glacier RGI2000-v7.0-G-13-44005, which is of type *Temporally ambiguous surge onset*

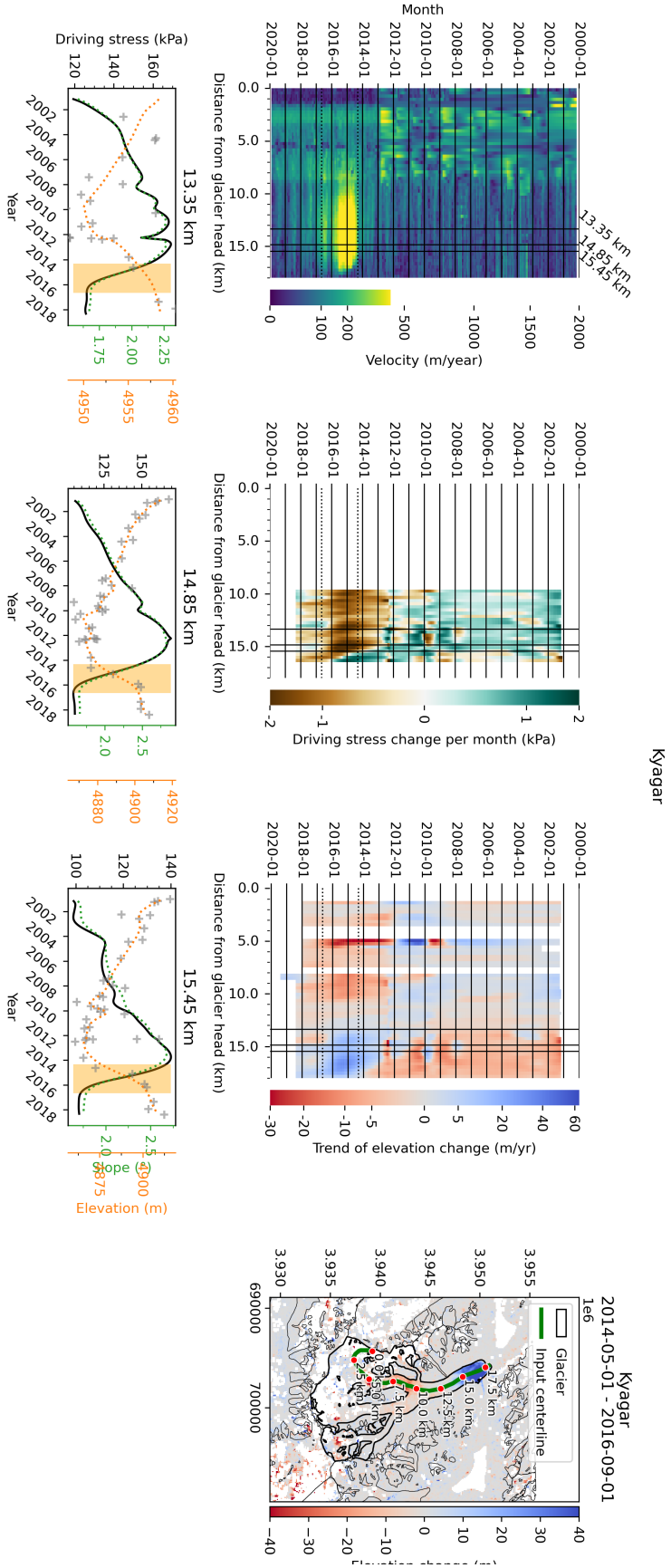

Figure B.23: Identical to Fig. 3.8, but for the Kyagar glacier, which is of type *Temporally ambiguous surge onset*

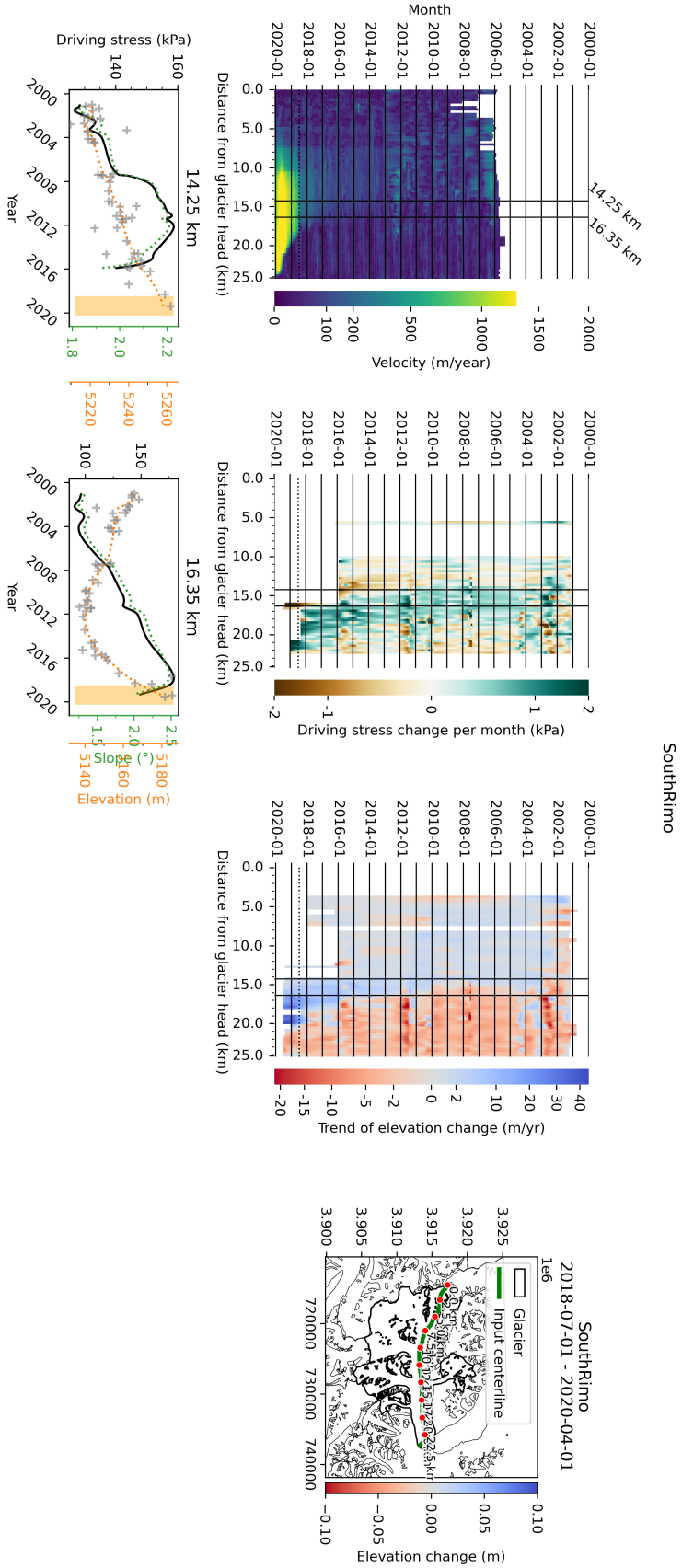

Figure B.24: Identical to Fig. 3.8, but for the South Rimo glacier, which is of type *Temporally ambiguous surge onset*

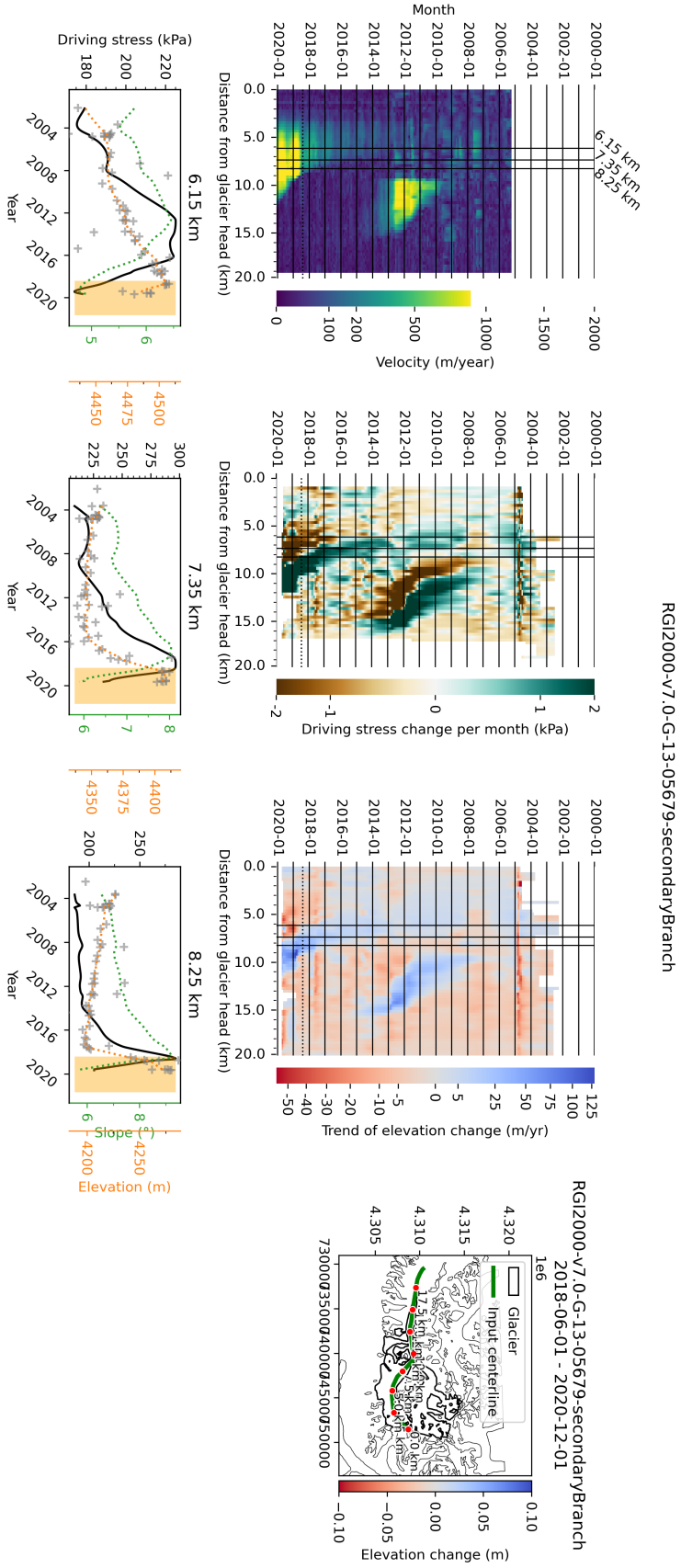

Figure B.25: Identical to Fig. 3.8, but for the secondary branch of glacier RGI2000-v7.0-G-13-05679, which is of type *Temporally ambiguous surge onset*

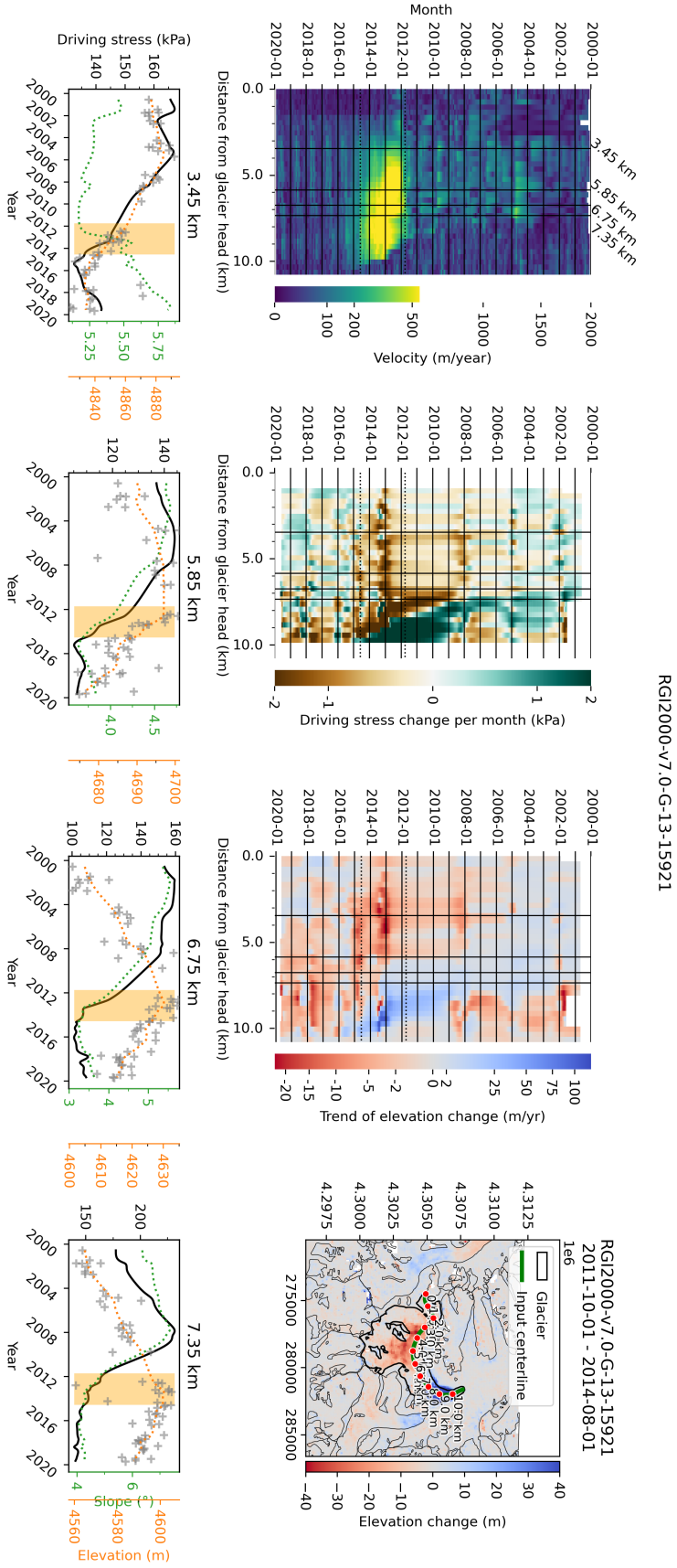

Figure B.26: Identical to Fig. 3.8, but for the glacier RGI2000-v7.0-G-13-15921, which is of type *Temporally ambiguous surge onset*

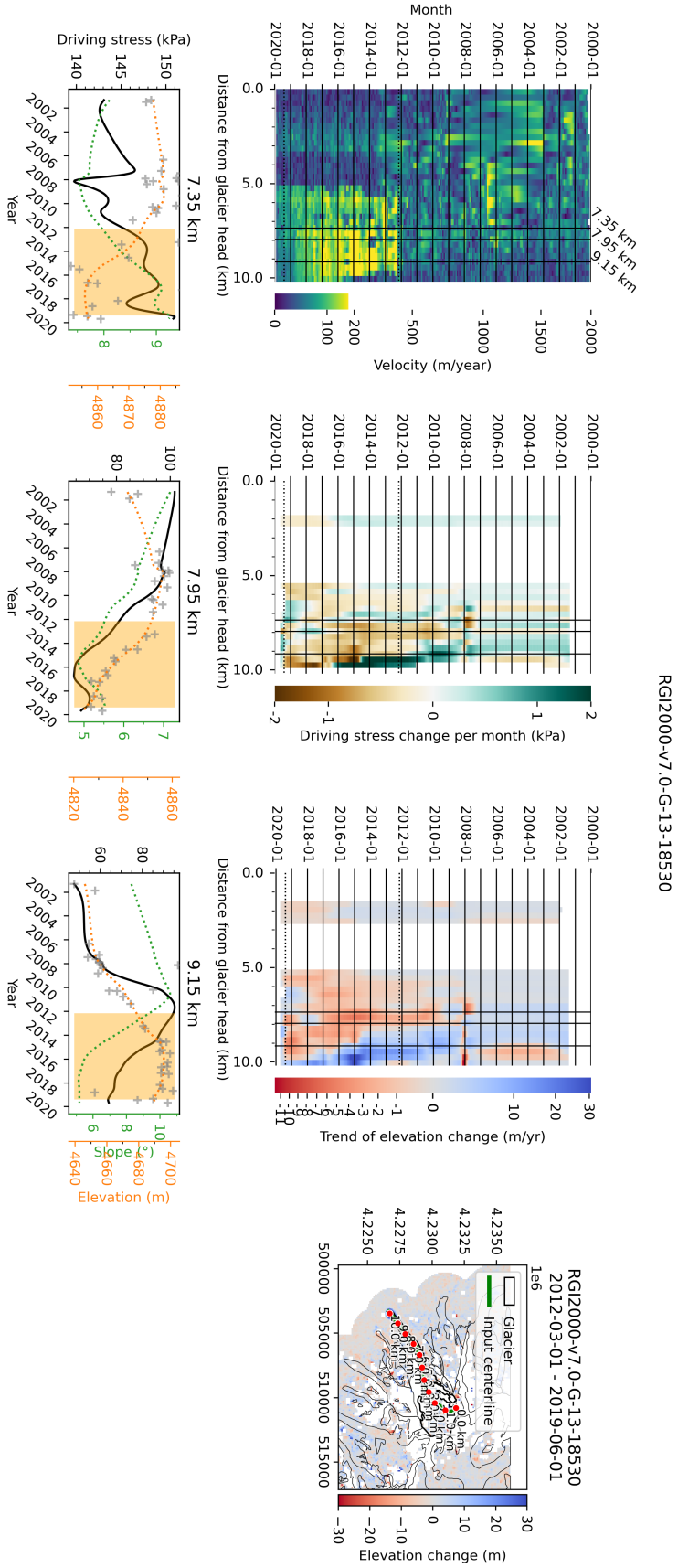

Figure B.27: Identical to Fig. 3.8, but for the glacier RGI2000-v7.0-G-13-18530, which is of type *Temporally ambiguous surge onset*

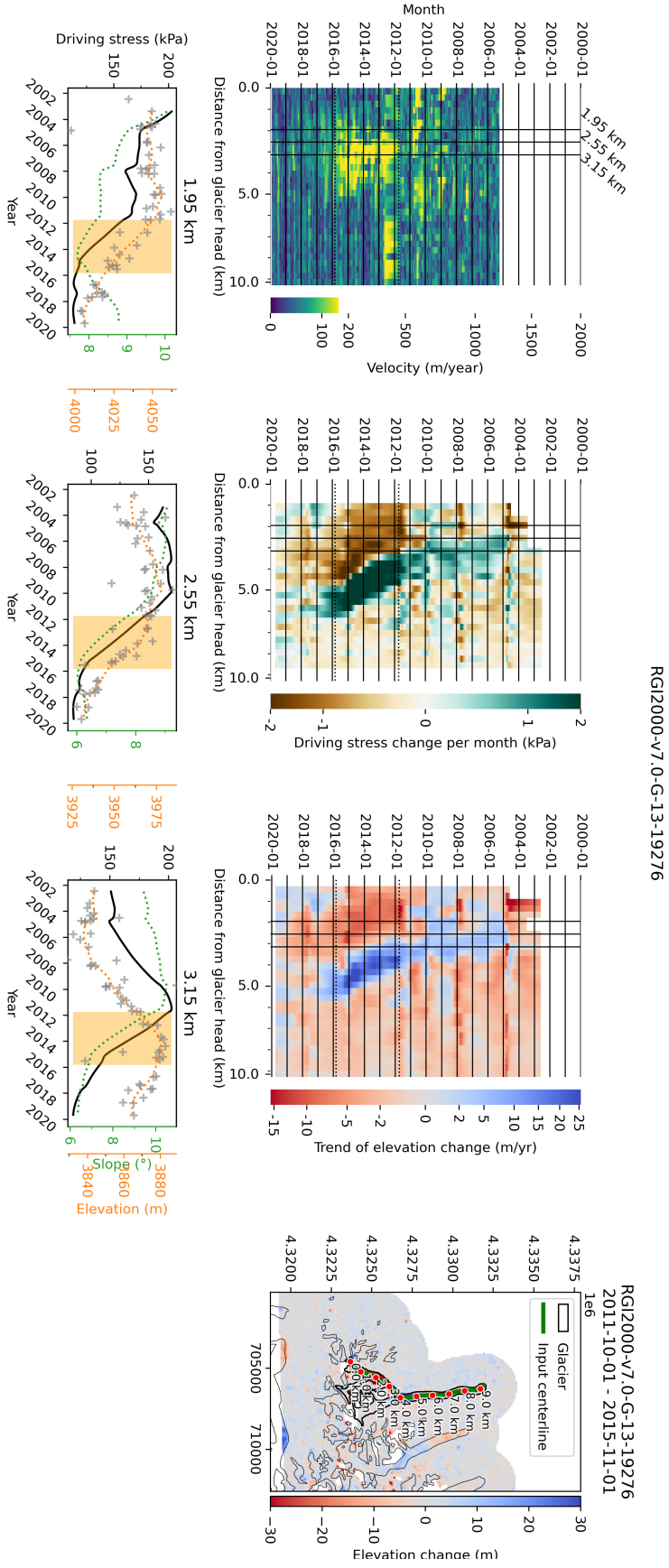

Figure B.28: Identical to Fig. 3.8, but for the glacier RGI2000-v7.0-G-13-19276, which is of type *Temporally ambiguous surge onset*

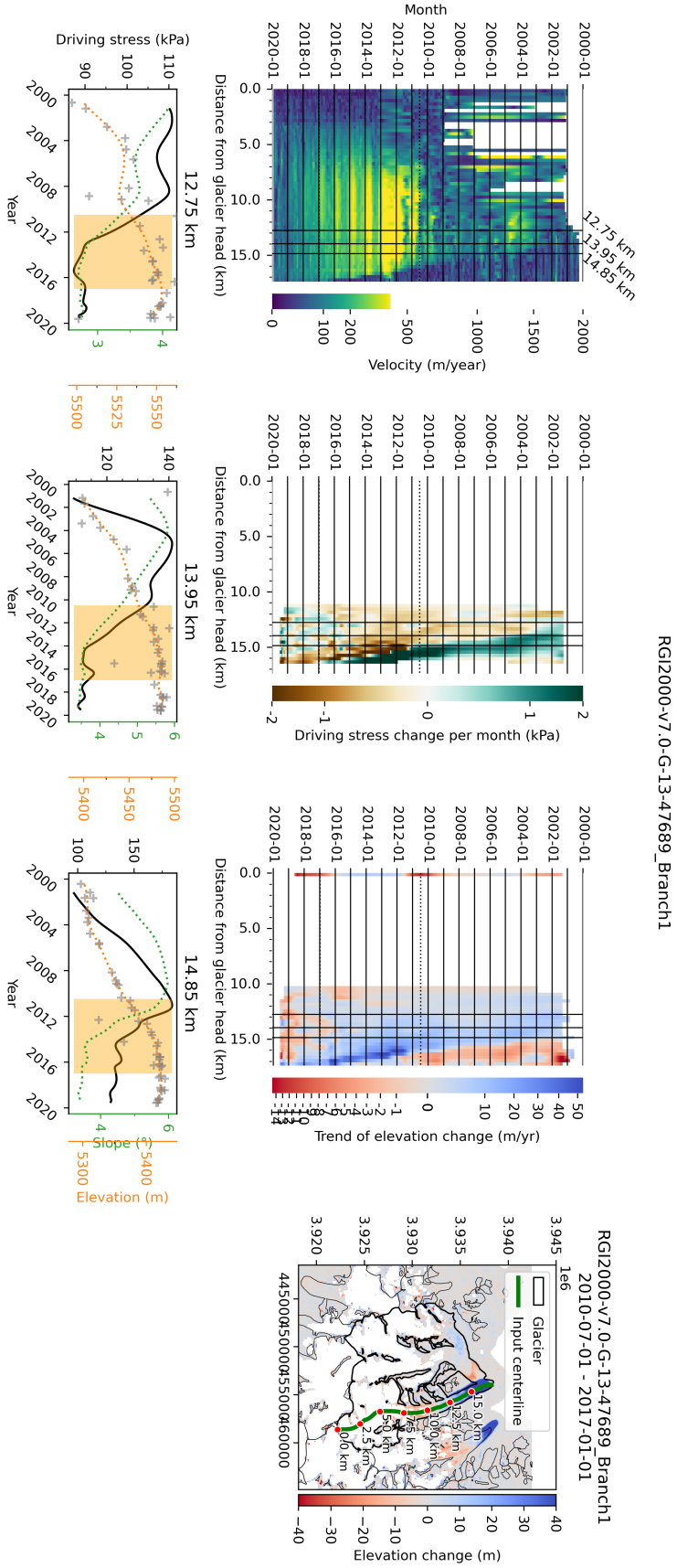

Figure B.29: Identical to Fig. 3.8, but for the first branch of the glacier RGI2000-v7.0-G-13-47689, which is of type *Temporally ambiguous surge onset*

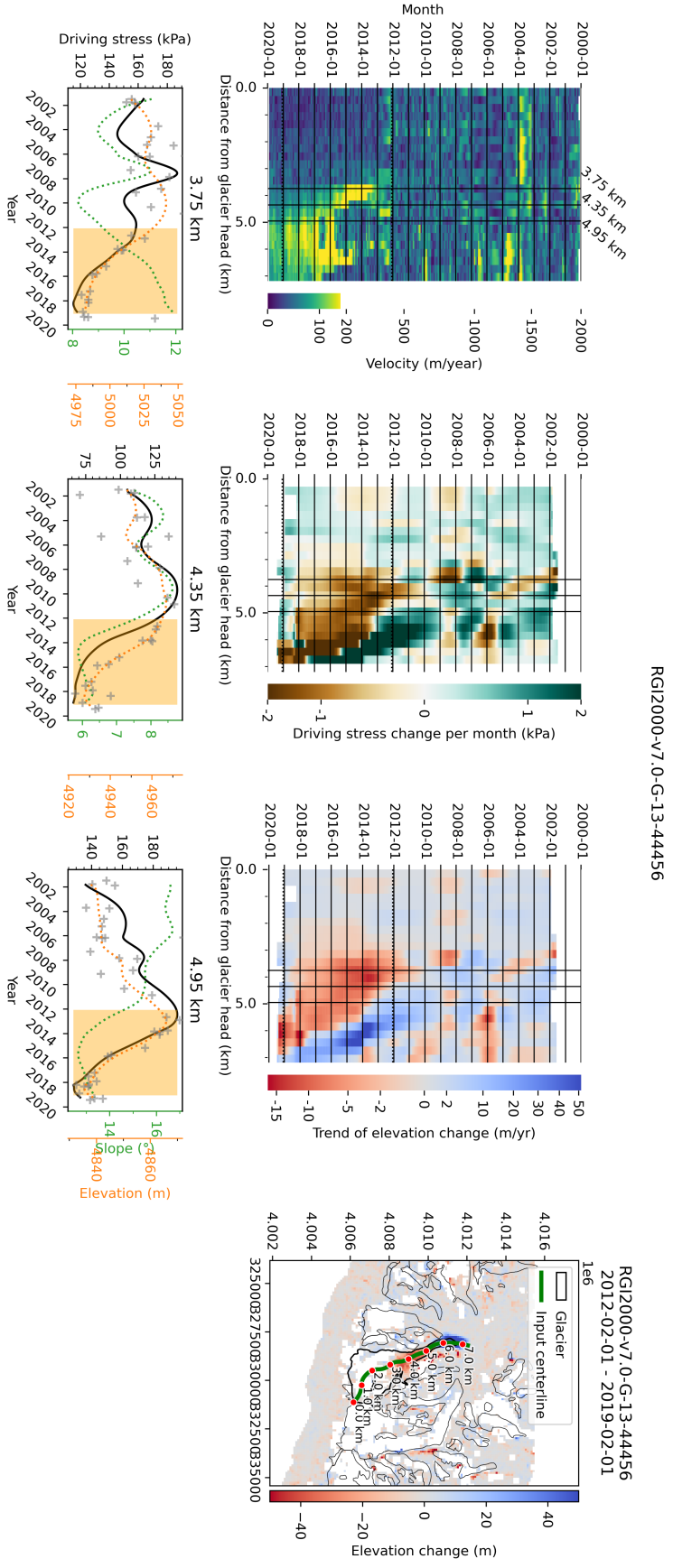

Figure B.30: Identical to Fig. 3.8, but for the glacier RGI2000-v7.0-G-13-44456, which is of type *Temporally ambiguous surge onset*

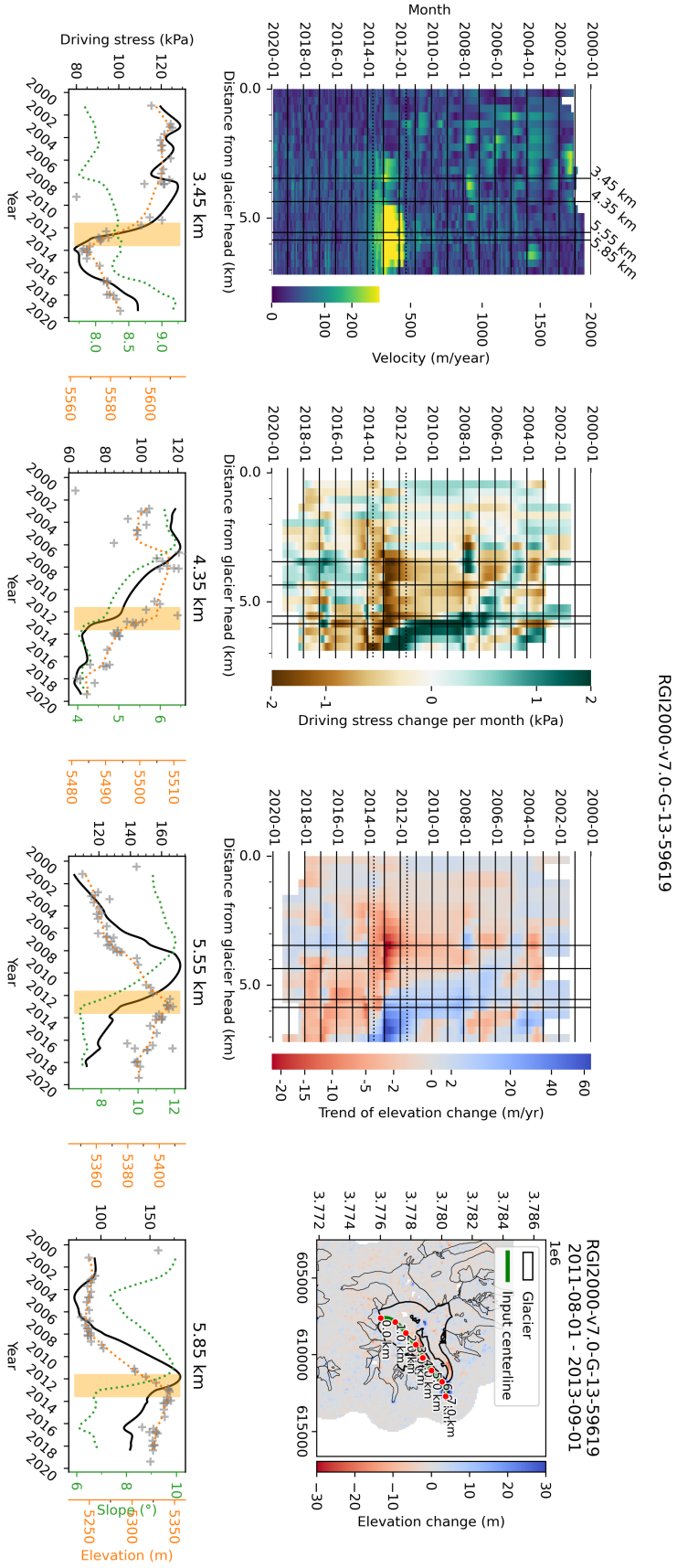

Figure B.31: Identical to Fig. 3.8, but for the glacier RGI2000-v7.0-G-13-59619, which is of type *Temporally ambiguous surge onset*

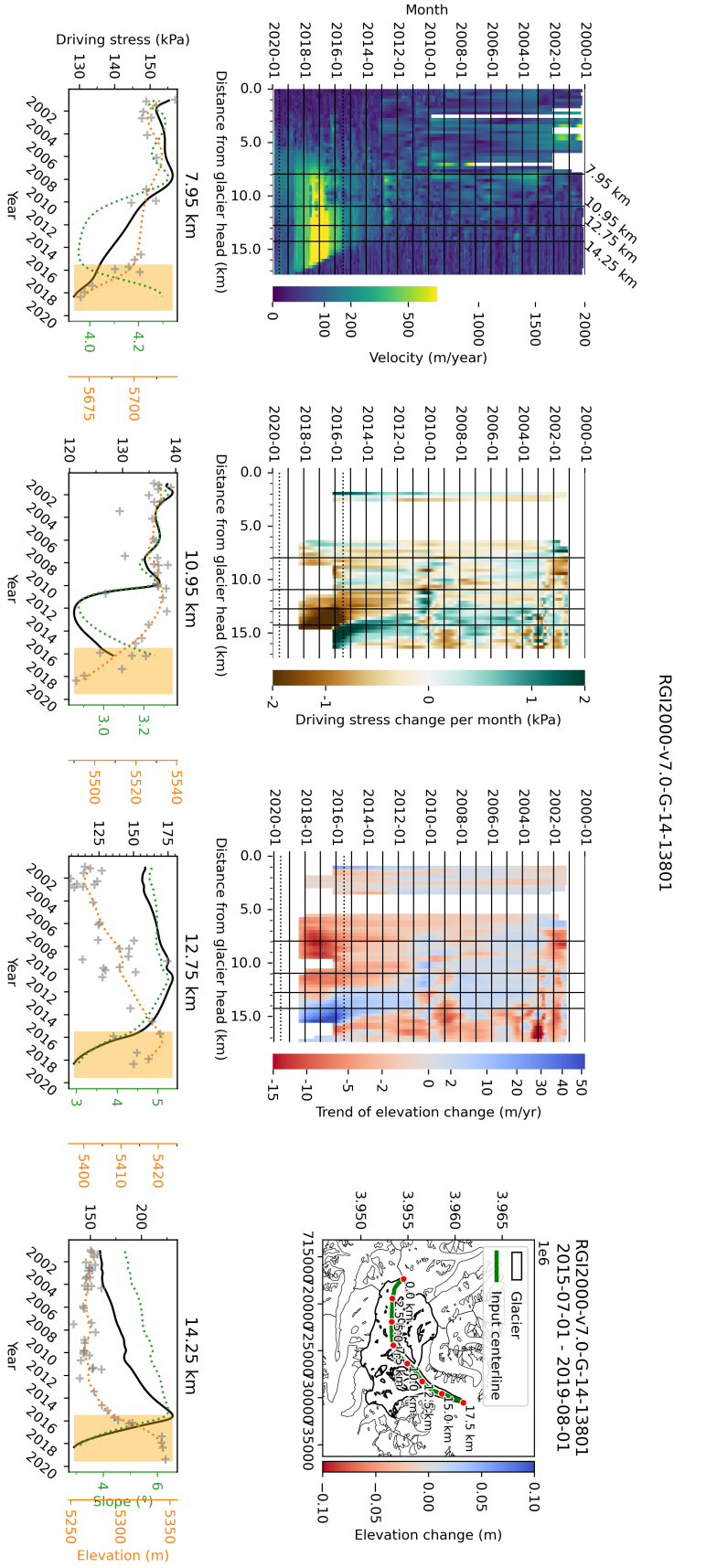

Figure B.32: Identical to Fig. 3.8, but for the glacier RGI2000-v7.0-G-14-13801, which is of type *Temporally ambiguous surge onset*

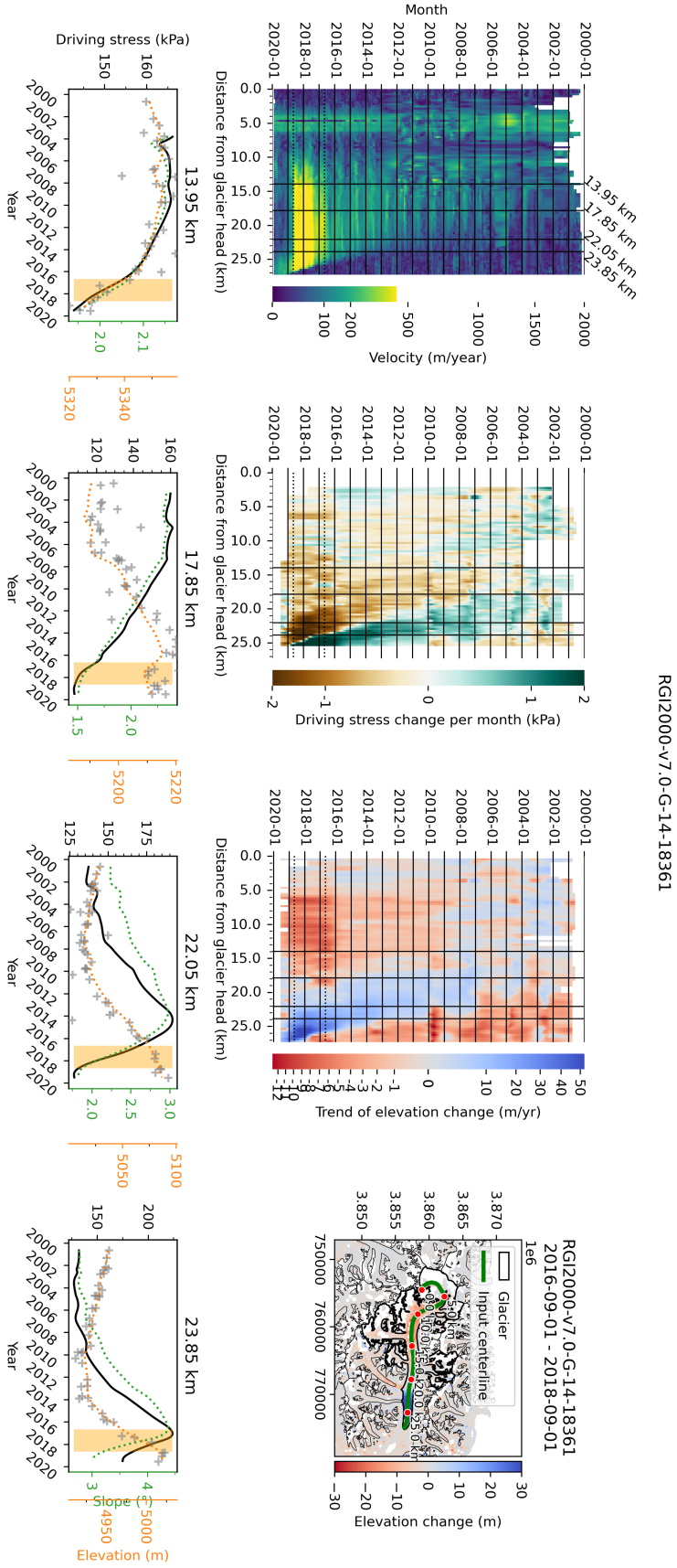

Figure B.33: Identical to Fig. 3.8, but for the glacier RGI2000-v7.0-G-14-18361, which is of type *Temporally ambiguous surge onset*

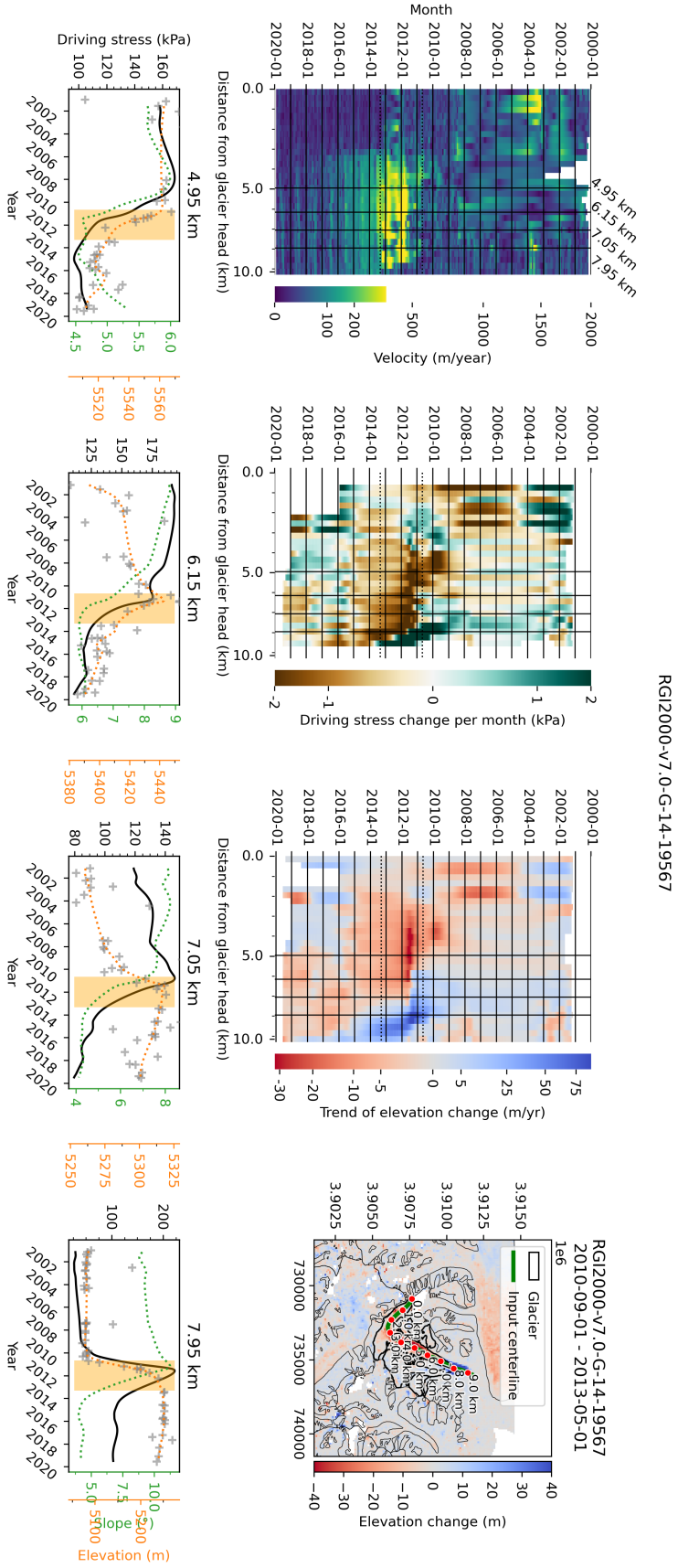

Figure B.34: Identical to Fig. 3.8, but for the glacier RGI2000-v7.0-G-14-19567, which is of type *Temporally ambiguous surge onset*

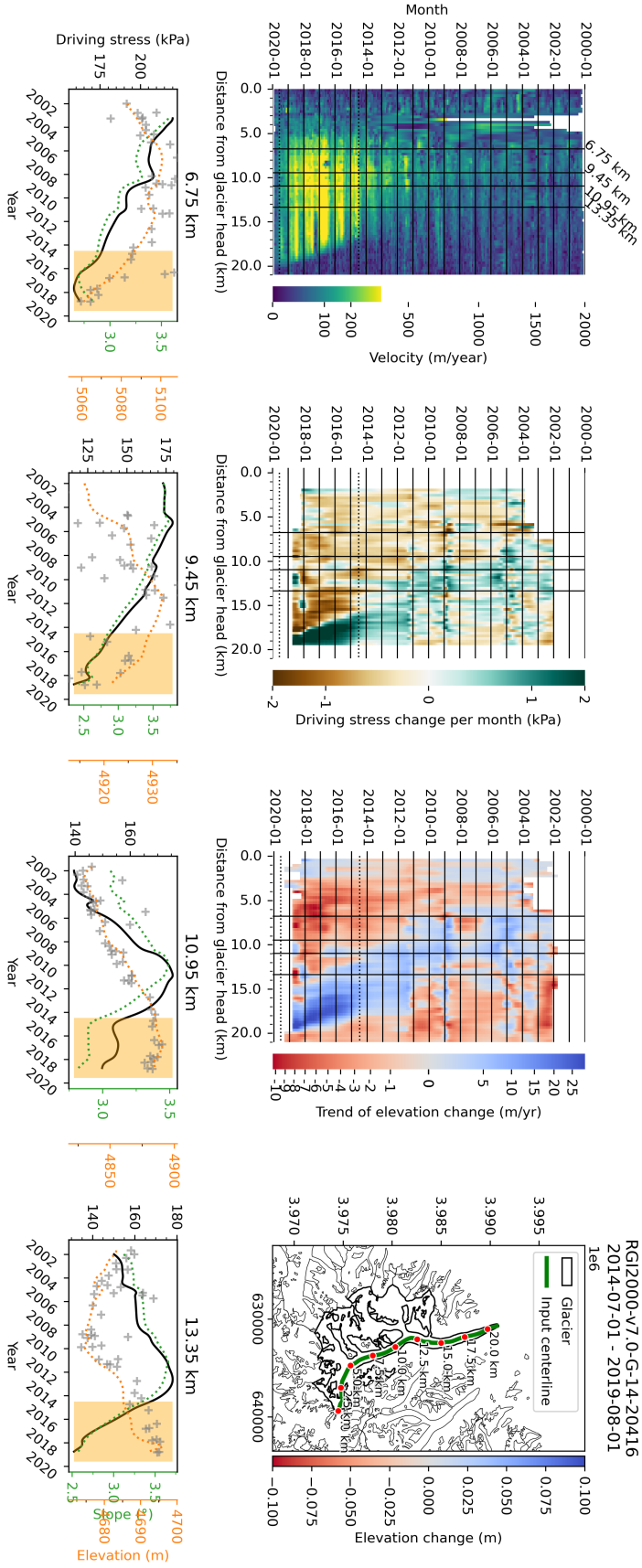

Figure B.35: Identical to Fig. 3.8, but for the glacier RGI2000-v7.0-G-14-20416, which is of type *Temporally ambiguous surge onset*

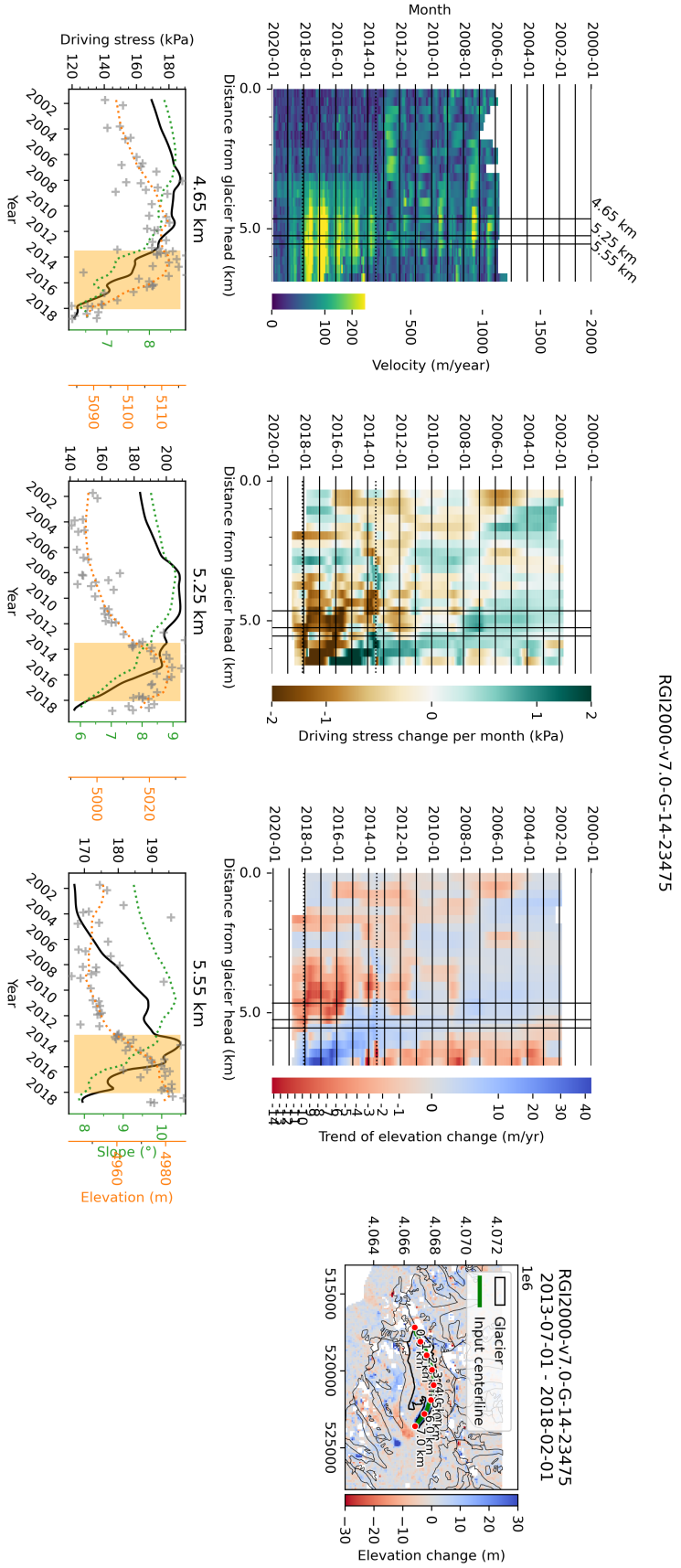

Figure B.36: Identical to Fig. 3.8, but for the glacier RGI2000-v7.0-G-14-23475, which is of type *Temporally ambiguous surge onset*

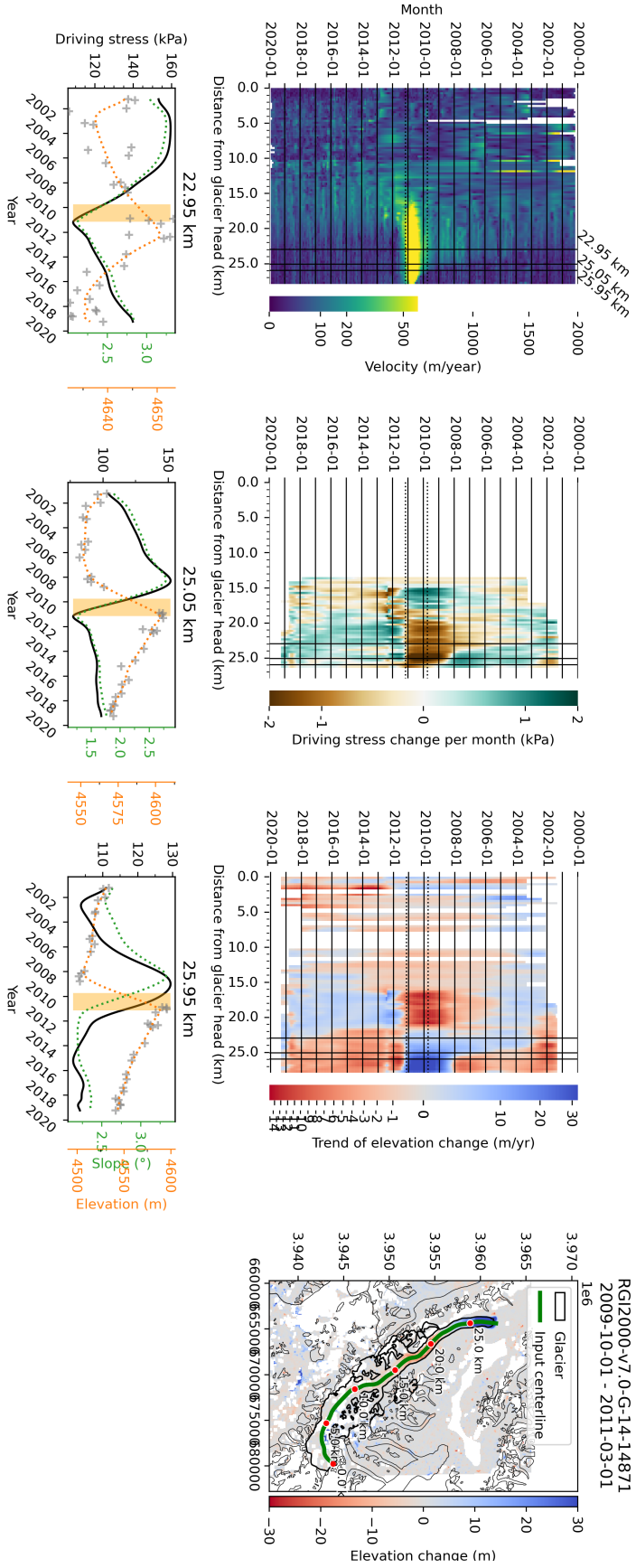

Figure B.37: Identical to Fig. 3.8, but for the glacier RGI2000-v7.0-G-14-14871, which is of type *Temporally ambiguous surge onset*

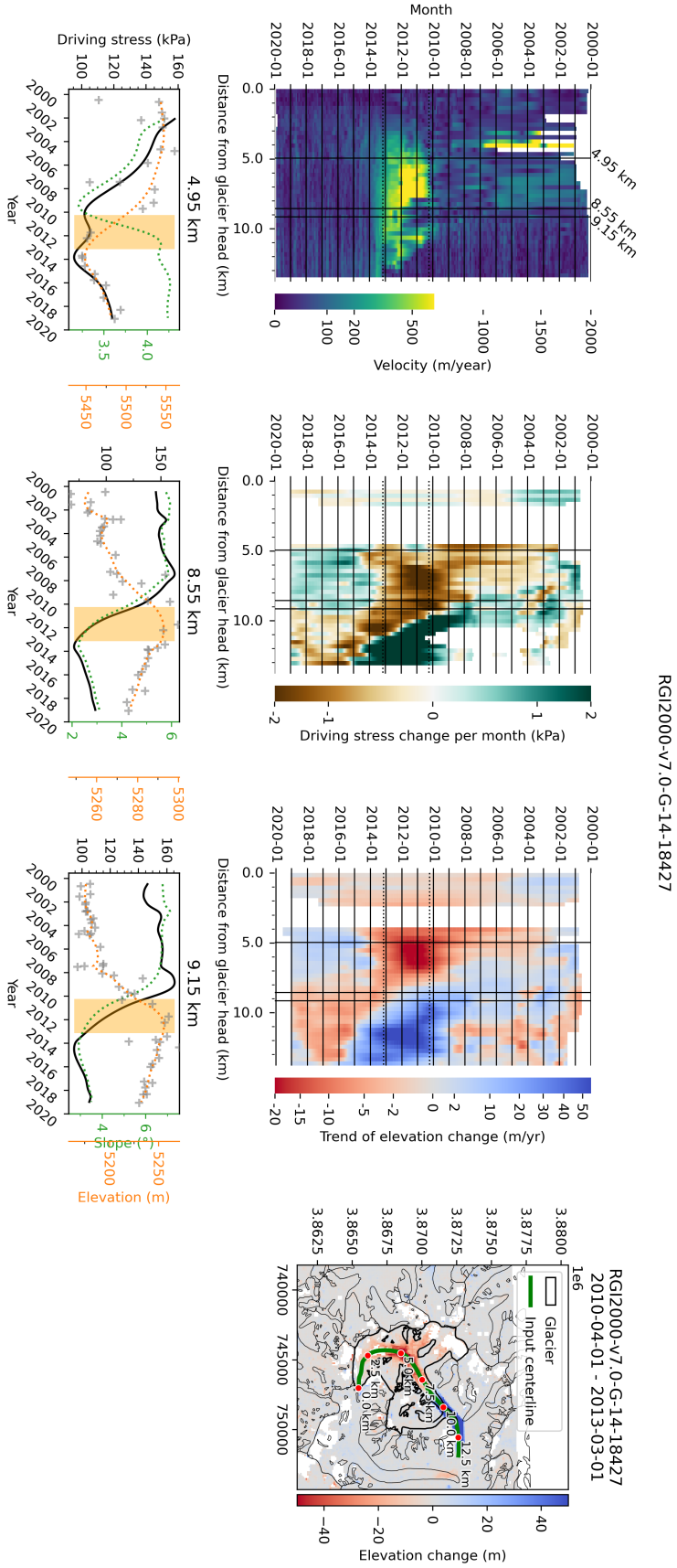

Figure B.38: Identical to Fig. 3.8, but for the glacier RGI2000-v7.0-G-14-18427, which is of type *Temporally ambiguous surge onset*

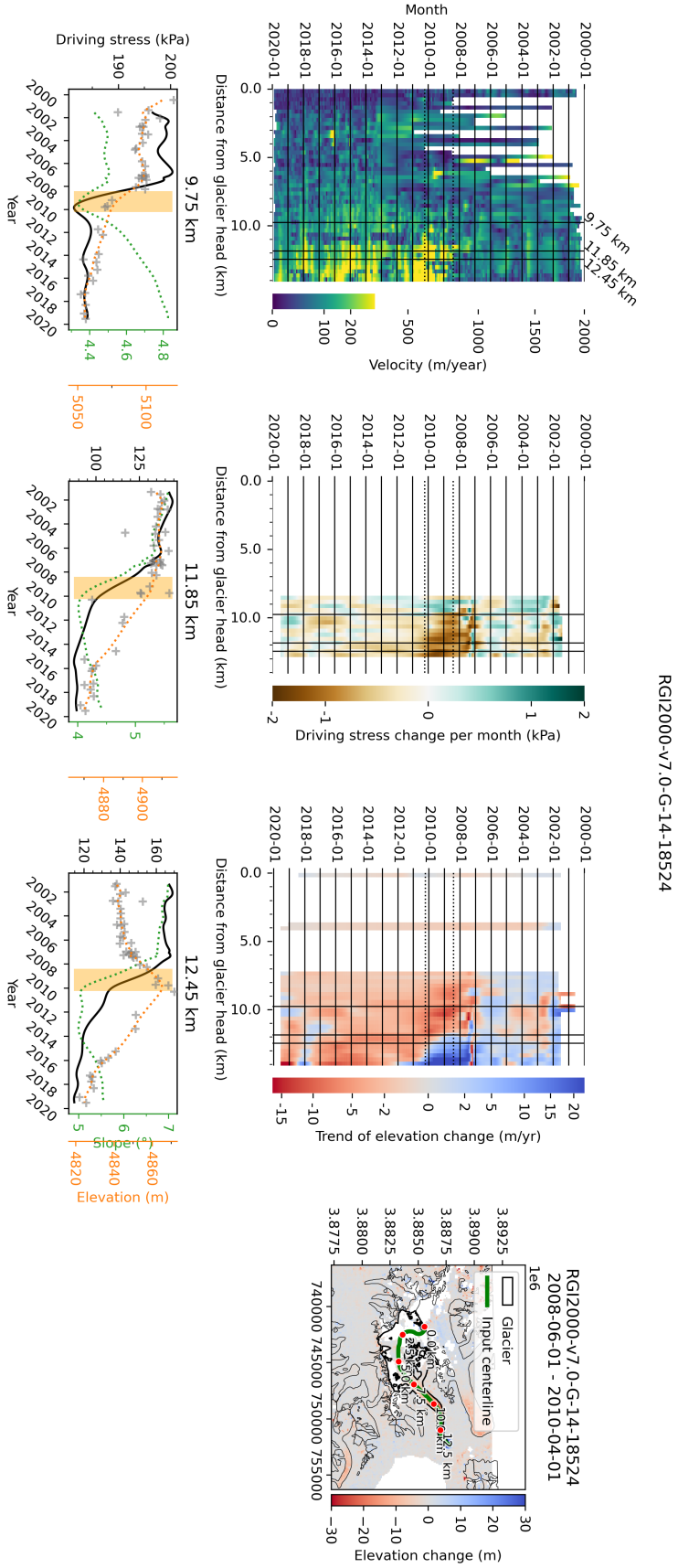

Figure B.39: Identical to Fig. 3.8, but for the glacier RGI2000-v7.0-G-14-18524, which is of type *Hydraulically-driven surge*

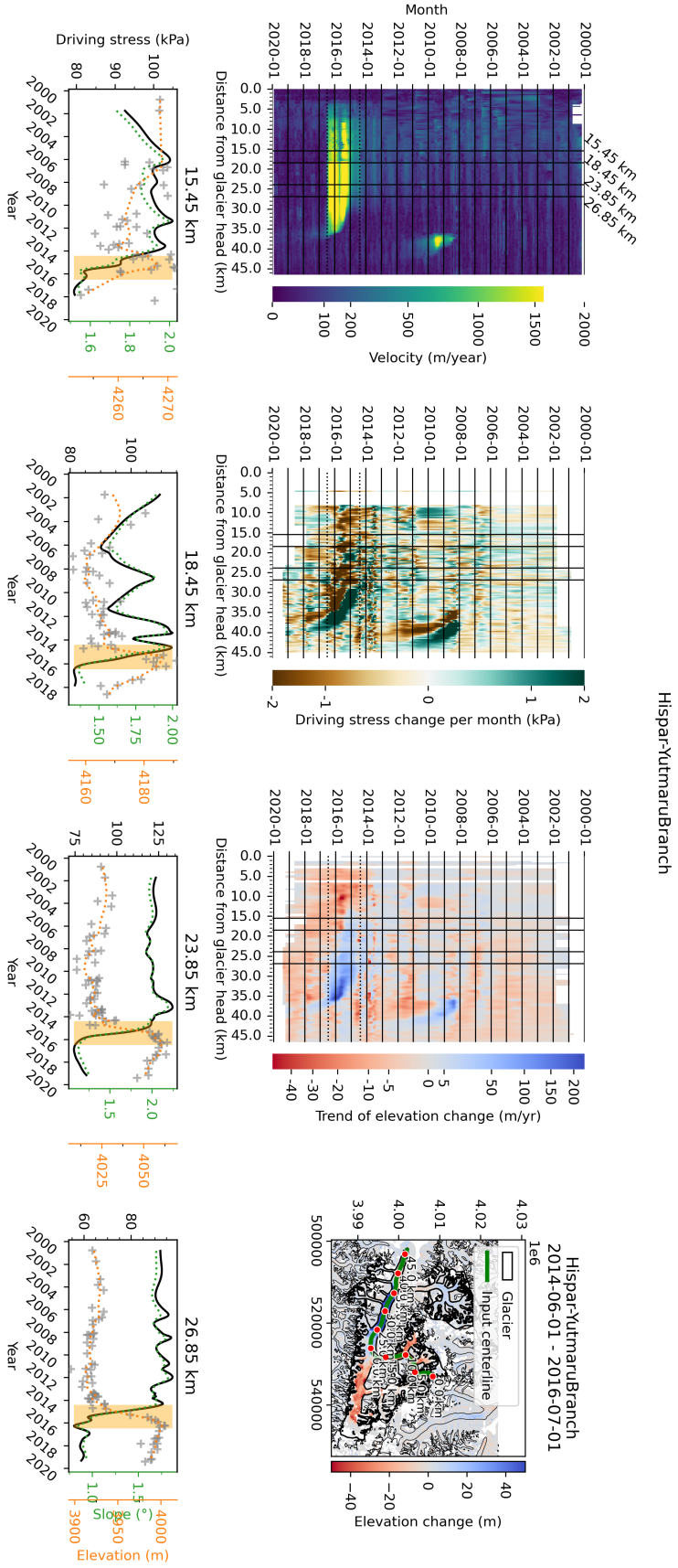

Figure B.40: Identical to Fig. 3.8, but for the Yutmaru branch of the Hispar glacier, which is of type *Hydraulically-driven surge*

Appendix C

Appendix - List of publications

C.1 List of publications related to my thesis work.

C.1.1 Publications as first author

- Content of Chapter 2: Beraud et al. (2025)
  Beraud, L., Brun, F., Dehecq, A., Hugonnet, R., and Shekhar, P.: Glacier surge monitoring from temporally dense elevation time series: application to an ASTER dataset over the Karakoram region, The Cryosphere, 19, 5075–5094, doi:https://doi.org/10.5194/tc-19-5075-2025, 2025.
  Associated repository of the code and the dataset: Beraud et al. (2024)
  Beraud, L., Brun, F., Dehecq, A., Hugonnet, R., and Shekhar, P.: Data and code for the publication of a surge-specific DEM workflow on ASTER DEMs., doi:https://doi.org/10.5281/zenodo.14045604 , 2024.

- Content of Chapter 3: in preparation

C.1.2 Publications as co-author

- Brun et al. (2025)
  Brun, F., Lambrecht, A., Mayer, C., Rezaei, J., Dehecq, A., **Beraud, L.**, Deschamps-Berger, C., Berthier, E., Völksen, C., and Kayumov, A.: Multi-temporal elevation changes of Fedchenko Glacier, Tajikistan, from 1928 to 2021, Journal of Glaciology, 71, e45, doi:https://doi.org/10.1017/jog.2024.101, 2025.

- Guo et al. (2025)
  Guo, L., Li, J., Charrier, L., Dehecq, A., **Beraud, L.**, Li, Z., Li, X., Zhu, J., Li, L., and Wang, Y.: Surging Processes and Mechanisms at Small Glaciers in the Qilian Mountains, Northwestern China, Revealed by Long-Term, Temporally Dense Remote Sensing Observations, Journal of Geophysical Research: Earth Surface, 130, e2024JF008 157, doi:https://doi.org/10.1029/2024JF008157, 2025.

Bibliography

Abe, T. and Furuya, M.: Winter speed-up of quiescent surge-type glaciers in Yukon, Canada, The Cryosphere, 9, 1183–1190, doi:10.5194/tc-9-1183-2015, URL https://tc.copernicus.org/articles/9/1183/2015/, 2015.

Allstadt, K. E., Shean, D. E., Campbell, A., Fahnestock, M., and Malone, S. D.: Observations of seasonal and diurnal glacier velocities at Mount Rainier, Washington, using terrestrial radar interferometry, The Cryosphere, 9, 2219–2235, doi:10.5194/tc-9-2219-2015, URL https://tc.copernicus.org/articles/9/2219/2015/, 2015.

Altena, B., Scambos, T., Fahnestock, M., and Kääb, A.: Extracting recent short-term glacier velocity evolution over southern Alaska and the Yukon from a large collection of Landsat data, The Cryosphere, 13, 795–814, doi:10.5194/tc-13-795-2019, URL https://tc.copernicus.org/articles/13/795/2019/, 2019.

Armstrong, W. H., Anderson, R. S., and Fahnestock, M. A.: Spatial Patterns of Summer Speedup on South Central Alaska Glaciers, Geophysical Research Letters, 44, 9379–9388, doi:10.1002/2017GL074370, URL https://agupubs.onlinelibrary.wiley.com/doi/10.1002/2017GL074370, 2017.

Auriac, A., Sigmundsson, F., Hooper, A., Spaans, K. H., Björnsson, H., Pálsson, F., Pinel, V., and Feigl, K. L.: InSAR observations and models of crustal deformation due to a glacial surge in Iceland, Geophysical Journal International, 198, 1329–1341, doi:10.1093/gji/ggu205, URL http://academic.oup.com/gji/article/198/3/1329/585587/InSAR-observations-and-models-of-crustal, 2014.

Aðalgeirsdóttir, G., Björnsson, H., Pálsson, F., and Magnússon, E.: Analyses of a surging outlet glacier of Vatnajökull ice cap, Iceland, Annals of Glaciology, 42, 23–28, doi:10.3189/172756405781812934, URL https://www.cambridge.org/core/product/identifier/S0260305500264781/type/journal_article, 2005.

Banerjee, D., Garg, V., and Thakur, P. K.: Geospatial investigation on transitional (quiescence to surge initiation) phase dynamics of Monacobreen tidewater glacier, Svalbard, Advances in Space Research, 69, 1813–1839, doi:10.1016/j.asr.2021.08.020, URL https://linkinghub.elsevier.com/retrieve/pii/S0273117721006700, 2022.

Bazai, N. A., Cui, P., Carling, P. A., Wang, H., Hassan, J., Liu, D., Zhang, G., and Jin, W.: Increasing glacial lake outburst flood hazard in response to surge glaciers in the Karakoram, Earth-Science Reviews, 212, 103 432, doi:10.1016/j.earscirev.2020.103432, URL https://linkinghub.elsevier.com/retrieve/pii/S0012825220304785, 2021.

Beaud, F., Aati, S., Delaney, I., Adhikari, S., and Avouac, J.-P.: Surge dynamics of Shisper Glacier revealed by time-series correlation of optical satellite images and their utility to substantiate a generalized sliding law, The Cryosphere, 16, 3123–3148, doi:10.5194/tc-16-3123-2022, URL https://tc.copernicus.org/articles/16/3123/2022/, 2022.

Benn, D. I., Fowler, A. C., Hewitt, I., and Sevestre, H.: A general theory of glacier surges, Journal of Glaciology, 65, 701–716, doi:10.1017/jog.2019.62, URL https://www.cambridge.org/core/product/identifier/S0022143019000625/type/journal_article, 2019a.

Benn, D. I., Jones, R. L., Luckman, A., Fürst, J. J., Hewitt, I., and Sommer, C.: Mass and enthalpy budget evolution during the surge of a polythermal glacier: a test of theory, Journal of Glaciology, 65, 717–731, doi:10.1017/jog.2019.63, URL https://www.cambridge.org/core/product/identifier/S0022143019000637/type/journal_article, 2019b.

Benn, D. I., Hewitt, I. J., and Luckman, A. J.: Enthalpy balance theory unifies diverse glacier surge behaviour, Annals of Glaciology, pp. 1–7, doi:10.1017/aog.2023.23, URL https://www.cambridge.org/core/product/identifier/S026030552300023X/type/journal_article, 2023.

Beraud, L., Brun, F., Dehecq, A., Hugonnet, R., and Shekhar, P.: Data and code for the publication of a surge-specific DEM workflow on ASTER DEMs., doi:10.5281/zenodo.14045604, URL https://zenodo.org/doi/10.5281/zenodo.14045604, 2024.

Beraud, L., Brun, F., Dehecq, A., Hugonnet, R., and Shekhar, P.: Glacier surge monitoring from temporally dense elevation time series: application to an ASTER dataset over the Karakoram region, The Cryosphere, 19, 5075–5094, doi:10.5194/tc-19-5075-2025, URL https://tc.copernicus.org/articles/19/5075/2025/, 2025.

Berthier, E. and Brun, F.: Karakoram geodetic glacier mass balances between 2008 and 2016: persistence of the anomaly and influence of a large rock avalanche on Siachen Glacier, Journal of Glaciology, 65, 494–507, doi:10.1017/jog.2019.32, URL https://www.cambridge.org/core/product/identifier/S0022143019000327/type/journal_article, 2019.

Berthier, E., Vincent, C., Magnússon, E., Gunnlaugsson, A. T., Pitte, P., Le Meur, E., Masiokas, M., Ruiz, L., Pálsson, F., Belart, J. M. C., and Wagnon, P.: Glacier topography and elevation changes derived from Pléiades sub-meter stereo images, The Cryosphere, 8, 2275–2291, doi:10.5194/tc-8-2275-2014, URL https://tc.copernicus.org/articles/8/2275/2014/, 2014.

Berthier, E., Floriciou, D., Gardner, A. S., Gourmelen, N., Jakob, L., Paul, F., Treichler, D., Wouters, B., Belart, J. M. C., Dehecq, A., Dussaillant, I., Hugonnet, R., Kääb, A., Krieger, L., Pálsson, F., and Zemp, M.: Measuring glacier mass changes from space—a review, Reports on Progress in Physics, 86, 036 801, doi:10.1088/1361-6633/acaf8e, URL https://iopscience.iop.org/article/10.1088/1361-6633/acaf8e, 2023.

Berthier, E., Kargel, J. S., Raup, B., and Zemp, M.: Earth-surface monitoring is at risk — more imaging tools are urgently needed, Nature, 630, 563–563, doi:10.1038/d41586-024-02052-x, URL https://www.nature.com/articles/d41586-024-02052-x, 2024a.

Berthier, E., Lebreton, J., Fontannaz, D., Hosford, S., Belart, J. M.-C., Brun, F., Andreassen, L. M., Menounos, B., and Blondel, C.: The Pléiades Glacier Observatory: high-resolution digital elevation models and ortho-imagery to monitor glacier change, The Cryosphere, 18, 5551–5571, doi:10.5194/tc-18-5551-2024, URL https://tc.copernicus.org/articles/18/5551/2024/, 2024b.

Bhambri, R., Hewitt, K., Kawishwar, P., and Pratap, B.: Surge-type and surge-modified glaciers in the Karakoram, Scientific Reports, 7, 15 391, doi:10.1038/s41598-017-15473-8, URL http://www.nature.com/articles/s41598-017-15473-8, 2017.

Bhambri, R., Watson, C. S., Hewitt, K., Haritashya, U. K., Kargel, J. S., Pratap Shahi, A., Chand, P., Kumar, A., Verma, A., and Govil, H.: The hazardous 2017–2019 surge and river damming by Shispare Glacier, Karakoram, Scientific Reports, 10, 4685, doi:10.1038/s41598-020-61277-8, URL http://www.nature.com/articles/s41598-020-61277-8, 2020.

Bhambri, R., Hewitt, K., Haritashya, U. K., Chand, P., Kumar, A., Verma, A., Tiwari, S. K., and Rai, S. K.: Characteristics of surge-type tributary glaciers, Karakoram, Geomorphology, 403, 108 161, doi:10.1016/j.geomorph.2022.108161, URL https://linkinghub.elsevier.com/retrieve/pii/S0169555X2200054X, 2022.

Bhattacharya, A., Bolch, T., Mukherjee, K., King, O., Menounos, B., Kapitsa, V., Neckel, N., Yang, W., and Yao, T.: High Mountain Asian glacier response to climate revealed by multi-temporal satellite observations since the 1960s, Nature Communications, 12, 4133, doi:10.1038/s41467-021-24180-y, URL https://www.nature.com/articles/s41467-021-24180-y, 2021.

Bindschadler, R.: The Importance of Pressurized Subglacial Water in Separation and Sliding at the Glacier Bed, Journal of Glaciology, 29, 3–19, doi:10.3189/S0022143000005104, URL https://www.cambridge.org/core/product/identifier/S0022143000005104/type/journal_article, 1983.

Björnsson, H., Pálsson, F., Sigurđsson, O., and Flowers, G. E.: Surges of glaciers in Iceland, Annals of Glaciology, 36, 82–90, doi:10.3189/172756403781816365, URL https://www.cambridge.org/core/product/identifier/S0260305500259260/type/journal_article, 2003.

Bolch, T., Shea, J. M., Liu, S., Azam, F. M., Gao, Y., Gruber, S., Immerzeel, W. W., Kulkarni, A., Li, H., Tahir, A. A., Zhang, G., and Zhang, Y.: Status and Change of the Cryosphere in the Extended Hindu Kush Himalaya Region, in: The Hindu Kush Himalaya Assessment, edited by Wester, P., Mishra, A., Mukherji, A., and Shrestha, A. B., pp. 209–255, Springer International Publishing, Cham, 2019.

Bradwell, T. and Benn, D. I.: Repeated surging and rapid retreat of a tidewater glacier in Scotland (Younger Dryas/Greenland Stadial 1), Journal of Quaternary Science, 40, 622–633, doi:10.1002/jqs.3701, URL https://onlinelibrary.wiley.com/doi/10.1002/jqs.3701, 2025.

Brun, F., Berthier, E., Wagnon, P., Kääb, A., and Treichler, D.: A spatially resolved estimate of High Mountain Asia glacier mass balances from 2000 to 2016, Nature Geoscience, 10, 668–673, doi:10.1038/ngeo2999, URL http://www.nature.com/articles/ngeo2999, 2017.

Brun, F., Wagnon, P., Berthier, E., Jomelli, V., Maharjan, S. B., Shrestha, F., and Kraaijenbrink, P. D. A.: Heterogeneous Influence of Glacier Morphology on the Mass Balance Variability in High Mountain Asia, Journal of Geophysical Research: Earth Surface, 124, 1331–1345, doi:10.1029/2018JF004838, URL https://agupubs.onlinelibrary.wiley.com/doi/10.1029/2018JF004838, 2019.

Brun, F., Lambrecht, A., Mayer, C., Rezaei, J., Dehecq, A., Beraud, L., Deschamps-Berger, C., Berthier, E., Völksen, C., and Kayumov, A.: Multi-temporal elevation changes of

Fedchenko Glacier, Tajikistan, from 1928 to 2021, Journal of Glaciology, 71, e45, doi:10.1017/jog.2024.101, URL https://www.cambridge.org/core/product/identifier/S0022143024001011/type/journal_article, 2025.

Burgess, E. W., Forster, R. R., Larsen, C. F., and Braun, M.: Surge dynamics on Bering Glacier, Alaska, in 2008–2011, The Cryosphere, 6, 1251–1262, doi:10.5194/tc-6-1251-2012, URL https://tc.copernicus.org/articles/6/1251/2012/, 2012.

Charrier, L., Yan, Y., Koeniguer, E. C., Leinss, S., and Trouve, E.: Extraction of Velocity Time Series With an Optimal Temporal Sampling From Displacement Observation Networks, IEEE Transactions on Geoscience and Remote Sensing, 60, 1–10, doi:10.1109/TGRS.2021.3128289, URL https://ieeexplore.ieee.org/document/9618734/, 2022.

Charrier, L., Dehecq, A., Guo, L., Brun, F., Millan, R., Lioret, N., Copland, L., Maier, N., Dow, C., and Halas, P.: TICOI: an operational Python package to generate regular glacier velocity time series, The Cryosphere, 19, 4555–4583, doi:10.5194/tc-19-4555-2025, URL https://tc.copernicus.org/articles/19/4555/2025/, 2025.

Chen, M., Chen, Y., Fang, G., Zheng, G., Li, Z., Li, Y., and Zhu, Z.: Risk assessment of glacial lake outburst flood in the Central Asian Tienshan Mountains, npj Climate and Atmospheric Science, 7, 209, doi:10.1038/s41612-024-00755-6, URL https://www.nature.com/articles/s41612-024-00755-6, 2024.

Chudley, T. R. and Willis, I. C.: Glacier surges in the north-west West Kunlun Shan inferred from 1972 to 2017 Landsat imagery, Journal of Glaciology, 65, 1–12, doi:10.1017/jog.2018.94, URL https://www.cambridge.org/core/product/identifier/S0022143018000941/type/journal_article, 2019.

Chudley, T. R., Howat, I. M., King, M. D., and MacKie, E. J.: Increased crevassing across accelerating Greenland Ice Sheet margins, Nature Geoscience, 18, 148–153, doi:10.1038/s41561-024-01636-6, URL https://www.nature.com/articles/s41561-024-01636-6, 2025.

Cleveland, W. S. and Devlin, S. J.: Locally Weighted Regression: An Approach to Regression Analysis by Local Fitting, Journal of the American Statistical Association, 83, 596–610, doi:10.1080/01621459.1988.10478639, URL http://www.tandfonline.com/doi/abs/10.1080/01621459.1988.10478639, 1988.

Compagno, L., Huss, M., Zekollari, H., Miles, E. S., and Farinotti, D.: Future growth and decline of high mountain Asia's ice-dammed lakes and associated risk, Communications Earth & Environment, 3, 191, doi:10.1038/s43247-022-00520-8, URL https://www.nature.com/articles/s43247-022-00520-8, 2022.

Copland, L., Sharp, M. J., and Nienow, P. W.: Links between short-term velocity variations and the subglacial hydrology of a predominantly cold polythermal glacier, Journal of Glaciology, 49, 337–348, doi:10.3189/172756503781830656, URL https://www.cambridge.org/core/product/identifier/S0022143000210551/type/journal_article, 2003.

Copland, L., Sylvestre, T., Bishop, M. P., Shroder, J. F., Seong, Y. B., Owen, L. A., Bush, A., and Kamp, U.: Expanded and Recently Increased Glacier Surging in the Karakoram, Arctic, Antarctic, and Alpine Research, 43, 503–516, doi:10.1657/1938-4246-43.4.503, URL https://www.tandfonline.com/doi/full/10.1657/1938-4246-43.4.503, 2011.

Cressie, N. A. C., ed.: Statistics for spatial data, Wiley series in probability and mathematical statistics Applied probability and statistics, Wiley, New York, rev. ed edn., 1993.

Crompton, J. W., Flowers, G. E., and Stead, D.: Bedrock Fracture Characteristics as a Possible Control on the Distribution of Surge-Type Glaciers, Journal of Geophysical Research: Earth Surface, 123, 853–873, doi:10.1002/2017JF004505, URL https://onlinelibrary.wiley.com/doi/10.1002/2017JF004505, 2018.

Cuffey, K. M. and Paterson, W. S. B.: The Physics of Glaciers, Elsevier Science, Burlington, 4th ed edn., oCLC: 761646843, 2010.

De Paoli, L. and Flowers, G. E.: Dynamics of a small surge-type glacier using one-dimensional geophysical inversion, Journal of Glaciology, 55, 1101–1112, doi:10.3189/002214309790794850, URL https://www.cambridge.org/core/product/identifier/S002214300020676X/type/journal_article, 2009.

Dehecq, A., Gourmelen, N., Gardner, A. S., Brun, F., Goldberg, D., Nienow, P. W., Berthier, E., Vincent, C., Wagnon, P., and Trouvé, E.: Twenty-first century glacier slowdown driven by mass loss in High Mountain Asia, Nature Geoscience, 12, 22–27, doi:10.1038/s41561-018-0271-9, URL http://www.nature.com/articles/s41561-018-0271-9, 2019.

Dehecq, A., Gardner, A. S., Alexandrov, O., McMichael, S., Hugonnet, R., Shean, D., and Marty, M.: Automated Processing of Declassified KH-9 Hexagon Satellite Images for Global Elevation Change Analysis Since the 1970s, Frontiers in Earth Science, 8, 566 802, doi:10.3389/feart.2020.566802, URL https://www.frontiersin.org/articles/10.3389/feart.2020.566802/full, 2020.

Dehecq, A., Altena, B., Gardner, A. S., Trouvé, E., and Leinss, S.: Surface Displacement Measurement from Remote Sensing Images, Wiley, 1 edn., doi:10.1002/9781119986843, URL https://onlinelibrary.wiley.com/doi/book/10.1002/9781119986843, 2022.

Derkacheva, A., Mouginot, J., Millan, R., Maier, N., and Gillet-Chaulet, F.: Data Reduction Using Statistical and Regression Approaches for Ice Velocity Derived by Landsat-8, Sentinel-1 and Sentinel-2, Remote Sensing, 12, 1935, doi:10.3390/rs12121935, URL https://www.mdpi.com/2072-4292/12/12/1935, 2020.

Dieterich, J. H.: Modeling of rock friction: 1. Experimental results and constitutive equations, Journal of Geophysical Research: Solid Earth, 84, 2161–2168, doi:10.1029/JB084iB05p02161, URL https://agupubs.onlinelibrary.wiley.com/doi/10.1029/JB084iB05p02161, 1979.

Dunse, T., Schellenberger, T., Hagen, J. O., Kääb, A., Schuler, T. V., and Reijmer, C. H.: Glacier-surge mechanisms promoted by a hydro-thermodynamic feedback to summer melt, The Cryosphere, 9, 197–215, doi:10.5194/tc-9-197-2015, URL https://tc.copernicus.org/articles/9/197/2015/, 2015.

Echelmeyer, K., Butterfield, R., and Cuillard, D.: Some Observations on a Recent Surge of Peters Glacier, Alaska, U.S.A., Journal of Glaciology, 33, 341–345, doi:10.3189/S0022143000008935, URL https://www.cambridge.org/core/product/identifier/S0022143000008935/type/journal_article, 1987.

Eisen, O., Harrison, W. D., and Raymond, C. F.: The surges of Variegated Glacier, Alaska, U.S.A., and their connection to climate and mass balance, Journal of Glaciology, 47,

351–358, doi:10.3189/172756501781832179, URL https://www.cambridge.org/core/product/identifier/S0022143000211076/type/journal_article, 2001.

Eisen, O., Harrison, W. D., Raymond, C. F., Echelmeyer, K. A., Bender, G. A., and Gorda, J. L.: Variegated Glacier, Alaska, USA: a century of surges, Journal of Glaciology, 51, 399–406, doi:10.3189/172756505781829250, URL https://www.cambridge.org/core/product/identifier/S0022143000209477/type/journal_article, 2005.

Engeln, O. D. V.: Glacial geomorphology and glacier motion, American Journal of Science, s5-35, 426–440, doi:10.2475/ajs.s5-35.210.426, URL https://ajsonline.org/article/61154, 1938.

European Space Agency and Airbus: Copernicus DEM, doi:10.5270/ESA-c5d3d65, URL https://spacedata.copernicus.eu/collections/copernicus-digital-elevation-model, institution: European Space Agency, 2022.

Falaschi, D., Bolch, T., Lenzano, M. G., Tadono, T., Lo Vecchio, A., and Lenzano, L.: New evidence of glacier surges in the Central Andes of Argentina and Chile, Progress in Physical Geography: Earth and Environment, 42, 792–825, doi:10.1177/0309133318803014, URL https://journals.sagepub.com/doi/10.1177/0309133318803014, 2018.

Farinotti, D., Huss, M., Fürst, J. J., Landmann, J., Machguth, H., Maussion, F., and Pandit, A.: A consensus estimate for the ice thickness distribution of all glaciers on Earth, Nature Geoscience, 12, 168–173, doi:10.1038/s41561-019-0300-3, URL http://www.nature.com/articles/s41561-019-0300-3, 2019.

Farinotti, D., Immerzeel, W. W., de Kok, R. J., Quincey, D. J., and Dehecq, A.: Manifestations and mechanisms of the Karakoram glacier Anomaly, Nature Geoscience, 13, 8–16, doi:10.1038/s41561-019-0513-5, URL http://www.nature.com/articles/s41561-019-0513-5, 2020.

Fatland, D. R. and Lingle, C. S.: Analysis of the 1993-95 Bering Glacier (Alaska) surge using differential SAR interferometry, Journal of Glaciology, 44, 532–546, doi:10.3189/S0022143000002057, URL https://www.cambridge.org/core/product/identifier/S0022143000002057/type/journal_article, 1998.

Fatland, D. R. and Lingle, C. S.: InSAR observations of the 1993–95 Bering Glacier (Alaska, U.S.A.) surge and a surge hypothesis, Journal of Glaciology, 48, 439–451, doi:10.3189/172756502781831296, URL https://www.cambridge.org/core/product/identifier/S002214300021188X/type/journal_article, 2002.

Flink, A. E., Noormets, R., Kirchner, N., Benn, D. I., Luckman, A., and Lovell, H.: The evolution of a submarine landform record following recent and multiple surges of Tunabreen glacier, Svalbard, Quaternary Science Reviews, 108, 37–50, doi:10.1016/j.quascirev.2014.11.006, URL https://linkinghub.elsevier.com/retrieve/pii/S0277379114004442, 2015.

Fowler, A. C.: A theory of glacier surges, Journal of Geophysical Research: Solid Earth, 92, 9111–9120, doi:10.1029/JB092iB09p09111, URL https://agupubs.onlinelibrary.wiley.com/doi/10.1029/JB092iB09p09111, 1987.

Fowler, A. C., Murray, T., and Ng, F. S. L.: Thermally controlled glacier surging, Journal of Glaciology, 47, 527–538, doi:10.3189/172756501781831792, URL https://www.cambridge.org/core/product/identifier/S0022143000212392/type/journal_article, 2001.

Frappé, T.-P. and Clarke, G. K. C.: Slow surge of Trapridge Glacier, Yukon Territory, Canada, Journal of Geophysical Research, 112, F03S32, doi:10.1029/2006JF000607, URL http://doi.wiley.com/10.1029/2006JF000607, 2007.

Gagliardini, O., Cohen, D., Råback, P., and Zwinger, T.: Finite-element modeling of subglacial cavities and related friction law, Journal of Geophysical Research: Earth Surface, 112, 2006JF000 576, doi:10.1029/2006JF000576, URL https://agupubs.onlinelibrary.wiley.com/doi/10.1029/2006JF000576, 2007.

Gao, Y., Liu, S., Qi, M., Yao, X., Zhu, Y., Xie, F., Wu, K., and Saifullah, M.: The Evolution of the Glacier Surges in the Tuanjie Peak, the Qilian Mountains, Remote Sensing, 14, 852, doi:10.3390/rs14040852, URL https://www.mdpi.com/2072-4292/14/4/852, 2022.

Gao, Y., Wang, J., Liu, S., Yao, X., Qi, M., Liang, P., Xie, F., Mu, J., and Ma, X.: Monitoring dynamics of Kyagar Glacier surge and repeated draining of Ice-dammed lake using multi-source remote sensing, Science of The Total Environment, 928, 172 467, doi:10.1016/j.scitotenv.2024.172467, URL https://linkinghub.elsevier.com/retrieve/pii/S0048969724026135, 2024.

Gao, Y.-P., Liu, S.-Y., Wang, J.-L., Yao, X.-J., Qi, M.-M., Liang, P.-B., Mu, J.-X., Ma, X.-G., Zhu, Y., Xie, F.-M., Jiang, Z.-L., and Zhang, Z.: Characteristics of Musta Glacier surges and their responses to climate change between 1976 and 2023, Advances in Climate Change Research, 16, 125–140, doi:10.1016/j.accre.2024.12.007, URL https://linkinghub.elsevier.com/retrieve/pii/S1674927824001849, 2025.

Gardelle, J., Berthier, E., Arnaud, Y., and Kääb, A.: Region-wide glacier mass balances over the Pamir-Karakoram-Himalaya during 1999–2011, The Cryosphere, 7, 1263–1286, doi:10.5194/tc-7-1263-2013, URL https://tc.copernicus.org/articles/7/1263/2013/, 2013.

Gardner, A., Fahnestock, M., Greene, C., Kennedy, J., Liukis, M., Lopez, L., and Scambos, T.: MEASURES ITS_LIVE Regional Glacier and Ice Sheet Surface Velocities, Version 2, Product used: Global Image-pair Velocities, doi:10.5067/JQ6337239C96, URL https://nsidc.org/data/nsidc-0776/versions/2, 2024.

Gardner, A. S., Greene, C. A., Kennedy, J. H., Fahnestock, M. A., Liukis, M., López, L. A., Lei, Y., Scambos, T. A., and Dehecq, A.: ITS_LIVE global glacier velocity data in near-real time, The Cryosphere, 19, 3517–3533, doi:10.5194/tc-19-3517-2025, URL https://tc.copernicus.org/articles/19/3517/2025/, 2025.

Gilbert, A., Gimbert, F., Thøgersen, K., Schuler, T. V., and Kääb, A.: A Consistent Framework for Coupling Basal Friction With Subglacial Hydrology on Hard-Bedded Glaciers, Geophysical Research Letters, 49, doi:10.1029/2021GL097507, URL https://onlinelibrary.wiley.com/doi/10.1029/2021GL097507, 2022.

Girod, L., Nuth, C., Kääb, A., McNabb, R., and Galland, O.: MMASTER: Improved ASTER DEMs for Elevation Change Monitoring, Remote Sensing, 9, 704, doi:10.3390/rs9070704, URL https://www.mdpi.com/2072-4292/9/7/704, 2017.

Glasser, N. F., Quincey, D. J., and King, O.: Changes in ice-surface debris, surface elevation and mass through the active phase of selected Karakoram glacier surges, Geomorphology, 410, 108 291, doi:10.1016/j.geomorph.2022.108291, URL https://linkinghub.elsevier.com/retrieve/pii/S0169555X22001842, 2022.

Goerlich, F., Bolch, T., Mukherjee, K., and Pieczonka, T.: Glacier Mass Loss during the 1960s and 1970s in the Ak-Shirak Range (Kyrgyzstan) from Multiple Stereoscopic Corona and Hexagon Imagery, Remote Sensing, 9, 275, doi:10.3390/rs9030275, URL https://www.mdpi.com/2072-4292/9/3/275, 2017.

Goerlich, F., Bolch, T., and Paul, F.: More dynamic than expected: an updated survey of surging glaciers in the Pamir, Earth System Science Data, 12, 3161–3176, doi:10.5194/essd-12-3161-2020, URL https://essd.copernicus.org/articles/12/3161/2020/, 2020.

Grant, K. L., Stokes, C. R., and Evans, I. S.: Identification and characteristics of surge-type glaciers on Novaya Zemlya, Russian Arctic, Journal of Glaciology, 55, 960–972, doi:10.3189/002214309790794940, URL https://www.cambridge.org/core/product/identifier/S0022143000206631/type/journal_article, 2009.

Gray, L., Burgess, D., Copland, L., Demuth, M. N., Dunse, T., Langley, K., and Schuler, T. V.: CryoSat-2 delivers monthly and inter-annual surface elevation change for Arctic ice caps, The Cryosphere, 9, 1895–1913, doi:10.5194/tc-9-1895-2015, URL https://tc.copernicus.org/articles/9/1895/2015/, 2015.

Guillet, G., King, O., Lv, M., Ghuffar, S., Benn, D., Quincey, D., and Bolch, T.: A regionally resolved inventory of High Mountain Asia surge-type glaciers, derived from a multi-factor remote sensing approach, The Cryosphere, 16, 603–623, doi:10.5194/tc-16-603-2022, URL https://tc.copernicus.org/articles/16/603/2022/, 2022.

Guillet, G., Benn, D., King, O., Shean, D., Mannerfelt, E. S., and Hugonnet, R.: Global detection of glacier surges from surface velocities, elevation change, and SAR backscatter data between 2000 and 2024 : a test of surge mechanism theories, Journal of Glaciology, pp. 1–41, doi:10.1017/jog.2025.10065, URL https://www.cambridge.org/core/product/identifier/S0022143025100658/type/journal_article, 2025.

Guo, L., Li, J., Li, Z., Wu, L., Li, X., Hu, J., Li, H., Li, H., Miao, Z., and Li, Z.: The Surge of the Hispar Glacier, Central Karakoram: SAR 3-D Flow Velocity Time Series and Thickness Changes, Journal of Geophysical Research: Solid Earth, 125, doi:10.1029/2019JB018945, URL https://onlinelibrary.wiley.com/doi/10.1029/2019JB018945, 2020.

Guo, L., Li, J., Dehecq, A., Li, Z., Li, X., and Zhu, J.: A new inventory of High Mountain Asia surging glaciers derived from multiple elevation datasets since the 1970s, Earth System Science Data, 15, 2841–2861, doi:10.5194/essd-15-2841-2023, URL https://essd.copernicus.org/articles/15/2841/2023/, 2023.

Guo, L., Li, J., Charrier, L., Dehecq, A., Beraud, L., Li, Z., Li, X., Zhu, J., Li, L., and Wang, Y.: Surging Processes and Mechanisms at Small Glaciers in the Qilian Mountains, Northwestern China, Revealed by Long-Term, Temporally Dense Remote Sensing Observations, Journal of Geophysical Research: Earth Surface, 130, e2024JF008 157, doi:10.1029/2024JF008157, URL https://agupubs.onlinelibrary.wiley.com/doi/10.1029/2024JF008157, 2025.

Handwerger, A. L., Rempel, A. W., Skarbek, R. M., Roering, J. J., and Hilley, G. E.: Rate-weakening friction characterizes both slow sliding and catastrophic failure of landslides, Proceedings of the National Academy of Sciences, 113, 10 281–10 286, doi:10.1073/pnas.1607009113, URL https://pnas.org/doi/full/10.1073/pnas.1607009113, 2016.

Harrison, W. D. and Post, A. S.: How much do we really know about glacier surging?, Annals of Glaciology, 36, 1–6, doi:10.3189/172756403781816185, URL https://www.cambridge.org/core/product/identifier/S0260305500259156/type/journal_article, 2003.

Harrison, W. D., Truffer, M., Echelmeyer, K. A., Pomraning, D. A., Abnett, K. A., and Ruhkick, R. H.: Probing the till beneath Black Rapids Glacier, Alaska, USA, Journal of Glaciology, 50, 608–614, doi:10.3189/172756504781829693, URL https://www.cambridge.org/core/product/identifier/S0022143000215384/type/journal_article, 2004.

Hart, J. K., Martinez, K., Basford, P. J., Clayton, A. I., Robson, B. A., and Young, D. S.: Surface melt driven summer diurnal and winter multi-day stick-slip motion and till sedimentology, Nature Communications, 10, 1599, doi:10.1038/s41467-019-09547-6, URL https://www.nature.com/articles/s41467-019-09547-6, 2019.

Helanow, C., Iverson, N. R., Woodard, J. B., and Zoet, L. K.: A slip law for hard-bedded glaciers derived from observed bed topography, Science Advances, 7, eabe7798, doi:10.1126/sciadv.abe7798, URL https://www.science.org/doi/10.1126/sciadv.abe7798, 2021.

Helmstetter, A. and Shaw, B. E.: Afterslip and aftershocks in the rate-and-state friction law, Journal of Geophysical Research: Solid Earth, 114, 2007JB005 077, doi:10.1029/2007JB005077, URL https://agupubs.onlinelibrary.wiley.com/doi/10.1029/2007JB005077, 2009.

Herreid, S. and Truffer, M.: Automated detection of unstable glacier flow and a spectrum of speedup behavior in the Alaska Range, Journal of Geophysical Research: Earth Surface, 121, 64–81, doi:10.1002/2015JF003502, URL https://onlinelibrary.wiley.com/doi/10.1002/2015JF003502, 2016.

Herzfeld, U. C., Trantow, T., Lawson, M., Hans, J., and Medley, G.: Surface heights and crevasse morphologies of surging and fast-moving glaciers from ICESat-2 laser altimeter data - Application of the density-dimension algorithm (DDA-ice) and evaluation using airborne altimeter and Planet SkySat data, Science of Remote Sensing, 3, 100 013, doi:10.1016/j.srs.2020.100013, URL https://linkinghub.elsevier.com/retrieve/pii/S2666017220300122, 2021.

Hewitt, K.: The Karakoram Anomaly? Glacier Expansion and the 'Elevation Effect,' Karakoram Himalaya, Mountain Research and Development, 25, 332–340, 2005.

Hewitt, K.: Tributary glacier surges: an exceptional concentration at Panmah Glacier, Karakoram Himalaya, Journal of Glaciology, 53, 181–188, doi:10.3189/172756507782202829, URL https://www.cambridge.org/core/product/identifier/S0022143000201275/type/journal_article, 2007.

Hewitt, K.: Glaciers of the Karakoram Himalaya, Advances in Asian Human-Environmental Research, Springer Netherlands, Dordrecht, doi:10.1007/978-94-007-6311-1, URL http://link.springer.com/10.1007/978-94-007-6311-1, 2014.

Hilmar Gudmundsson, G., Aðalgeirsdóttir, G., and Björnsson, H.: Observational verification of predicted increase in bedrock-to-surface amplitude transfer during a glacier surge, Annals of Glaciology, 36, 91–96, doi:10.3189/172756403781816248, URL https://www.cambridge.org/core/product/identifier/S0260305500259272/type/journal_article, 2003.

Hoinkes, H. C.: Surges of the Vernagtferner in the Ötztal Alps since 1599, Canadian Journal of Earth Sciences, 6, 853–861, doi:10.1139/e69-086, URL http://www.nrcresearchpress.com/doi/10.1139/e69-086, 1969.

Hugonnet, R., McNabb, R., Berthier, E., Menounos, B., Nuth, C., Girod, L., Farinotti, D., Huss, M., Dussaillant, I., Brun, F., and Kääb, A.: Accelerated global glacier mass loss in the early twenty-first century, Nature, 592, 726–731, doi:10.1038/s41586-021-03436-z, URL http://www.nature.com/articles/s41586-021-03436-z, 2021.

Immerzeel, W. W., Lutz, A. F., Andrade, M., Bahl, A., Biemans, H., Bolch, T., Hyde, S., Brumby, S., Davies, B. J., Elmore, A. C., Emmer, A., Feng, M., Fernández, A., Haritashya, U., Kargel, J. S., Koppes, M., Kraaijenbrink, P. D. A., Kulkarni, A. V., Mayewski, P. A., Nepal, S., Pacheco, P., Painter, T. H., Pellicciotti, F., Rajaram, H., Rupper, S., Sinisalo, A., Shrestha, A. B., Viviroli, D., Wada, Y., Xiao, C., Yao, T., and Baillie, J. E. M.: Importance and vulnerability of the world's water towers, Nature, 577, 364–369, doi:10.1038/s41586-019-1822-y, URL http://www.nature.com/articles/s41586-019-1822-y, 2020.

Imran, M. and Ahmad, U.: Geospatially analysing the dynamics of the Khurdopin Glacier surge using multispectral and temporal remote sensing and ground observations, Natural Hazards, 108, 847–866, doi:10.1007/s11069-021-04708-7, URL https://link.springer.com/10.1007/s11069-021-04708-7, 2021.

Intergovernmental Panel On Climate Change (Ipcc): Climate Change 2022 – Impacts, Adaptation and Vulnerability: Working Group II Contribution to the Sixth Assessment Report of the Intergovernmental Panel on Climate Change, Cambridge University Press, 1 edn., doi:10.1017/9781009325844, URL https://www.cambridge.org/core/product/identifier/9781009325844/type/book, 2023.

IPCC: The Ocean and Cryosphere in a Changing Climate: Special Report of the Intergovernmental Panel on Climate Change, Cambridge University Press, 1 edn., doi:10.1017/9781009157964, URL https://www.cambridge.org/core/product/identifier/9781009157964/type/book, 2022.

Jay-Allemand, M., Gillet-Chaulet, F., Gagliardini, O., and Nodet, M.: Investigating changes in basal conditions of Variegated Glacier prior to and during its 1982–1983 surge, The Cryosphere, 5, 659–672, doi:10.5194/tc-5-659-2011, URL https://tc.copernicus.org/articles/5/659/2011/, 2011.

Jiang, Z., Wu, K., Liu, S., Wang, X., Zhang, Y., Tahir, A. A., and Long, S.: Surging dynamics of South Rimo Glacier, Eastern Karakoram, Environmental Research Letters, 16, 114 044, doi:10.1088/1748-9326/ac3175, URL https://iopscience.iop.org/article/10.1088/1748-9326/ac3175, 2021.

Jiskoot, H., Fox, T. A., and Van Wychen, W.: Flow and structure in a dendritic glacier with bedrock steps, Journal of Glaciology, 63, 912–928, doi:10.1017/jog.2017.58, URL https://www.cambridge.org/core/product/identifier/S0022143017000582/type/journal_article, 2017.

Jouberton, A., Shaw, T. E., Miles, E., Kneib, M., Fugger, S., Buri, P., McCarthy, M., Kayumov, A., Navruzshoev, H., Halimov, A., Kabutov, K., Homidov, F., and Pellicciotti, F.: Snowfall decrease in recent years undermines glacier health and meltwater resources in the Northwestern Pamirs, Communications Earth & Environment, 6, 691, doi:10.1038/s43247-025-02611-8, URL https://www.nature.com/articles/s43247-025-02611-8, 2025.

Jouvet, G.: Inversion of a Stokes glacier flow model emulated by deep learning, Journal of Glaciology, 69, 13–26, doi:10.1017/jog.2022.41, URL https://www.cambridge.org/core/product/identifier/S0022143022000417/type/journal_article, 2023.

Jouvet, G. and Cordonnier, G.: Ice-flow model emulator based on physics-informed deep learning, Journal of Glaciology, pp. 1–15, doi:10.1017/jog.2023.73, URL https://www.cambridge.org/core/product/identifier/S0022143023000734/type/journal_article, 2023.

Kacimi, S., Jaruwatanadilok, S., and Kwok, R.: SWOT Observations Over Sea Ice: A First Look, Geophysical Research Letters, 52, e2025GL116 079, doi:10.1029/2025GL116079, URL https://agupubs.onlinelibrary.wiley.com/doi/10.1029/2025GL116079, 2025.

Kamb, B., Raymond, C. F., Harrison, W. D., Engelhardt, H., Echelmeyer, K. A., Humphrey, N., Brugman, M. M., and Pfeffer, T.: Glacier Surge Mechanism: 1982-1983 Surge of Variegated Glacier, Alaska, Science, 227, 469–479, doi:10.1126/science.227.4686.469, URL https://www.science.org/doi/10.1126/science.227.4686.469, 1985.

Kavan, J., Strzelecki, M. C., Benn, D. I., Luckman, A., Roman, M., and Zagórski, P.: Glacier surge as a trigger for the fastest delta growth in the Arctic, Communications Earth & Environment, 5, 700, doi:10.1038/s43247-024-01877-8, URL https://www.nature.com/articles/s43247-024-01877-8, 2024.

Ke, L., Zhang, J., Fan, C., Zhou, J., and Song, C.: Large-Scale Monitoring of Glacier Surges by Integrating High-Temporal- and -Spatial-Resolution Satellite Observations: A Case Study in the Karakoram, Remote Sensing, 14, 4668, doi:10.3390/rs14184668, URL https://www.mdpi.com/2072-4292/14/18/4668, 2022.

King, O., Bhattacharya, A., Bhambri, R., and Bolch, T.: Glacial lakes exacerbate Himalayan glacier mass loss, Scientific Reports, 9, 18 145, doi:10.1038/s41598-019-53733-x, URL http://www.nature.com/articles/s41598-019-53733-x, 2019.

King, O., Bhattacharya, A., and Bolch, T.: The presence and influence of glacier surging around the Geladandong ice caps, North East Tibetan Plateau, Advances in Climate Change Research, 12, 299–312, doi:10.1016/j.accre.2021.05.001, URL https://linkinghub.elsevier.com/retrieve/pii/S1674927821000721, 2021.

Kneib, M., Dehecq, A., Gilbert, A., Basset, A., Miles, E. S., Jouvet, G., Jourdain, B., Ducasse, E., Beraud, L., Rabatel, A., Mouginot, J., Carcanade, G., Laarman, O., Brun, F., and Six, D.: Distributed surface mass balance of an avalanche-fed glacier, The Cryosphere, 18, 5965–5983, doi:10.5194/tc-18-5965-2024, URL https://tc.copernicus.org/articles/18/5965/2024/, 2024.

Koch, M., Seehaus, T., Friedl, P., and Braun, M.: Automated Detection of Glacier Surges from Sentinel-1 Surface Velocity Time Series—An Example from Svalbard, Remote Sensing, 15, 1545, doi:10.3390/rs15061545, URL https://www.mdpi.com/2072-4292/15/6/1545, 2023.

Kochtitzky, W., Jiskoot, H., Copland, L., Enderlin, E., Mcnabb, R., Kreutz, K., and Main, B.: Terminus advance, kinematics and mass redistribution during eight surges of Donjek Glacier, St. Elias Range, Canada, 1935 to 2016, Journal of Glaciology, 65, 565–579, doi:10.1017/jog.2019.34, URL https://www.cambridge.org/core/product/identifier/S0022143019000340/type/journal_article, 2019.

Kotlyakov, V. M., Chernova, L. P., Khromova, T. E., Muraviev, A. Y., Kachalin, A. B., and Tiuflin, A. S.: Unique Surges of Medvezhy Glacier, Doklady Earth Sciences, 483, 1547–1552, doi:10.1134/S1028334X18120152, URL http://link.springer.com/10.1134/S1028334X18120152, 2018.

Kronenberg, M., Machguth, H., Eichler, A., Schwikowski, M., and Hoelzle, M.: Comparison of historical and recent accumulation rates on Abramov Glacier, Pamir Alay, Journal of Glaciology, 67, 253–268, doi:10.1017/jog.2020.103, URL https://www.cambridge.org/core/product/identifier/S0022143020001033/type/journal_article, 2021.

Kääb, A., Jacquemart, M., Gilbert, A., Leinss, S., Girod, L., Huggel, C., Falaschi, D., Ugalde, F., Petrakov, D., Chernomorets, S., Dokukin, M., Paul, F., Gascoin, S., Berthier, E., and Kargel, J. S.: Sudden large-volume detachments of low-angle mountain glaciers – more frequent than thought?, The Cryosphere, 15, 1751–1785, doi:10.5194/tc-15-1751-2021, URL https://tc.copernicus.org/articles/15/1751/2021/, 2021.

Kääb, A., Bazilova, V., Leclercq, P. W., Mannerfelt, E. S., and Strozzi, T.: Global clustering of recent glacier surges from radar backscatter data, 2017–2022, Journal of Glaciology, pp. 1–9, doi:10.1017/jog.2023.35, URL https://www.cambridge.org/core/product/identifier/S0022143023000357/type/journal_article, 2023.

Lauzon, B., Copland, L., Van Wychen, W., Kochtitzky, W., McNabb, R., and Dahl-Jensen, D.: Dynamics throughout a complete surge of Iceberg Glacier on western Axel Heiberg Island, Canadian High Arctic, Journal of Glaciology, pp. 1–18, doi:10.1017/jog.2023.20, URL https://www.cambridge.org/core/product/identifier/S0022143023000205/type/journal_article, 2023.

Leclercq, P. W., Kääb, A., and Altena, B.: Brief communication: Detection of glacier surge activity using cloud computing of Sentinel-1 radar data, The Cryosphere, 15, 4901–4907, doi:10.5194/tc-15-4901-2021, URL https://tc.copernicus.org/articles/15/4901/2021/, 2021.

Li, G., Lv, M., Quincey, D. J., Taylor, L. S., Li, X., Yan, S., Sun, Y., and Guo, H.: Characterizing the surge behaviour and associated ice-dammed lake evolution of the Kyagar Glacier in the Karakoram, The Cryosphere, 17, 2891–2907, doi:10.5194/tc-17-2891-2023, URL https://tc.copernicus.org/articles/17/2891/2023/, 2023.

Liu, J., Enderlin, E. M., Bartholomaus, T. C., Terleth, Y., Mikesell, T. D., and Beaud, F.: Propagating speedups during quiescence escalate to the 2020–2021 surge of Sít' Kusá, southeast Alaska, Journal of Glaciology, pp. 1–12, doi:10.1017/jog.2023.99, URL https://www.cambridge.org/core/product/identifier/S0022143023000990/type/journal_article, 2024.

Liu, Y., Cheng, X., Hui, F., Wang, X., Wang, F., and Cheng, C.: Detection of crevasses over polar ice shelves using Satellite Laser Altimeter, Science China Earth Sciences, 57, 1267–1277, doi:10.1007/s11430-013-4796-x, URL http://link.springer.com/10.1007/s11430-013-4796-x, 2014.

Lovell, A. M., Carr, J. R., and Stokes, C. R.: Topographic controls on the surging behaviour of Sabche Glacier, Nepal (1967 to 2017), Remote Sensing of Environment, 210, 434–443, doi:10.1016/j.rse.2018.03.036, URL https://linkinghub.elsevier.com/retrieve/pii/S0034425718301378, 2018.

Lovell, H., Carrivick, J. L., King, O., Sutherland, J. L., Yde, J. C., Boston, C. M., and Małecki, J.: Surge-type glaciers in Kalaallit Nunaat (Greenland): distribution,

temporal patterns and climatic controls, Journal of Glaciology, 69, 1785–1802, doi:10.1017/jog.2023.61, URL https://www.cambridge.org/core/product/identifier/S0022143023000618/type/journal_article, 2023.

Lv, M., Guo, H., Yan, J., Wu, K., Liu, G., Lu, X., Ruan, Z., and Yan, S.: Distinguishing Glaciers between Surging and Advancing by Remote Sensing: A Case Study in the Eastern Karakoram, Remote Sensing, 12, 2297, doi:10.3390/rs12142297, URL https://www.mdpi.com/2072-4292/12/14/2297, 2020.

Mann, D., Wilson, P., Gaglioti, B., Groves, P., and Young, M.: Surges of the Black Rapids Glacier tracked climate over the last 600 years, Quaternary Science Reviews, 344, 108 969, doi:10.1016/j.quascirev.2024.108969, URL https://linkinghub.elsevier.com/retrieve/pii/S0277379124004700, 2024.

Mannerfelt, E. S., Schellenberger, T., and Kääb, A. M.: Tracking glacier surge evolution using interferometric SAR coherence—examples from Svalbard, Journal of Glaciology, 71, e43, doi:10.1017/jog.2025.27, URL https://www.cambridge.org/core/product/identifier/S0022143025000279/type/journal_article, 2025.

Mattea, E., Berthier, E., Dehecq, A., Bolch, T., Bhattacharya, A., Ghuffar, S., Barandun, M., and Hoelzle, M.: Five decades of Abramov glacier dynamics reconstructed with multi-sensor optical remote sensing, The Cryosphere, 19, 219–247, doi:10.5194/tc-19-219-2025, URL https://tc.copernicus.org/articles/19/219/2025/, 2025a.

Mattea, E., Bhattacharya, A., Ghuffar, S., Khatun, J., Barandun, M., and Hoelzle, M.: Predicted and observed glacier pulsations in the Hissar-Alay of Central Asia, doi:10.5194/egusphere-2025-4068, URL https://egusphere.copernicus.org/preprints/2025/egusphere-2025-4068/, 2025b.

Matthews, J. A. and Briffa, K. R.: The 'little ice age': re-evaluation of an evolving concept, Geografiska Annaler: Series A, Physical Geography, 87, 17–36, doi:10.1111/j.0435-3676.2005.00242.x, URL https://www.tandfonline.com/doi/full/10.1111/j.0435-3676.2005.00242.x, 2005.

Maussion, F., Scherer, D., Mölg, T., Collier, E., Curio, J., and Finkelnburg, R.: Precipitation Seasonality and Variability over the Tibetan Plateau as Resolved by the High Asia Reanalysis*, Journal of Climate, 27, 1910–1927, doi:10.1175/JCLI-D-13-00282.1, URL http://journals.ametsoc.org/doi/10.1175/JCLI-D-13-00282.1, 2014.

Meier, M. F. and Post, A.: What are glacier surges?, Canadian Journal of Earth Sciences, 6, 807–817, doi:10.1139/e69-081, URL http://www.nrcresearchpress.com/doi/10.1139/e69-081, 1969.

Menzies, J. and Shilts, B. W.: Subglacial environments, in: Modern and Past Glacial Environments, pp. 183–278, Elsevier, doi:10.1016/B978-075064226-2/50011-8, URL https://linkinghub.elsevier.com/retrieve/pii/B9780750642262500118, 2002.

Millan, R., Mouginot, J., Rabatel, A., and Morlighem, M.: Ice velocity and thickness of the world's glaciers, Nature Geoscience, 15, 124–129, doi:10.1038/s41561-021-00885-z, URL https://www.nature.com/articles/s41561-021-00885-z, 2022.

Minchew, B. and Joughin, I.: Toward a universal glacier slip law, Science, 368, 29–30, doi:10.1126/science.abb3566, URL https://www.science.org/doi/10.1126/science.abb3566, 2020.

Minchew, B. M. and Meyer, C. R.: Dilation of subglacial sediment governs incipient surge motion in glaciers with deformable beds, Proceedings of the Royal Society A: Mathematical, Physical and Engineering Sciences, 476, 20200 033, doi:10.1098/rspa.2020.0033, URL https://royalsocietypublishing.org/doi/10.1098/rspa.2020.0033, 2020.

Morin, A., Flowers, G. E., Nolan, A., Brinkerhoff, D., and Berthier, E.: Exploiting high-slip flow regimes to improve inference of glacier bed topography, Journal of Glaciology, pp. 1–7, doi:10.1017/jog.2022.121, URL https://www.cambridge.org/core/product/identifier/S0022143022001216/type/journal_article, 2023.

Muhammad, S., Li, J., Steiner, J. F., Shrestha, F., Shah, G. M., Berthier, E., Guo, L., Wu, L.-x., and Tian, L.: A holistic view of Shisper Glacier surge and outburst floods: from physical processes to downstream impacts, Geomatics, Natural Hazards and Risk, 12, 2755–2775, doi:10.1080/19475705.2021.1975833, URL https://www.tandfonline.com/doi/full/10.1080/19475705.2021.1975833, 2021.

Mukherjee, K., Bolch, T., Goerlich, F., Kutuzov, S., Osmonov, A., Pieczonka, T., and Shesterova, I.: Surge-Type Glaciers in the Tien Shan (Central Asia), Arctic, Antarctic, and Alpine Research, 49, 147–171, doi:10.1657/AAAR0016-021, URL https://www.tandfonline.com/doi/full/10.1657/AAAR0016-021, 2017.

Murray, T., Luckman, A., Strozzi, T., and Nuttall, A.-M.: The initiation of glacier surging at Fridtjovbreen, Svalbard, Annals of Glaciology, 36, 110–116, doi:10.3189/172756403781816275, URL https://www.cambridge.org/core/product/identifier/S0260305500259302/type/journal_article, 2003a.

Murray, T., Strozzi, T., Luckman, A., Jiskoot, H., and Christakos, P.: Is there a single surge mechanism? Contrasts in dynamics between glacier surges in Svalbard and other regions: IS THERE A SINGLE SURGE MECHANISM?, Journal of Geophysical Research: Solid Earth, 108, doi:10.1029/2002JB001906, URL http://doi.wiley.com/10.1029/2002JB001906, 2003b.

Nanni, U., Scherler, D., Ayoub, F., Millan, R., Herman, F., and Avouac, J.-P.: Climatic control on seasonal variations in mountain glacier surface velocity, The Cryosphere, 17, 1567–1583, doi:10.5194/tc-17-1567-2023, URL https://tc.copernicus.org/articles/17/1567/2023/, 2023.

Nolan, A., Kochtitzky, W., Enderlin, E. M., McNabb, R., and Kreutz, K. J.: Kinematics of the exceptionally-short surge cycles of Sít' Kusá (Turner Glacier), Alaska, from 1983 to 2013, Journal of Glaciology, 67, 744–758, doi:10.1017/jog.2021.29, URL https://www.cambridge.org/core/product/identifier/S0022143021000290/type/journal_article, 2021.

Nolan, M.: The "Galloping Glacier" trots: decadal-scale speed oscillations within the quiescent phase, Annals of Glaciology, 36, 7–13, doi:10.3189/172756403781816149, URL https://www.cambridge.org/core/product/identifier/S0260305500259168/type/journal_article, 2003.

Nosavan, J., Henry, P., and Moreau, A.: Spot world heritage: exploring the past, in: Sensors, Systems, and Next-Generation Satellites XXII, edited by Neeck, S. P., Kimura, T., and Martimort, P., p. 28, SPIE, Berlin, Germany, doi:10.1117/12.2324675, URL https://www.spiedigitallibrary.org/conference-proceedings-of-spie/10785/2324675/Spot-world-heritage-exploring-the-past/10.1117/12.2324675.full, 2018.

Oerlemans, J. and van Pelt, W. J. J.: A model study of Abrahamsenbreen, a surging glacier in northern Spitsbergen, The Cryosphere, 9, 767–779, doi:10.5194/tc-9-767-2015, URL https://tc.copernicus.org/articles/9/767/2015/, 2015.

Partington, G., Copland, L., Lauzon, B., Medrzycka, D., Main, B., Kochtitzky, W., and Dow, C.: Surge history and dynamics of Fisher Glacier, Yukon, 1948-2022, Journal of Glaciology, pp. 1–41, doi:10.1017/jog.2025.10084, URL https://www.cambridge.org/core/product/identifier/S0022143025100841/type/journal_article, 2025.

Paul, F.: Revealing glacier flow and surge dynamics from animated satellite image sequences: examples from the Karakoram, The Cryosphere, 9, 2201–2214, doi:10.5194/tc-9-2201-2015, URL https://tc.copernicus.org/articles/9/2201/2015/, 2015.

Paul, F.: A 60-year chronology of glacier surges in the central Karakoram from the analysis of satellite image time-series, Geomorphology, 352, 106 993, doi:10.1016/j.geomorph.2019.106993, URL https://linkinghub.elsevier.com/retrieve/pii/S0169555X19304842, 2020.

Paul, F., Strozzi, T., Schellenberger, T., and Kääb, A.: The 2015 Surge of Hispar Glacier in the Karakoram, Remote Sensing, 9, 888, doi:10.3390/rs9090888, URL http://www.mdpi.com/2072-4292/9/9/888, 2017.

Paul, F., Piermattei, L., Treichler, D., Gilbert, L., Girod, L., Kääb, A., Libert, L., Nagler, T., Strozzi, T., and Wuite, J.: Three different glacier surges at a spot: what satellites observe and what not, The Cryosphere, 16, 2505–2526, doi:10.5194/tc-16-2505-2022, URL https://tc.copernicus.org/articles/16/2505/2022/, 2022.

Pritchard, H.: Glacier surge dynamics of Sortebræ, east Greenland, from synthetic aperture radar feature tracking, Journal of Geophysical Research, 110, F03 005, doi:10.1029/2004JF000233, URL http://doi.wiley.com/10.1029/2004JF000233, 2005.

Pu, S.: Optimizing Gaussian processes: Powerful kernels and efficiency improvements, p. 030009, Shanghai, China, doi:10.1063/5.0222476, URL https://pubs.aip.org/aip/acp/article-lookup/doi/10.1063/5.0222476, 2024.

Quincey, D. J. and Luckman, A.: Brief Communication: On the magnitude and frequency of Khurdopin glacier surge events, The Cryosphere, 8, 571–574, doi:10.5194/tc-8-571-2014, URL https://tc.copernicus.org/articles/8/571/2014/, 2014.

Quincey, D. J., Braun, M., Glasser, N. F., Bishop, M. P., Hewitt, K., and Luckman, A.: Karakoram glacier surge dynamics: KARAKORAM GLACIER SURGE DYNAMICS, Geophysical Research Letters, 38, n/a–n/a, doi:10.1029/2011GL049004, URL http://doi.wiley.com/10.1029/2011GL049004, 2011.

Quincey, D. J., Glasser, N. F., Cook, S. J., and Luckman, A.: Heterogeneity in Karakoram glacier surges: KARAKORAM GLACIER SURGE HETEROGENEITY, Journal of Geophysical Research: Earth Surface, 120, 1288–1300, doi:10.1002/2015JF003515, URL http://doi.wiley.com/10.1002/2015JF003515, 2015.

Rankl, M., Kienholz, C., and Braun, M.: Glacier changes in the Karakoram region mapped by multimission satellite imagery, The Cryosphere, 8, 977–989, doi:10.5194/tc-8-977-2014, URL https://tc.copernicus.org/articles/8/977/2014/, 2014.

Rashid, I., Abdullah, T., Glasser, N. F., Naz, H., and Romshoo, S. A.: Surge of Hispar Glacier, Pakistan, between 2013 and 2017 detected from remote sensing observations, Geomorphology, 303, 410–416, doi:10.1016/j.geomorph.2017.12.018, URL https://linkinghub.elsevier.com/retrieve/pii/S0169555X17305275, 2018.

Rasmussen, C. E. and Williams, C. K. I.: Gaussian Processes for Machine Learning, The MIT Press, doi:10.7551/mitpress/3206.001.0001, URL https://direct.mit.edu/books/book/2320/Gaussian-Processes-for-Machine-Learning, 2005.

Raymond, C. F.: How do glaciers surge? A review, Journal of Geophysical Research: Solid Earth, 92, 9121–9134, doi:10.1029/JB092iB09p09121, URL https://agupubs.onlinelibrary.wiley.com/doi/10.1029/JB092iB09p09121, 1987.

Raymond, C. F. and Malone, S.: Propagating Strain Anomalies during Mini-Surges of Variegated Glacier, Alaska, U.S.A., Journal of Glaciology, 32, 178–191, doi:10.3189/S0022143000015495, URL https://www.cambridge.org/core/product/identifier/S0022143000015495/type/journal_article, 1986.

Reinwarth, O.: VERNAGTFERNER 1979-1982, AUSTRIA, 1:10,000 (Thematic map), 1993.

RGI Consortium: Randolph Glacier Inventory - A Dataset of Global Glacier Outlines, Version 7, doi:10.5067/F6JMOVY5NAVZ, URL https://nsidc.org/data/nsidc-0770/versions/7, 2023.

Rizzoli, P., Martone, M., Gonzalez, C., Wecklich, C., Borla Tridon, D., Bräutigam, B., Bachmann, M., Schulze, D., Fritz, T., Huber, M., Wessel, B., Krieger, G., Zink, M., and Moreira, A.: Generation and performance assessment of the global TanDEM-X digital elevation model, ISPRS Journal of Photogrammetry and Remote Sensing, 132, 119–139, doi:10.1016/j.isprsjprs.2017.08.008, URL https://linkinghub.elsevier.com/retrieve/pii/S092427161730093X, 2017.

Rounce, D. R., Hock, R., Maussion, F., Hugonnet, R., Kochtitzky, W., Huss, M., Berthier, E., Brinkerhoff, D., Compagno, L., Copland, L., Farinotti, D., Menounos, B., and McNabb, R. W.: Global glacier change in the 21st century: Every increase in temperature matters, Science, 379, 78–83, doi:10.1126/science.abo1324, URL https://www.science.org/doi/10.1126/science.abo1324, 2023.

Round, V., Leinss, S., Huss, M., Haemmig, C., and Hajnsek, I.: Surge dynamics and lake outbursts of Kyagar Glacier, Karakoram, The Cryosphere, 11, 723–739, doi:10.5194/tc-11-723-2017, URL https://tc.copernicus.org/articles/11/723/2017/, 2017.

Roush, J. J., Lingle, C. S., Guritz, R. M., Fatland, D. R., and Voronina, V. A.: Surge-front propagation and velocities during the early-1993–95 surge of Bering Glacier, Alaska, U.S.A., from sequential SAR imagery, Annals of Glaciology, 36, 37–44, doi:10.3189/172756403781816266, URL https://www.cambridge.org/core/product/identifier/S026030550025920X/type/journal_article, 2003.

Rupnik, E., Daakir, M., and Pierrot Deseilligny, M.: MicMac – a free, open-source solution for photogrammetry, Open Geospatial Data, Software and Standards, 2, 14, doi:10.1186/s40965-017-0027-2, URL http://opengeospatialdata.springeropen.com/articles/10.1186/s40965-017-0027-2, 2017.

Ruppert, D., Wand, M. P., and Carroll, R. J.: Semiparametric regression, Cambridge series in statistical and probabilistic mathematics, Cambridge Univ. Press, Cambridge, repr edn., 2009.

Serrano, E. and Martín-Moreno, R.: Surge glaciers during the Little Ice Age in the Pyrenees, Cuadernos de Investigación Geográfica, 44, 213–244, doi:10.18172/cig.3399, URL https://publicaciones.unirioja.es/ojs/index.php/cig/article/view/3399, 2018.

Sevestre, H. and Benn, D. I.: Climatic and geometric controls on the global distribution of surge-type glaciers: implications for a unifying model of surging, Journal of Glaciology, 61, 646–662, doi:10.3189/2015JoG14J136, URL https://www.cambridge.org/core/product/identifier/S0022143000202487/type/journal_article, 2015.

Sevestre, H., Benn, D. I., Hulton, N. R. J., and Bælum, K.: Thermal structure of Svalbard glaciers and implications for thermal switch models of glacier surging, Journal of Geophysical Research: Earth Surface, 120, 2220–2236, doi:10.1002/2015JF003517, URL https://onlinelibrary.wiley.com/doi/abs/10.1002/2015JF003517, 2015.

Sevestre, H., Benn, D. I., Luckman, A., Nuth, C., Kohler, J., Lindbäck, K., and Pettersson, R.: Tidewater Glacier Surges Initiated at the Terminus, Journal of Geophysical Research: Earth Surface, 123, 1035–1051, doi:10.1029/2017JF004358, URL https://agupubs.onlinelibrary.wiley.com/doi/10.1029/2017JF004358, 2018.

Shean, D.: High Mountain Asia 8-meter DEM Mosaics Derived from Optical Imagery, Version 1, doi:10.5067/KXOVQ9L172S2, URL https://nsidc.org/data/HMA_DEM8m_MOS/versions/1, 2017.

Shean, D. E., Bhushan, S., Montesano, P., Rounce, D. R., Arendt, A., and Osmanoglu, B.: A Systematic, Regional Assessment of High Mountain Asia Glacier Mass Balance, Frontiers in Earth Science, 7, 363, doi:10.3389/feart.2019.00363, URL https://www.frontiersin.org/article/10.3389/feart.2019.00363/full, 2020.

Shekhar, P., Csatho, B., Schenk, T., Roberts, C., and Patra, A. K.: ALPS: A Unified Framework for Modeling Time Series of Land Ice Changes, IEEE Transactions on Geoscience and Remote Sensing, 59, 6466–6481, doi:10.1109/TGRS.2020.3027190, URL https://ieeexplore.ieee.org/document/9226474/, 2021.

Shen, X., Ke, C.-Q., Yu, X., Cai, Y., and Fan, Y.: Evaluation of Ice, Cloud, And Land Elevation Satellite-2 (ICESat-2) land ice surface heights using Airborne Topographic Mapper (ATM) data in Antarctica, International Journal of Remote Sensing, 42, 2556–2573, doi:10.1080/01431161.2020.1856962, URL https://www.tandfonline.com/doi/full/10.1080/01431161.2020.1856962, 2021.

Singh, R. M., Govil, H., Shahi, A. P., and Bhambri, R.: Characterizing the glacier surge dynamics in Yarkand basin, Karakoram using remote sensing, Quaternary International, 575-576, 190–203, doi:10.1016/j.quaint.2020.06.042, URL https://linkinghub.elsevier.com/retrieve/pii/S1040618220303542, 2021.

Singh, V. P., Singh, P., and Haritashya, U. K.: Encyclopedia of snow, ice and glaciers, The encyclopedia of earth sciences series, Springer, Dordrecht London, 2011.

Steiner, J. F., Kraaijenbrink, P. D. A., Jiduc, S. G., and Immerzeel, W. W.: Brief communication: The Khurdopin glacier surge revisited – extreme flow velocities and formation of a dammed lake in 2017, The Cryosphere, 12, 95–101, doi:10.5194/tc-12-95-2018, URL https://tc.copernicus.org/articles/12/95/2018/, 2018.

Striberger, J., Björck, S., Benediktsson, I. O., Snowball, I., Uvo, C. B., Ingólfsson, O., and Kjær, K. H.: Climatic control of the surge periodicity of an Icelandic outlet glacier, Journal of Quaternary Science, 26, 561–565, doi:10.1002/jqs.1527, URL https://onlinelibrary.wiley.com/doi/10.1002/jqs.1527, 2011.

Sund, M., Eiken, T., Hagen, J. O., and Kääb, A.: Svalbard surge dynamics derived from geometric changes, Annals of Glaciology, 50, 50–60, doi:10.3189/172756409789624265,

URL https://www.cambridge.org/core/product/identifier/S0260305500250180/type/journal_article, 2009.

Terleth, Y., Van Pelt, W. J. J., Pohjola, V. A., and Pettersson, R.: Complementary Approaches Towards a Universal Model of Glacier Surges, Frontiers in Earth Science, 9, 732 962, doi:10.3389/feart.2021.732962, URL https://www.frontiersin.org/articles/10.3389/feart.2021.732962/full, 2021.

Terleth, Y., Bartholomaus, T. C., Enderlin, E., Mikesell, T. D., and Liu, J.: Glacier Surges and Seasonal Speedups Integrated Into a Single, Enthalpy-Based Model Framework, Geophysical Research Letters, 51, e2024GL112 514, doi:10.1029/2024GL112514, URL https://agupubs.onlinelibrary.wiley.com/doi/10.1029/2024GL112514, 2024a.

Terleth, Y., Bartholomaus, T. C., Liu, J., Beaud, F., Mikesell, T. D., and Enderlin, E. M.: Transient subglacial water routing efficiency modulates ice velocities prior to surge termination on Sít' Kusá, AK, Journal of Glaciology, pp. 1–42, doi:10.1017/jog.2024.38, URL https://www.cambridge.org/core/product/identifier/S0022143024000388/type/journal_article, 2024b.

The GlaMBIE Team, Zemp, M., Jakob, L., Dussaillant, I., Nussbaumer, S. U., Gourmelen, N., Dubber, S., A, G., Abdullahi, S., Andreassen, L. M., Berthier, E., Bhattacharya, A., Blazquez, A., Boehm Vock, L. F., Bolch, T., Box, J., Braun, M. H., Brun, F., Cicero, E., Colgan, W., Eckert, N., Farinotti, D., Florentine, C., Floricioiu, D., Gardner, A., Harig, C., Hassan, J., Hugonnet, R., Huss, M., Jóhannesson, T., Liang, C.-C. A., Ke, C.-Q., Khan, S. A., King, O., Kneib, M., Krieger, L., Maussion, F., Mattea, E., McNabb, R., Menounos, B., Miles, E., Moholdt, G., Nilsson, J., Pálsson, F., Pfeffer, J., Piermattei, L., Plummer, S., Richter, A., Sasgen, I., Schuster, L., Seehaus, T., Shen, X., Sommer, C., Sutterley, T., Treichler, D., Velicogna, I., Wouters, B., Zekollari, H., and Zheng, W.: Community estimate of global glacier mass changes from 2000 to 2023, Nature, doi:10.1038/s41586-024-08545-z, URL https://www.nature.com/articles/s41586-024-08545-z, 2025.

Thøgersen, K., Gilbert, A., Schuler, T. V., and Malthe-Sørenssen, A.: Rate-and-state friction explains glacier surge propagation, Nature Communications, 10, 2823, doi:10.1038/s41467-019-10506-4, URL http://www.nature.com/articles/s41467-019-10506-4, 2019.

Thøgersen, K., Gilbert, A., Bouchayer, C., and Schuler, T. V.: Glacier Surges Controlled by the Close Interplay Between Subglacial Friction and Drainage, Journal of Geophysical Research: Earth Surface, 129, e2023JF007 441, doi:10.1029/2023JF007441, URL https://agupubs.onlinelibrary.wiley.com/doi/10.1029/2023JF007441, 2024.

Togaibekov, A., Gimbert, F., Gilbert, A., and Walpersdorf, A.: Observing and Modeling Short-Term Changes in Basal Friction During Rain-Induced Speed-Ups on an Alpine Glacier, Geophysical Research Letters, 51, e2023GL107 999, doi:10.1029/2023GL107999, URL https://agupubs.onlinelibrary.wiley.com/doi/10.1029/2023GL107999, 2024.

Toutin, T. and Cheng, P.: A Comparison of Automated DEM Extraction Results Using Along-Track ASTER and Across-Track SPOT Stereo Images, Tech. rep., doi:10.4095/219914, URL https://ostrnrcan-dostrncan.canada.ca/handle/1845/256932, 2002.

Trantow, T. and Herzfeld, U. C.: Spatiotemporal mapping of a large mountain glacier from CryoSat-2 altimeter data: surface elevation and elevation change of Bering Glacier during surge (2011–2014), International Journal of Remote Sensing, 37, 2962–2989,

doi:10.1080/01431161.2016.1187318, URL https://www.tandfonline.com/doi/full/10.1080/01431161.2016.1187318, 2016.

Trantow, T. and Herzfeld, U. C.: Progression of the surge in the Negribreen Glacier System from two years of ICESat-2 measurements, Journal of Glaciology, pp. 1–42, doi:10.1017/jog.2024.58, URL https://www.cambridge.org/core/product/identifier/S0022143024000583/type/journal_article, 2024.

Truffer, M., Harrison, W. D., and Echelmeyer, K. A.: Glacier motion dominated by processes deep in underlying till, Journal of Glaciology, 46, 213–221, doi:10.3189/172756500781832909, URL https://www.cambridge.org/core/product/identifier/S0022143000213427/type/journal_article, 2000.

Truffer, M., Kääb, A., Harrison, W. D., Osipova, G. B., Nosenko, G. A., Espizua, L., Gilbert, A., Fischer, L., Huggel, C., Craw Burns, P. A., and Lai, A. W.: Glacier surges, in: Snow and Ice-Related Hazards, Risks, and Disasters, pp. 417–466, Elsevier, doi:10.1016/B978-0-12-817129-5.00003-2, URL https://linkinghub.elsevier.com/retrieve/pii/B9780128171295000032, 2021.

Turrin, J., Forster, R. R., Larsen, C., and Sauber, J.: The propagation of a surge front on Bering Glacier, Alaska, 2001–2011, Annals of Glaciology, 54, 221–228, doi:10.3189/2013AoG63A341, URL https://www.cambridge.org/core/product/identifier/S026030550026076X/type/journal_article, 2013.

Turrin, J. B., Forster, R. R., Sauber, J. M., Hall, D. K., and Bruhn, R. L.: Effects of bedrock lithology and subglacial till on the motion of Ruth Glacier, Alaska, deduced from five pulses from 1973 to 2012, Journal of Glaciology, 60, 771–781, doi:10.3189/2014JoG13J182, URL https://www.cambridge.org/core/product/identifier/S0022143000203122/type/journal_article, 2014.

Vale, A. B., Arnold, N. S., Rees, W. G., and Lea, J. M.: Remote Detection of Surge-Related Glacier Terminus Change across High Mountain Asia, Remote Sensing, 13, 1309, doi:10.3390/rs13071309, URL https://www.mdpi.com/2072-4292/13/7/1309, 2021.

Van Wychen, W., Jiskoot, H., Shannon, K., and Gorwill, C.: The long multiphase trunk–tributary surge history of the high-Arctic Chapman Glacier, 1959–2023, Arctic, Antarctic, and Alpine Research, 57, 2441 541, doi:10.1080/15230430.2024.2441541, URL https://www.tandfonline.com/doi/full/10.1080/15230430.2024.2441541, 2025.

Vincent, C. and Moreau, L.: Sliding velocity fluctuations and subglacial hydrology over the last two decades on Argentière glacier, Mont Blanc area, Journal of Glaciology, 62, 805–815, doi:10.1017/jog.2016.35, URL https://www.cambridge.org/core/product/identifier/S0022143016000356/type/journal_article, 2016.

Wahba, G.: Spline Models for Observational Data, Society for Industrial and Applied Mathematics, doi:10.1137/1.9781611970128, URL http://epubs.siam.org/doi/book/10.1137/1.9781611970128, 1990.

Wang, D. and Kääb, A.: Modeling Glacier Elevation Change from DEM Time Series, Remote Sensing, 7, 10 117–10 142, doi:10.3390/rs70810117, URL https://www.mdpi.com/2072-4292/7/8/10117, 2015.

Wang, Z., Jiang, Z., Wu, K., Liu, S., Zhang, Y., Wang, X., Zhang, Z., and Wei, J.: Characteristics of Glaciers Surging in the Western Pamirs, Remote Sensing, 15, 1319, doi:10.3390/rs15051319, URL https://www.mdpi.com/2072-4292/15/5/1319, 2023.

Wendt, A., Mayer, C., Lambrecht, A., and Floricioiu, D.: A Glacier Surge of Bivachny Glacier, Pamir Mountains, Observed by a Time Series of High-Resolution Digital Elevation Models and Glacier Velocities, Remote Sensing, 9, 388, doi:10.3390/rs9040388, URL http://www.mdpi.com/2072-4292/9/4/388, 2017.

Wester, P., Mishra, A., Mukherji, A., and Shrestha, A. B., eds.: The Hindu Kush Himalaya Assessment: Mountains, Climate Change, Sustainability and People, Springer International Publishing, doi:10.1007/978-3-319-92288-1, 2019.

Williams, C. K. I.: Gaussian Processes for Machine Learning, URL http://www.newton.ac.uk/files/seminar/20070809140015001-150844.pdf, 2007.

Wu, S., Cai, Y., Ke, C.-Q., Xiao, Y., Li, H., He, Z., and Duan, Z.: SWOT mission enables high-precision and wide-coverage lake water levels monitoring on the Tibetan Plateau, Journal of Hydrology: Regional Studies, 59, 102 357, doi:10.1016/j.ejrh.2025.102357, URL https://linkinghub.elsevier.com/retrieve/pii/S221458182500182X, 2025.

Xie, F., Liu, S., Zhu, Y., Qing, X., Tan, S., Gao, Y., Qi, M., Yi, Y., Ye, H., Afzal, M. M., Zhang, X., and Zhou, J.: Retrieval of high-resolution melting-season albedo and its implications for the Karakoram Anomaly, Remote Sensing of Environment, 315, 114 438, doi:10.1016/j.rse.2024.114438, URL https://linkinghub.elsevier.com/retrieve/pii/S0034425724004644, 2024.

Xu, X., Wang, W., Huang, D., Hu, X., and Fu, W.: Assessment of interannual and seasonal glacier mass changes in the Karakoram during 2018-2022 using ICESat-2 data, Journal of Hydrology, p. 130223, doi:10.1016/j.jhydrol.2023.130223, URL https://linkinghub.elsevier.com/retrieve/pii/S0022169423011654, 2023.

Yao, T., Bolch, T., Chen, D., Gao, J., Immerzeel, W., Piao, S., Su, F., Thompson, L., Wada, Y., Wang, L., Wang, T., Wu, G., Xu, B., Yang, W., Zhang, G., and Zhao, P.: The imbalance of the Asian water tower, Nature Reviews Earth & Environment, 3, 618–632, doi:10.1038/s43017-022-00299-4, URL https://www.nature.com/articles/s43017-022-00299-4, 2022.

Yao, X., Zhou, S., Sun, M., Duan, H., and Zhang, Y.: Surging Glaciers in High Mountain Asia between 1986 and 2021, Remote Sensing, 15, 4595, doi:10.3390/rs15184595, URL https://www.mdpi.com/2072-4292/15/18/4595, 2023.

Yasuda, T. and Furuya, M.: Dynamics of surge-type glaciers in West Kunlun Shan, Northwestern Tibet, Journal of Geophysical Research: Earth Surface, 120, 2393–2405, doi:10.1002/2015JF003511, URL https://onlinelibrary.wiley.com/doi/abs/10.1002/2015JF003511, 2015.

Zhang, G., Bolch, T., Yao, T., Rounce, D. R., Chen, W., Veh, G., King, O., Allen, S. K., Wang, M., and Wang, W.: Underestimated mass loss from lake-terminating glaciers in the greater Himalaya, Nature Geoscience, 16, 333–338, doi:10.1038/s41561-023-01150-1, URL https://www.nature.com/articles/s41561-023-01150-1, 2023a.

Zhang, Z., Zhao, J., Liu, S., Zhang, Q., Jiang, Z., Xu, Y., and Su, H.: Characterization of Three Surges of the Kyagar Glacier, Karakoram, Remote Sensing, 15, 2113, doi:10.3390/rs15082113, URL https://www.mdpi.com/2072-4292/15/8/2113, 2023b.

Zhu, Q., Ke, C.-Q., and Li, H.: Monitoring glacier surges in the Kongur Tagh area of the Tibetan Plateau using Sentinel-1 SAR data, Geomorphology, 390, 107 869, doi:10.1016/j.geomorph.2021.107869, URL https://linkinghub.elsevier.com/retrieve/pii/S0169555X21002774, 2021.

Zhu, Q. H., Ke, C. Q., Li, H. L., and Yu, X. N.: Identification of Unstable Glacier Flow in the Western Tibetan Plateau and Karakoram Using Machine Learning, Journal of Geophysical Research: Earth Surface, 127, doi:10.1029/2022JF006623, URL https://onlinelibrary.wiley.com/doi/10.1029/2022JF006623, 2022.

Zhu, Q. H., Li, H. L., and Ke, C. Q.: Consecutive Glacier Sub-Surge Events Within Five Years Were Identified in an Unexplored Glacier of the Karakoram, Journal of Geophysical Research: Earth Surface, 130, e2024JF007 974, doi:10.1029/2024JF007974, URL https://agupubs.onlinelibrary.wiley.com/doi/10.1029/2024JF007974, 2025.

Zoet, L. K. and Iverson, N. R.: Rate-weakening drag during glacier sliding, Journal of Geophysical Research: Earth Surface, 121, 1206–1217, doi:10.1002/2016JF003909, URL https://agupubs.onlinelibrary.wiley.com/doi/10.1002/2016JF003909, 2016.

Zoet, L. K. and Iverson, N. R.: A slip law for glaciers on deformable beds, Science, 368, 76–78, doi:10.1126/science.aaz1183, URL https://www.science.org/doi/10.1126/science.aaz1183, 2020.

Zoet, L. K., Iverson, N. R., Andrews, L., and Helanow, C.: Transient evolution of basal drag during glacier slip, Journal of Glaciology, 68, 741–750, doi:10.1017/jog.2021.131, URL https://www.cambridge.org/core/product/identifier/S0022143021001313/type/journal_article, 2022.